

# **Microstructure Evaluation & Process Optimization of Ti6Al4V-xB & Tool Steel Produced by Laser Powder Bed Fusion**

Submitted in partial fulfillment of the requirements for the degree of

Doctor of Philosophy in

Department of Materials Science and Engineering

Yining He

B.S., Materials Science and Engineering, Shandong University

M.S., Materials Science and Engineering, Carnegie Mellon University

Carnegie Mellon University

Pittsburgh, PA

May 2020

## Acknowledgment

First, I would like to express my sincere appreciation to my advisor, Professor Bryan A. Webler. I am always grateful to him for offering inspiring and insightful guidance throughout the four years of my Ph.D. study and for giving me encouragement and trust to explore new research directions. His insightful suggestion and continuous supports help me overcome many challenges in both research and career. The joy and enthusiasm he has for scientific research were contagious and motivational for me, which inspires me to pursue a career in the scientific field. It is my privilege to have him as my advisor and mentor through my Ph.D. study.

Next, I would like to express my gratitude to the committee members, Professor P.Chris Pistorius, Professor Anthony D. Rollett, Professor Jack Beuth, for devoting their time and knowledge to provide constructive comments and feedback that significantly improved my research work. I would also like to extend my gratitude to Professor P.Chris Pistorius for his dedicated guidance as my master research supervisor, which greatly sharpened my ability of critical thinking.

I owe special thanks to Dr. Sandra DeVincent Wolf and Dr. Zhuqing Wang, who have devoted their time and effort to my career development. They are and will always remain my role model for a scientist and career mentor.

I would like to thank all the past and current group members: Haoyuan Mu, Jia Tan, Rafael Giacomini, Mary Story, Steve Kachur, Ming Zhong, Anna Weiss, Rachel English, Debomita Basu, Mohammad Abdulsalam, Andrew Huck, Ke Xu, Chengsong Liu. I am grateful for their insightful discussion and assistance on my research work and for making our group such a fun and pleasant place to work in.

I would like to acknowledge the students in Professor Beuth's Research Group at Carnegie Mellon University, particularly Nick Jones, Colt Montgomery and Luke Scime, without whom much of my Ph.D. research work would not have been possible.

I would also like to thank all the staff members in NextManufacturing center and CMU MSE department for providing professional suggestions and experimental assistance. I would like to sincerely thank Todd Baer, Betsy Clark and Tom Nuhfer regarding their help on LPBF experiments and characterization tests.

And I feel so grateful to have the support from my friends, including the new friends I met during my Ph.D. years and my old friends back in China. Their friendship is one of the most valuable things I cherished in my life.

Lastly, I would like to express my deepest thanks to my parents, Benchu Cheng and Aijun He. Your unconditional love is the source of my courage and strength to start and go through this journey.

This research was supported by the Carnegie Mellon University Manufacturing Futures Initiative, made possible by the Richard King Mellon Foundation. Support from the NextManufacturing Center at Carnegie Mellon University is acknowledged. The use of the Materials Characterization Facility at Carnegie Mellon University by grant MCF-677785 is also acknowledged.

## Abstract

Laser powder bed fusion (LPBF) is one of the most popular metallic AM processes. It produces a 3D-parts by repeated powder layer deposition followed by laser scanning. A major obstacle of LPBF investigation is the difficulty to obtain lab-scale LPBF-powder for compositions of interest. In this regard, this work used “powder-free approach” to explore the effects of LPBF processing on microstructure and properties. Three alloy systems were investigated, each not widely used in LPBF processing, H13 tool steel, M2 tool steel, and boron-modified Ti6Al4V.

Melt pools made without powder were similar in dimensions, geometry, and microstructures to melt pools made with powder. Dimensions were quantified for Ti6Al4V and H13. The balling phenomenon occurred at lower power and velocity combinations when powder was presented. The single-track test results enabled an empirical model to be developed for laser absorptivity.

Chapter 6 presented the work on LPBF process optimization for tool steel. Two steel grades, H13 and M2 steel, were investigated. For H13 steel, a sequential set of studies was performed: single laser tracks, multi-track pads, and 3D cubes, with 40 P-V settings tested for single tracks. Tracks and pads were made by both no-powder and powder-added laser scan. For M2 steel, no-powder single-track tests were conducted, with 28 P-V settings tested. P-V process mappings of melt pool geometry were developed for H13 and M2 steel. They identify the P-V regions where keyholing, balling and under-melt occurred. The P-V mappings for H13 and M2 steel show different keyholing P-V thresholds, indicating the influence of high-boiling-temperature element on keyholing behavior. The no-powder and powder-added P-V mappings for H13 steel show that the presence of powder layer resulted in a slight shift in the balling P-V threshold.

Microstructure inhomogeneity was observed for both H13 and M2-steel melt pool: For H13 steel, a cellular-network microstructure and an isolated-whisker microstructure co-existed at different regions in the same melt pool. Solute pile-up due to solidification microsegregation was observed at the cellular boundaries, where retained austenite was present. Relative amounts of the microstructure types in each melt pool varied with P-V parameter. Consistency in microstructure inhomogeneity was observed for tracks and pads produced at the same P-V sets. Cracks were found in some pads, which appeared to propagate through the isolated whisker microstructure. Based on this, P-V windows of different cracking tendencies were predicted based on the microstructure P-V map. 3D-cubes built by P-V sets in different windows showed crack densities in line with the predictions. A microstructure evolution mechanism was proposed, which explains the microstructure inhomogeneity as a result of

varied microsegregation levels at different regions in the melt pool. Based on the proposed mechanism, melt pool microstructure was predicted by coupling DICTRA simulation with melt pool thermal profile calculation, showing good agreement to the experimental observation. For M2 steel, microstructure inhomogeneity was induced by columnar-to-equiaxed transition (CET) in the melt pool. Single-tracks for the 28 selected P-V sets showed either fully columnar, columnar+equiaxed mixed or mainly equiaxed dendritic microstructure. A CET criteria was combined with melt pool thermal profile calculation to predict P-V process map for M2-steel microstructure (columnar/equiaxed). The predicted and experimental P-V maps showed good agreement in the P-V space.

Chapter 7 presented the work on LPBF composition evaluation for five Ti6Al4V-xB trial composition: Ti6Al4V + (0, 1, 2, 5, 10, wt.%) B. Single-tracks, multi-track pads and overlap-track pads were made on the surface of arc-melted Ti6Al4V-xB buttons. For each Ti6Al4V-xB composition, melt pools were produced by 14 P-V sets over wide P-, V-ranges, with melt pool geometry and microstructure information gathered into P-V maps. By varying wt.% B and P-V parameter, four TiB precipitate morphologies were produced. Melt pool microhardness showed evident enhancement from arc-melted baseline for all Ti6Al4V-xB compositions. Ti6Al4V-xB with 2-5 wt% B as a promising composition range for LPBF processing. The four TiB morphologies observed at different [B%, P-V] combinations were considered as the product of different solidification mode (primary  $\beta$ -Ti, primary TiB and coupled eutectic). An analytical model was developed to determine the criteria of LPBF solidification mode transition as a function of P-V parameters and Ti6Al4V-xB material properties. The calculated P-V maps for LPBF solidification mode transition showed good agreement with experimental results. This model suggested that certain P-V window leads to coupled-eutectic solidification and non-equilibrium primary- $\beta$  solidification mode even for highly hyper-eutectic Ti6Al4V-5%B, in turn leading to TiB presenting continuous network and discontinuous network agglomeration of nano-scale TiB whiskers.

# Table of Contents

Acknowledgment .....	2
Abstract .....	4
Table of Contents .....	6
List of Tables .....	9
List of Figures .....	11
1 Introduction .....	22
1.1 LPBF process and “powder-free” method.....	22
2 Technical Background.....	25
2.1 LPBF melt pool solidification .....	25
2.1.1 Heat transfer during melt pool deposition.....	25
2.1.2 Keyholing and its influence.....	29
2.1.3 Balling and its influence.....	30
2.2 Non-equilibrium LPBF solidification.....	33
2.2.1 Microsegregation during rapid solidification .....	33
2.2.2 Columnar-to-equiaxed transition during rapid solidification.....	37
2.2.3 Solidification mode transition during rapid solidification .....	39
2.3 LPBF of tool steel.....	41
2.4 LPBF of Ti6Al4V-xB.....	45
3 Hypotheses and Approach.....	48
4 Experimental .....	50
4.1 Materials .....	50
4.1.1 Tool steels .....	50
4.1.2 Ti6Al4V-xB .....	51
4.2 LPBF laser scan experiments .....	52
4.3 Characterization Methods.....	58
Results and Discussion: Chapter 5-7.....	61
5 Powder/bulk absorptivity estimation.....	61

6	LPBF of tool steel: process optimization .....	68
6.1	Melt pool geometry investigation .....	68
6.1.1	P-V mapping of melt pool geometry .....	68
6.1.2	Influence of powder presence on melt pool geometry .....	74
6.1.3	Influence of steel composition on melt pool geometry .....	76
6.2	LPBF microstructure inhomogeneity for tool steel .....	76
6.2.1	Microstructure inhomogeneity: observation .....	76
	• H13 steel: .....	77
	• M2 steel:.....	82
6.2.2	Microstructure P-V mapping.....	83
	• H13 steel: no powder vs. powder added .....	83
	• M2 steel: no powder.....	87
6.2.3	Mechanism for H13 steel microstructure inhomogeneity: .....	90
	• Proposed mechanism: .....	91
	microsegregation-induced microstructure inhomogeneity .....	91
	• Validate mechanism:.....	97
	microstructure prediction vs. experimental observation .....	97
6.2.4	Criteria for M2-steel columnar-to-equiaxed transition (CET) .....	102
	• Developing G-R criteria for the CET.....	103
	• Verifying G-R criteria:.....	108
6.2.5	Microstructure inhomogeneity and hardness .....	111
	• H13 steel .....	111
	• M2 steel.....	112
6.3	P-V process optimization for LPBF of tool steel .....	113
6.3.1	H13 steel: P-V process optimization for cracking.....	113
	• Multi-track observation.....	113

• 3D cube observation .....	116
6.3.2 M2 steel: P-V process optimization for promoting CET .....	120
6.4 Results Summary .....	124
7 LPBF of Ti6Al4V-xB: composition evaluation .....	127
7.1 Assessment of test material (arc-melted Ti6Al4V-xB buttons) .....	127
7.2 Melt pool dimensions .....	129
7.3 Melt pool geometry .....	130
7.3.1 P-V mapping for melt pool geometry.....	130
7.3.2 P-V window for porosity control .....	131
7.4 Melt pool microstructure .....	133
7.4.1 Single-track: Microstructure P-V mapping .....	133
7.4.2 Single-track vs. Multi-track vs. Overlap-track.....	139
7.5 Melt pool hardness.....	142
7.6 Promising LPBF composition identification .....	144
7.7 LPBF solidification mode transition criteria .....	147
7.7.1 Model for solidification mode transition.....	147
7.7.2 Model evaluation.....	153
7.8 Powder-free method: range of application .....	156
7.9 Results Summary .....	158
8 Conclusion and Hypotheses Revisited .....	160
9 Project major contribution.....	167
Reference.....	168
Appendix .....	186

## List of Tables

Table 1 chemical composition (wt.%) of M2-, H13-steel bulk plate and H13-steel powder determined by ICP-AES and LECO Combustion .....	50
Table 2 characterization result for powder flowability .....	51
Table 3 List of LPBF laser scan tests conducted in this work with number of P-V sets (P: laser power; V: scan velocity), material and laser scan pattern adopted in each laser scan test.....	53
Table 4 P-V settings tested for Ti6Al4V-xB single-bead laser scan test .....	54
Table 5 Alloy properties used for calculation [29,130,131].....	54
Table 6 laser P-V settings tested for Ti6Al4V-xB multiple-bead and overlap-bead laser scan test .....	56
Table 7 P-V settings selected for tool steel laser scan test: for M2-steel no-powder test:28 P-V sets: P-V#1-#28, H13-steel no-powder and powder-added single-bead test: all 40 P-V sets, H13-steel multiple-bead test: 18 P-V sets: indicated by “p”, H13-steel 3-D cube build test:8 P-V sets: indicated by “c” .....	57
Table 8 summary of characterization methods and corresponding characterization location conducted for laser-track, pad, and cube samples .....	60
Table 9 Summary of absorptivity values from literature for each material system .....	61
Table 10 fitting parameter in absorptivity model for Ti6Al4V and H13-steel (powder/bulk) ....	63
Table 11 dataset used for absorptivity model generation for each test material .....	63
Table 12 fitting model for the Q-V threshold of different melt pool geometry for H-13 and M2 steel.....	73
Table 13 Comparison of experimental and calculated equiaxed dendrite% ( $\phi$ ) in melt pools for the three microstructure categories in P-V process map .....	89
Table 14 Comparison of experimental and calculated vol% of type (A) microstructure in melt pools for different P-V sets .....	98
Table 15 material properties for CET criteria calculation.....	105

Table 16 fitting model for the Q-V thresholds of different melt pool geometry for Ti6Al4V-1,2,5%B .....	132
Table 17 five types of Ti6Al4V-xB melt pool microstructure: comparison of TiB precipitate feature, solidification mode and existence for laser deposition of Ti6Al4V-1,2,5% B .....	137
Table 18 entropy of fusion for Ti-TiB system .....	149
Table 19 equation model for interfacial temperature of each solidification phase .....	150
Table 20 Parameters for interfacial temperature equations in Table 19.....	150
Table 21 values for Ti6Al4V-xB material properties used in calculation of material-related parameters in Table 20 .....	151
Table 22 no-powder and powder-added melt pool width deviation at same Q-V combination for Ti6Al4V and H13 steel .....	187
Table 23 Experimental measurement for vol.% of type (A) microstructure in no-powder and powder-added melt pool fabricated by P-V no.#1-#40 (see Table 7) .....	189

## List of Figures

Fig 1 schematic of LPBF- additive manufacturing system (based on EOS M290 machine model)	22
Fig 2. schematic of heat transfer during LPBF melt pool deposition[14]	26
Fig 3 laser deposition in keyhole mode: schematic of physical phenomena and molten melt pool temperature distribution in keyhole mode (a)[37] and typical examples of the resulting melt pool geometry by keyhole-mode laser deposition(b)[38]; keyhole-induced porosity: indicated in (b) .....	29
Fig 4 melt pool geometry variation along laser-deposited track of balling formation[40][41]: (a) laser track top view; (a-1): melt pool cross section at bead-up location of laser track (indicated by yellow line in (a)); (a-2): melt pool cross section at other location of laser track (indicated by green line in (a)) .....	30
Fig 5 balling-induced porosity: mechanism (a) and experimental observation (b)[43] .....	31
Fig 6 schematic of two balling mechanism (b1, b2) and their corresponding P-V process window(a); P: laser power; V: laser scan velocity; (b1): balling induced by melt pool flow with Raleigh instability; (b2) balling induced by high viscosity solid-liquid mixture melt pool flow, reproduced from [44] and [45] .....	32
Fig 7 comparison of Scheil-predicted & equilibrium-predicted solidification route for H13 steel from Thermo-Calc [35], focusing on liquid, $\delta$ -Fe & $\gamma$ -Fe phases (solid lines refer to equilibrium conditions; dashed lines refer to Scheil solidification) .....	34
Fig 8 Planar model representing half cellular size used for the DICTRA simulation of solidification segregation for LPBF melt pool of H13 steel .....	35
Fig 9 Solid fraction versus temperature for two steels: (a) Fe–5Cr–1C and (b) Fe–Cr–0.92%C estimated by equilibrium-, Scheil-, DICTRA- and partial equilibrium calculation [59] .....	36
Fig 10 Vertical section of Fe–Ni–Cr phase diagram at 59% Fe showing the equilibrium solidification mode of seven alloys of investigation (a) and solidification mode of electron beam welds as a function of beam scan speed for the seven investigated alloys (b); in (a) and (b): letter L, A, F indicate liquid phase, primary austenite phase and primary ferrite phase, respectively; in (b): both solidification mode and microstructure morphology were summarized [83] [21] .....	40

Fig 11 Effect of laser welding velocity on solidification mode and hot cracking susceptibility for 304 stainless steel laser welding; letter “AF”, “FA” denote primary austenite solidification and primary ferrite solidification mode respectively; “FA+AF” mode: schematically shown in the figure on the right [71].....	41
Fig 12 Solidification phase transformation for M2 steel (left) and H13-steel (right) calculated by Scheil-Gulliver Model; symbols: $\delta$ -Fe: ferrite; $\gamma$ -Fe: austenite; $M_6C$ , $M_7C_3$ , MC: carbide .....	44
Fig 13 size distribution of H13 powder particles used in this work.....	50
Fig 14 Pseudo-binary phase diagram of Ti6Al4V-B system: trial compositions of this study indicated by red dashed line .....	51
Fig 15 Schematic diagram of (a) Ti6Al4V-xB alloy button; (b) button holder in the EOS M290 machine .....	52
Fig 16 Selected P-V sets for Ti6Al4V-xB laser scan test with lines of constant cooling rate approximated from the Rosenthal equation (Equation 8); P-V value: see Table 4.....	54
Fig 17 schematics of three different laser scan experiment to fabricate (a) single-track, (b) single-layer pad, (c) 2-layer pad on the arc-melted Ti6Al4V-xB buttons .....	55
Fig 18 40 P-V sets selected for H13-steel no-powder & powder-added single bead laser scan test with predicted constant cooling-rate curves (indicated by solid lines with different colors) .....	58
Fig 19 Schematic of the LPBF-built cubes for H13-steel illustrating the three cross-sections for microstructure and cracking characterization.....	60
Fig 20 Comparison of melt pool width between laser scan on Ti64 bulk alloy and Ti64 powder layer for 3 datasets (data source: this work and [38]) by adopting: (a) varying absorptivity model in Equation 10; (b) constant absorptivity; non-keyhole data point outlier: marked by red dashed circle .....	65
Fig 21 Comparison of melt pool width between laser scan on bulk H13-steel and H13-steel powder layer for 3 datasets by adopting: (a) varying absorptivity model in Equation 10; (b) constant absorptivity; non-keyhole data point outlier: marked by red dashed circle; note: no-powder(2) dataset: validation data not used for data fitting.....	65

Fig 22 comparison of 4 different types of melt pool geometries observed for H-13 steel melt pool: (a) normal geometry; (b) key-holing geometry; (c) under-melt geometry; (d) balling geometry; melt pool boundary: marked by red dashed lines .....69

Fig 23 P-V process map of melt pool geometry for H13-steel single track; (a): powder-added; (b): no-powder (4 types of melt pool geometry categories in the map: shown in Fig 22.).....70

Fig 24 comparison of P-V process map of melt pool geometry for M2 steel(a) and H13 steel(b); (a)-(b): based on no-powder single track experimental result (4 types of melt pool geometry categories in the map: shown in Fig 22.).....70

Fig 25 examples of melt pool presenting both keyholing and balling geometry features; example provided by H13 steel melt pool fabricated by P-V set #27 [350W-1200mm/s].....71

Fig 26 example OM images of H13 steel single-track with different melt pool geometries (left) and their corresponding multi-track (right) generated by same P-V set; (a) normal geometry; (b) keyholing geometry; (c) under-melt geometry; (d) balling geometry, exemplified by P-V #29 [125W-1200mm/s], P-V#4[150W-800mm/s], P-V#22[300W-1200mm/s], and P-V#20 [300W-800mm/s] in Table 7 respectively, melt pool boundary: marked by yellow dashed line .....72

Fig 27 A process window (shadow area in (b), i.e., area enclosed by dashed lines) using the melt pool geometry P-V map (example shown for H13-steel) .....73

Fig 28 H13-steel single-track with and without powder addition at same P-V sets showing different balling behavior; example provided: P-V #38 [150W-1400mm/s]; non-balling for no-powder case (a1-a2), balling for powder-added case(b1-b2);.....74

Fig 29 top surface images of H13-steel multiple-track pad showing different balling behavior with and without powder addition generated at same P-V set; example provided by P-V set #38 [150W-1400mm/s] for (a1)(a2), P-V #25[300W-1800mm/s] for (b1)(b2): non-balling for no-powder case (a1), balling for powder-added case(a2); slight balling for no-powder case (b1), severe balling for powder-added case(b2) .....75

Fig 30 typical observation of microstructure inhomogeneity in H-13 steel single-track melt pool; in (i), melt pool boundary: marked by white dashed line, example provided by P-V#4; melt pool in (i): exhibited two localized region with different microstructure (distinguish by bright-contrast and dark-contrast, separated by a “loop-shape” boundary marked by red dashed line), referred to as type (A) and (B) microstructure, indicated by letter “A” and “B” in (i), shown in high magnification image

(ii) and (iii) (close-up of the yellow and green box in (i)); yellow box in (a)-(d): examples of randomly scattered type (A) microstructure in localized type (B) microstructure; Table at right: TEM and EBSD phase identification for each microstructure feature .....77

Fig 31 typical microstructure observation for H13-steel track longitudinal section (a); example provided by P-V #9; the corresponding melt pool cross-section of same P-V set: shown in Fig 30; Track showed coexistence of cellular-network microstructure (type (A)) and isolated microstructure (type (B)), distinguished by dark contrast and bright contrast; white dashed line: indicates the boundary separating the region with type (A) and (B) microstructure; (b), (c): close-up for region in yellow and green box in (a) respectively, showing high magnification image for type (A) and type (B) microstructure; cracks: observed in type (B) microstructure, indicated by white arrow .....79

Fig 32 typical SEM image (a) and TEM bright field (BF) image (b) for type (A) microstructure in H13-steel melt pool (see Fig 30). BF image shows two phases, identified as ferrite and austenite (indicated by letter “ $\alpha$ ” and “ $\beta$ ”). Red box in (a) indicates the location for TEM characterization. The interface between the two phases is indicated by the white arrow. (b-1) and (b-2) shows the SAED patterns characterized at the region with the ferrite phase and austenite phase respectively. SAED characterization location: indicated by red and blue arrows. ....80

Fig 33 typical SEM image (a) and TEM bright field (BF) image (b) for type (B) microstructure in H13-steel melt pool (see Fig 30). BF image shows two phases, identified as ferrite and martensite (indicated by letter “ $\alpha$ ” and “m”), corresponding to the matrix and needle-phase in (a). (b-1) and (b-2) shows the SAED patterns characterized at the region with ferrite phase and martensite phase respectively. SAED characterization location: indicated by red and blue boxes. TEM-BF image in (c) shows a suspected twin-dislocation observed in type (B) microstructure .....80

Fig 34 STEM-HAADF image (a) for FIB specimen lifted-out from the local region with type (A) microstructure (see Fig 32) in H13-steel single-track melt pool with the corresponding STEM-EDX maps showing segregation of C, Cr, V, Mo at the cellular boundary where austenite presents (see Fig 32).....82

Fig 35 typical examples for 3 types of melt pool microstructure observed for the M2-steel single tracks fabricated by the 28 selected P-V sets (see Table 7); examples provided by P-V #13, #9, #3; equiaxed and columnar dendrite microstructure coexisted in each melt pool in (a)-(c), shown in high magnification image (b-1) and (b-2) (close-up of the red and green box in (b-2)); in each melt pool:

region with equiaxed and columnar dendrite: distinguished by dark and bright contrast respectively, indicated by letter “equiaxed” and “columnar” .....83

Fig 36 typical examples for 4 types of melt pool microstructure observed for H13-steel single tracks fabricated by the 40 selected P-V sets (Table 7); examples provided by P-V #20, #6, #4, #36 (value of P, V: labeled below each figure); note: (d-1), (d-2): two cross-sections taken at different location of the same sing-track; in (a)-(d): white dashed line: melt pool boundary; red dashed line: loop-shape boundary separating localized type(A) and (B) microstructures in each melt pool (see Fig 30(ii), (iii)); region with type (A) microstructure: bright contrast, region with type (B) microstructure: dark contrast, indicated by letter “A” and “B”; yellow/green box in (a)-(d): examples of randomly scattered type (A)/(B) microstructure in localized type (B)/(A) microstructure .....84

Fig 37 H13-steel microstructure P-V process map for single-track melt pool with (a) powder-added laser-scan condition and (b) no-powder laser-scan condition, based on the categorization of four microstructure types presented in Fig 36 .....87

Fig 38 Comparison between experimental (a) and predicted (b) microstructure P-V process map for M2 steel single-track, with balling P-V threshold overlapped. (P-V thresholds: developed by the Q-V thresholds in Table 12, chapter 6.1.1) .....89

Fig 39 typical example of M2-steel melt pool showing varied microstructure at different location along laser track, corresponding to “varied microstructure” category in process map (Fig 39); noted: (a), (b) are two cross sections taken at different location of the same sing-track; example provided by P-V#25 (300W-1800mm/s) .....90

Fig 40 C and V wt.% in  $\gamma$ -Fe versus temperature for H13-steel solidification (a) and H13-steel solidification phase transformation route (b); (a) and (b): calculated by Scheil-Gulliver Model; symbols in (b):  $\delta$ -Fe: ferrite;  $\gamma$ -Fe: austenite;  $M_7C_3$ , MC: carbide .....93

Fig 41 change of  $M_s$  temperature for  $\gamma$ -Fe formed from beginning to end of H13-steel solidification; calculation: based on comp% profile calculated by Scheil-Gulliver model (see Fig 40); low- $M_s$   $\gamma$ -Fe: referred to  $\gamma$ -Fe with  $M_s < 130^\circ\text{C}$ , as  $50^\circ\text{C}$  above preheat temperature .....94

Fig 42 schematic of microstructure evolution mechanism for type (A) & (B) microstructure located at the near-top and near-bottom region of H13 steel melt pool (see Fig 30); high- $M_s$   $\gamma$ , low- $M_s$   $\gamma$ -Fe: austenite with  $M_s > 130^\circ\text{C}$  and  $M_s < 130^\circ\text{C}$ , defined in Fig 41;  $\gamma$  and  $\gamma'$ : austenite formed from solidification and solid-state phase transformation; M: martensite .....97

Fig 43 Comparison of predicted results(a,b-2) and experimental results(a,b-1) for H13-steel melt pool microstructure showing coexistence of type (A) and type (B) microstructure on cross section with process setting specified as P-V#5, #8, presented in (a-1,2,3) and (b-1,2,3) respectively; in (a,b-1): red dashed line indicates the boundary separating region with type (A) and (B) microstructure in melt pool, location of the two microstructure: indicated by letter “A” and “B”; microstructure prediction: based on calculation result for melt pool cooling rate profile (a,b-3) at end of solidification for corresponding P-V set. ....99

Fig 44 carbon concentration (wt.%) vs. distance from cell core to cell boundary (i.e., half of cellular network spacing ( $\lambda$ )) in type (A) microstructure of H13 steel (see Fig 30) for different solidification cooling rate (T) calculated by DICTRA simulation and compared with Scheil-Gulliver simulation; selected solidification cooling rates: within the range of LPBF melt pool solidification cooling rate estimated by melt pool thermal numerical calculation (see Fig 43); in (a): DICTRA setup adopted constant  $\lambda$  for different cooling rates; in (b): DICTRA setup adopted different  $\lambda$  for each cooling rates based on the relation of  $\lambda \propto T - 1/3$ ; Noted: (b) shows some curve fluctuation for setup of  $\lambda < 0.3\mu\text{m}$  potentially due to convergence issue ..... 101

Fig 45 G-R microstructure map (c) for M2 steel showing the G-R condition for promoting equiaxed and columnar dendrite growth, as indicated by the dark and light shade in (c); criteria for CET occurrence: indicated by dashed line in (c); the three color-lines inserted in (c): represent the correlation between G and R for each location across whole melt pool depth at melt pool centerline, calculated for process condition of P-V#3, #9, #13; arrow on color line: indicate direction from melt pool surface to bottom; point “A”, “B”, “C”: represent the location at melt pool centerline separating equiaxed and columnar microstructure in melt pool of P-V#3, #9, #13; (a) and (b) show the evolution of G and R as function of Z at melt pool centerline(Z: melt pool depth; melt pool surface: Z=0); Note: whole melt pool thermal profile and microstructure prediction for the three P-V sets shown in Fig 46 ..... 107

Fig 46 M2-steel single track top surface microstructure (a) used for measuring distance between adjacent equiaxed dendrite measurement (b); in (a): the white dashed lines: single-track boundary; in the single-track: local regions with equiaxed and columnar dendrite are separated by red dashed lines and indicated by label above (a); (b) is the high magnification image of the red box in (a); in (b): double-arrow red line indicates the distance between adjacent equiaxed dendrite ..... 107

Fig 47 Comparison of calculated results(a,b,c-2) and experimental results(a,b,c-1) for equiaxed and columnar dendrite in M2-steel melt pool microstructure with process setting of P-V#13, #9, #3; experimental results in (a,b,c-1): equiaxed and columnar dendrite distribution: distinguished by dark-contrast and bright-contrast; microstructure prediction in (a,b,c-2): based on calculation of melt pool thermal profile at end of solidification for corresponding P-V sets (solidification velocity: a,b,c-3; temperature gradient:a,b,c-4);.Note: P-V #13, #9, #3 belong to different microstructure group in experimental microstructure process map of M2-steel (Fig 38(a));..... 109

Fig 48 microhardness for track, pad, cube fabricated by P-V set #4, #14, #20, #10, each in different microstructure categories in P-V map (Fig 37), as presented in table below the chart; microhardness: measured for different microstructure found in track/pad/cube, as indicated by the label (microstructure: type (A), (B) see Fig.10(ii), (iii) for track, Fig 49(b-1),(b-2) for pad; type (A') and (B') see Fig 51(b), (c) for cube) ..... 112

Fig 49 typical melt pool hardness measurement for P-V sets in CET promoting and suppressing group (microstructure groups: indicated by the labels at the top); for P-V sets of promoting group: local microhardness compared for the regions with equiaxed and columnar dendrite within same melt pool..... 113

Fig 50 typical multi-track melt pool microstructure for P-V set of “large-A” type (a) and “small-A” type (b) in microstructure P-V map (Fig 37); exemplified by P-V #20 [300W-800mm/s] and P-V #4 [150W-800mm/s] (Fig 36(a), (c): corresponding single-track melt pool microstructure at same P-V set); microstructure inhomogeneity similar to single-track (Fig 30) was observed: each multi-track melt pool (melt pool boundary: marked by white dashed line) presented two types of microstructures, referred to type (A) and (B) microstructure, shown in (b-1) and (b-2) (zoom-in images of yellow and green box in (b)); in (a),(b): red dashed lines indicate the loop-shape boundary separating region with type (A) and (B) microstructure in each melt pool, distinguished by bright and dark contrast and denoted by letter “A” and “B”..... 115

Fig 51 Typical cracking observation for H13 multi-track pad with “small-A” type microstructure; (b): zoom-in image of red box in (a); crack: indicated by white arrows; white dashed lines: melt pool boundary; a loop-shape boundary (partially marked by red-dashed line) separates local region with type (A) microstructure (bright contrast, indicated by “A”) and region with type (B) microstructure (dark contrast, indicated by “B”) in melt pool; (type (A) and (B) microstructure, see Fig 30(b-1) and (b-2)); ..... 116

Fig 52 typical microstructure for H-13 cube with severe cracking (example provided by P-V#4); in (a): white dashed line: melt pool boundary (denoted as “M.P. boundary”) and red arrow: cracks; two microstructures observed in one melt pool: referred to as type (A’) and (B’), shown in (b) and (c) respectively; (b), (c): zone in image of yellow and green box in (a) ..... 117

Fig 53 XRD pattern for H13 steel cube (a) and pad (b) processed by same P-V set (example provided by P-V set#20 [300W-800mm/s] compared to un-laser treated H13 steel matrix (c); microstructure: see Fig 50(a)); austenite vol.% for (a)-(c): listed on the right ..... 117

Fig 54 crack density measurement for H-13 steel cubes built by 8 P-V sets selected in this study (marked by “c” in Table 7), with their corresponding melt pool microstructure category summarized in the table below the figure; average crack density: measured from 120 sections (1mm<sup>2</sup>) per cube ..... 118

Fig 55 typical H-13 steel cube crack observation for P-V sets of “small-A” and “varied microstructure” categories (a) and P-V sets of “medium-A” and “large-A” microstructure categories (b), examples provided by cube of P-V # 36 and #14; (c): zoom-in image of the red box in (b); microstructure category: see chapter 6.2.2 and Fig 36..... 119

Fig 56 SEM images (BSE mode) of arc-melted microstructure for Ti6Al4V-xB alloy buttons of 4 trial compositions: Ti6Al4V-1B, 2B, 5B, 10B, shown in (a), (b), (c), (d) respectively; TiB<sub>eut</sub>—eutectic TiB; TiB<sub>pri</sub>—primary TiB; (e): measured TiB vol.% in laser-scanned region by SEM image process vs. predicted TiB vol.% for alloy buttons with different trial compositions; error bar (standard deviation) indicated by red label ..... 128

Fig 57 Comparison of single-bead melt pool width for different Ti6Al4V-xB trial compositions (Q: absorbed laser power; V: laser scan speed); melt pool width for each P-V sets; error bars were added to one of the data points for each trial Ti6Al4V-xB composition, representing the average standard deviation for 3 melt pool cross sections of each Ti6Al4V-xB trial compositions..... 129

Fig 58 Melt pool geometry P-V mapping for B-free Ti6Al4V ((a)) and four Ti6Al4V-xB compositions (1%, 2%, 5%, 10%B: (b), (c), (d), (e))..... 130

Fig 59 example showing change in melt pool geometry by different B addition with same P-V set (example shown for P-V set#9: 115W-800mm/s); (a): Ti6Al4V; (b): Ti6Al4V-1%B; (c): Ti6Al4V-10%B ..... 131

Fig 60 Workflow for generating preliminary process window for porosity control (shadow area in (b), i.e., area enclosed by dashed lines) for Ti6Al4V-xB using the melt pool geometry P-V map (example shown for Ti6Al4V-1%B)..... 133

Fig 61 Typical SEM images of 5 different Ti6Al4V-xB melt pool microstructure observed for 56 tested [Ti6Al4V-xB, P-V ] combination, referred to as Type (i)~(v) microstructure, respectively showing uniformly-distributed TiB<sub>eut</sub> whisker ((a-1), (a-2)), continuous TiB network ((b-1), (b-2)), discontinuous TiB network ((c-1), (c-2)), nano scale TiB<sub>eut</sub> needle+ TiB<sub>pri</sub> rod ((d-1), (d-2)) and dendritic TiB<sub>pri</sub> rod+ nano-scale TiB<sub>eut</sub> needle ((e-1), (e-2)). TiB<sub>eut</sub>: eutectic TiB; TiB<sub>pri</sub>: primary TiB; (i-2) image on the right: high magnification image of green box in (i-1) image on the left, with i as a, b, c, d, e..... 136

Fig 62 melt pool microstructure P-V mapping for each Ti6Al4V-xB candidate compositions, with Ti6Al4V-1%B, 2%B, 5%B, 10%B shown in (a), (b), (c), (d) respectively; Note: labels with multiple colors (e.g. #11 for Ti6Al4V-1%B in (a)) corresponds to different microstructures observed on a single melt pool cross section..... 138

Fig 63 Ti6Al4V-xB melt pool showing local microstructure inhomogeneity: (a) melt pool cross section; white dashed line in (a): mark melt pool boundary; (b), (c): zoom-in image of yellow and red box in (a); blue arrow in (b)(c): mark TiB precipitate; (d): possible melt pool fluid flow scenario causing the melt pool microstructure inhomogeneity in (a)..... 139

Fig 64 example OM image showing melt pool cross section for regular pad (a) & overlap pad (b):melt pool boundaries for regular-pad and first layer in overlap-pad: white; second-layer melt pool boundary in overlap pad: red; microstructure characterization location: indicated by inserted box in (a)-(c)..... 140

Fig 65 Typical melt pool microstructure observation of single-track, multi-track, overlap-track generated at same B wt.% level and P-V sets, with the corresponding single-track showing type (i)-(iv) melt pool microstructure (see chapter 7.4.1 and Fig 60 for details of type (i)-(iv) microstructure); [B wt%, P-V] of each examples: listed on the left side; microstructure characterization: at center of melt pool (yellow box in Fig 63(a)-(c)); TiB precipitate and Ti-matrix: marked by white and blue arrows respectively; red dashed lines in (4-a,b,c): mark prior  $\beta$ -Ti boundaries ..... 141

Fig 66 microstructure inconsistency in Ti6Al4V-xB pad (a): localized region near boundary between adjacent melt pools (marked by red dashed line in (a)-(c)) show different TiB distribution

spacing (b) or different TiB morphology (c) compared to rest of the pad; M.P.: stands for “melt pool”; (b): zoom-in image of the white box in (a); examples provided by [2 wt.%B, P-V#a] and [1% wt.%B, P-V#a] for (b) and (c)..... 142

Fig 67 comparison of arc-melted Ti6Al4V-xB hardness & single bead Ti6Al4V-xB melt pool hardness. Max & min labels are indicated for the normal-geometry melt pool (see Fig 22, chapter 6.1.1)..... 143

Fig 68 melt pool hardness for Ti6Al4V-0,1,2,5 wt.%B at different laser scan velocity when laser power fixed at 215W (a) and 280W(b); melt pool microstructure: indicated by different labels, with each microstructure category summarized in Table 17 and Fig 60..... 144

Fig 69 general workflow to develop LPBF process map for solidification microstructure selection for hypo-eutectic Ti6Al4V-xB alloy (a-1~3) and hyper-eutectic Ti6Al4V-xB alloy (b-1~3): (a-1), (b-1): schematic phase diagram; (a-2), (b-2): schematic showing the change of interfacial temperature of each solidification phase with absorbed power(Q) and laser scan velocity (V) for [Q, V] combinations with a fixed (Q·V) product; (a-3), (b-3): schematic to show how to develop Q-V threshold for solidification mode transition ..... 152

Fig 70 LPBF process map for solidification mode selection for Ti6Al4V-1, 2, 5 wt.%B: black bold and dashed lines: solidification mode transition thresholds, developed from equation models in Table 19; experimental data points: obtained from this work and studies from Cai et al[182] and Attar et al. [120], different labels represent different melt pool microstructure, with the typical image and solidification mode presented in Fig 60 and Table 17. .... 154

Fig 71 coarse boride pre-existing from arc-melting: (a) whole melt pool; (b) high magnification image of red circle area in (a)..... 157

Fig 72 Change of absorptivity with laser scan velocity at laser power fixed at 150W, 200W, 250W for H13-steel in bulk-state(a) and powder-state(b) and Ti6Al4V in bulk-state(c) and powder-state(d);(a)-(d) adopts the P,V, material-related absorptivity model developed in this study (see Table 10)..... 186

Fig 73 Comparison of melt pool depth between laser scan on bulk H13-steel and H13-steel powder layer for 3 datasets by adopting: (a) varying absorptivity model in Equation 10; (b) constant absorptivity; non-keyhole data point outlier: marked by red dashed circle; note: no-powder(2) dataset: validation data not used for data fitting..... 186

Fig 74 Fitness of the two absorptivity models for Ti6Al4V in powder state in Table 10 to the Ti6Al4V powder-added  $\eta_{pre}$  absorptivity datasets; (a) P-V varied absorptivity model and (b) constant absorptivity model; datasets: 48 data points included, corresponding to Powder-Ti64 dataset in Table 11;  $\eta_{pre}$ : defined in Equation 11, derived from experimental measurement of Ti6Al4V powder-added melt pool dimension ..... 187

Fig 75 Observation of unmelted powder for H13 steel melt pool; (b): zoom-in image of the red box inserted in (a); (b) shows unmelted powder presents larger-scale cellular networking than the surrounding melt pool solidification microstructure ..... 187

# 1 Introduction

## 1.1 LPBF process and “powder-free” method

Additive manufacturing (AM) technology introduces revolutionizing opportunities to the manufacturing industry, due to its unique layer-by-layer part build process and attractive advantages including minimizing material waste and enabling geometrically sophisticated part design. The quick mature and great advancement of AM technology recently shows promising potential for its commercialization on metallic part fabrication [1]. Based on their material feedstock, the mainstream metallic AM processing systems were categorized into wire-feed, powder-feed and powder-bed system, equipped with either electron beam or laser heat source. There are several different metal AM processes. This work focuses on laser powder bed fusion (LPBF) additive manufacturing, also known as selective laser melting (SLM).

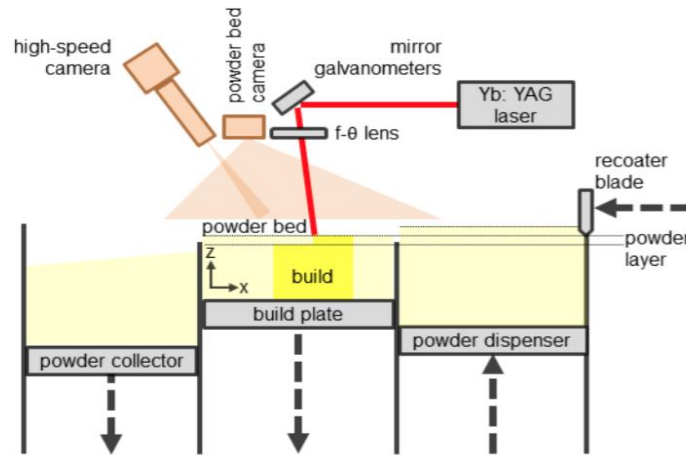


Fig 1 schematic of LPBF- additive manufacturing system (based on EOS M290 machine model)

Among various AM systems in the market, LPBF is one of the most popular AM systems for metallic part fabrication, which is based on powder-feed system and equipped with a laser heat source. Fig 1 shows a schematic LPBF system AM machine (model: EOS M290), which is the equipment utilized in this study. During LPBF-part build process, the recoater-blade sweeps across the build plate to deposit a thin layer of powder with a specified layer thickness (20~60  $\mu\text{m}$ ) on the surface of previously-built bulk metallic part, followed by which a laser beam scans on selective area of the powder layer with programmed scan pattern. This powder spread-laser scan process is repeated to build a three-dimensional part layer by layer.

LPBF exhibits a series of beneficial features over other AM processes, including (1) it has less material restriction than other AM systems. For instance, EBM-AM system could only consider materials with good electrical conductivity as well as thermal conductivity, while LPBF process does not have such restriction; (2) compared to powder-feed and wire-feed AM system, it has a more stable material feed process and smaller local melting volume, allowing higher dimensional resolution & better surface quality for the parts compared to other AM-fabricated parts.

Powder availability is a primary obstacle to experimental LPBF investigation, especially LPBF alloy development investigation. LPBF powder feedstocks generally have strict requirements [2][3][4], including uniform size, good flowability, and low porosity. It is impractical and costly to produce small-scale powder batch for all the trial alloys of interest. In consequence, currently the number of metallic materials optimized for LPBF process is highly limited. For instance, the list of material optimized for EOS-M290 machine utilized in this study only includes 2 titanium alloys (Ti6Al4V and commercially pure Ti) [5][6] and 1 tool steel (maraging 300) [7] across the titanium alloy class and tool steel class.

Computational modeling is an important part of the solution and there are currently many efforts on the macro-scale ( $10^{-3}$ ~1 m) and meso-scale modeling ( $10^{-6}$ ~ $10^{-3}$ m) [8][9]. With the increasing model sophistication, the thermal modeling and stress modeling work shows reliable prediction from the melt pool scale to the 3D-part scale, such as the studies from Li et al (Li et al., 2018), Fu et al (Fu and Guo, 2014) and Hussein et al (Hussein et al., 2013). However, LPBF process still remains complicated and challenging to fully describe, which makes the current modeling work on predicting LPBF melt pool microstructure evolution immature [8]. Recent attempts at LPBF microstructure modeling, including phase-field modeling and Monte Carlo modeling [10][11] commonly present problems of oversimplifying microstructure features or unsatisfying accuracy and thus fail to validate the experimental results. Moreover, there is less experimental data available for model benchmarking than for conventional processing modeling. In general, at the current stage, we might still lack the confidence to rely upon computational modeling to obtain accurate LPBF microstructure information. Thus, if solely based on computational modeling, wrong LPBF performance evaluation is quite likely to be generated due to inaccurate LPBF microstructure information. Experimental observation, especially on LPBF melt pool microstructure, is still essential for LPBF investigation, especially in the case of current work, which investigated LPBF process optimization for unexplored commercial composition and LPBF alloy development with non-commercialized trial composition.

Therefore, this study intends to obtain reliable LPBF melt pool information (geometry, microstructure, hardness, etc.) for alloy systems of interest without the need for tedious and costly powder fabrication experimental work. On this basis, this study proposes a systematic experimental methodology, referred to as “powder-free approach” in this document. This approach assumes laser-deposited melt pool on bulk alloy surface (referred to as “no-powder melt pool” in this document) to provide sufficient approximation for as-deposited melt pool during LPBF build, which is essentially melt pool deposited on bulk alloy with a powder layer present (referred to as “powder-added melt pool” in this document). Based on this assumption, the powder-free approach was used to conduct a series of LPBF laser-scan tests with different scan patterns and P-V process combinations on bulk alloy surface with a series of test compositions, assessing the positive and negative attributes of LPBF part build performance with each process-composition combination by evaluating the obtained melt pool geometry, microstructure and micro-hardness information. The main advantages of this powder-free approach include: (1) due to the greater convenience of obtaining bulk alloy buttons than powder feedstock, this powder-free approach gives us much more freedom on test composition selection; (2) by leaving out the time-consuming LPBF part build procedure, this powder-free approach allows rapid assessment of a large number of process settings for composition of interest. Two cases were demonstrated in this study for adopting this powder-free approach for LPBF-related studies: One is alloy development for LPBF process, with boron-modified Ti6Al4V-xB as alloy of interest, and a broad composition range from 1wt.%~10wt.%B addition was investigated; the other is LPBF process optimization for two tool steel grades: M2 and H13 steel. The results were presented in chapter 7 for the former and chapter 6 for the latter.

## 2 Technical Background

This chapter provides the technical background for the models and microstructure mechanisms presented in this study. Chapter 2.1.1 presented the basic concepts and modeling work for LPBF melt pool heat transfer. The model used for melt pool thermal profile calculation in this study was also introduced. In this study, a major focus was developing P-V process window for defect control and P-V process mapping for microstructure control for each tested alloy. Keyholing and balling were two defect-inducing mechanisms of investigation. Their typical melt pool behavior, relation to P-V parameter and influence on LPBF part quality were described in chapter 2.1.2 and chapter 2.1.3. In this study, two mechanisms related to microsegregation and columnar-to-equiaxed transition (CET) were proposed to explain the microstructure inhomogeneity observed in H13 and M2-steel melt pool. Chapter 2.2.1 and chapter **Error! Reference source not found.** described the models for estimating microsegregation and CET in previous studies, with a focus on Scheil model, DICTRA model and CET model from Gäumann et al [12], which were the models utilized in this study. Chapter 2.2.1 and chapter **Error! Reference source not found.** also summarized the experimental observation for microsegregation and CET occurrence under LPBF and laser welding rapid solidification as well as their relation to cracking. In this study, solidification mode transition was observed for LPBF melt pools of Ti6Al4V-xB. Chapter 2.2.3 presented the literature review for solidification mode transition in welding process, including its experimental observation, its relation to welding process parameter and its underlying competitive growth mechanisms. Finally, Chapter 2.3 and chapter 2.4 provide the literature review for LPBF processing of tool steel and Ti6Al4V-xB, with a focus on process-microstructure relation.

### 2.1 LPBF melt pool solidification

#### 2.1.1 Heat transfer during melt pool deposition

In LPBF process, the high-energy-density laser irradiates and heats the powder layer. When the temperature achieves the alloy melting point, a moving melt pool is created by quickly melting and solidifying the material from the newly-deposited powder layer and the material from the underlying bulk metal substrate together. Heat transfer during this process is schematically shown in Fig 2 [13][14], which consists of radiation and convection from material-environment interaction and conduction between the melt pool and the solidified substrate. LPBF melt pool deposition has two heat transfer modes: conduction mode and keyholing mode, similar to the heat transfer in fusion

welding process. In conduction mode, heat transfer is dominated by conduction through the previously-built substrate underneath the melt pool, while radiation and convection take up a small portion of the heat flow. However, it should be noted that LPBF conduction mode could differ from that of welding and some wire-feed or powder-feed AM process in that in LPBF process, the previously-built substrate is surrounded by loose powder, which acts as a thermal insulator to inhibit heat conduction[15][16]. Study by Montgomery et al [16] showed that this effect was small for LPBF part build except for overhang structure. In keyholing mode, a considerable portion of heat flow is through convection by significant metal evaporation. Unlike heat transfer in conduction mode, heat transfer in keyholing mode needs to consider both conduction and convection due to the presence of a deep vapor cavity during melt pool deposition. This is further described in chapter 2.1.2.

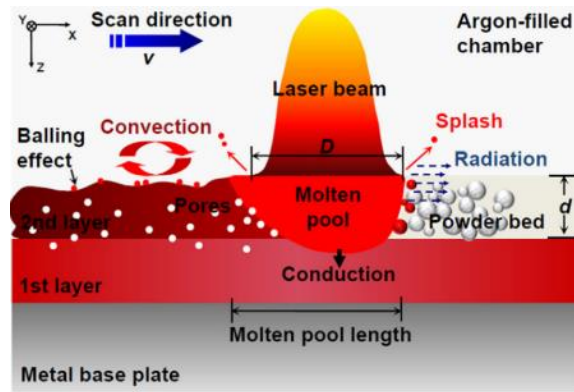


Fig 2. schematic of heat transfer during LPBF melt pool deposition[14]

Abundant studies[17][18][19][13] as well as this work showed that melt pool thermal analysis was beneficial for understanding LPBF microstructure evolution. Therefore, continuous efforts have been made to formulate and refine heat transfer models to describe LPBF melt pool deposition. Various analytical and numerical models have been developed, as summarized in several relevant literature reviews [20][15] [13]. One of the most well-known analytical models is the Rosenthal solution [21], which was originally developed for welding process and also found its application in several AM-related studies[22][23][24]. It describes the three-dimensional temperature field for a moving point heat source, as shown in Equation 1. It used several assumptions to simplify its calculation, including steady-state heat flow, point heat source, no convection, no heat of fusion and constant thermal properties. These assumptions limit its application for many LPBF process scenarios. For instance, the Rosenthal solution usually provides inaccurate prediction for melt pool deposited by keyhole-mode laser scan due to the assumption that convection does not play a significant role [25] [21][26].

This was also found in this study, as shown further in chapter 5. Its steady-state assumption makes it difficult to predict melt pool deposition by complex laser scan paths [27]. Its point heat source assumption could introduce inaccuracy for melt pool thermal profile calculation because in reality LPBF laser power presents a Gaussian energy distribution[28]. However, within the process range where these assumptions were acceptable, the Rosenthal solution shows the great benefits of low computational costs and providing reasonable estimates. Several studies reported that Rosenthal-predicted melt pool geometry agreed with experimental ones for melt pools formed by conduction-mode laser deposition [23,29–31]

$$T = T_0 + \frac{Q}{2\pi Rk} \exp\left[\frac{-V(\xi + R)}{2\alpha}\right] \quad \text{Equation 1}$$

where  $T$  is the local temperature,  $T_0$  is the plate temperature,  $Q$  is the absorbed power,  $k$  is thermal conductivity,  $V$  is beam travel speed,  $\alpha$  is thermal diffusivity,  $R = (\xi^2 + y^2 + z^2)^{1/2}$  is the radial distance from the beam position,  $\xi$  is the distance from the beam position along the travel direction,  $y$  is the distance parallel to the workpiece surface perpendicular to the beam travel direction, and  $z$  is the depth below the workpiece surface.

This study adopts the heat transfer model developed by Nick Jones (in-house) for melt pool thermal profile calculation, as shown further in chapter 6.2. It was based on the Eager-Tsai analytical model rather than the Rosenthal Model. The Eager-Tsai model [32] describes the temperature profile for a traveling heat source with a Gaussian energy distribution, as shown in Equation 2. Compared to the Rosenthal Model, it provides a more realistic distributed heat source for LPBF melt pool estimation. However, it still uses all assumptions except that of a point-heat-source one in the Rosenthal model. Thus, the Eager-Tsai model might not be feasible to fully address the details of LPBF melt pool thermal behavior owing to the same reasons mentioned above for the Rosenthal model. Compared to analytical models such as the Eager-Tsai and the Rosenthal models, numerical models are expected to give more realistic estimates of a LPBF melt pool thermal profile due to its transient heat transfer nature and availability to integrate the heat transfer model with a melt pool fluid flow model[33][34]. Software for LPBF melt pool thermal numerical modeling includes ANSYS, ABAQUS, COMSOL and ALE3D. However, the major drawback of numerical modeling lies in its high computational cost, which goes against the purpose of rapid LPBF process optimization and composition screening for this research.

$$T = T_0 + \frac{Q}{\pi \rho c_p (4\pi \alpha)^{1/2}} \int_0^t \frac{(t - t')^{-1/2}}{2\alpha(t - t') + r^2} \exp \left[ -\frac{\xi^2 + y^2}{4\alpha(t - t') + 2r^2} + \frac{z^2}{4\alpha(t - t')} \right] dt' \quad \text{Equation 2}$$

Where  $t$  is total beam time,  $t'$  is instantaneous time,  $r$  is beam radius,  $c_p$  is specific heat,  $\rho$  is density

To lower computational cost, a semi-analytical heat transfer model ( in-house, developed by Nick Jones) rather than a full numerical model was adopted for estimating LPBF melt pool thermal profile in this study. The adopted semi-analytical heat transfer model integrates ANSYS numerical modeling, the Eager-Tsai analytical modeling and CALPHAD thermal properties calculation. Its general workflow is presented below:

First, temperature-dependent material properties and thermal effects of phase transformation for the alloy of investigation were obtained by CALPHAD calculation using Thermal-Calc software [35] or collected from literature. They were adopted for melt pool geometry calculation by both numerical modeling with ANSYS software and analytical modeling with the Eager-Tsai solution at assigned P-V process settings. It should be noted that melt pool geometry was iteratively estimated by the Eager-Tsai model using constant material properties at a series of temperatures in the range of 300-1000°C. When using material properties at a certain temperature, the Eager-Tsai model estimated melt pool geometry would give a good approximation to the Ansys-calculated one. This temperature was referred to as “evaluation temperature”. Then the Eager-Tsai model would adopt the material property values at the evaluation temperature to calculate melt pool thermal profile, including distribution of temperature gradient, solidification velocity and cooling rate across melt pool during melt pool solidification. It should be noted that the evaluation temperature varies with alloy systems and P-V parameters. For instance, for H13 steel melt pool of P-V#4, the evaluation temperature was 780°C, which means that when using material properties at 780°C, the Eager-Tsai analytical model and ANSYS numerical calculation give consistent melt pool geometry estimates, even though the former requires much less computation cost than the latter. Thus, the Eager-Tsai model with material properties at 780°C was used for melt pool thermal profile calculation. For the H13 steel melt pool of P-V#6, the evaluation temperature was found to be 715°C. By replacing the numerical modeling with The Eager-Tsai calculation at the evaluation temperature, the adopted heat transfer model could effectively decrease computational cost without scarifying melt pool thermal analysis accuracy. As shown further in chapter 6.2, the melt pool thermal profiles calculated by this model were essential

components for predicting LPBF melt pool microstructure of H13 steel and M2 steel. The reliability of the model thermal calculation was supported by the good agreement between experimental observation and the microstructure prediction across a wide P-V range.

### 2.1.2 Keyholing and its influence

For laser deposition, the melt pool heat transfer is divided into conduction mode and keyholing mode [36]. Fig 3 (a) presents the physical phenomena during laser deposition in keyhole mode[37]. Fig 3 (a) shows that a deep vapor cavity, referred to as “keyhole”, occurs in the molten melt pool, which is filled with high-temperature metallic vapor or plasma. In contrast, in conduction mode, the melt pool does not show significant metal evaporation. Thus, unlike conduction mode, for keyhole-mode heat transfer, heat convection by metal evaporation cannot be neglected. In the welding community, melt pool geometry showing a large melt pool depth to width ratio ( $D/W$ ) was often adopted as an indicator for keyhole formation. An example is provided in Fig 3 (b)[38].

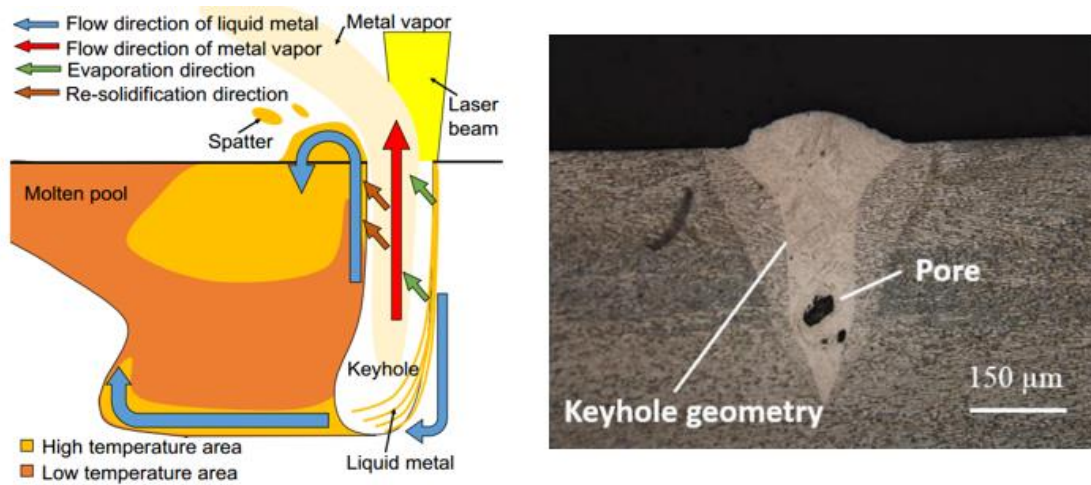


Fig 3 laser deposition in keyhole mode: schematic of physical phenomena and molten melt pool temperature distribution in keyhole mode (a)[37] and typical examples of the resulting melt pool geometry by keyhole-mode laser deposition(b)[38]; keyhole-induced porosity: indicated in (b)

Keyholing is usually considered as a major source of LPBF part porosity. In keyhole mode, porosity could be generated as a result of periodical oscillation of the vapor depression in the molten melt pool. Keyhole-induced porosity in laser melting was experimentally observed by Cunningham et al [39] using synchrotron X-ray imaging. Compared to porosity induced by other mechanisms (e.g., lack-of-fusion porosity), keyhole-induced porosity presents larger dimension scale, which is detrimental to fatigue resistance and cracking resistance of LPBF part build.

On the other hand, the keyhole mode provides the opportunity for high-efficiency laser processing. In key-holing mode, the vapor cavity in the molten melt pool traps the laser light, resulting in internal laser reflection at the cavity wall and in turn greatly enhancing laser absorption. Trapp et al [25] showed by the experimental observation that the laser absorptivity of 316L stainless steel increases from  $\sim 0.3$  to  $\sim 0.8$  when laser melting changes from conduction mode to keyholing mode. A similar observation of absorptivity increase with keyholing occurrence is also indicated in this study, as presented in chapter 5.

Key-holing is generated by laser deposition with sufficiently high energy density to cause metal evaporation to occur. Therefore, the P-V space leading to key-holing is generally considered to be the space with high-power and low-scan velocity. However, recent studies[39] show that metal evaporation could also occur in a relatively low-power range, which is consistent with the unexpected keyholing observation with a low-power P-V setting in this study.

### 2.1.3 Balling and its influence

The occurrence of balling is an important factor inducing porosity in LPBF-built components. Balling occurrence could be distinguished by melt pool geometry with “bead-up” from cross section and large surface fluctuation of laser tracks with occasional ball formation from track top view, as shown in Fig 4[40][41].

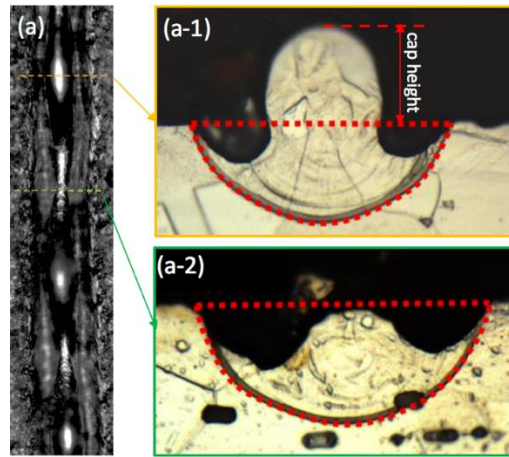


Fig 4 melt pool geometry variation along laser-deposited track of balling formation[40][41]: (a) laser track top view; (a-1): melt pool cross section at bead-up location of laser track (indicated by yellow line in (a)); (a-2): melt pool cross section at other location of laser track (indicated by green line in (a))

Previous work [42,43] showed that balling occurrence might induce the following problems that severely degrades the LPBF part quality:

- 1) the uneven laser track surface, especially the occasional “bead up” with a large cap height, might impede smooth powder layer spreading for the successive layer build, in turn leading to defects of cracking and porosity in the LPBF part (Fig 5). Study from Li et al[43] presents the mechanism and experimental observation for LPBF part porosity induced by balling.
- 2) with balling melt pool formation, the surface roughness of LPBF part is usually unsatisfactory and in turn results in inferior fatigue resistance and low cracking resistance.
- 3) the causal relation between unstable melt pool flow and balling occurrence indicates inconsistent melt pool solidification thermodynamic along laser track deposition, which might cause microstructure inhomogeneity in LPBF part.

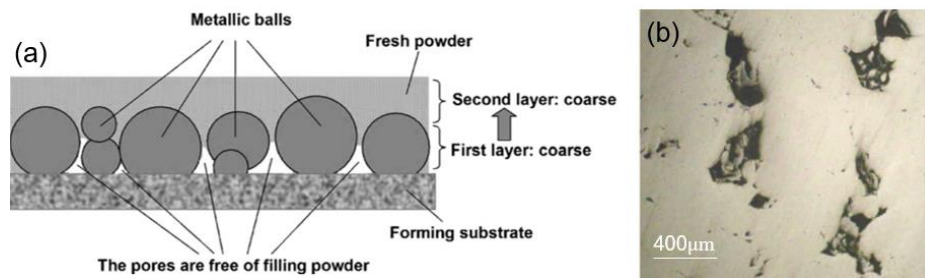


Fig 5 balling-induced porosity: mechanism (a) and experimental observation (b)[43]

Balling could originate from two mechanisms. Fig 6 presents a P-V process map schematically showing the process ranges for the two balling-induced mechanisms[44] [45]. The first mechanism considers balling formation induced by unstable melt pool flow due to Rayleigh instability[46]. Raleigh-Plateau instability [46] states that the melt pool length to width ratio ( $L/W$ ) has a threshold, which makes the surface area of melt pool equal to the surface area of a sphere with the same volume of the melt pool. When  $L/W$  ratio is higher than this threshold, the melt pool flow would spheroidise and break up into several bead-up droplets due to the driving force to minimize surface tension. This was usually related to the process window of high laser power ( $P$ ) and high laser scan velocity( $v$ ), since this P-V process range corresponds to high  $L/W$  value for melt pool formation, as schematically shown in Fig 6.

Another mechanism for balling formation is related to a considerably low laser power ( $P$ ). In this case, laser energy density is sufficiently low and could not fully melt through the powder layer.

Instead, it provides a superliquidus sintering effect [45] to the powder layer, creating the melt pool as a solid-liquid mixture. Compared to the fully-molten metal pool, this solid-liquid melt pool has a higher viscosity and poor wettability. Consequently, as the laser beam moves, the solid-liquid mixture formed at each irradiating zone tends to aggregate into a string of unconnected balls with the diameter similar to the laser beam diameter along the laser scan direction. The occurrence of this type of balling in the process window of low laser power was observed for both DMLS and LPBF processing with 316L stainless steel [44] [45] and LPBF processing with Ti6Al4V[38][47]. This mechanism indicates the influence of powder for balling formation, which might help to explain the phenomena observed in this work, namely a difference in no-powder and powder-added melt pool with balling geometry, as shown further in chapter 6.1.2.

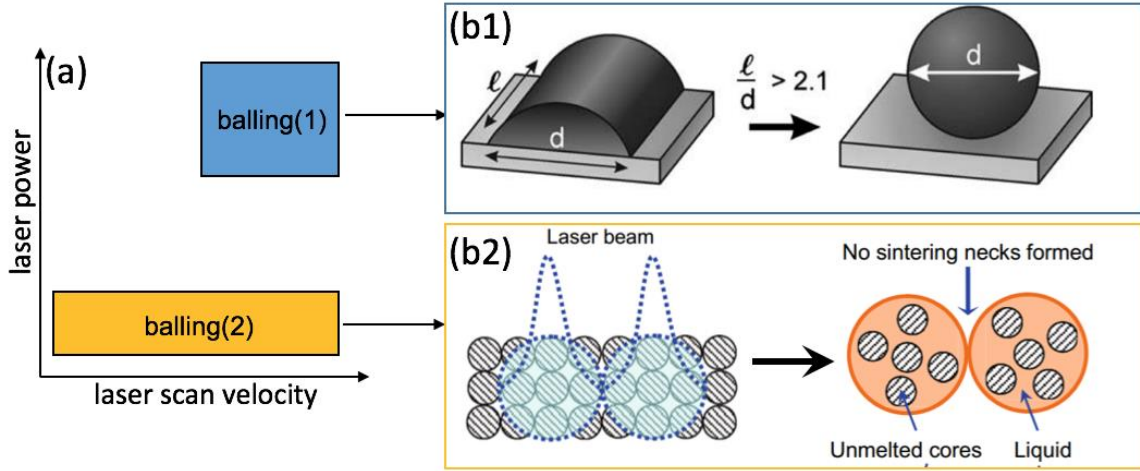


Fig 6 schematic of two balling mechanism (b1, b2) and their corresponding P-V process window(a);  
 P: laser power; V: laser scan velocity; (b1): balling induced by melt pool flow with Raleigh instability; (b2) balling induced by high viscosity solid-liquid mixture melt pool flow, reproduced from [44] and [45]

Balling could be avoided by adopting P-V parameters outside of the two process ranges in Fig 6. Yadroitsev et al. [46] identified the P-V process window to avoid balling formation for a series of alloy system (SS grade 904L, 316L, tool steel H13, copper alloy CuNi10, superalloy Inconel 625) and reported that for alloy with higher thermal conductivity, the process window is narrower.

## 2.2 Non-equilibrium LPBF solidification

### 2.2.1 Microsegregation during rapid solidification

Recently, a series of studies investigated the cooling rate of LPBF melt pool solidification by in-situ characterization[48][49]. Hooper [49] investigated the melt pool dynamics of LPBF with Ti6Al4V by both in-situ experimental measurement and numerical calculation, showing that the cooling rate in melt pool varies from  $10^6$ - $4 \times 10^6$  K/s. Scipioni [48] investigated the melt pool cooling rate for LPBF of 316L stainless steel by integrating high imaging video in-situ measurement, COMSOL simulation and microstructure characterization. The result shows that melt pool cooling rate could change from  $10^6$  to  $7 \times 10^6$  K/s with different P-V parameters. These results confirm the high cooling rate of LPBF solidification the order of  $10^6$  K/s, indicating the likelihood of solidification microsegregation [50][51].

In this work, microsegregation was experimentally observed for LPBF melt pool of H13 steel, as shown in chapter 6.2.1. A similar observation was also reported in previous studies for LPBF of H13 steel [52–54]. Understanding microsegregation during LPBF melt pool solidification is important in that abundant studies reported its correlation with LPBF cracking [50,55,56].

The two extreme cases for solidification could be calculated by the equilibrium method (Equation 3) and the Scheil-Gulliver method (Equation 4) The major difference between Scheil-Gulliver and equilibrium solidification lies in that the former considers complete diffusion in liquid but no diffusion in solid, while the latter considers complete diffusion in both solid and liquid.

$$\text{equilibrium solidification} \begin{cases} C_l = C_0 / [f_l + k(1 - f_l)] \\ C_s = kC_0 / [(1 - f_s) + kf_s] \end{cases} \quad \text{Equation 3}$$

$$\text{Scheil solidification} \begin{cases} C_l = C_0 (f_l)^{k-1} \\ C_s = kC_0 (1 - f_s)^{k-1} \end{cases} \quad \text{Equation 4}$$

where  $C_0$  is the average solute composition in the alloy,  $C_s$  is the composition in the solid at the solidification front,  $k$  is partition coefficient, and  $f_s$ ,  $f_l$  is the mass fraction of solid & liquid phase.

Comparing the solidification routes estimated by these two extreme cases provides initial assessment for the role of cooling rate on solidification microsegregation for the alloy of investigation. Fig 7 shows the comparison of equilibrium- and Scheil-calculated solidification route for H13 steel using Thermo-Calc software[35]. From Fig 7, it shows 250°C difference in freezing mol.% of  $\delta$ -Fe and mol.% of  $\gamma$ -Fe for Scheil- and equilibrium-conditions. These are potential consequences of

microsegregation in H13 during rapid solidification. Further results observations are presented in chapter 6.2.1. Compared to the equilibrium-calculated result, the Scheil-calculated result in Fig 7 might give a more proper estimation for LPBF solidification of H13 steel considering the high-level cooling rate of LPBF process.

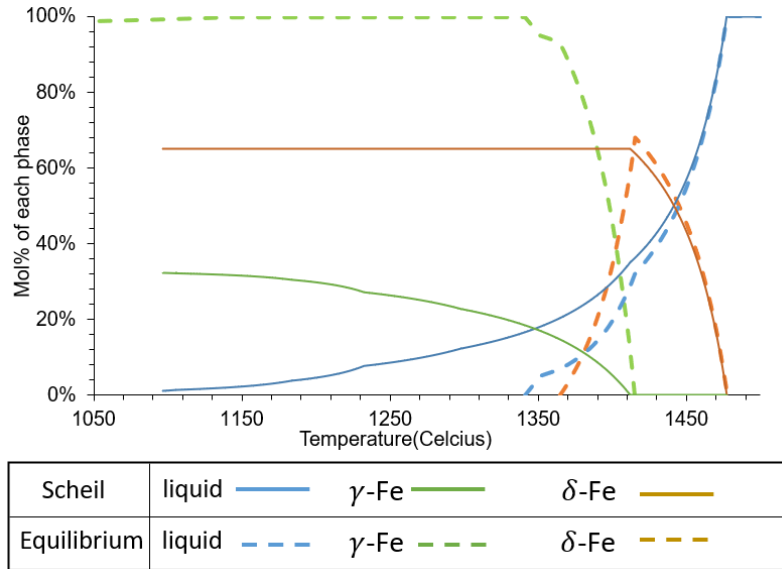


Fig 7 comparison of Scheil-predicted & equilibrium-predicted solidification route for H13 steel from Thermo-Calc [35], focusing on liquid,  $\delta$ -Fe &  $\gamma$ -Fe phases (solid lines refer to equilibrium conditions; dashed lines refer to Scheil solidification)

The Scheil-Gulliver model is likely to provide a reasonable approximation for alloy systems with substitutional solute such as Al-Si and Ti-Ni systems [57], but not for alloys with interstitial solutes such as steel systems (interstitial: C). Substitutional solute diffusion in solid-state is usually slow and could be neglected, which makes the no solid-state diffusion assumption of Scheil solidification a safe approximation. However, Scheil-Gulliver simulation is likely to overestimate the segregation for LPBF solidification of steel, due to its unrealistic assumption of completely excluding solid-phase diffusion [58,59]

Considering this potential problem, this work adopts DICTRA simulation instead of Scheil to estimate the segregation for LPBF melt pool solidification of H13 steel, as further presented in chapter 6.2.3. DICTRA[35] is a computational tool that allows fully integration of thermodynamic and kinetic calculation, which is expected to give a more practical estimation for H13 steel segregation under the local thermal condition in LPBF melt pool. Several studies have adopted DICTRA for welding

solidification investigation[60–62] and confirmed its accuracy by experimental measurement. In the case of H13 steel LPBF solidification presented in this work, a cellular network microstructure was observed. Correspondingly, this work adopts a planar model with ferrite, austenite and liquid as shown in Fig 8 was used for DICTRA simulation, representing a half cellular. A similar DICTRA model was used by Gregori and Nilsson [62] to estimate austenite% formed during solidification for GTA welding with duplex stainless steel. They compared DICTRA simulation results with Scheil simulation, showing a higher austenite% value predicted by DICTRA than Scheil. The experiment results showed better agreement with the DICTRA simulation.

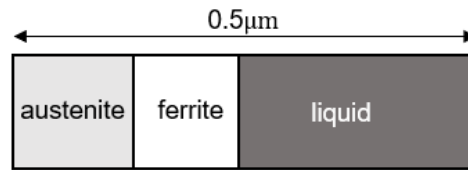


Fig 8 Planar model representing half cellular size used for the DICTRA simulation of solidification segregation for LPBF melt pool of H13 steel

The difference between DICTRA and Scheil simulation for solidification microsegregation of steel systems might arise from the influence of carbon back diffusion on steel solidification. This was indicated by the work from Chen and Sundman [59] as presented in Fig 9. They presented a numerical approach, referred to as “partial equilibrium” approach to estimate steel solidification microsegregation. This approach was built on the assumption that only considers interstitial back diffusion (C in this case) and completely neglects substitutional back diffusion (Cr in this case). Fig 9 shows great consistency between DICTRA and partial equilibrium-calculated results, while they both show a noticeable discrepancy with the Scheil calculated results which completely ignore back diffusion. Comparison of Fig 9 (a) and (b) shows that an increase in C% led to a larger difference between Scheil and DICTRA results, while the agreement between DICTRA and the partial-equilibrium result remains. The work from [59] indicates that for steel rapid solidification, it might be safe to neglect back diffusion of most components except carbon.

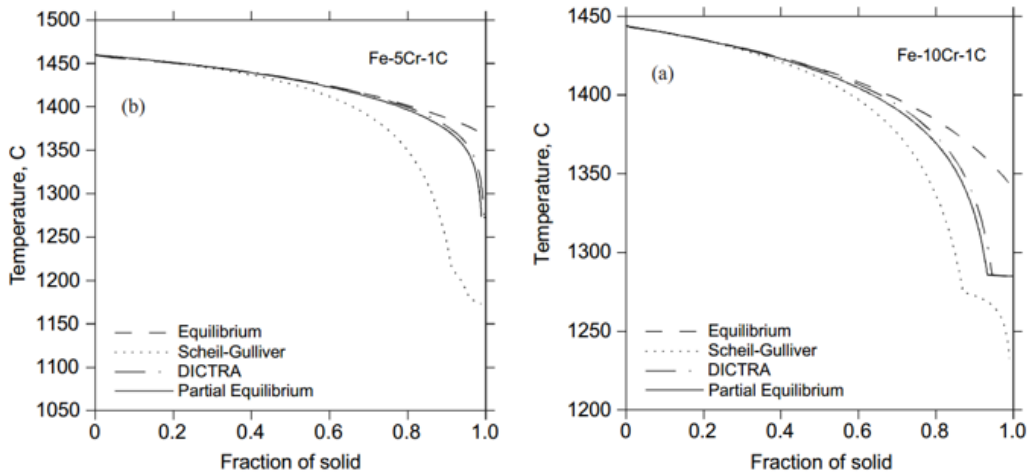


Fig 9 Solid fraction versus temperature for two steels: (a) Fe-5Cr-1C and (b) Fe-Cr-0.92%C estimated by equilibrium-, Scheil-, DICTRA- and partial equilibrium calculation [59]

The higher accuracy of DICTRA simulation than Scheil as exemplified by [62] indicates the significance of solid-state diffusion under welding rapid solidification condition.

Considering the similarity between welding and LPBF solidification and the fact that solidification cooling rate is by no means uniform in the LPBF melt pool, it is reasonable to assume that some regions with relatively lower solidification cooling rate in LPBF melt pool of H13 steel might not present such extreme phase transformation and solute segregation as predicted by the Scheil-Gulliver model. The different levels of microsegregation across different locations of melt pool was in fact experimentally observed by Brook et al. [63] and Kou et al. [64] and suggests solid-state diffusion occurs during solidification of steel with  $\delta$ -Fe as primary solidification phase. Other studies [65][66] also show that with primary solidification phase as  $\delta$ -Fe, solid-state diffusion is obvious; while with primary solidification phase as  $\gamma$ -Fe, solid-state diffusion is not noticeable.

Besides DICTRA numerical model, Brooks et al. [67] developed finite difference solidification microsegregation model considering solid-state diffusion in dendrite minor axis direction, which also showed good agreement with the experimental measurement of Cr and Ni microsegregation.

Therefore, compared to Scheil, DICTRA calculation which accounts for limited solid-state diffusion such as carbon back diffusion in H13 steel might help to develop a more realistic understanding of the level of microsegregation for the exact local thermal condition presented in LPBF melt pool of steel system.

Microsegregation induced by rapid solidification is important for LPBF part quality because it could lead to unpredictable phase transition and in turn result in cracking. The correlation between solidification microsegregation and cracking was abundantly reported in laser-process related & welding-related studies. For instance, microsegregation could result in impurity segregating at the grain boundaries, in turn promoting low-melting compound (E.g., FeS) and brittle phase precipitation at the grain boundary, and finally result in severe solidification cracking [68] [69]. Microsegregation could also lead to cracking by remarkably increasing freezing range to result in a different type of eutectic reaction at the location with segregated composition or influence the liquid distribution at the terminal stage of solidification to promote cracking propagation [56][70].

These unexpected microstructure evolutions induced by microsegregation was experimentally observed to result in severe cracking in weldments [68,71–73]. These problems observed for welding solidification indicate the likelihood of microsegregation during rapid solidification of LPBF, which might in turn induce cracking in LPBF product. This was the case for H13 steel LPBF-melt pool solidification presented in this work, which suggests microsegregation to cause microstructure inhomogeneity in H13 steel LPBF-melt pool, which in turn influenced the cracking tendency of H13 cubes (see chapter 6.3.1).

### **2.2.2 Columnar-to-equiaxed transition during rapid solidification**

Thermal analysis for LPBF single track [13] shows that solidification of the as-deposited melt pool not only experience high values of temperature gradient (G) and solidification velocity (R), but also shows large variation for G and R at different locations within the melt pool. For instance, Fu and Guo [74] estimated melt pool thermal profile for LPBF processing with Ti6Al4V using a three-dimensional finite element (FE) method, showing that the average temperature gradient reaches the order of  $10^6$  K/mm in top half of melt pool but only  $10^4$  K/mm at bottom half, and that the temperature gradient increases as laser power increases, as does the extent of variation. This thermal profile with high, yet varied G- and R-value in LPBF melt pool suggests the possibility of columnar-to-equiaxed transition (CET) according to the analytical model proposed by Hunt [75] and a series of revised model based on it, such as the model developed by Gäumann et al [12]. This CET model will be detailed further in chapter 6.2.4 and briefly discussed here.

Models of the CET determine the influence of G and R on dendritic tip undercooling. Generally, during LPBF melt pool solidification, columnar grain morphology was favored to form as a result of epitaxial growth from the previously deposited substrate and unidirectional heat flux. Hunt's model

[75] states that the growth of columnar or equiaxed grain was dictated by the volume fraction of equiaxed grain. They used a concept of extended equiaxed volume fraction ( $\phi_E$ ) as defined in Equation 5 and proposed the criteria as in Equation 5 for fully equiaxed microstructure. One variable involved is radius of equiaxed grain, which could be considered as the time integral of equiaxed grain growth velocity ( $V_e$ ). It could be further be derived as the integral of undercooling as shown in Equation 6 if assuming steady state condition, which gives  $d\Delta T/dt=GR$ . By combining Equation 5 and Equation 6, the criteria for fully equiaxed microstructure could be derived as function of temperature gradient ( $G$ ), undercooling ( $\Delta T$ ) and nuclei density ( $N_0$ ), as shown in Equation 7.

$$\text{fully equiaxed when } \phi_E = \frac{4\pi}{3} N_0 r^3 > 0.66 \quad \text{Equation 5}$$

$$r = \int_0^t V_e dt = \int_{\Delta T_N}^{\Delta T} \frac{A\Delta T}{GRc_0} d\Delta T \quad \text{Equation 6}$$

$$\text{fully equiaxed when } G < 0.617N_0^{1/3} [1 - (\frac{\Delta T_N}{\Delta T_c})^3] \Delta T_c \quad \text{Equation 7}$$

Where  $\phi_E$  is extended volume fraction of equiaxed,  $N_0$  is nuclei density,  $r$  is equiaxed grain radius,  $V_e$  is equiaxed grain growth velocity,  $G$  is temperature gradient,  $R$  is solidification velocity,  $\Delta T$  is dendrite tip undercooling,  $\Delta T_c$  is columnar growth front undercooling,  $\Delta T_N$  is heterogeneous nucleation temperature,  $c_0$  is composition.

As further presented in chapter 6.2.4,  $G$  and  $R$  condition are important factor for  $\Delta T$ . Above equations indicated two approaches to manipulate the CET: one is composition modification to influence nuclei density by adding nucleant particles; the second is LPBF process control to affect  $G$ ,  $R$ -profile for melt pool solidification by selecting different process parameters. In this study, the second approach was adopted, which developed a P-V process mapping for CET control specified for LPBF of M2 steel, as presented in chapter 6.2.4.

The CET transition was not only numerically predicted, but also experimentally observed in melt pool created by AM process. Bermingham et al [76] fabricated Ti6Al4V by wire+arc additive manufacturing (WAAM). By experimentally measuring temperature gradient and approximating the solidification rate as deposition rate, Bermingham et al [76] predicted on the basis of  $G$ - $R$  solidification map that CET transition would occur for the process condition of investigation. They then validated their prediction as WAAM-processed Ti6Al4V with corresponding process conditions all presented a columnar+equiaxed grain mixed microstructure. Wei et al [77] showed that for IN718

alloy fabricated by laser-assisted AM process, CET transition took place at the upper part of each layer, creating a mixture of columnar and equiaxed grain in the as-built microstructure. They [77] then estimated the G- and R-value for the experimentally tested process condition using a heat transfer-fluid flow coupled numerical simulation. The predicted G-R value also suggests mixed columnar-equiaxed microstructure, consistent with the experimental observation. As shown by the previous studies, G-, R-profile during melt pool solidification could be effective indicators to predict the existence of CET microstructural transition for LPBF process.

As shown above, understanding CET in LPBF melt pool solidification is of significance for LPBF microstructure control. Besides, abundant welding studies showed the correlation of hot cracking susceptibility with CET tendency in the weldments [78][79][80][81]. The correlation between CET tendency and cracking observed in welding might be extended to LPBF processing considering that LPBF presents similar thermal condition as that of welding [82]. This indicates the great research value for investigating CET under LPBF solidification condition.

### **2.2.3 Solidification mode transition during rapid solidification**

During LPBF melt pool solidification, the phase transformation of the alloy might be altered by choosing different LPBF process parameters (laser power, scan speed, preheat temperature, etc.). This was indicated by abundant welding-related studies showing that increasing traveling speed of the heat source (laser, electron beam, arc, etc.) led to transition of the primary solidification mode for various weld alloys. Two examples are shown in Fig 10[83] and Fig 11[71] for electron beam welding of Fe-Ni-Cr alloys and laser welding of 304 stainless steel. The first example was provided by the study of Elmer et al[83], which investigated seven Fe-Ni-Cr alloys across wide Cr/Ni composition range. Their equilibrium solidification mode was presented in the phase diagram in Fig 10(a), covering primary austenite solidification (alloys #1 and #2), primary austenite solidification (alloys #5-#7), ferrite+austenite eutectic solidification mode (alloys #3 and #4). Fig 10(b) presents the solidification mode of single-track welds for each alloy made by electron beam scanning across a wide range of beam scan speed. Comparison between Fig 10(a) and (b) shows that at low scan speed, each alloy presents the same solidification mode as the phase diagram prediction. However, at high scan speed, all the alloys present different solidification mode than the phase diagram prediction. This study shows the feasibility for rapid solidification processing such as electron beam welding to alter solidification mode of Fe-Ni-Cr alloys across a wide composition range, as long as beam scan speed achieves a critical value. Fig 10(b) shows that this critical beam scan speed varies with alloy

composition but generally lies in the range of 100-1000mm/s. This is in line with the process range of LPBF laser scan tests investigated in this study, indicating the possibility for LPBF to alter the primary solidification mode for the alloys of investigation (tool steel, Ti6Al4V-xB) by choosing different P-V parameters selected in this study. This was indeed the case for LPBF processing with Ti6Al4V-xB investigated by this study, as shown further in chapter 7.7.

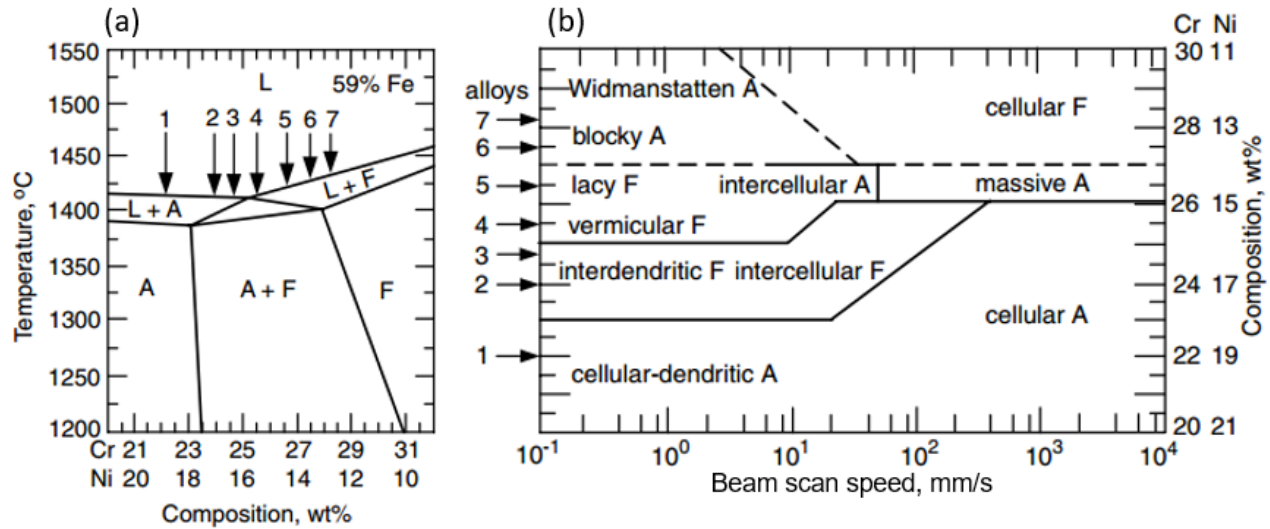


Fig 10 Vertical section of Fe–Ni–Cr phase diagram at 59% Fe showing the equilibrium solidification mode of seven alloys of investigation (a) and solidification mode of electron beam welds as a function of beam scan speed for the seven investigated alloys (b); in (a) and (b): letter L, A, F indicate liquid phase, primary austenite phase and primary ferrite phase, respectively; in (b): both solidification mode and microstructure morphology were summarized [83] [21]

Similar to the study of Elmer et al [83] and Nishimoto and Mori [71] also showed that for laser welding of 304 stainless steel, a typical austenitic steel, its solidification mode was altered from primary ferrite to primary austenite solidification mode as laser scan speed increases, as shown in Fig 11. They adopted a theoretical model to predict the solidification mode transition. This model was based on the principle of competitive growth mechanism [84], which determines the primary solidification phase as the phase with higher solidification front temperature. They adopted the tip undercooling equation model from Kurz–Giovanola–Trivedi [85] to estimate the solidification front temperature. The detailed description for this model is shown further in chapter 7.7. Nishimoto and Mori [71] showed that the model prediction agreed well with the experimental results. Several studies [86] [87][88] adopted the competitive growth model to predict solidification mode transition for welding of Al-Si alloy, Al-Cu alloy and H13 tool steel, which all reported good consistency between

prediction and experimental observation. These studies supported the applicability of the competitive growth model to estimate solidification mode transition under laser welding condition and hence LPBF condition considering the analogy between LPBF solidification and laser welding solidification. In this regard, the competitive growth model was adopted in this research for theoretical analysis of solidification mode transition observed for LPBF of Ti6Al4V-xB, which will be shown further in chapter 7.7.

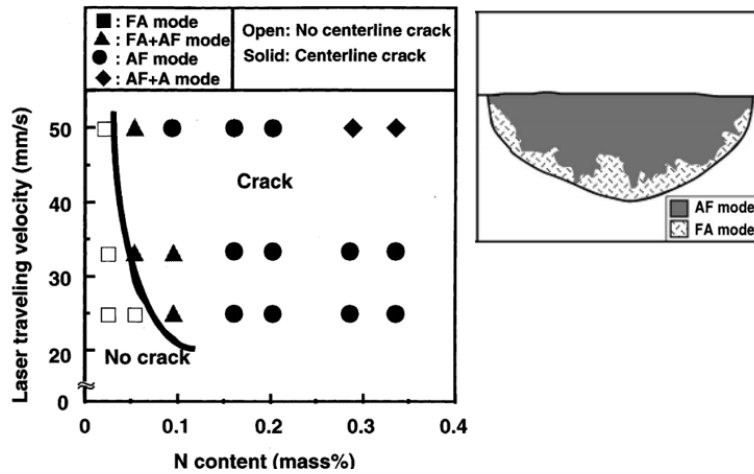


Fig 11 Effect of laser welding velocity on solidification mode and hot cracking susceptibility for 304 stainless steel laser welding; letter “AF”, “FA” denote primary austenite solidification and primary ferrite solidification mode respectively; “FA+AF” mode: schematically shown in the figure on the right [71]

Understanding solidification mode transition in LPBF process condition is important, as solidification mode dictates the phase constituent and microstructure morphology for the solidified melt pool, which have a fundamental influence on LPBF part quality. Abundant welding-related studies [89][90][71] [88] showed that primary solidification phase is an important factor for weld cracking susceptibility. Therefore, continuous efforts have been made to develop process maps and composition maps for solidification mode selection, such as the one shown in Fig 11. Such process maps were developed for welding processing with a series of stainless steels as summarized in the review of LIPPOLD [89], which were experimentally proved as effective indicators for weld cracking control.

## 2.3 LPBF of tool steel

In this study, LPBF process with tool steel was investigated, with H13 steel and M2 steel as the materials of focus. H13 steel is a typical hot work steel, commonly adopted for application in forging

dies, extrusion dies and pressure die casting [91][92]. It is designed with a relatively high chromium content (3-5.5%, wt.%) to achieve better resistance to heat softening [91][93]. M2 steel is one of the most popular steel grades for cutting tool fabrication[94]. It has a similar chromium content (~4 wt.%) as H13 steel, but it is heavily alloyed with tungsten (~6 wt.%) and molybdenum(~5 wt.%), and its carbon content (~0.8 wt.%) is twice that of H13 steel(~0.4 wt.%). It exhibits a combination of high strength, excellent wear resistance and high hardness at elevated temperature[95].

Recently, LPBF technique has received great interest from the tooling industry. The unique layer-by-layer part production process for LPBF provides it a series of advantages over conventional manufacturing technique for tooling component fabrication, including fabricating components that are geometrically unachievable by conventional manufacturing, expediting prototyping process or low volume production, and allowing customized design for metallic components. Tool shape is often geometrically complicated as it needs to be customized for each manufacturing process, and the optimized tool shape is usually determined by a series of trial prototypes. LPBF process is a promising choice for tooling production to cope with the increasing need for geometrical complex tools as well as rapid tooling prototyping[78].

Although the geometrical requirements can be satisfied, LPBF-fabricated tooling components often fail to meet mechanical properties due to processing-induced defects, including porosity, warping, distortion, cracking and delamination. For the two steel grades (H13, M2 steel) under investigation, one of the most common defects reported for their LPBF-processed parts is cracking,

So far, some investigations have been conducted to understand the connections among process parameter, microstructure and cracking in LPBF part builds with H13 steel and M2 steel as summarized below:

For H13 steel, Narvan et al [96]observed long cracks traversing from surface to center of LPBF-built H13 steel parts and Krell et al [52] measured crack densities as high as 50 m/mm<sup>2</sup>. Cottam et al [98]showed that residual stress in H13 parts could be modified by changing the laser scan pattern, which should change both the cracking and fatigue resistance. Mertens et al [99] showed that H13 steel parts built at a preheat temperature at 400°C showed enhanced mechanical properties (hardness, Young's modulus, etc.) than ones built at preheat temperatures of 200°C and lower. Krell et al [52] showed that increasing preheat temperature from 100°C to 300°C led to a decrease in crack density of H13-steel parts. All these studies reported a noticeable increase in retained austenite vol.% in the H13 parts built at higher preheat temperatures. For M2 steel, Liu et al [100], Asgharzadeh and Simchi

[101] both investigated LPBF fabrication of M2-steel parts with various process settings tested, including varied scan pattern, laser power, scan velocity and preheat temperature. In their results, pronounced cracking was observed for all the M2-steel components except that produced with 200°C preheat temperature.

However, the cracking mechanism for H13 steel and M2 steel was not yet determined due to lack of in-depth microstructure study. For instance, there is an unresolved question about LPBF microstructure of H13 steel: Cottam et al [97] reported a refined cellular network microstructure with the major constituents as martensite and retained austenite. Similar microstructures were also observed in the above-mentioned studies on cracking of LPBF-processed H13 steel, including the work by Mertens et al. [99] and Krell et al. [52]. However, these studies do not address questions about how the cellular microstructure evolves, how cracking initiates, and how wide ranges of LPBF process parameters influence microstructure.

Previous studies on LPBF of H13 steel and M2 steel as shown above suggests that cracking is at least partially related to microstructure unpredictability and instability for LPBF-processed H13 and M2 steel. LPBF solidification occurs with steep temperature gradients, rapid cooling rates and is often combined with complicated melt pool dynamics including Marangoni flow and metal evaporation. After melt pool solidification, further microstructural changes could occur as a result of repeated thermal cycling due to successive track and layer deposition. These factors introduce microstructure inhomogeneity in the as-deposited melt pool. Fig 12 presents the equilibrium and Scheil-calculated solidification route for M2 and H13 steel, with the former showing a much smaller freezing range than the latter. Scheil calculation indicates rapid solidification condition. In this regard, the larger freezing range for the Scheil-calculated solidification route as shown in Fig 12 suggests a much higher solidification cracking tendency for M2 and H13 steel when they go through the non-equilibrium rapid solidification such as in LPBF process.

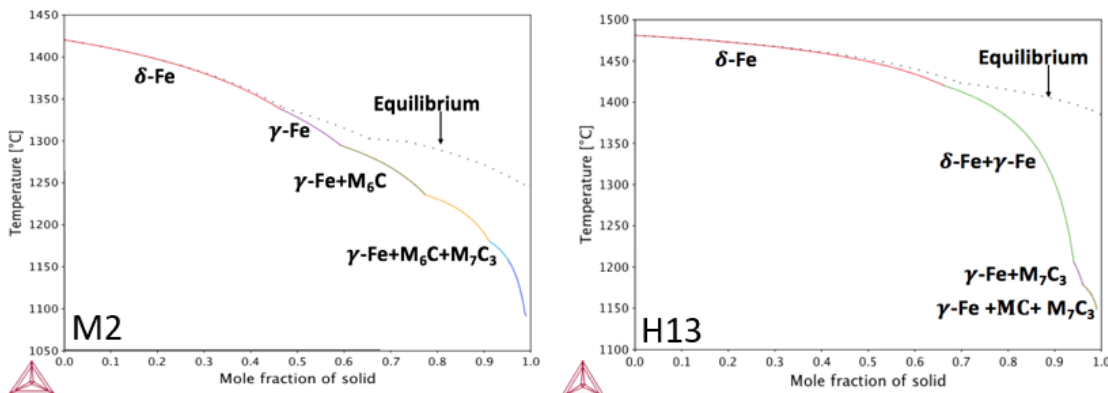


Fig 12 Solidification phase transformation for M2 steel (left) and H13-steel (right) calculated by Scheil-Gulliver Model; symbols:  $\delta$ -Fe: ferrite:  $\gamma$ -Fe: austenite:  $M_6C$ ,  $M_7C_3$ , MC: carbide

However, for LPBF of H13 steel, previous studies mostly focus on investigating the influence of preheat temperature on thermal-induced cracking, leaving the influence of non-equilibrium solidification on the cracking tendency of LPBF-processed H13 steel unexplored. A series of studies on LPBF and laser-related processing technology showed the capability of P-V parameter to alter solidification behavior and in turn leading to change their cracking tendency[55,71,102–104]. While for LPBF of H13 steel and M2 steel, the effect of P-V process parameters on their LPBF solidification microstructure and cracking tendency has not yet been investigated in detail.

In this regard, this study investigated the influence of P-V parameters on LPBF-processed H13 steel microstructure, using a sequence of single-tracks, multi-tracks and cubic samples, and showed that a fraction of tested P-V process parameters led to noticeable microstructure inhomogeneity for LPBF melt pool of H13 steel. By integrating DICTRA simulation, melt pool thermal profile calculation and experimental characterization, we presented a mechanism to explain the aforementioned question about cellular microstructure evolution in LPBF-microstructure of H13 steel and a P-V process for microstructure inhomogeneity tendency. We also showed that the presented P-V process window for microstructure inhomogeneity could be used as guidance to predict LPBF cracking tendency for H13 steel. The results from this work can be used to both understand melt pool microstructure development and guide process optimization of H13 steel parts produced by LPBF.

For M2 steel, one of the major findings in this study is that a fraction of tested P-V process parameters led to columnar-to-equiaxed transition (CET) in the LPBF melt pool of M2 steel, leading to columnar+equiaxed mixed microstructure, while other P-V parameter led to fully columnar microstructure. The correlation between hot cracking susceptibility and CET tendency in weldments was widely reported in previous studies, as summarized in chapter 2.2 earlier. This suggests the possibility that for LPBF-processed M2 steel, cracking might be controlled by manipulating LPBF microstructure (columnar/equiaxed). In this regard, this study focus on understanding how P-V process condition can be manipulated to achieve different microstructure (columnar or equiaxed) for M2-steel solidification under LPBF condition and developed a P-V processing map to provide guidance for LPBF columnar/equiaxed microstructure control. Following the same experimental framework, future studies could develop a similar P-V process map for LPBF with other alloy material of interest, which might be helpful for understanding and controlling LPBF microstructure.

## 2.4 LPBF of Ti6Al4V-xB

The material system Ti6Al4V-xB was chosen for this study because of the prevalence of Ti6Al4V as an LPBF material and the possible benefits of B additions as observed for traditional Ti6Al4V-xB. Boron-modified Titanium alloy is a promising material candidate for aerospace and naval industry since it combines light weight and good toughness of titanium alloy matrix with the high strength and stiffness of the TiB ceramic precipitates [105–107]. TiB precipitate is an ideal choice as titanium matrix reinforcements, owing to its unique advantages over other ceramic precipitates, such as TiC, SiC and TiB<sub>2</sub> [108–111]: Firstly, TiB has a much higher strength and modulus but similar density as titanium, leading to efficient strength and stiffness enhancement for titanium alloys without weight increase. Secondly, TiB precipitates show excellent chemical and thermal stability in titanium matrix even at elevated temperature, which ensures that the property enhancement by TiB reinforcement is not degraded at high temperature. Thirdly, TiB has a similar thermal expansion coefficient as titanium, which minimizes the problem of thermal stress formation at TiB-Ti matrix interface. Fourth, TiB precipitates in a titanium matrix could lead to a significant refinement effect for prior  $\beta$ -Ti and  $\alpha$ -Ti grains [112][113]. The possible reason is that TiB precipitates might act as pinning sites to restrict prior  $\beta$ -Ti and  $\alpha$ -Ti grain growth. These advantages bring evident property enhancement for B-added titanium alloy compared to their boron-free counterpart, including enhancement in wear resistance, fatigue resistance and elevated-temperature performance [108,109,113,114].

However, B-added titanium alloy, especially with high-B% addition in the hyper-eutectic B% range, faces a major risk of forming coarse primary TiB precipitates in the Ti-matrix, which might greatly degrade ductility and fracture toughness due to premature fracture initiation from these coarse TiB particles [106]. Therefore, control over TiB precipitate size is crucial to obtain a good strength-ductility combination for B-added titanium alloy. In addition to TiB precipitate size, the morphology and distribution of TiB precipitate as well as Ti-matrix microstructure, such as prior  $\beta$  grain size and morphology, all greatly influence the effectiveness of TiB-TMC material property enhancement (TMC: titanium matrix composite) [105][106][115]. Wang et al [116] tailored TiB-reinforced Ti6Al4V composite microstructure with a novel TiB network architecture using a complicated reactive hot pressing (RHP) process, which was reported to result in not only significant improvements in creep resistance but also a higher ductility compared to the counterparts with uniformly distributed TiB whisker microstructure. This unique TiB network microstructure showing enhanced performance was also observed by Fan et al [117] for TiB-Ti composites fabricated by melt

spinning process. However, these manufacturing approaches, including the RHP and melt spinning process, usually involve a complicated multi-step fabrication route, with disadvantages such as high energy consumption and tedious secondary forming process, and thus in turn results in high price of TiB-TMC material. The problems of coarse TiB precipitate formation at high B% level and fabrication difficulties might be potentially addressed by laser-based additive manufacturing (AM) technology. Banerjee et al [115][118] compared the microstructure of Ti6Al4V-2B (wt.%) produced by laser-engineered net shaping (LENS) process and by traditional arc melting process and observed that the average size of arc-melted and laser-deposited primary TiB precipitate was around 100 $\mu$ m and 2.5  $\mu$ m, respectively. Besides, the unique TiB network architecture tailored by Wang et al. and Fan et al. as mentioned earlier[116] [117] was successfully fabricated by LENS-processing of Ti-1.6B(wt.%) material [119], and greatly enhanced yield strength compared to the counterpart with TiB whisker microstructure was reported.

LPBF process might be a promising fabrication approach for B-added titanium alloy since its rapid solidification characteristic might potentially lead to effective TiB precipitate size refinement that is not achievable by traditional fabrication routes. However, LPBF fabrication of TiB-TMC material has only been explored by limited studies [120–123], with a very small TiB-TMC composition range investigated (TiB vol% limited in ~5% to ~7% vol.%), and the range of AM process settings tested for each composition are also highly limited. Titanium matrix composite (TMC) fabrication by LPBF processing has been studied using a powder mixture of pure Ti mixed with CrB<sub>2</sub> [121], B<sub>4</sub>C [123] and TiB<sub>2</sub> [120][124]. The results showed promising grain refinement and property enhancement (yield stress, wear resistance, corrosion resistance) compared to the LPBF-fabricated commercially pure Ti. , B-modified Ti6Al4V alloy with B% from 0.1-0.25 wt.% was investigated with wire-feed laser directed energy deposition (L-DED) AM process, with prior- $\beta$  grain refinement and mechanical property enhancement observed [125][126]. With such large LPBF process space and TiB-TMC composition space unexplored, it is far from enough to fully understand the microstructure engineering potential of LPBF processing for B-added titanium alloy.

The current status of insufficient investigation for LPBF-processing of Ti6Al4V-xB might be partially related to LPBF powder unavailability for Ti6Al4V-xB alloy systems. In this regard, this work employed the powder-free methodology (see chapter 1.1) to identify Ti6Al4V-xB compositions suitable for LPBF processing by evaluating four different Ti6Al4V-xB compositions over a wide composition range from 0-10 wt.% B, with each composition tested over a large P- V space. The high-

B% Ti6Al4V-xB selected in this study might show the capability of LPBF to fabricate metal matrix composite (MMC). 70 different combinations of B wt.% composition and P- V process parameter were investigated in this study, resulting in melt pools with very different geometries, microstructures and hardness. Some unique microstructures were observed, such as sub-micron-size TiB cellular networks. From the current results, a few promising P-V-B% combinations were identified, which would be considered for future powder production and further investigation. The abundant microstructural information for the total 70 different [B%, P, V] combinations presented in this study might also be used as experimental validation data for many LPBF microstructure simulation models. In addition, microstructure process mappings were constructed for each selected Ti6Al4V-xB composition based on melt pool characterization, showing how TiB microstructure alters in LPBF P-V space for different Ti6Al4V-xB compositions ranging from 1wt.% to 10 wt.%B. Furthermore, this study introduced an analytical model to develop the LPBF solidification mode transition criteria as an integrated function of LPBF P-V parameter and B% of TiB-TMC material. This analytical equation model, combined with the experimentally-observed microstructure Q-V mapping, show theoretically and experimentally that certain LPBF P-V windows could lead to coupled-eutectic solidification even for high-B% hyper-eutectic Ti6Al4V-xB material, which in turn lead to the unique TiB network microstructure. The equation model and the experimental Ti6Al4V-xB microstructure Q-V mapping might provide some useful guideline on selecting the appropriate Ti6Al4V-xB composition range and LPBF P-V window for TiB-TMC microstructure engineering,

### 3 Hypotheses and Approach

This work investigated LPBF process-microstructure-property relation for tool steel (grades: H13, M2) and Ti6Al4V-xB (x=1,2,5,10 wt.%) based on a powder-free methodology. In the current work, the following hypotheses were investigated:

1) For the same P-V parameters and alloy compositions, melt pools generated by laser re-melting bulk alloy surface (no-powder case) are representative of the dimension, geometry and microstructure of melt pools generated by laser melting of bulk alloy substrate with one powder layer addition (powder-added case).

- This was evaluated by experimental measurements. The dimension approximation was considered to be reasonable if the difference between no-powder and powder-added melt pool width measurement is within 7%. The geometry approximation was considered to be reasonable if P-V maps of no-powder and powder-added melt pool geometry provide the same P-V windows for balling, keyholing and undermelt. The microstructure approximation was considered to be reasonable if the same microstructure constituents are present in both melt pools. As detailed further below there are cases where significant inhomogeneities exist in the microstructure of a single melt pool. In these cases the no-power case was taken to be similar to the powder-added microstructure if the difference in local vol% of inhomogeneous microstructure for no-powder and powder-added H13-steel melt pool was within 10%.

2) LPBF melt pools of H13 steel and M2 steel were observed to show microstructure inhomogeneity. The source of the observed inhomogeneity was local thermal condition variation at different regions in the melt pool during solidification:

For H13 steel, the local cooling rate variation in melt pool result in different microsegregation behavior at different regions in the melt pool, in turn causing melt pool microstructure inhomogeneity.

For M2 steel, the local temperature gradient and solidification rate variation in melt pool causes columnar-to-equiaxed transition to occur in the melt pool.

- Evaluation approach: comparison between microstructure prediction and experimental observation. For H13 microsegregation predictions made by coupling DICTRA simulation and melt pool cooling rate simulations. For M2, microstructures were predicted by coupling of G-R thermal

criteria for CET occurrence with simulated melt pool G- and R-profile (G: temperature gradient; R: solidification velocity)

3) For LPBF processing of Ti6Al4V-xB system, the rapid solidification during melt pool deposition leads to non-equilibrium coupled-eutectic solidification for hyper-eutectic Ti6Al4V-xB material

- Evaluation approach: comparison between P-V map for solidification mode (predicted) and P-V map for solidification microstructure (experimental). The Ti6Al4V-xB solidification mode was predicted by a model based on the competitive growth principle.

## 4 Experimental

### 4.1 Materials

#### 4.1.1 Tool steels

Two tool steel grades were investigated in this study, which are M2 and H13 steel. For H13 steel, both powder sample and bulk plates were used for laser scan tests. For M2 steel, only bulk plates were used. Table 1 showed the chemical compositions for bulk M2, H13 steel plate and powder H13 steel material, measured by Inductively Coupled Plasma Spectroscopy (ICP) and Carbon-Sulfur analysis (LECO combustion equipment). The bulk M2 and H13 plates were commercially available. The plate surface was polished and cleaned before the laser scan tests, which gave  $\pm 2\mu\text{m}$  surface finish. H13 steel powders were produced by gas-atomization, supplied by LPW Technology Ltd. Powder size distributions are shown in Fig 13, showing an average powder size as  $19\mu\text{m}$ . Powder flowability was characterized, with the result presented in Table 2, suggesting good powder flowability.

Table 1 chemical composition (wt.%) of M2-, H13-steel bulk plate and H13-steel powder determined by ICP-AES and LECO Combustion

Element	W	Cr	Mo	Mn	V	Ni	Si	C	Fe
M2-bulk	6.0	4.0	4.7	0.3	1.83	0.25	0.3	0.86	Bal.
H13-bulk	NA	4.9	1.25	0.4	0.75	0.16	1.1	0.40	Bal.
H13-powder	NA	5.2	1.3	0.3	1.0	0.1	1.2	0.37	Bal.

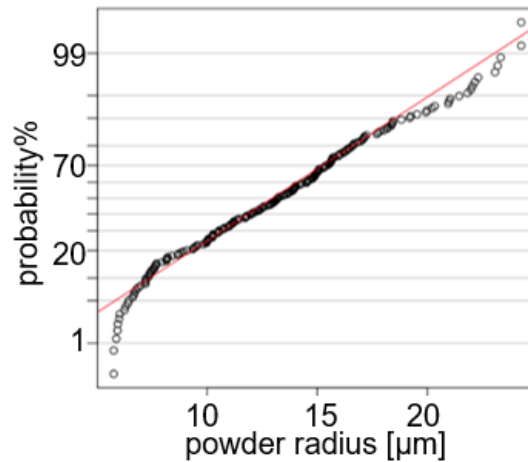


Fig 13 size distribution of H13 powder particles used in this work

Table 2 characterization result for powder flowability

Material	Apparent Density(g/cm <sup>3</sup> )	Tapped Density(g/cm <sup>3</sup> )	Hausner Ratio (Tapped/Apparent)	BFE(mJ)	SE(mJ/g)
H13-powder	4.1	5	1.23	756	2.78

#### 4.1.2 Ti6Al4V-xB

Five Ti6Al4V-xB compositions (x=0, 1, 2, 5, 10, wt% B) were selected for evaluation. The pseudo-binary phase diagram for the Ti6Al4V-B system is shown in Fig 14, which is calculated at constant 6 wt. Al% and 4 wt.% V for the Ti-Al-V-B quaternary system. The diagram was generated by Thermo-Calc software [35], using data for the Ti-Al-V-B quaternary system from the COST507 light metal database [127]. All alloys selected were expected to form only TiB, except for Ti6Al4V-10B, for which some primary TiB<sub>2</sub> was expected. The compositions were selected to compare hypo- and hyper-eutectic alloys, and to assess melt pools containing various TiB precipitate vol.%, as shown later in Fig 56.

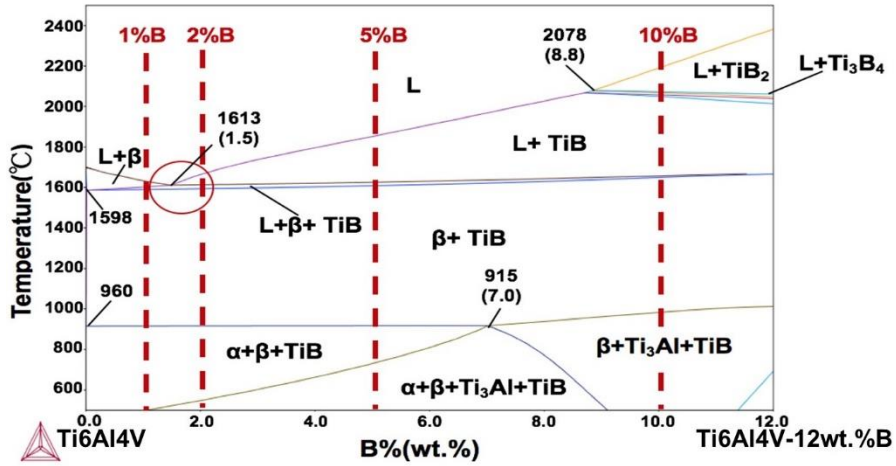


Fig 14 Pseudo-binary phase diagram of Ti6Al4V-B system: trial compositions of this study indicated by red dashed line

The test materials were fabricated by arc-melting charges of B powder (supplier: Alfa Aesar) and bulk pieces of Ti6Al4V (supplier: ATI) under Ar atmosphere, holding in a well-stirred molten state for 50-60s before cooling. For each trial Ti6Al4V-xB compositions, multiple alloy ingots (approximately 35g each) were fabricated. Each ingot was re-melted 4-5 times to ensure composition homogeneity. The B content of the alloy buttons, especially their local B content at the near-surface

region, was confirmed by examining the vol% of TiB precipitates measured by image processing with SEM backscattered electron images using grey-scale contrast in ImageJ software [128], as presented in chapter 7.1. After re-melting, the arc-melted ingots were then machined into disk-shape (diameter 28mm; height 6mm) as schematically shown in Fig 15(a), in order to fit in the pockets of a customized button holder (Fig 15(b)) for the EOS M290 machine used in this study. They were referred to as buttons in this paper.

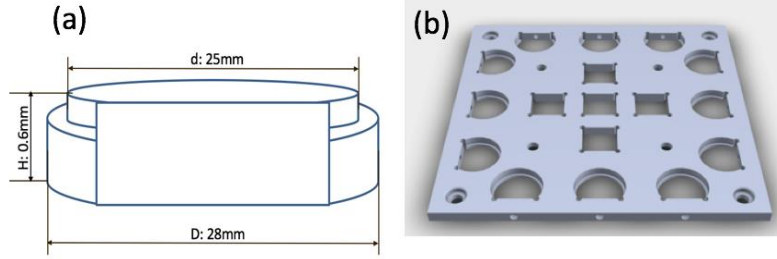


Fig 15 Schematic diagram of (a) Ti6Al4V-xB alloy button; (b) button holder in the EOS M290 machine

## 4.2 LPBF laser scan experiments

Laser scan experiments were performed with an EOS M290 metal LPBF AM machine. This machine is equipped with a diode-pumped Yb laser with beam focus diameter of 100  $\mu\text{m}$  and maximum power of 400 W. All experiments were conducted under Ar atmosphere. The preheating temperature was 35°C for tests with Ti6Al4V-xB and 80°C for tests with tool steels, which are the EOS M290 program default setting for part build with Ti6Al4V and 316L stainless steel.

It should be noted that for the Ti6Al4V-xB test, a customized button holder as shown in Fig 15(b) was used to position and fix the Ti6Al4V-xB button samples on the build plate of the EOS M290 machine and to ensure the button surfaces were maintained at the same level. The holder could be flipped so that laser scans could be made on both sides of the button.

A series of laser scan tests were carried out as shown in Table 3, reported with the test material and number of P-V sets tested for each case. In Table 3, no-powder test was referred to laser scan conducted directly on the surface of bulk alloy (Ti6Al4V-xB arc-melted button or tool steel plate). Powder-added tests were only conducted for H13 steel, which referred to laser scan by spreading one layer of H13 powder across an H13 tool steel plate. The thickness of the powder layer is 20 $\mu\text{m}$ , which is the default powder layer thickness for steel part build suggested by EOS M290 machine. The

purpose of conducting both no-powder and powder-added test was to evaluate the influence of powder presence on melt pool solidification.

Table 3 List of LPBF laser scan tests conducted in this work with number of P-V sets (P: laser power; V: scan velocity), material and laser scan pattern adopted in each laser scan test

material	LPBF laser scan test		
	Material state	Laser scan pattern	Number of P-V sets
H13 steel	No-powder	Single-bead	40
		Multiple-bead	19
	Powder-added	Single-bead	40
		Multiple-bead	19
	3D-cube build	multiple-bead +66° rotate per layer	8
M2 steel	No-powder	Single-bead	28
Ti6Al4V -1, 2,5 wt.%B	No-powder	Single-bead	14
		Multiple-bead	3
		overlap-bead	3
Ti6Al4V-10wt.%B	No-powder	Single-bead	14
Ti6Al4V	No-powder	Single-bead	14

As shown in Table 3, for Ti6Al4V-xB, three types of laser scan experiments were conducted in no-powder version, referred to as single-bead, multiple-bead and successive-bead, as schematically shown in Fig 17(a), (b), (c). For single-bead laser scan experiment, one button per Ti6Al4V-xB trial composition was used, and seven single-tracks (length:13mm, 2mm spacing between tracks) were made on each side of the Ti6Al4V-xB button, as shown in Fig 17(a). Each track adopts a different P-V setting, as listed in Table 1. Therefore, 14 different P-V settings were tested per trial TI6Al4V-xB composition.

Selection of the 14 P-V settings was guided by the processing map approach [129] to effectively reduce the number of trial P-V settings required to investigate melt pool solidification with different thermal conditions. Based on the processing map approach, the cooling rates for the P-V settings were first estimated from the Rosenthal solution in Equation 8 [21] using the data listed in Table 5. P-V combinations with similar cooling rates were connected to obtain constant-cooling curves. The 14 P-

V settings in Table 4 were selected, which form four constant-cooling curves (solid lines in Fig 16).

$$\dot{T} = 2\pi k(T_{sol} - T_0)(T_{liq} - T_0) \frac{V}{\eta P} \quad \text{Equation 8}$$

Where  $\dot{T}$  is average surface cooling rate between melt pool solid/liquid boundary at the maximum length of melt pool along laser scan direction,  $T_{sol}$ ,  $T_{liq}$  are solidus & liquidus temperature,  $T_0$  is temperature far from melt pool, taken as preheat temperature for the laser scan test,  $k$  is thermal conductivity,  $V$  is laser scan speed,  $P$  is the laser output power,  $\eta$  is absorptivity, which was obtained from an absorptivity model discussed later in this paper.

Table 4 P-V settings tested for Ti6Al4V-xB single-bead laser scan test

(P: laser power; V: scan velocity)

#track	#1	#2	#3	#4	#5	#6	#7	#8	#9	#10	#11	#12	#13	#14
<b>P(W)</b>	280	280	280	280	215	215	215	115	115	155	155	155	215	370
<b>V(mm/s)</b>	800	1200	1600	2200	580	800	1200	580	800	580	1200	1600	1600	1050

Table 5 Alloy properties used for calculation [29,130,131]

Material	Absorptivity	Melting temperature (K)	Thermal conductivity (W/m · K)	Density (kg/m <sup>3</sup> )	Heat capacity (J/kg · K)
Ti6Al4V	Equation 10	1913	6.7	4430	526
H13-steel	Equation 10	1681	25.9	7750	460

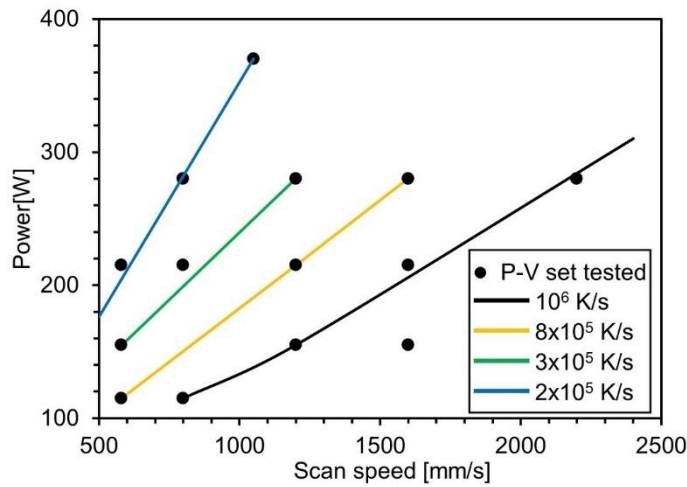


Fig 16 Selected P-V sets for Ti6Al4V-xB laser scan test with lines of constant cooling rate approximated from the Rosenthal equation (Equation 8); P-V value: see Table 4

Multiple-bead and overlap-bead tests were conducted for Ti6Al4V-1,2,5 wt.%B but not Ti6Al4V-10%B, in that Ti6Al4V-10%B was screened out as inferior composition based on the single-track experiment results. This will be presented in chapter 7.6. For multiple-bead experiment, a single-layer pad (L:15mm; W:13mm) was created on each side of button surface, as shown in Fig 17(b), while for overlap-bead experiment, a two-layer pad was created (Fig 17(c)): In the first layer, laser beam deposited on button surface to create a pad (15mm\*13mm), shown as the red region in Fig 17(c); in second layer, laser beam deposited on the previously-formed pad with same scan direction but different [P, V, hatch spacing] setting, which was adjusted to have smaller energy density than first-layer laser scan. Thus the second-layer pad was created with a much smaller melt pool than that of first-layer, marked as the yellow region in Fig 17(c). For each Ti6Al4V-xB composition of selection, three arc-melted buttons were used for fabricating 3 1-layer pads and 3 2-layer pads. Each pad was created by a different [P, V, hatch spacing] process setting as listed in Table 6. In Table 6, P-V #a-#c were used to create the 1-layer pads and also the first-layer of 2-layer pads. P-V #ao-#co were used to create the second-layer of the 2-layer pads.

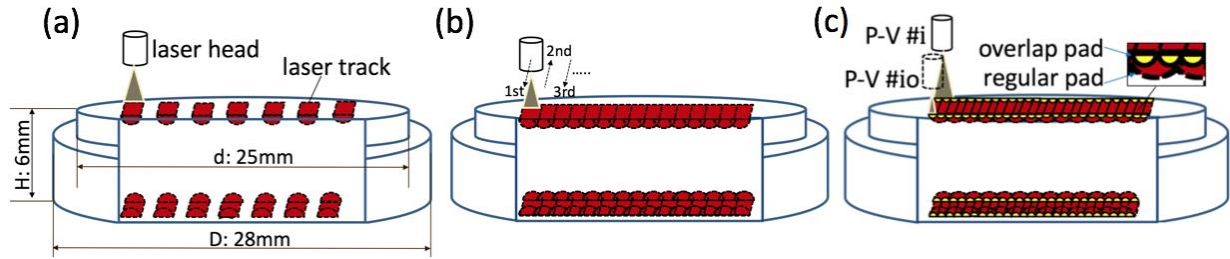


Fig 17 schematics of three different laser scan experiment to fabricate (a) single-track, (b) single-layer pad, (c) 2-layer pad on the arc-melted Ti6Al4V-xB buttons

The selection of P-V #a-#c in Table 6 was guided by single-track melt pool observation. They are P-V set #2, #6 and #7 in Table 4. As shown further in chapter 7.4.1 and 7.3.2, they cover up all types of single-track melt pool microstructure observed for Ti6Al4V-1,2,5 wt.%B microstructure P-V process mapping (Fig 62), and meanwhile all fall in the porosity control process window developed for each Ti6Al4V-xB trial compositions (Fig 60). For the 2-layer pads, the P-V sets for the second-layer scan, i.e., P-V #ao-co, were determined by scaling their corresponding P-V sets for the first-layer scan, i.e., P-V #a-c, according to Equation 9, which were expected to result in melt pool depth ( $D_{MP}$ ) for the second-layer pad as  $1/4$  of  $D_{MP}$  for first-layer pad.  $D_{MP}$  for first-layer pad was approximated from the melt pool depth measurement for single-track with corresponding [B%, P-V] combination. It should

be noted that for the three Ti6Al4V-xB trial composition, hatch spacing for the same P-V setting was different, which was determined by scaling the melt pool width measured for single-track with corresponding [B%, P-V] combination by a nominal overlap of 30%.

Table 6 laser P-V settings tested for Ti6Al4V-xB multiple-bead and overlap-bead laser scan test

#Pad	#a	#b	#c	#ao	#bo	#co
P(W)	280	215	215	140	108	108
V(mm/s)	1200	800	1200	1800	1200	1800
Hatch spacing	vary with different Ti6Al4V-xB composition					

(#i: regular pad, #io: overlap pad on #i)

$$D_{MP} \approx \sqrt{\frac{\eta P}{e\pi\rho C(T_{liq} + T_{sol} - 2T_0)V}} \quad \text{Equation 9}$$

Where  $D_{MP}$  is melt pool depth,  $\rho$  is density,  $C$  is heat capacity,  $e$  is Euler's number,  $\eta$  (laser absorptivity) adopts the self-developed model in Equation 10. The details for generating the absorptivity model and the reliability to approximate the absorptivity of Ti6Al4V-x%B by the Ti6Al4V absorptivity in Equation 10 could be found in chapter 5 and chapter 7.2.

A series of laser scan tests were conducted for tool steel, as summarized earlier in Table 3. For H13 steel, single-bead and multiple-bead laser scan tests were conducted in both no-powder and powder-added version, with the selected P-V settings summarized in Table 7. There were 40 P-V settings tested for H13 steel single-track laser scan experiment in both no-powder and powder-added cases. Three tracks were fabricated for each P-V setting. Tracks were 32mm in length and there was 1.5mm spacing between tracks. Selection of these 40 P-V settings was also guided by the process map approach as presented earlier for P-V selection of Ti6Al4V-xB laser scan and thus were not repeated here. The 40 P-V sets selected in Table 7 are presented in Fig 18, lying along 7 constant-cooling curves that were expected to show evidently different solidification cooling rate, as indicated by the solid lines with different colors in Fig 18. The cooling rate was estimated by Equation 8, using the material property data in Table 5. Eighteen P-V sets of them (marked by a “p” superscript in Table 7) were selected for no-powder and powder-added multiple-track laser scan tests, labeled as test (b) & (d) in Table 7. One laser-deposited pad (10mmx10mm) was created for each P-V set. Selection of these 18 P-V sets was guided by the single-track results.

Besides laser scan test, 3D cube build experiments were also conducted for H13 steel. From the 18

P-V sets tested for both single-bead and multiple-bead tests, eight were selected for 3D-cube build test, as marked by a “c” subscript in Table 7. One cube with dimensions 15mmx10mmx10mm was built per P-V sets. The P-V sets were selected based on single-track and pad results. The cube build layer thickness is 20μm, same as the powder layer thickness for powder-added tests.

Table 7 P-V settings selected for tool steel laser scan test: for M2-steel no-powder test:28 P-V sets:

P-V#1-#28, H13-steel no-powder and powder-added single-bead test: all 40 P-V sets, H13-steel multiple-bead test: 18 P-V sets: indicated by “p”, H13-steel 3-D cube build test:8 P-V sets: indicated by “c”

No.	P (W)	V (mm/s)	No. (continue)	P (W)	V (mm/s)
#1	100	600	#21 <sup>p</sup>	300	1000
#2	100	800	#22 <sup>p</sup>	300	1200
#3 <sup>p</sup>	150	600	#23	300	1400
#4 <sup>p</sup> <sub>c</sub>	150	800	#24	300	1600
#5	150	1000	#25 <sup>p</sup>	300	1800
#6	150	1200	#26 <sup>p</sup>	350	1000
#7 <sup>p</sup> <sub>c</sub>	200	600	#27	350	1200
#8	200	800	#28	350	1400
#9 <sup>p</sup> <sub>c</sub>	200	1000	#29	125	1200
#10 <sup>p</sup> <sub>c</sub>	200	1200	#30	125	1600
#11	200	1400	#31 <sup>p</sup>	150	1600
#12	200	1600	#32	120	2000
#13	250	600	#33	200	1500
#14 <sup>p</sup> <sub>c</sub>	250	800	#34	150	2000
#15 <sup>p</sup> <sub>c</sub>	250	1000	#35	200	1750
#16 <sup>p</sup>	250	1200	#36 <sup>p</sup> <sub>c</sub>	280	1500
#17 <sup>p</sup>	250	1400	#37 <sup>p</sup>	225	1200
#18	250	1600	#38 <sup>p</sup>	150	1400
#19	250	1800	#39	200	1800
#20 <sup>p</sup> <sub>c</sub>	300	800	#40	300	600

For H13-steel multi-bead test and 3D cube builds, each P-V set was assigned with a different hatch spacing, which was designed by increasing the melt pool width measured from single tracks by 30%. The same design approach for hatch spacing design was adopted for the Ti6Al4V-xB laser scan test, as shown earlier in this chapter. The layer thickness for powder-added and 3D build tests was designed as 30 $\mu$ m, the same as the default powder layer thickness setting for 316L stainless steel provided by EOS machine.

For M2 steel, only no-powder single-bead test was conducted. 28 well-separated laser-remelt tracks (length:13mm, 1mm spacing between tracks) were fabricated on a M2 steel plate surface. Each track adopts a different P-V setting, which are P-V#1-#28 as listed in Table 7. These 28 P-V settings were also tested for H13 steel.

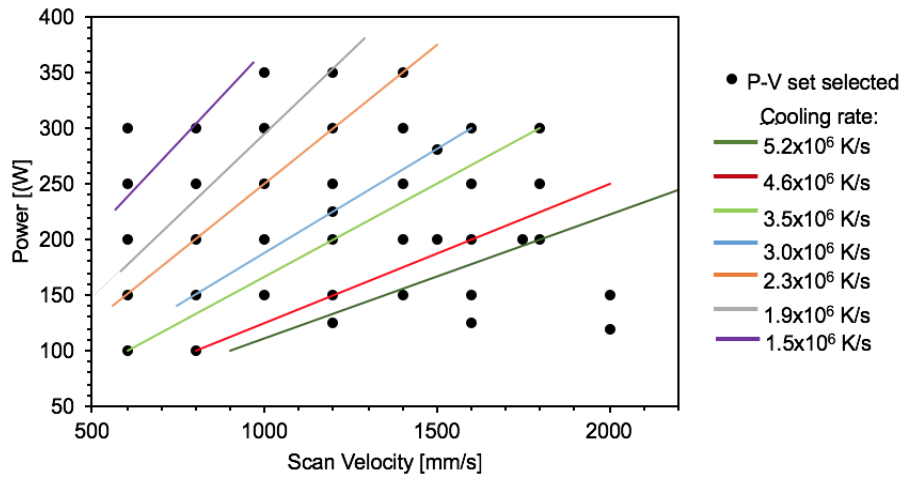


Fig 18 40 P-V sets selected for H13-steel no-powder & powder-added single bead laser scan test with predicted constant cooling-rate curves (indicated by solid lines with different colors)

### 4.3 Characterization Methods

A series of characterizations were conducted for laser track, pad & cube samples. They were listed with their corresponding characterization location in Table 9. First, for each laser-deposited tracks and pads, the top surface was characterized across whole track length and pad surface by optical microscopy (OM) to determine balling occurrence.

Then each track, pad and cube were sectioned: tracks and pads were sectioned normal to laser scan direction at three locations well away from the two ends of the tracks to examine melt pool cross-sections. Cross-sections were taken away from the track or pad ends to ensure steady-state conditions.

Since there were three tracks made for each P-V set, nine single-track melt pool cross-sections were characterized for each P-V setting. Some H13-steel pads were sectioned and gradually ground along laser scan direction to reveal longitudinal sections through the center-line of the laser trace for microstructure investigation. Cubes were sectioned parallel to the build direction to produce three cross-sections as schematically shown in Fig 19.

All sections were ground and polished. The obtained Ti6Al4V-xB samples were etched with Kroll's etchant and the tool steel samples were etched with Vilella's etchant (1g picric acid, 5ml HCL, 100ml ethanol). Melt pool dimension and geometry were measured using melt pool cross-section images taken by a Zeiss optical microscope. Melt pool cross-section and longitudinal-section microstructure were characterized by SEM/EDS characterization (FEI Quanta 600) in both backscatter electron mode (BSE) and secondary electron mode (SE). Besides, un-laser treated Ti6Al4V-xB microstructure (i.e., arc-melted microstructure) was also characterized by SEM/EDS and XRD analysis (Panalytical XPert Pro). X-ray diffraction (XRD) (Cu source for Ti6Al4V-xB, Co-source for tool steel) was conducted on the top surface of some laser-deposited pads and on cross-sections of cubes for phase identification and phase vol.% quantification.

Nano-indentation experiments were carried out to assess melt pool hardness using an MTS Nano Indentation instrument with indentation depth of 1000nm. Indentation tests were carried out at five to seven locations in each melt pool and across multiple melt pools for pad- and cube-sample to ensure obtaining representative average hardness value for the melt pool.

For single-track and pads, the melt pool dimension, microstructure and micro-hardness results presented in chapter 6 and chapter 7 were the average results summarized from all three cross-sections per track and pad.

Additional characterization was conducted for H13-steel steel track, pad and 3D cube samples, including melt pool phase identification, microsegregation characterization and cracking density measurement. Two TEM foils were made from the H13 steel single-track melt pool cross section. As shown further in chapter 6.2, the top and bottom local region in H13 steel melt pool presents two different microstructures, referred to as type (A) and (B) microstructure (see Fig 30(ii) and (iii)). For the two TEM foils, one was made from the top region of melt pool with type (A) microstructure and the other was made from the bottom region with type (B) microstructure. TEM foils were fabricated by using a variation of the focused-ion-beam (FIB) in situ lift-out technique by an FEI Dual Beam FIB-SEM. The TEM measurements were conducted at a nominal acceleration voltage of 200-KeV.

FEI Tecnai F20 Field Emission Transmission Electron Microscope and FEI Titan G2 80-300 Transmission Electron Microscope were used to examine the thin foils. Microsegregation characterization and phase identification were analyzed by high angle annular dark field (STEM-HAADF) images and selected area electron diffraction patterns (SADPs), captured in TEM characterization. Electron backscatter diffraction (EBSD) was also conducted for phase identification. Cracking characterization was conducted qualitatively for H13 steel pads and quantitatively for cubes. Crack density of each cube was determined by counting the number of cracks per unit area of cube cross-sections. Forty areas, each  $1\text{mm}^2$ , were taken from each of the three cross-sections in Fig 19, and thus in total 120 crack measurements were made per cube. The same crack density measurement was adopted in the study presented by Harrison et al [68].

Table 8 summary of characterization methods and corresponding characterization location conducted for laser-track, pad, and cube samples

Sample	Location	Characterization					
		OM	SEM/EDX	XRD	EBSD	TEM	nano-indentation
Track	top surface	√	√		√	√	√
	cross section	√	√				√
	longitudinal section		√				
Pad	top surface	√	√	√			√
	cross section	√	√				√
cube	XY-, XZ-, YZ-section	√	√	√			√

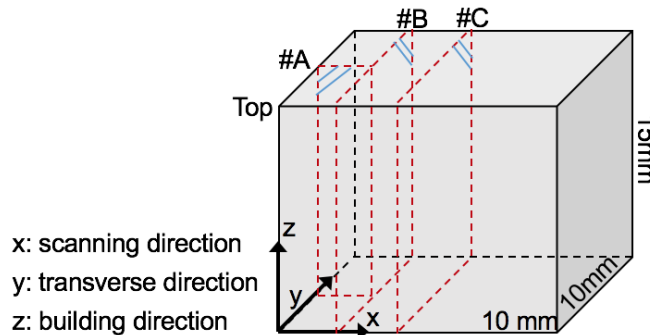


Fig 19 Schematic of the LPBF-built cubes for H13-steel illustrating the three cross-sections for microstructure and cracking characterization

## Results and Discussion: Chapter 5-7

### 5 Powder/bulk absorptivity estimation

Appropriate estimation of laser absorptivity was important for LPBF investigation. This study developed an empirical absorptivity model for Ti6Al4V and H13 steel as shown in Equation 10 and Table 10. Noted that in this study, all the related calculation for absorbed power (Q) of Ti6Al4V-xB and H13 steel used the varied absorptivity models instead of the constant absorptivity in Table 10. The absorptivity estimation was conducted for the following reasons: First, by summarizing existing publications, this work found that for the same alloy, absorptivity values reported from different sources vary from each other. This could be seen from Table 9 for each alloy of investigation. Second, published information on laser absorptivity only includes data for a limited range of alloy systems. For the alloy systems investigated in this work, their absorptivity data are rarely reported or even unobtainable since they are either not common material candidates for laser treatment or have non-commercial compositions. Thirdly, it was expected that laser absorptivity would vary with P, V, and material state (powder/bulk). For instance, Yan et al. [131] reported that the laser absorptivity of P20 steel powders changes from 0.4 to 0.55 for powders with different surface oxide level. Trapp et al. [25] reported that the 316L stainless steel increases from 0.3 to 0.8 as laser power changes from 100 W to 400 W. Tolochko et al. [132] reported different absorptivity of Ni-based alloy powder for laser power density at 250W/cm<sup>2</sup> and 100W/cm<sup>2</sup>.

Table 9 Summary of absorptivity values from literature for each material system

Material System	$\eta$	reference
Ti6Al4V	0.44;	[133]
	0.34;	[134]
	0.48;	[22]
H13-steel	0.48;	[135]
	0.38;	[131]
M2-steel	0.33;	[135]
	0.51;	[135]
	0.45	[136]

Therefore, this work intends to develop an absorptivity model for each tested alloy as a function of P,V, and material state (powder/bulk) ( $\eta=f(P, V, \text{material state})$ ). The model was developed by experimental data fitting of melt pool width measurement using the Eureka software, which is an automating data model generation tool [137], with the Rosenthal analytical solution as a physical

basis[21]. Table 10 summarizes the final optimized result for the absorptivity of each alloy system in their corresponding material state(powder/bulk). The general workflow for obtaining the absorptivity models in Table 10 was shown below, exemplified by powder- and bulk-Ti6Al4V absorptivity model generation:

First, experimental data of melt pool width (W) were collected from single-track laser scan tests conducted on Ti6Al4V with three different material states: (i) on Ti6Al4V arc-melted buttons, (ii) on Ti6Al4V alloy baseplate (referred to as the no-powder test), and (iii) on one 30  $\mu\text{m}$  thick layer of Ti6Al4V powder spread across Ti6Al4V baseplate (referred to as the powder-added test). The tests of state (i) were conducted as part of this study and those for (ii) and (iii) were part of a previous study with details reported in [38]. Then melt pool width was measured for three melt pool cross-sections along each laser track, with their average melt pool width value summarized into three different datasets:

1. width (W) of 48 melt pools from no-powder test and their corresponding P-V sets [38];
2. width of 48 melt pools from powder-added test and their corresponding P-V sets [38];
3. width of 14 melt pools made on arc-melted Ti6Al4V button and their corresponding P-V sets (this work, Table 4).

The absorptivity model was developed from datasets (1) and (2), with dataset (3) kept for validation. First, datasets (1) and (2) were filtered to remove melt pools with keyholing geometry. This was because the model fitting used the Rosenthal model (Equation 11) as a basis, which often fails to provide an accurate prediction for keyhole melt pool dimension [25] [21][26]. The experimental data W, P, V was processed by Equation 11, which is a Rosenthal-based relation[21], to derive a “predicted” absorptivity ( $\eta_{\text{pre}}$ ) for each melt pool.

$$\eta = KP^aV^b \quad \text{Equation 10}$$

where K, a, b are fitting parameters, with two sets generated: one for melt pools made with powder, the other for melt pools made without powder. Table 10 shows the final optimized values of these parameters.

$$\eta_{\text{pre}} = \frac{\pi k(T_m - T_0)W + 0.125e\pi\rho C(T_m - T_0)VW^2}{P} \quad \text{Equation 11}$$

Where W is melt pool width,  $\rho$  is density, C is heat capacity,  $T_m$  is melting temperature (average of liquidus temperature & solidus temperature), e is Euler’s number. The value for alloy properties used in Equation 11 was listed in Table 5.

The open-source code go-eureqa [137] was used to find the best function that would describe the variation in  $\eta_{pre}$  with P and V. The following relation was obtained

Table 10 fitting parameter in absorptivity model for Ti6Al4V and H13-steel (powder/bulk)

Material System	Material State	model: $\eta = KP^aV^b$					model: $\eta = \text{const.}$	
		K	a	b	$\eta$ : Range	R <sup>2</sup> of fit	$\eta$	R <sup>2</sup> of fit
Ti6Al4V	Powder	0.11	0.15	0.07	0.29-0.52	0.66	0.40	-0.03
	Bulk	0.06	0.43	-0.09	0.25-0.44	0.72	0.33	-0.07
H13-steel	Powder	0.71	0.12	-0.17	0.34-0.46	0.46	0.39	-0.006
	Bulk	0.18	0.37	-0.16	0.32-0.48	0.48	0.38	-0.04

Two points should be emphasized: first, the fitting of no-powder absorptivity model (with dataset (1)) and powder-added absorptivity model (with dataset (2)) were independent from each other. Second, none of the data from dataset (3), the model validation dataset, were included as data input of model fitting, and the 14 P-V settings selected for dataset (3) did not overlap with any of the 48 P-V settings for dataset (1) and (2).

Absorptivity models as shown in Table 10 were obtained for powder- and bulk-H13 steel by following above data fitting procedure with their corresponding melt pool experimental data. Table 11 summarizes the list of datasets adopted in absorptivity model development for each alloy system.

Table 11 dataset used for absorptivity model generation for each test material

Dataset	Powder-Ti64	Bulk-Ti64(1)	Bulk-Ti64(2)	Powder-H13	Bulk-H13(1)	Bulk-H13(2)
#Data point	48	48	14	31	31	8
P-V sets	[38]	[38]	Table 4	Table 7	Table 7	Table 7

The validity of the developed absorptivity models was supported by the aspects below:

First, Table 10 presented the range of  $\eta$  for each alloy system based on their corresponding optimized absorptivity model, which could be found to be within the absorptivity measured from other studies, as shown in Table 9.

Second, as a comparison, the aforementioned data fitting process generates a constant absorptivity for each alloy system, as shown in Table 10. Table 10 also compared the R<sup>2</sup> of fitness for the P-V

varied absorptivity model and constant absorptivity model. The  $R^2$  values reflect the fitness of the two absorptivity models to the predicted absorptivity dataset in Equation 11. As shown in in Table 10, for all the alloy system tested, in either bulk- or powder-state, the developed P-V varied  $\eta$  model in Equation 10 shows a significantly higher  $R^2$  value than the constant  $\eta$  model, suggesting a generally better agreement to the predicted absorptivity in Equation 11 for the  $\eta$ -model in Equation 10 rather than the constant  $\eta$ . This comparison is more directly presented in Fig 74 in the Appendix, which shows the comparison of the predicted absorptivity with the two fitted absorptivity models in Table 10. Noted again that the predicted absorptivity was obtained from the experimental measurement of melt pool dimension, as shown in Equation 11. For this reason, the P-V varied absorptivity model in Table 10 was considered as a better absorptivity approximation than the constant absorptivity model, and thus all the related calculation for Ti6Al4V-xB and H13 steel in this study use the varied absorptivity models instead of the constant absorptivity in Table 10 (e.g., equations in Table 12 and Table 19).

Third, Fig 20 and Fig 21 present the relation between melt pool width and square root of absorbed power density ( $Q/V$ ) for each datapoint in dataset (1)-(3) measured for Ti6Al4V and H13 steel. The absorbed power ( $Q$ ) is related to the laser beam power ( $P$ ) by  $Q = \eta P$ , with Fig 20(a) and Fig 21(a) adopting the absorptivity model developed in this work and a constant absorptivity value reported in previous study [134] respectively. Melt pool dimension is essentially determined by absorbed power density ( $Q/V$ ), regardless of the powder presence and the specific P-V value. As mentioned earlier, dataset (1) and (3) are measured for the case of no powder presence, while dataset (2) measured with powder presence; for dataset (3), as the validation dataset, its datapoints have P-V value different from that of dataset (1) and (2). Based on this, if the absorptivity is properly estimated, then the data points from dataset (1)-(3) would overlap at the same  $Q/V$  value in Fig 20 and Fig 21 despite their differences in powder presence and P-V parameter. This was the case for Fig 20(a) and Fig 21(a), while there was more scatter in Fig 20(b) and Fig 21(b). Thus, the absorptivity model in Equation 10 gave a more accurate estimation than the constant absorptivity adopted in Fig 20(b) and Fig 21(b).

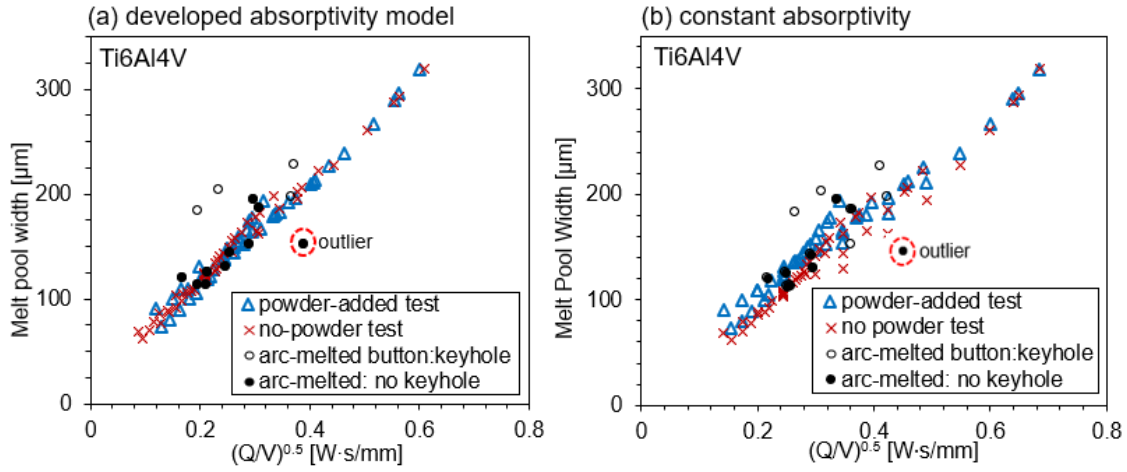


Fig 20 Comparison of melt pool width between laser scan on Ti64 bulk alloy and Ti64 powder layer for 3 datasets (data source: this work and [38]) by adopting: (a) varying absorptivity model in Equation 10; (b) constant absorptivity; non-keyhole data point outlier: marked by red dashed circle

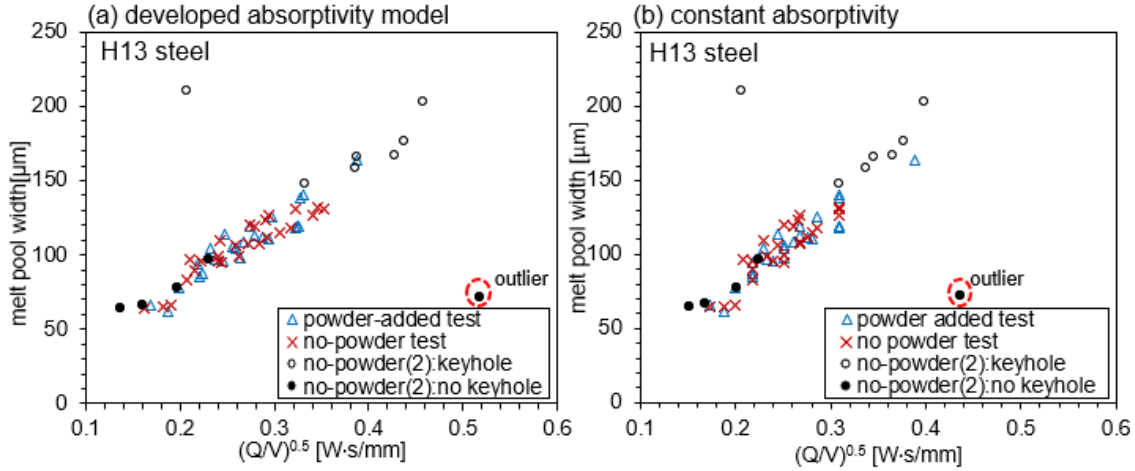


Fig 21 Comparison of melt pool width between laser scan on bulk H13-steel and H13-steel powder layer for 3 datasets by adopting: (a) varying absorptivity model in Equation 10; (b) constant absorptivity; non-keyhole data point outlier: marked by red dashed circle; note: no-powder(2) dataset: validation data not used for data fitting

Fig 20 and Fig 21 also suggest that for both Ti6Al4V and H13 steel, with the proposed laser absorptivity model in Equation 10, high-level dimensional similarity was ensured between the no-powder and powder-added melt pool at same Q-V condition for most case. While two exceptions exist: One is melt pools with keyhole geometry, as indicated by the black hollow circle in Fig 20 and Fig 21. This was expected since the laser absorptivity changes significantly when deep keyholes form, which was difficult to be accurately assessed by Equation 11, a Rosenthal-based relation. Second is

melt pools generated at  $P = 370 \text{ W}$ , as indicated by the dashed-line circled point in Fig 20 and Fig 21 (labeled as “outlier”). This was close to the power output limit of the EOS M290 machine (400 W) and under these conditions, there were possible deviations between actual and programmed laser power output. As shown earlier in the introduction, this study adopts a powder-free approach for LPBF investigation. It assumes that melt pool directly deposited on bulk alloy could give a reasonable approximation to melt pool deposited on bulk alloy with a powder layer addition, referred to as assumption of bulk/powder melt pool similarity.

Therefore, the results presented in Fig 20 and Fig 21 suggests the application range of this assumption by showing the no-powder melt pool could give sufficient dimensional approximation for no-powder melt pool for most of the P-V process space except when keyholing occurred or the maximum laser power was approached. For further validation, we evaluated the difference between no-powder and powder-added melt pool width measurements at the same Q-V combinations for the data points presented in Fig 20 and Fig 21. The results were summarized in Table 22. The maximum dimension deviation in Table 22 indicates that no matter for H13 steel or Ti6Al4V, the difference between no-powder and powder-added melt pool dimension (width and depth) at the same Q-V combination was less than 10% for all the tested P-V sets except the two exceptions as mentioned above. The potential problems with the two exceptions were further discussed in chapter 7.8 for the application range of the powder-free method.

The comparison between Fig 20 (a) and (b) as well as between Fig 21(a) and (b) suggests that for both Ti6Al4V and H13 steel, no-powder melt pool gives a more accurate approximation for powder-added melt pool when adopting the absorptivity model developed in this work rather than the constant absorptivity. This was also indicated by Table 22 (Appendix), which shows that for a large amount of melt pool measurements, no-powder vs. powder-added melt pool dimension deviation at same Q-V combinations shows smaller average and maximum value when adopting the absorptivity model developed in this work compared to that of the constant absorptivity. This study considers no-powder melt pool as a sufficient approximation for powder-added melt pool if the difference between no-powder and powder-added melt pool width measurement is within 7%. Such approximation was better fulfilled when the absorptivity developed in this work instead of the constant absorptivity was adopted, as indicated by Table 22, Fig 20 and Fig 21. Therefore, the self-developed absorptivity model in Equation 10 and Table 10 was adopted in this study for LPBF investigation of tool steel and Ti6Al4V-xB.

Noted that for M2 steel, constant absorptivity was adopted, with  $\eta$  taken as 0.33, which was experimentally measured by [135]. In this case, The absorptivity model in Equation 10 was not adopted for two reasons: one is the experimental data insufficiency for model fitting: as indicated by Table 7, only 28 [W, P-V] data was obtained for M2 steel; the other is lacking evaluation of powder-added experimental data as only no-powder test was conducted for M2 steel.

## **6 LPBF of tool steel: process optimization**

This chapter discussed LPBF process optimization for H13 and M2 tool steel through investigating the relation among P-V process parameter, melt pool geometry/microstructure inhomogeneity and property (hardness and cracking).

Chapter 6.1 focuses on melt pool geometry investigation. In chapter 6.1.1, an initial P-V process window for porosity control was developed for H13 and M2 steel based on P-V mapping for melt pool geometry. Chapter 6.1.2 and chapter 6.1.3, discussed the influence of powder layer presence and steel composition on melt pool geometry based on the comparison of P-V mappings with and without powder presence and P-V mappings for different steel grades.

Chapter 6.2 focuses on the microstructure inhomogeneity investigation. H13 and M2 steel both showed two different microstructures coexisting in the same melt pool, but their microstructure inhomogeneity were induced by two different mechanisms. Chapter 6.2.1 presents the experimental characterization results for melt pool local microstructure. Chapter 6.2.2 presents the P-V mappings for microstructure inhomogeneity, as well as the influence of powder presence on melt pool microstructure. The mechanism for H13 steel microstructure inhomogeneity and the analytical criteria for M2 columnar-to-equiaxed transition in LPBF condition were presented and evaluated in chapter 6.2.3 and chapter 6.2.4.

Based on the microstructure inhomogeneity theoretical and experimental investigation, P-V process optimization for H13 steel cracking control and P-V process optimization for M2 steel CET promotion were discussed in chapter 6.3. Chapter 6.3 also shows the H13 steel microstructure evolution from single-track, multi-track to 3D cube.

### **6.1 Melt pool geometry investigation**

#### **6.1.1 P-V mapping of melt pool geometry**

In this study, melt pool geometry of single-tracks was categorized into four types based on melt pool width (W), depth (D) and cap height (H) observed from cross-sections and track surface morphology from top-down imaging. The example OM images for these four melt pool geometries are shown in Fig 22. They are: (1) normal geometry, showing D/W ratio close to 1/2; (2) key-holing geometry, showing D/W much approaching or larger than 1; (3) balling geometry, characterized by a distorted and fluctuating laser track top surface, with undercutting and cap heights protruding above the base

plate; and (4) under-melt geometry, characterized by a melt pool depth less than the powder layer thickness. For tool steel investigated in this study, under-melt criteria is  $D < 30\mu\text{m}$ .

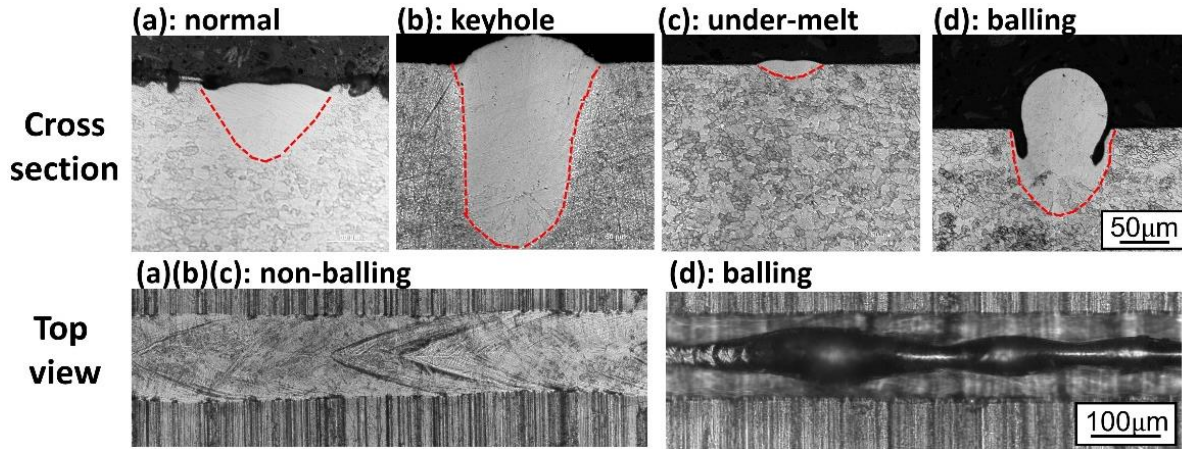


Fig 22 comparison of 4 different types of melt pool geometries observed for H-13 steel melt pool: (a) normal geometry; (b) key-holing geometry; (c) under-melt geometry; (d) balling geometry; melt pool boundary: marked by red dashed lines

Based on this melt pool geometry categorization, the P-V sets tested for the single-track test in this study (Table 7) were summarized into P-V process maps, as shown in Fig 23 and Fig 24. Fig 23 (a) and (b) show the P-V map for no-powder and powder-added single-track of H13-steel respectively. Fig 24 (a), (b) and (c) show the P-V map for no-powder single-track of H13-steel and M2-steel respectively. Fig 23 and Fig 24 indicate the influence of powder presence and steel composition on melt pool geometry, which is further discussed in chapter 6.1.2 and chapter 6.1.3.

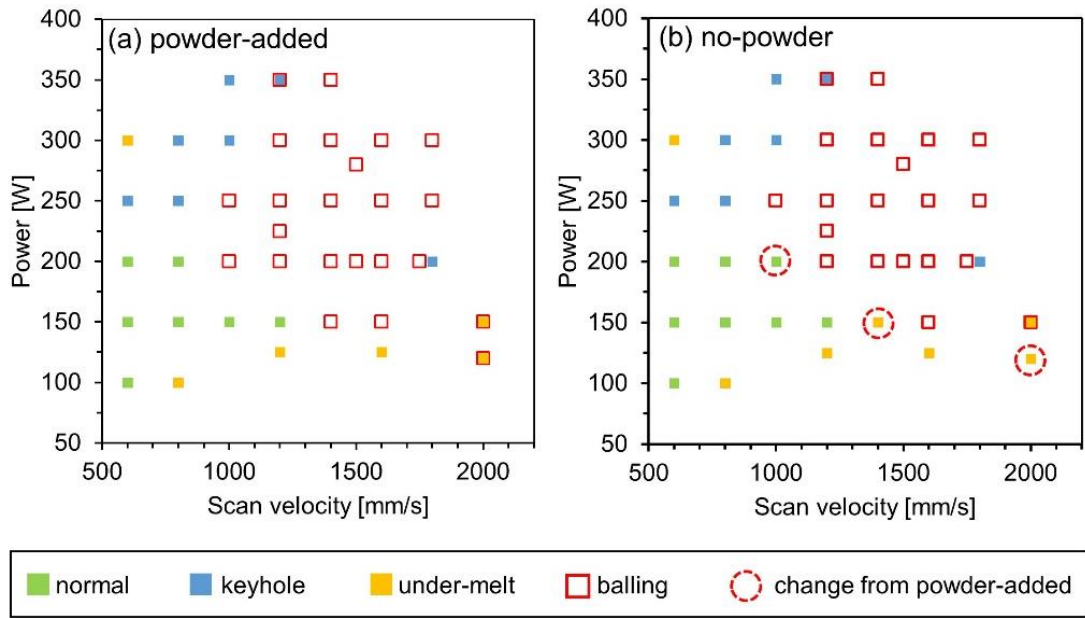


Fig 23 P-V process map of melt pool geometry for H13-steel single track; (a): powder-added; (b): no-powder (4 types of melt pool geometry categories in the map: shown in Fig 22.)

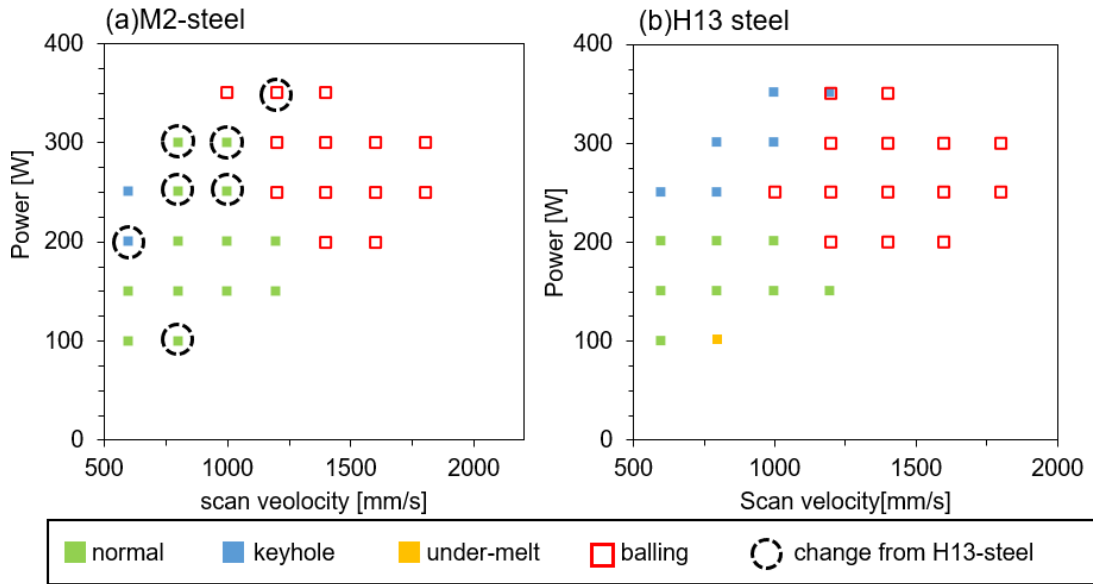


Fig 24 comparison of P-V process map of melt pool geometry for M2 steel(a) and H13 steel(b); (a)-(b): based on no-powder single track experimental result (4 types of melt pool geometry categories in the map: shown in Fig 22.)

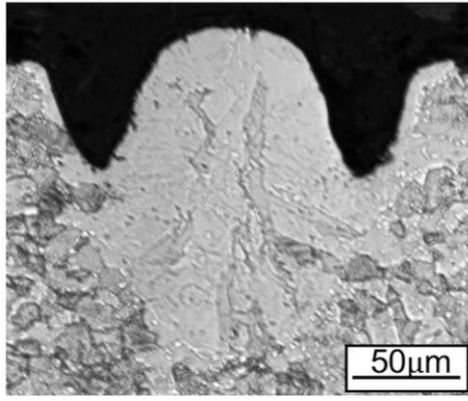


Fig 25 examples of melt pool presenting both keyholing and balling geometry features; example provided by H13 steel melt pool fabricated by P-V set #27 [350W-1200mm/s]

This study proposed a P-V process window for LPBF porosity control as the P-V combinations from the single-track experiments that produced a normal melt pool geometry (Fig 22). The causal relation between balling, keyholing and undermelt melt pool geometries with LPBF part defects and inferior properties was shown experimentally in a series of studies[26,43,46,138–140]. This was further supported by observations of powder-added H13 steel multi-track pad: 18 P-V sets were selected for the multiple-track tests (labeled by “P” in Table 7) based on the single-track P-V maps of melt pool geometry (Fig 23) and microstructure (Fig 37). Typical pad characterization for melt pool geometry is presented in Fig 26, which showed that the P-V sets corresponding to keyholing and balling melt pool geometries in the single-track P-V map (Fig 23) resulted in unstable multi-track layer deposition, causing evident variation in melt pool dimension across adjacent tracks. The P-V sets corresponding to normal and under-melt melt pool geometries ensured stable melt pool dimension across the whole multi-track layer. However, the under-melt condition can potentially lead to lack-of-fusion porosity in LPBF part build due to insufficient overlap between layers as suggested by Tang et al[29]. On this basis, the P-V combinations producing normal melt pool geometries (Fig 23 and Fig 24) should be those most likely to produce parts with low porosity.

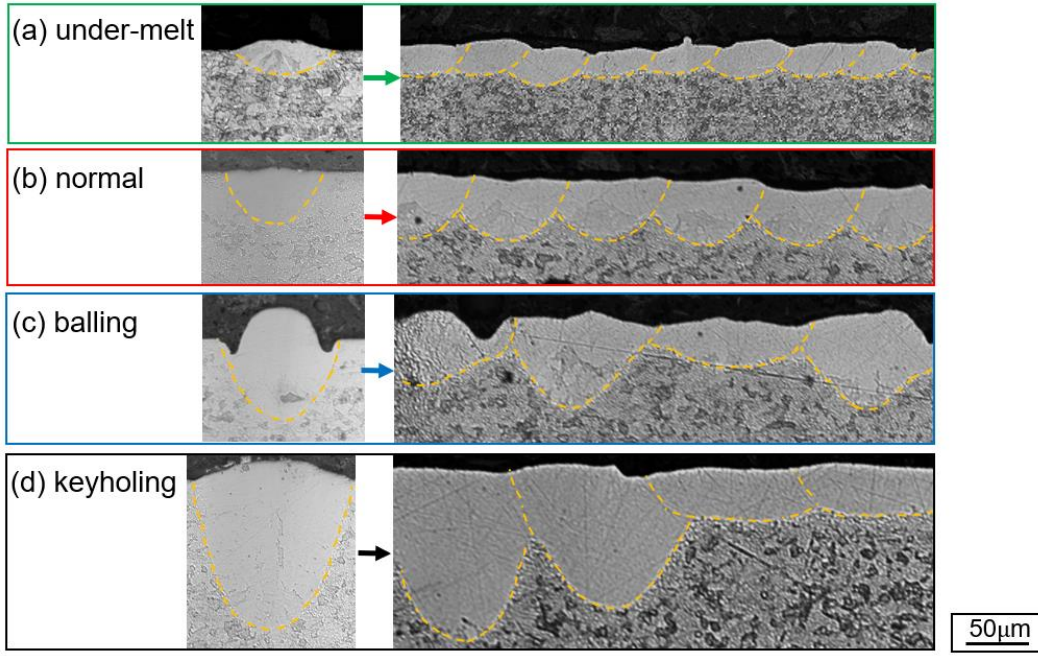


Fig 26 example OM images of H13 steel single-track with different melt pool geometries (left) and their corresponding multi-track (right) generated by same P-V set; (a) normal geometry; (b) keyholing geometry; (c) under-melt geometry; (d) balling geometry, exemplified by P-V #29 [125W-1200mm/s], P-V#4[150W-800mm/s], P-V#22[300W-1200mm/s], and P-V#20 [300W-800mm/s] in Table 7 respectively, melt pool boundary: marked by yellow dashed line

Simple, analytic relations could be used to outline the boundaries of the normal melt pool geometry. For each P-V map in Fig 23 and Fig 24, the thresholds for the undesirable key-holing, balling- and under-melt geometries could be derived from Q-V thresholds listed in Table 12, which were obtained by fitting parameters. Each fitting model in Table 12 was derived from literature-collected models, with their fitting parameter ( $m_1$ - $m_3$ ) depend solely on material properties or on material properties and powder layer thickness. For the single-tracks of this study,  $m_1$ ,  $m_2$ ,  $m_3$  were constants across Q-V space for each composition. They were determined by searching boundary using least squares regression to classify data points of normal-type from keyholing-, balling-, undermelt-type in P-V map (Fig 24). The P-V data points for melt pool showing two melt pool geometry features, as exemplified in Fig 25, was considered to lie on the Q-V thresholds.

Table 12 fitting model for the Q-V threshold of different melt pool geometry for H-13 and M2 steel

Melt pool geometry	Q-V threshold: Fitting model	Model parameter: definition	Model parameter: fitted value
Key-holing Ref: [47]	$\frac{Q}{\sqrt{V}} \geq m_1$	$m_1 = \frac{kT_b d^3 \sqrt{\pi^3}}{\sqrt{D_1}}$	H13: $m_1=4.0$ M2: $m_1=3.4$
Balling Ref: [141]	$QV > m_2$	$m_2 = \frac{3\pi^3 k \alpha (T_f - T_0)}{4e}$	H13: $m_2=85240$ M2: $m_2=92400$
Under-melting Ref: [22]	$\frac{Q}{V} < m_3$	$m_3 = \frac{e\pi\rho C(T_f - T_0)d^2}{2}$	H13: $m_3=0.046$ M2: not found

(Where  $k$  is thermal conductivity,  $D_1$  is thermal diffusivity of molten material,  $d$  is layer thickness ( $d$  for single-track and single-layer: see experiment design for powder-added test in chapter 4.2),  $T_b$  is boiling temperature,  $T_m$  is melting temperature;  $\alpha$  is thermal diffusivity;  $Q$  values: calculated by the absorptivity model in Equation 10)

The predicted melt pool geometry Q-V threshold (Table 12) was exemplified in Fig 27, with H13 steel as an example. Fig 27 (b) shows experimentally-observed P-V mapping (shown earlier in Fig 23). The  $P$  values were converted from  $Q$  values using the absorptivity model in Equation 10. This enables the experimental results to be compared to the Q-V thresholds calculated from Table 12, as shown in Fig 27 (a). Good agreement was obtained for the region where a normal melt pool geometry would be expected, as indicated by the shadow area in Fig 27 (b).

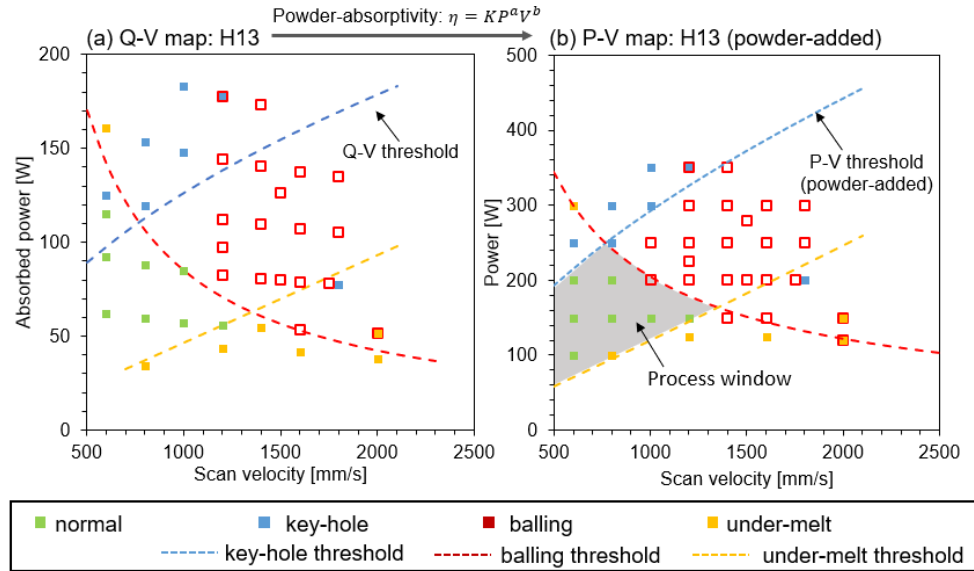


Fig 27 A process window (shadow area in (b), i.e., area enclosed by dashed lines) using the melt pool geometry P-V map (example shown for H13-steel)

### 6.1.2 Influence of powder presence on melt pool geometry

The influence of powder presence on melt pool geometry could be assessed by the comparison between no-powder and powder-added melt pool geometry P-V maps for H13 steel in Fig 23(a) and (b). For the 40 P-V sets tested, most resulted in same melt pool geometry regardless of powder addition, except for the three P-V sets marked out by red circles in Fig 23(b). These correspond to P-V #9, #32, #38 in Table 7, which all result in melt pool geometry changing from non-balling to balling with the addition of powder. An example is given in Fig 28 for P-V set #38 (150W-1400mm/s). This suggests that the powder absence or addition changes the range of P-V process parameter leading to the occurrence of balling.

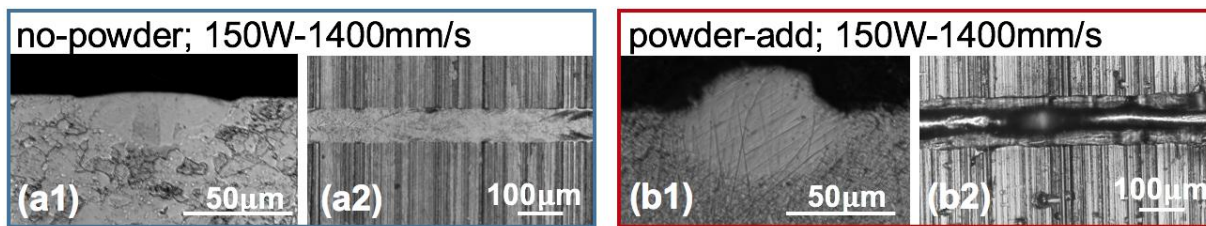


Fig 28 H13-steel single-track with and without powder addition at same P-V sets showing different balling behavior; example provided: P-V #38 [150W-1400mm/s]; non-balling for no-powder case (a1-a2), balling for powder-added case(b1-b2);

P-V#9 and #38 were specifically selected for the H13 steel multiple-track test, conducted in both no-powder and powder-added version. As mentioned in chapter 6.1.1, they were P-V sets showing non-balling geometry for no-powder single-track but balling for powder-added single-track. This difference in balling occurrence with and without powder addition still existed for multiple-track pads generated by these 2 P-V sets, as exemplified in Fig 29(a1) and (a2) for P-V #38. Moreover, it is worth noticing that for the other P-V settings leading to balling in both no-powder and powder-added case, powder-added pads usually showed more severe balling behavior than their corresponding no-powder pads at same P-V set. An example is shown for P-V #25 (300W-1800mm/s) in Fig 29 (b1) and (b2), with the extent of balling suggested by the worse surface quality of powder-added pad than the no-powder one.

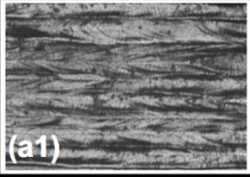
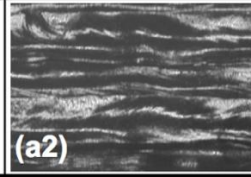
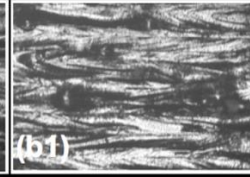
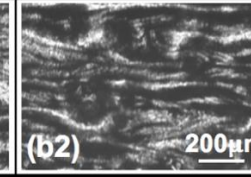
Laser pattern	P-V #38		P-V#25	
	No-powder	Powder-added	No-powder	Powder-added
Multiple bead	 (a1)	 (a2)	 (b1)	 (b2)

Fig 29 top surface images of H13-steel multiple-track pad showing different balling behavior with and without powder addition generated at same P-V set; example provided by P-V set #38 [150W-1400mm/s] for (a1)(a2), P-V #25[300W-1800mm/s] for (b1)(b2): non-balling for no-powder case (a1), balling for powder-added case(a2); slight balling for no-powder case (b1), severe balling for powder-added case(b2)

The above observation suggested that the powder presence would lead to a slight shift of P-V threshold for balling formation, leaving the powder-added process map with a larger P-V space for balling formation than the no-powder process map. This might further indicate the possibility of control balling behavior by adjusting powder-related parameters (powder size distribution, layer thickness, etc.).

The powder-free approach proposed in this work assumes that the no-powder melt pool could provide a reasonable approximation for the powder-added melt pool. The above observation confirms the validity of such approximation for melt pool geometry in most P-V space, except the P-V space near the balling threshold. While it could be shown by Fig 27 that when combined with the powder/bulk varied absorptivity in Equation 10 and Table 12, the Q-V thresholds derived by no-powder melt pool data in Fig 27(a) could provide accurate estimation for the P-V window of each melt pool geometry in powder-added case: The data points in Fig 27 (b) are the 40 P-V data points for powder-added melt pool geometry observation, as shown earlier in Fig 23(a). They could all fit correspondingly into the P-V space enclosed by the no-powder data developed Q-V thresholds, including the three P-V sets (P-V #9, #32, #38), which show deviation between the no-powder and powder-added melt pool geometry. Based on this, we confirmed the validity of the powder-free approach's assumption by showing the consistency in Q-V thresholds of each melt pool geometry for no-powder and powder-added melt pool when adopting the powder/bulk-varied absorptivity model developed in this work. This suggests the applicability of adopting the powder-free method to develop the P-V window for LPBF porosity control (shaded area in Fig 27 (b)).

### **6.1.3 Influence of steel composition on melt pool geometry**

Fig 24(a)-(b) compares the P-V mappings of melt pool geometry for H13 and M2 tool steel. In P-V mapping of M2 steel, data points are marked by dashed circles if the corresponding melt pool shows a geometrical change from the H13 melt pool generated by the same P-V sets. These data points show a shift in keyholing P-V threshold (and thus Q-V threshold) between H13 and M2 steel. Fig 24 indicated that the P-V window of normal melt pool geometry shrunk as the material changed from M2 to H13.

Fig 24 indicates different keyholing behavior between M2 and H13 steel under the same P-V process condition, which might attribute to their difference in high-boiling-temperature alloying element content. For all elements in the periodic table, W and Mo are among the ones with the highest boiling temperature, which are about 2500K and 1800K higher than that of Fe respectively[142]. Table 1 shows that M2 steel used in this work contains about 6 wt.% W and 4.7 wt.% Mo, while H13 steel has 0 wt.% W and 0.7 wt% Mo. The difference in W and Mo content between M2 and H13 steel suggested a higher boiling temperature range for M2 steel than H13 steel. The keyholing Q-V threshold model in Table 12 shows that the Q-V threshold would shift to higher-Q and lower-V range as boiling temperature increases. This is consistent with the experimental observation in the P-V mapping (Fig 24), showing the keyholing Q-V threshold of M2 steel locates at higher-P and lower-V range than that of H13 steel. This consistency supports the proposed explanation that considers the different keyholing tendencies between M2 and H13 steel as a result of their different boiling temperature, which further suggests the potential of altering keyholing behavior by modifying the content of high-boiling-temperature alloying element for the alloy of investigation. This could be considered for future work.

## **6.2 LPBF microstructure inhomogeneity for tool steel**

### **6.2.1 Microstructure inhomogeneity: observation**

In this work, noticeable microstructure inhomogeneity was observed in single-track melt pools for H13 steel and M2 steel at some of the P-V sets tested in this study. The characterization result for H13 steel and M2 steel microstructure inhomogeneity was presented below:

- **H13 steel:**

Fig 30 presents a typical observation for H13-steel melt pool showing microstructure inhomogeneity. The melt pool in Fig 30(i) shows two different microstructures in one melt pool cross section, which could be distinguished by the brighter and darker contrast. They were referred to as type (A) and (B) in this work. High magnification images showed type (A) microstructure (Fig 30(ii)) consisted of a continuous cellular network. The network spacing varied across melt pools of different P-V sets, generally increasing in size as the cooling rate decreased. The range of spacing was 0.4 to 1  $\mu\text{m}$ . Type (B) microstructure shown in Fig 30(iii) exhibited two kinds of isolated needles with different length scales and distribution. The smaller needles were 0.2-0.7  $\mu\text{m}$  in major axis length and were uniformly distributed with sub-micron spacing, while the larger needles were approximately 3-5  $\mu\text{m}$  in major axis length and only occasionally occurred.

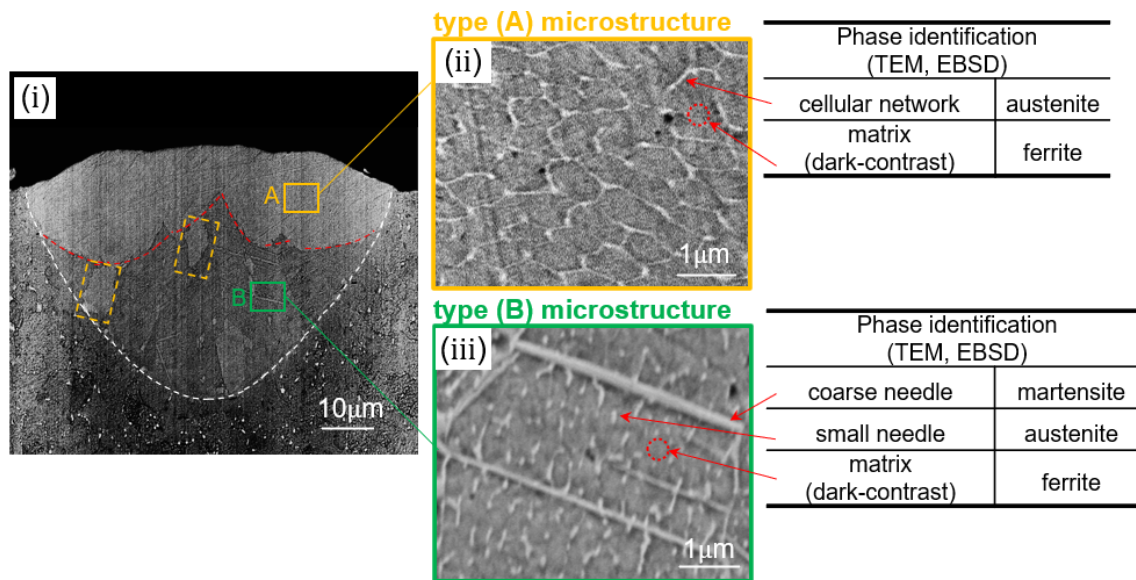


Fig 30 typical observation of microstructure inhomogeneity in H-13 steel single-track melt pool; in (i), melt pool boundary: marked by white dashed line, example provided by P-V#4; melt pool in (i): exhibited two localized region with different microstructure (distinguish by bright-contrast and dark-contrast, separated by a “loop-shape” boundary marked by red dashed line), referred to as type (A) and (B) microstructure, indicated by letter “A” and “B” in (i), shown in high magnification image (ii) and (iii) (close-up of the yellow and green box in (i)); yellow box in (a)-(d): examples of randomly scattered type (A) microstructure in localized type (B) microstructure; Table at right:

TEM and EBSD phase identification for each microstructure feature

From the melt pool cross-section in Fig 30(i), a boundary could be observed separating two local regions in the melt pool, as indicated by the red dashed lines. It presented a unique shape of two loops intersecting at a tip near the melt pool centerline. The near-top region above the boundary exhibited type (A) microstructure while the near-bottom region below the boundary exhibited type (B) microstructure. Besides, scattered islands with type (A) microstructure was found in the near-bottom region dominated by type (B) microstructure, as indicated by the yellow box in Fig 30(i).

The consistency of the microstructure inhomogeneity along laser track length is indicated by the microstructure observation for the track longitudinal section, as shown in Fig 31(a). Similar to the melt pool cross-section observation in Fig 30, Fig 31 (a) also presents type (A) microstructure with bright contrast and type (B) microstructure with dark contrast. In Fig 31, the near-top region dominated by type (A) microstructure and the near-bottom region dominated by type (B) microstructure were separated by a relatively straight boundary, as indicated by the white dashed line in Fig 31 (a). It corresponds to the loop-shape boundary in Fig 30. The stable boundary depth to track top suggests that the vol.% of type (A) microstructure near melt pool top remain consistent across laser track length. By combining Fig 30 and Fig 31, it reveals the vol% consistency of the type (A) microstructure distribution above the loop-shape boundary across the track length. In addition, the longitudinal section characterization shows that cracks frequently occur in the local regions with type (B) microstructure across the track length, as indicated by the white arrow in Fig 31 (a). This shows the potential correlation between microstructure inhomogeneity and the cracking tendency of LPBF-processed H13 steel, which will be further presented in chapter 6.3.1.

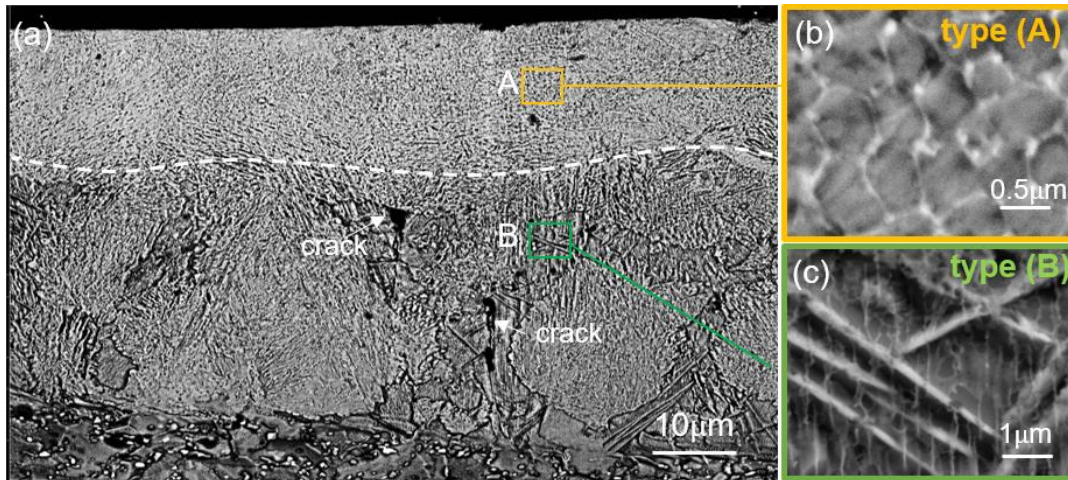


Fig 31 typical microstructure observation for H13-steel track longitudinal section (a); example provided by P-V #9; the corresponding melt pool cross-section of same P-V set: shown in Fig 30;

Track showed coexistence of cellular-network microstructure (type (A)) and isolated microstructure (type (B)), distinguished by dark contrast and bright contrast; white dashed line: indicates the boundary separating the region with type (A) and (B) microstructure; (b), (c): close-up for region in yellow and green box in (a) respectively, showing high magnification image for type (A) and type (B) microstructure; cracks: observed in type (B) microstructure, indicated by white arrow

Phase identification was conducted for each microstructure features by TEM and EBSD, with the result summarized in the table inserted in Fig 30. Fig 32 and Fig 33 shows the TEM characterization result carried out for type (A) and (B) microstructure separately, along with the selected area electron diffraction (SAED) for each microstructure features in type (A) and (B) microstructure, as shown in Fig 32 (b-1,2) and Fig 33 (b-1,2). Fig 32 revealed the brighter-contrast cellular network and the darker-contrast matrix in type (A) microstructure as austenite phase and ferrite phase respectively. The interface between the austenite and ferrite phase could be observed in Fig 32(b). Fig 33 revealed the brighter-contrast large needle and the darker-contrast matrix in type (B) microstructure as martensite phase and ferrite phase respectively. Some suspected twin-dislocations were also found in type (B) microstructure, as shown in Fig 33(c). Noted that this was not observed in type (A) microstructure.

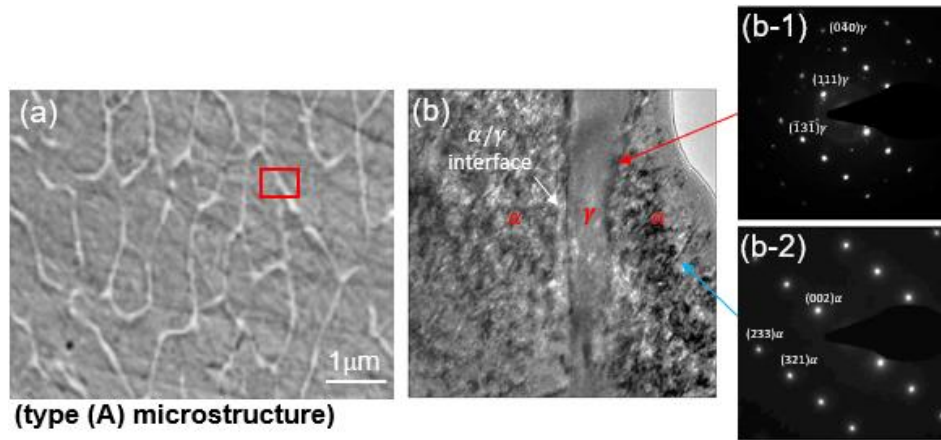


Fig 32 typical SEM image (a) and TEM bright field (BF) image (b) for type (A) microstructure in H13-steel melt pool (see Fig 30). BF image shows two phases, identified as ferrite and austenite (indicated by letter “ $\alpha$ ” and “ $\beta$ ”). Red box in (a) indicates the location for TEM characterization. The interface between the two phases is indicated by the white arrow. (b-1) and (b-2) shows the SAED patterns characterized at the region with the ferrite phase and austenite phase respectively.

SAED characterization location: indicated by red and blue arrows.

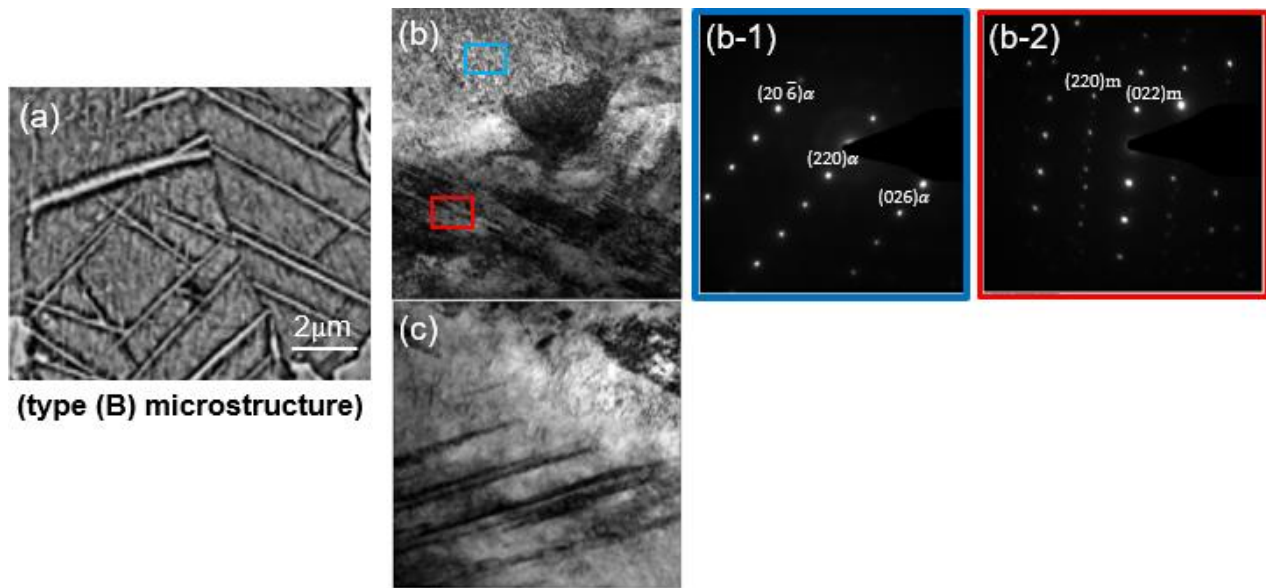


Fig 33 typical SEM image (a) and TEM bright field (BF) image (b) for type (B) microstructure in H13-steel melt pool (see Fig 30). BF image shows two phases, identified as ferrite and martensite (indicated by letter “ $\alpha$ ” and “ $m$ ”), corresponding to the matrix and needle-phase in (a). (b-1) and (b-2) shows the SAED patterns characterized at the region with ferrite phase and martensite phase respectively. SAED characterization location: indicated by red and blue boxes. TEM-BF image in (c) shows a suspected twin-dislocation observed in type (B) microstructure

It is also worth noticing that to avoid accidentally mixing the phase identification of type (A) and (B) microstructures, TEM was applied on two FIB samples taken from the local regions with solely type (A) and (B) microstructures in the melt pool. EBSD characterizations (point identification) were also conducted for further phase identification across multiple melt pools generated by different P-V sets, which identify the brighter-contrast cellular network and darker-contrast cell core in type (A) microstructure as FCC and BCC structure respectively. For type (B) microstructure, EBSD result identifies the brighter-contrast large-needle and darker-contrast matrix both as BCC for both type (A) and type (B), while the uniformly-distributed small needles were recognized as FCC structure. The EBSD analysis shows good consistency with the aforementioned SAED results, and also indicates austenite phase for the small needle morphology in type (B) microstructure. For this microstructure feature, it was found to be difficult to distinguish its SAED pattern due to the uncertainty of its location from TEM-bright field observation.

Besides phase identification, this work also investigated element segregation for type (A) and (B) microstructure. Fig 34 shows the result of STEM-EDS mapping and corresponding high-angle annular dark-field (HAADF) imaging for type (A) microstructure. By combining Fig 34 and Fig 32, it shows segregation of C, Cr, Mo and V at the cellular network where austenite evolved in for type (A) microstructure. For type (B) microstructure, segregation was not observed between the matrix and large needle, and thus the HAADF result is not presented. Several studies[54][143] on LPBF processing of H13 steel suspected the existence of composition segregation in LPBF-part build. The observations in this study provide evidence of this behavior. However, these studies state that composition segregation in the LPBF-built H13 steel part, if existing, would occur in solid-state due to solute partitioning during the repeated heating-cooling cycles from the successive layers. In this study, the occurrence of composition segregation in single-track melt pools of H13 steel indicates that segregation occurred during solidification, rather than by the solid-state repeated heating-cooling cycle, which contradicts the assumption in these studies[54,143]. The influence of the observed microsegregation from solidification was discussed in chapter 6.2.3.

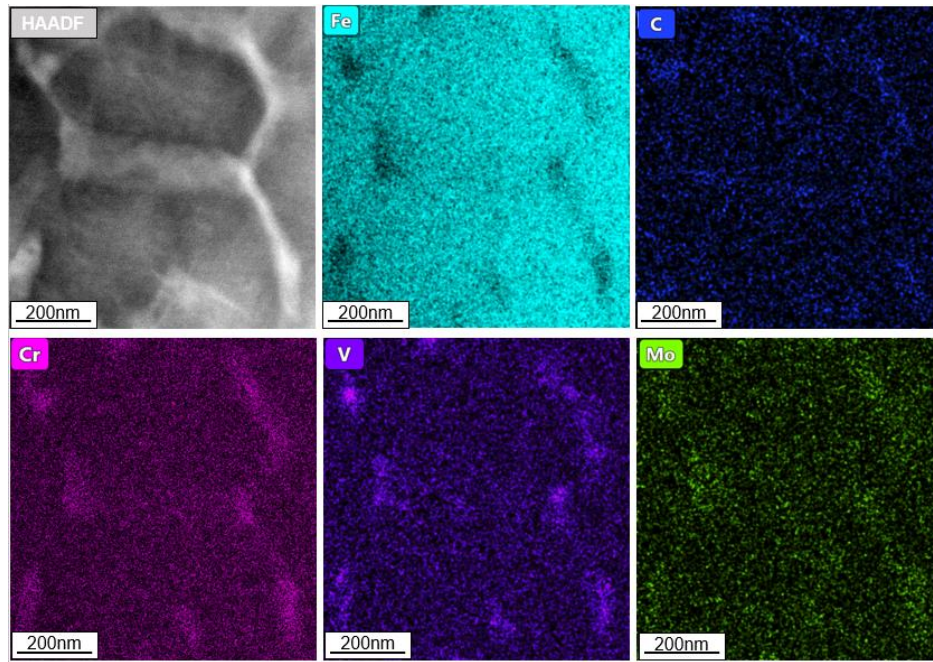


Fig 34 STEM-HAADF image (a) for FIB specimen lifted-out from the local region with type (A) microstructure (see Fig 32) in H13-steel single-track melt pool with the corresponding STEM-EDX maps showing segregation of C, Cr, V, Mo at the cellular boundary where austenite presents (see Fig 32).

- **M2 steel:**

Melt pool microstructure inhomogeneity of M2 steel is different from that of H13 steel. Fig 35 presents a typical observation for M2-steel melt pools showing microstructure inhomogeneity. From Fig 35, two microstructures could be observed to localize in different regions within the melt pool cross-section, as distinguished by the dark and bright-contrast. They correspond to equiaxed-dendrite and columnar-dendrite morphologies respectively as shown by the high magnification images in Fig 35 (b-1) and Fig 35 (b-2). This suggested the occurrence of columnar-to-equiaxed transition (CET) in M2 steel melt pool. Fig 35 also shows M2-steel melt pools of different P-V set presenting different vol.% of equiaxed dendrite, which will be discussed further in chapter 6.2.2. Noted that for melt pool showing equiaxed dendrite presence, the equiaxed dendrites were always located at, but not limited to, the top center region of the melt pool.

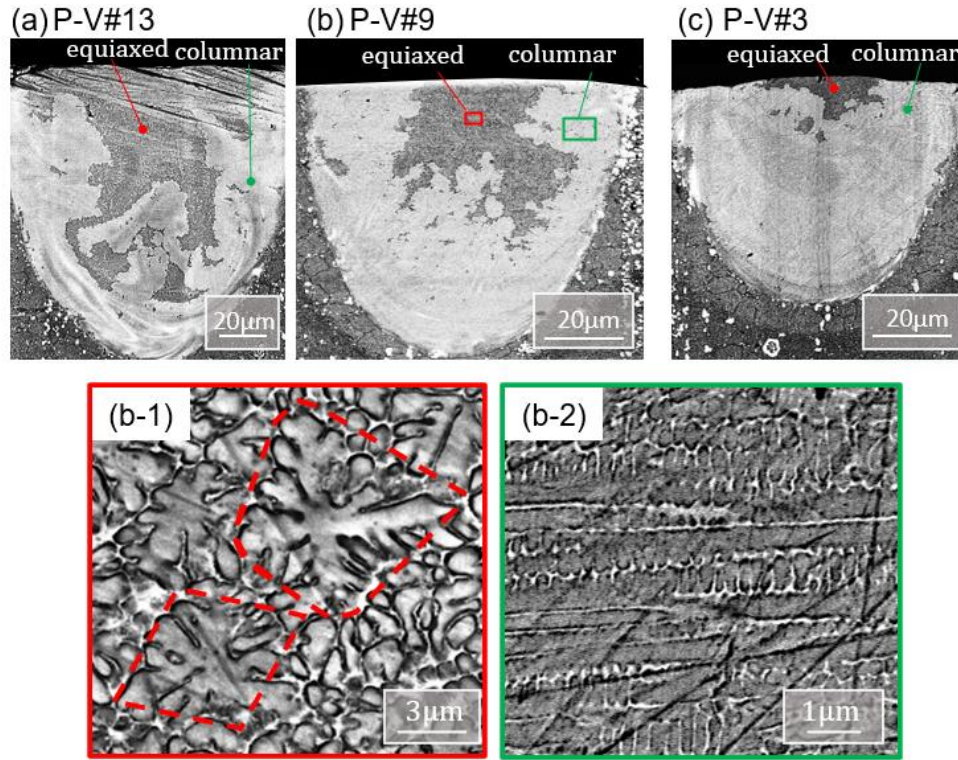


Fig 35 typical examples for 3 types of melt pool microstructure observed for the M2-steel single tracks fabricated by the 28 selected P-V sets (see Table 7); examples provided by P-V #13, #9, #3; equiaxed and columnar dendrite microstructure coexisted in each melt pool in (a)-(c), shown in high magnification image (b-1) and (b-2) (close-up of the red and green box in (b-2)); in each melt pool: region with equiaxed and columnar dendrite: distinguished by dark and bright contrast respectively, indicated by letter “equiaxed” and “columnar”

### 6.2.2 Microstructure P-V mapping

For both H13 steel and M2 steel, the extent of microstructure inhomogeneity was observed to vary with P-V parameters. Microstructure P-V mapping was developed for H13 and M2 steel to identify the P-V window leading to high-level and low-level microstructure inhomogeneity in the melt pool.

- **H13 steel: no powder vs. powder added**

As shown in chapter 6.2.1, H13 steel presented two types of microstructure within the same melt pool, which are the type (A) microstructure (Fig 30(ii)) with cellular network morphology and type (B) microstructure (Fig 30(iii)) with isolated large needles. By summarizing the melt pool microstructure for the 40 P-V sets tested in this study, it could be found that the vol% of type (A) and (B) microstructure in the melt pool changed with P-V parameters. Based on the vol% of type (A)

microstructure in the melt pool, melt pools produced by the 40 tested P-V sets in this study were categorized into four types, referred to as “large-A”, “medium-A”, “small-A” and “varied microstructure” respectively. Their typical SEM images were shown in Fig 36(a)-(d).

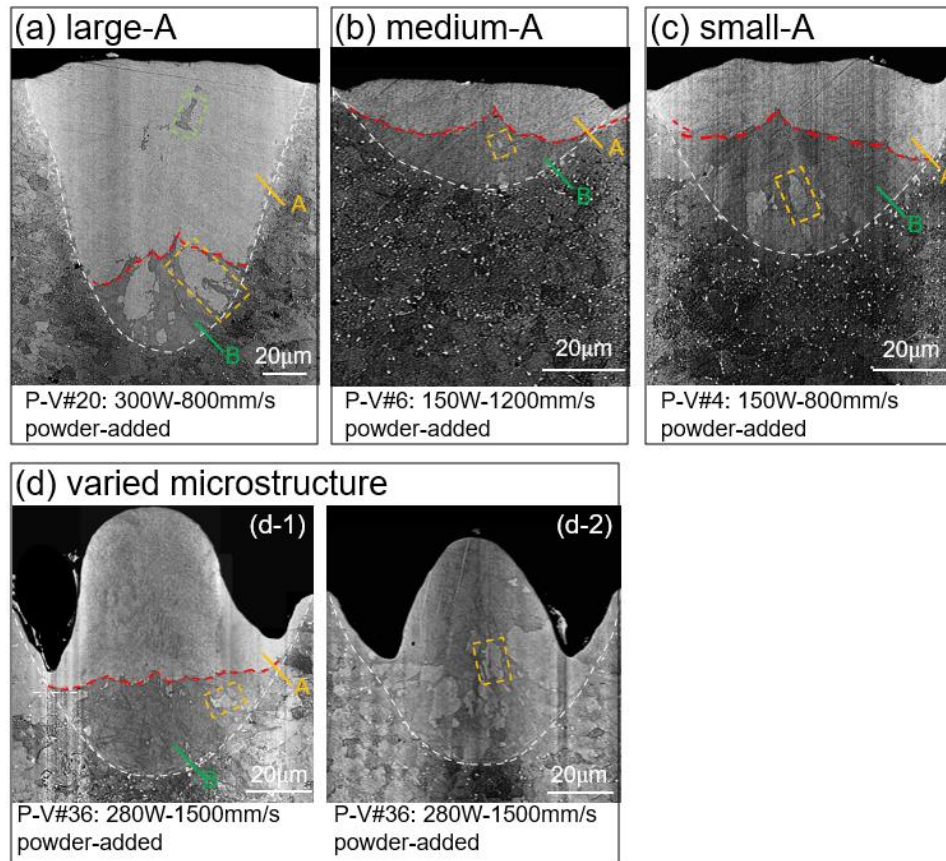


Fig 36 typical examples for 4 types of melt pool microstructure observed for H13-steel single tracks fabricated by the 40 selected P-V sets (Table 7); examples provided by P-V #20, #6, #4, #36 (value of P, V: labeled below each figure); note: (d-1), (d-2): two cross-sections taken at different location of the same sing-track; in (a)-(d): white dashed line: melt pool boundary; red dashed line: loop-shape boundary separating localized type(A) and (B) microstructures in each melt pool (see Fig 30(ii), (iii)); region with type (A) microstructure: bright contrast, region with type (B) microstructure: dark contrast, indicated by letter “A” and “B”; yellow/green box in (a)-(d): examples of randomly scattered type (A)/(B) microstructure in localized type (B)/(A) microstructure

The microstructure categorization criteria were as follows:

This study approximated the vol.% of type (A) microstructure in each single-track by the area% above the loop-shape boundary that separating type (A) and (B) microstructure in melt pool cross section

(red dashed line in Fig 36). This is because as mentioned earlier in chapter 6.2.1, the near-top region enclosed by the loop-shape boundary in melt pool was dominated by type (A) microstructure (Fig 30(ii)) and the track longitudinal-section characterization (Fig 31) shows consistent vol% across the laser track length, which gives confidence for such approximation. It should be noted that some scattered islands of type (A) microstructure (yellow box in Fig 30) could also be found in the region below the loop-shape boundary where type (B) microstructure dominated. However, the longitudinal microstructure characterization reveals that these islands with type (A) microstructure randomly occurred across the track length. Due to their randomness, the vol% of type (A) microstructure in these scattered islands was not taken into account when evaluating the vol% of type (A) microstructure in each single-track.

On this basis, the “large-A”, “medium-A” and “small-A” melt pool categories were classified as melt pools presenting vol.% of type (A) microstructure >75%, 45-65% and <30% respectively, as exemplified by melt pool in Fig 36(a)-(c). Their difference in vol.% of type (A) microstructure was indicated by the different ratio of the loop-shape boundary depth to the melt pool depth presented by each melt pool. Besides, for some P-V parameters, their corresponding single-tracks showed variation in melt pool microstructure at different locations along the track. In this case, the melt pool microstructure was categorized as “varied microstructure”. An example was provided for track generated by P-V #36 (280W-1500mm/s) in Fig 36(d). Fig 36(d-1) and (d-2) were two melt pool cross sections characterized at different locations along the same track generated by P-V#36. The cross-section in Fig 36(d-2) showed melt pool microstructure with type (A) and (B) microstructure randomly scattered rather than localized in near-top and near-bottom regions. In this case, the boundary separating the two types of microstructure was not defined.

Based on this categorization, microstructure P-V process maps were developed for single-track melt pools of H13 steel with both powder-added and no-powder case, as presented in Fig 37(a) and (b) respectively. Three observations for the microstructure P-V map are worth noticing:

First, by combining the melt pool geometry P-V map (Fig 23 in chapter 6.1.1) and the microstructure P-V map (Fig 37) for H13 steel, it could be found that most of the P-V space with the “varied-microstructure” (Fig 36(d)) overlapped with the P-V space showing balling melt pool geometry (Fig 22(d)). Thus, for the “varied microstructure” type melt pool, its microstructure inconsistency along the track direction might be explained by the inconsistent melt pool flow along the laser scan direction, as indicated by the occasional “balling” formation across the track.

Second, in the non-balling P-V space (see Fig 23), the microstructure P-V process map (Fig 37) indicates a general trend between microstructure inhomogeneity and the melt pool solidification cooling rate during solidification. Fig 18 shows the cooling rate estimated for the selected P-V sets in the microstructure process map. By combining Fig 37 and Fig 18, it could be seen that within the non-balling P-V space, from the slower-cooling P-V space to faster-cooling P-V space, the melt pool microstructure changed from “small-A” to “medium-A” or “large-A”. This suggests that as melt pool solidification cooling rate increases, more vol% of type (A) microstructure is present in the melt pool. A more quantifiable relation among P-V parameter, melt pool solidification cooling rate, and melt pool microstructure inhomogeneity is further presented in Chapter 6.2.3.

Third, the powder-added and no-powder microstructure P-V mapping in Fig 37 (a) and (b) showed the same microstructure categorization for 36 out of the 40 P-V sets tested. The exceptions were P-V #10, #27, #28, #29. For the first three P-V sets, they all led to balling occurrence during melt pool solidification, as indicated by the melt pool geometry P-V map (Fig 23). And the difference between no-powder and powder-added melt pool lies in the level of microstructure inconsistency along the same track, as indicated by the “varied microstructure” category, rather than the level of microstructure inhomogeneity represented by the vol.% of type (A) microstructure in the melt pool. The microstructure inconsistency along laser track was likely to be a result of unstable melt pool fluid flow along the laser scan direction. Therefore, for these three P-V sets, the difference between no-powder and powder-added melt pool microstructure might be attributed to the influence of powder addition on balling occurrence which led to different melt pool fluid flow behavior and thus different level of microstructure consistency for tracks with and without powder addition. The influence of powder presence on balling was also demonstrated in chapter 6.1.2. For P-V set #29, the microstructure difference between no-powder and powder-added melt pool was attributed to its low energy density, the lowest among all P-V sets tested. The melt pool geometry process map showed “under-melt” geometry for P-V set#29, suggesting melt pool depth smaller than the powder layer thickness. The change in heat transfer behavior due to powder likely resulted in the different microstructure types for this P-V set #29.

The other P-V sets tested in this study showed microstructure consistency with or without powder addition, which suggested a rather small influence of powder addition on as-deposited melt pool microstructure for most of the P-V space. Table 23 in the Appendix shows the measured result for vol.% of type (A) microstructure for the no-powder and powder-added melt pool with the 40 selected P-V sets. From Table 23, it shows that for all 40 P-V sets except the abovementioned 4 P-V sets, the

difference in vol.% of type (A) microstructure between no-powder and powder-added melt pool is smaller than 10%. This was also indicated by the consistency between no powder and powder added microstructure P-V map as shown in Fig 37. Such microstructure consistency across wide P-V space validates that the powder-added LPBF melt pool solidification microstructure could be sufficiently approximated by the no-powder melt pool microstructure, which validates the applicability of adopting the powder-free method for LPBF melt pool microstructure investigation.

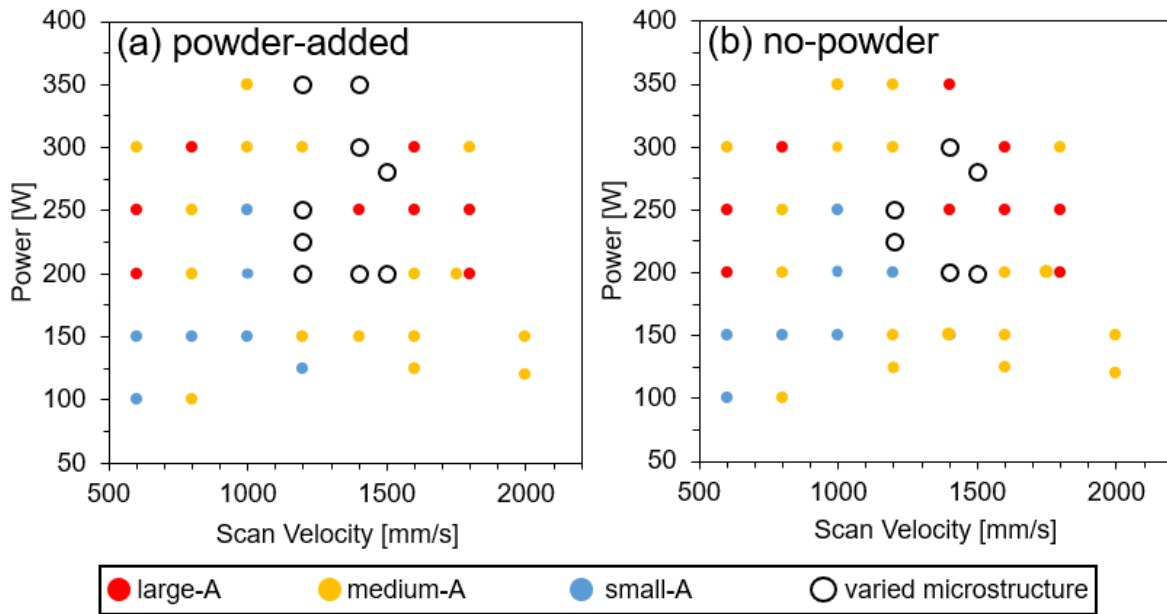


Fig 37 H13-steel microstructure P-V process map for single-track melt pool with (a) powder-added laser-scan condition and (b) no-powder laser-scan condition, based on the categorization of four microstructure types presented in Fig 36

The microstructure P-V process maps for H13 steel in Fig 37 not only presented the combined influence of laser power, laser scan velocity and powder presence on melt pool microstructure inhomogeneity but also indicated cracking tendency of LPBF-H13 steel for different P-V window. This will be shown further in chapter 6.3.1.

- **M2 steel: no powder**

As shown in chapter 6.2.1, M2 steel presents the coexistence of columnar and equiaxed dendrite within the same melt pool, indicating the CET occurrence during M2-steel melt pool solidification. As shown in Fig 35, for the 28 P-V sets selected in this study, three different melt pool microstructures were observed, which present different levels of vol.% of equiaxed dendrite in the melt pool. The

typical SEM images for the three types of melt pools are listed in Fig 35(a)-(c), with the examples provided by melt pool microstructure for P-V#13, #9 and #3 tested in this study. The equiaxed vol.% in melt pool was approximated by the area% of equiaxed microstructure observed in melt pool cross section: For melt pools in Fig 35(a)-(c), the local region with dark and bright-contrast within the melt pool cross section correspond to equiaxed-dendrite and columnar-dendrite morphologies respectively, as shown by the high magnification images in Fig 35(b-1) and (b-2). The microstructure images were analyzed by ImageJ software[128], which showed that the melt pool in Fig 35(a) presented mainly equiaxed dendrite microstructure, with 40-60 area% occupied by equiaxed dendrite in the melt pool. For the melt pool in Fig 35 (b), it still presents the coexistence of equiaxed and columnar dendrite morphologies. However, unlike the melt pool in Fig 35 (a), the melt pool in Fig 35 (b) mainly presents columnar dendritic microstructure, leaving only 10-30 area% showing equiaxed morphology. For the melt pool in Fig 35 (c), it presents an almost fully columnar dendrite microstructure, with a negligible portion of the melt pool (<5 area%) occupied by equiaxed dendrite. For these three types of melt pool, their evident difference in equiaxed dendrite vol.% indicates different CET tendency for solidification under the corresponding P-V parameters.

Table 13 summarized the categorization criteria for the three types of melt pool microstructure as described above. Based on this microstructural categorization, a microstructure process map for M2 steel was established for the single-track microstructure of the 28 P-V sets tested in this study, as shown in Fig 38(a). In Fig 38 (a), P-V sets are divided into three groups, namely CET promoting, transition and suppressing group, if their resulting single-track present melt pool microstructure fall in the microstructure categories in Table 13, as exemplified by the three melt pools in Fig 35.(a)-(c) respectively. The microstructure prediction results in Table 13 and the predicted microstructure process map in Fig 38(b) are further explained in chapter 6.2.4. The experimental process map in Fig 38(a) presents a general trend of higher CET tendency as laser power and scan velocity both increase. It should be noted that in this study each single-track is sectioned to reveal three melt pool cross sections. If different cross sections of one single track present different types of melt pool microstructure, then the corresponding P-V set is also labeled as “varied-microstructure”, indicated by the square label in the process map in Fig 38(a). By combining the melt pool geometry P-V process map (Fig 24(b)) with the microstructure P-V process map Fig 38(a) for M2-steel, it could be found that tracks with varied microstructure along scan direction are always observed to show balling melt pool geometry feature. An example is provided by Fig 39. The two melt pool cross sections in Fig 39(a) and (b) are from the same single track fabricated by P-V#11, with one presenting high vol% of

equiaxed microstructure while the other showing almost 0 vol % (i.e., fully columnar microstructure) respectively. Thus, the inconsistent melt pool microstructure for these P-V sets might be a result of the unstable fluid flow along scan direction for melt pool solidification with balling occurrence. The influence of balling on CET occurrence as well as the correlation between P-V parameter and vol% of equiaxed microstructure are further discussed in chapter 6.2.4.

Table 13 Comparison of experimental and calculated equiaxed dendrite% ( $\phi$ ) in melt pools for the three microstructure categories in P-V process map

category	CET promoting	CET transition	CET suppressing
criteria	$\Phi$ : 40-60 %	$\Phi$ : 10-30 %	$\Phi$ : <5 %
example	P-V#13: 250W-600mm/s	P-V#9: 200W-1000mm/s	P-V#3: 150W-600mm/s
experimental	46.5%	16.4%	3.3%
calculated	43.2%	18.2%	5.2%

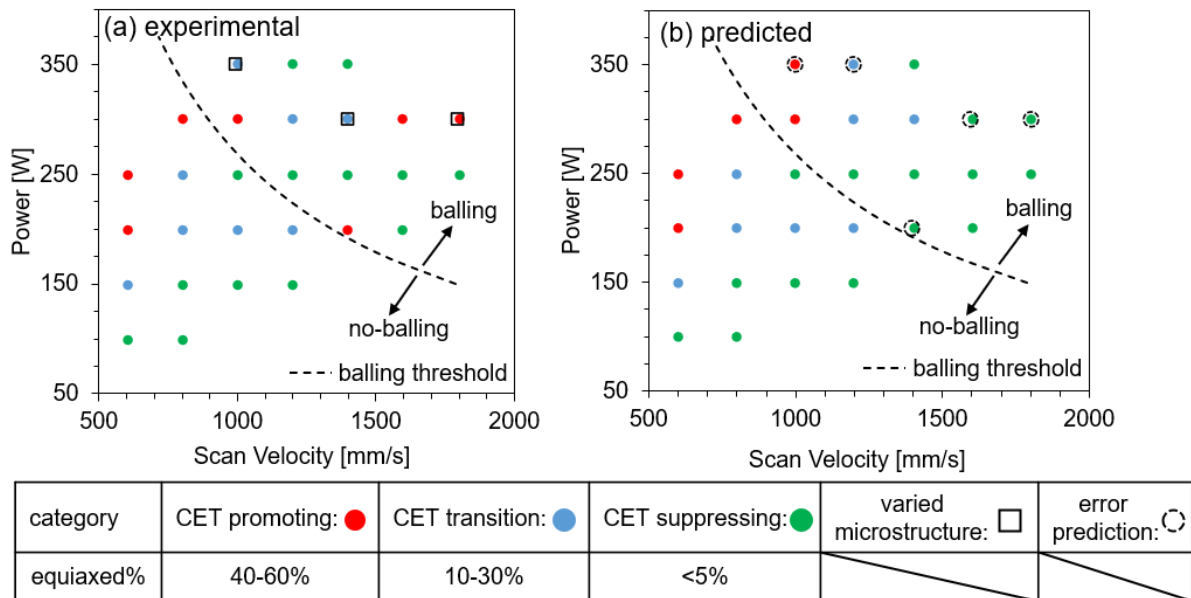


Fig 38 Comparison between experimental (a) and predicted (b) microstructure P-V process map for M2 steel single-track, with balling P-V threshold overlapped. (P-V thresholds: developed by the Q-V thresholds in Table 12, chapter 6.1.1)

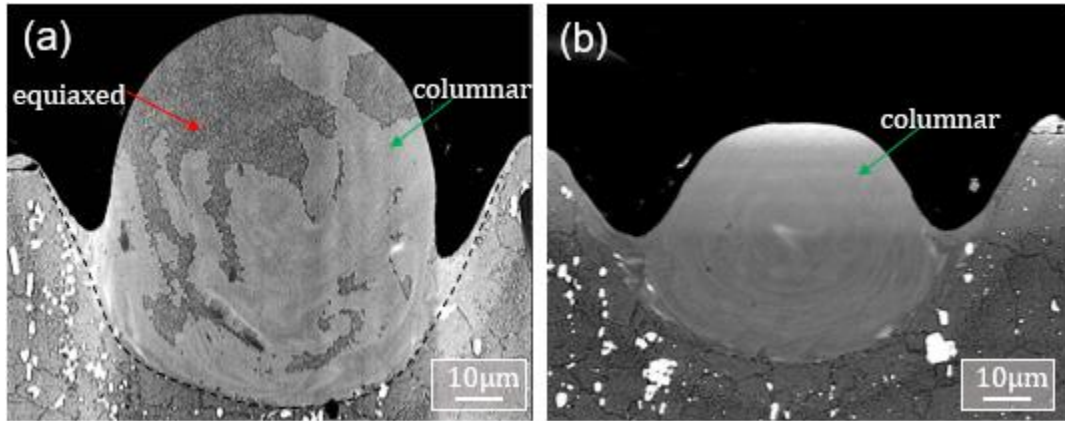


Fig 39 typical example of M2-steel melt pool showing varied microstructure at different location along laser track, corresponding to “varied microstructure” category in process map (Fig 39); noted: (a), (b) are two cross sections taken at different location of the same sing-track; example provided by P-V#25 (300W-1800mm/s)

An issue worth mentioning is no presence of powder for the M2-steel microstructure investigation. The powder-free method proposed in this work assumes that no-powder melt pool microstructure could provide enough approximation for the powder-added melt pool microstructure. This assumption is supported by the result for H13 steel melt pool in chapter 6.2.2, which shows that the microstructure P-V mapping for no-powder melt pool (Fig 37(b)) is in good agreement to microstructure P-V mapping for powder-added melt pool (Fig 37(a)), suggesting minimal influence of powder presence for LPBF melt pool microstructure. Consistent observation was reported in other studies showing similarity for LPBF melt pool deposited on bulk alloy and powder layer of stainless steel 17-4[16], Ti6Al4V[38], Incone-625[144] and Ti-Nb alloy[145]. This suggests that the microstructure process map based on the no-powder melt pool result might give a safe approximation for LPBF melt pool microstructure of M2 steel. Further discussion on the applicability of the no-powder melt pool microstructure to approximate LPBF microstructure is presented in chapter 7.8.

### 6.2.3 Mechanism for H13 steel microstructure inhomogeneity:

Chapter 6.2.1 shows that microstructure inhomogeneity for H13 steel melt pool is manifested by the coexistence of two microstructure within the same melt pool. These two microstructures are referred to as type (A) and (B) microstructure, as shown in Fig 30. The characterization result in chapter 6.2.1 shows the following differences between these two microstructures:

- (1) microstructure morphology: type (A): cellular network; type (B): isolated needle;
- (2) phase constituent: type (A): ferrite (cell core) + austenite (cell boundary); type (B): ferrite (matrix) + martensite (large needle);
- (3) microsegregation: type (A): segregation of C, Cr, Mo, V at cell boundary; type (B): not observed
- (4) distribution: type (A): melt pool top; type (B): melt pool bottom;

A microstructure evolution mechanism was proposed for the non-equilibrium solidification of H13 steel melt pool, as shown in chapter 6.2.3. This mechanism appears to clarify the questions of how the above differences exist for type (A) and (B) microstructure as well as the phenomenon of austenite evolving in a ferritic steel. In chapter 6.2.3, the validity of the mechanism was evaluated by the comparison of experimental observation and calculation results by coupling DICTRA simulation and melt pool thermal profile simulation.

- **Proposed mechanism:**

**microsegregation-induced microstructure inhomogeneity**

The cellular arrangement of ferrite/ austenite phase as presented by type (A) microstructure was commonly observed for the as-built microstructure of LPBF-H13 steel [53,54,143,146,147]. There are two prevailing theories explaining the presence of austenite phase at the cellular boundary in as-built H13 steel microstructure:

The first theory considers LPBF process similar to a quenching and partitioning (Q&P) process[148]. It hypothesized that the rapid solidification of LPBF presents a thermal condition similar to quenching, which results in martensitic microstructure in the as-solidified melt pool. Then the solidified melt pool would go through a repeated heat-cooling cycle due to the successive layer deposition. The reheating process transforms the martensitic microstructure into austenite. The austenite could not fully transform to martensite during the repeated cooling cycle because the repeated cooling cycle usually shows a cooling rate considerably slower than the as-deposited cycle and thus the final temperature of the repeated cooling cycle could not reach the martensite-finish-temperature ( $M_f$ ). The remaining austenite can then be stabilized by solid-state carbon diffusion from martensite into the austenite, similar to the Q&P process [148] and thus preserved to the final microstructure of as-built H13 steel.

The second theory, on the other hand, assumed that during LPBF process, solidification of as-deposited melt pool has a sufficiently fast cooling rate, leading to extensive carbon and alloying solute pile up in the last-solidified austenite due to microsegregation. This in turn stabilizes the last solidified austenite due to its local chemical concentration different from the nominal one. Liang et al [149] also showed a similar causal relation between high cooling rate and solute pile up for laser deposition of nickel-base super alloy. In addition, they reported that in the melt pool, some local regions with higher cooling rate presents higher degree of solute pile-up. The austenite preserved in the as-solidified melt pool is possible to remain in the final microstructure of as-built H13 steel as the local segregation formed by rapid solidification might not be balanced during the successive layer deposition of the build considering its temperatures and durations might not be enough to achieve a complete homogenization.

In this work, retained austenite was found in H3-steel single-track melt pool, presenting cellular boundary distribution in type (A) microstructure (see Fig 30 and Fig 32). The current work indicates that the retained austenite in type (A) microstructure was likely to be a result of segregation instead of the “Q & P” effect for the following reasons:

First, the Q&P theory as mentioned above shows minimal likelihood simply because type (A) microstructure was found in the single track melt pool which has no successive layer deposition involved and in turn no possibility for the austenitizing and solid-state diffusion to occur during repeated heating and cooling. Second, this work confirmed experimentally the existence of carbon and alloy solute pile-up at the cellular boundary, which was the location of austenite phase presence. The experimental results were summarized in Fig 32 and Fig 34 in chapter 6.2.1, This shows that microsegregation indeed exists during solidification and show correspondence to the presence of austenite phase. The experimental result observed in this study supports the assumption proposed in the second theory.

Based on the second theory as mentioned above, this work assumes that microsegregation during solidification exists and is responsible for preserving austenite phase after solidification due to its influence on martensitic-starting temperature ( $M_s$ ). As an initial evaluation for the assumption, Scheil-Gulliver calculation using Thermo-Calc software[35] was conducted to estimate  $\gamma$ -Fe composition formed at different stages of H13-steel melt pool solidification. The results show a large composition variation for  $\gamma$ -Fe formed at the early stage and terminal stage of solidification. An example is shown in Fig 40(a) for the predicted C wt.% and V wt.% of  $\gamma$ -Fe as solidification proceeds.

Fig 40(b) shows the solidification route for H13 steel calculated by the Scheil-Gulliver model. Fig 40(a) and (b) show noticeable composition variation for  $\gamma$ -Fe formed at different stages of solidification and sudden change in  $\gamma$ -Fe composition as a new carbide phase evolved. This indicates the possibility of a large variation in Ms temperature between the early-solidified and later-solidified  $\gamma$ -Fe.

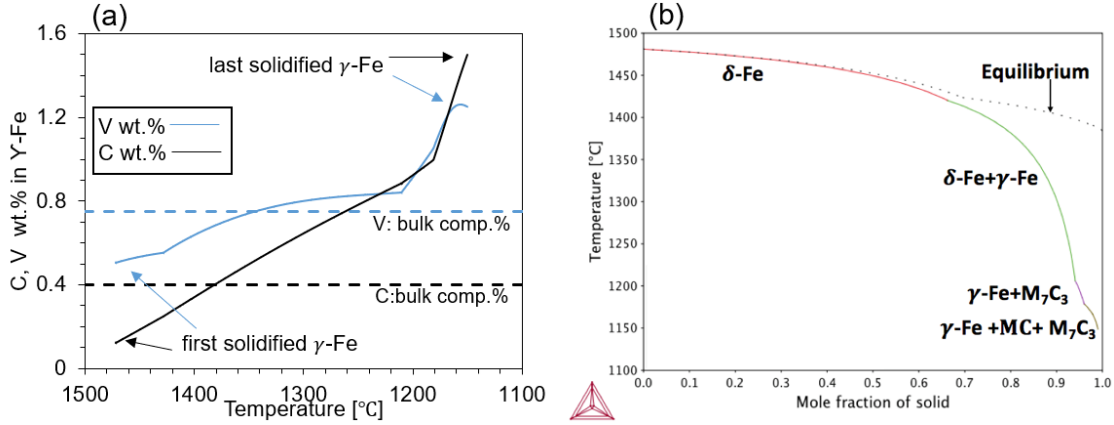


Fig 40 C and V wt.% in  $\gamma$ -Fe versus temperature for H13-steel solidification (a) and H13-steel solidification phase transformation route (b); (a) and (b): calculated by Scheil-Gulliver Model; symbols in (b):  $\delta$ -Fe: ferrite;  $\gamma$ -Fe: austenite;  $M_7C_3$ , MC: carbide

In this work, Ms temperature for  $\gamma$ -Fe formed at different stages of solidification was calculated by Ms relation developed by Barbier [150] in Equation 12.

$$Ms = 545 - 601.2 \cdot [1 - e^{-0.868 \cdot C\%}] - 34.4 \cdot Mn\% - 13.7 \cdot Si\% - 9.2 \cdot Cr\% - 17.3 \cdot Ni\% - 15.4 \cdot Mo\% + 10.8 \cdot V\% + 4.7 \cdot Co\% - 1.4 \cdot Al\% - 16.3 \cdot Cu\% - 361 \cdot Nb\% - 2.44 \cdot Ti\% - 3447 \cdot B\% \quad \text{Equation 12}$$

Where Ms is martensitic starting temperature (°C) and i% is local composition in melt pool (wt.%)

The result was presented in Fig 41, which shows that the Ms temperature drops from around 400°C for the first-solidified  $\gamma$ -Fe to 37°C for the last-solidified  $\gamma$ -Fe. The comp% of first- and last-solidified  $\gamma$ -Fe was indicated in Fig 40(a). The Scheil-Gulliver calculation as shown in Fig 41 indicates that for H13 steel rapid solidification, the  $\gamma$ -Fe formed at the terminal stage of solidification might not transform into martensite due to its low Ms value, and thus might be preserved in the solidified single-track melt pool. As an initial estimation, we considered that  $\gamma$ -Fe with Ms lower than 130°C might be preserved in the single-track melt pool, presenting as the cellular-network  $\gamma$ -Fe in the type (A) microstructure. The threshold of 130°C is designed according to the chamber preheat temperature

for the LPBF tests, which was set as 80°C for all single-track, multi-track and 3D-cubes tests for H13 steel in this study. Roberts et al[151] simulated the transient temperature field for LPBF single-track build, which take into account the thermal effect of powder layer presence by element birth and death method. The simulation showed that when chamber preheat temperature was set at 80°C, the resulting temporal profile for single-layer build presented a slight rise in the steady-state temperature to around 130°C, and as successive layers were built, this steady-state temperature showed small and consistent increase. Based on this, we set the threshold of low- $M_s$   $\gamma$ -Fe as  $\gamma$ -Fe with  $M_s < 130^\circ\text{C}$ . Fig 41 shows that the vol.% of low- $M_s$   $\gamma$ -Fe is around 5%, which agrees with the area fraction of cellular-network in SEM image, which is about 3-6% based on ImageJ analysis. A more comprehensive evaluation for the proposed mechanism is presented in chapter 6.2.3, which couples DICTRA simulation and numerical calculation of melt pool cooling rate profile to predict low- $M_s$   $\gamma$ -Fe%.

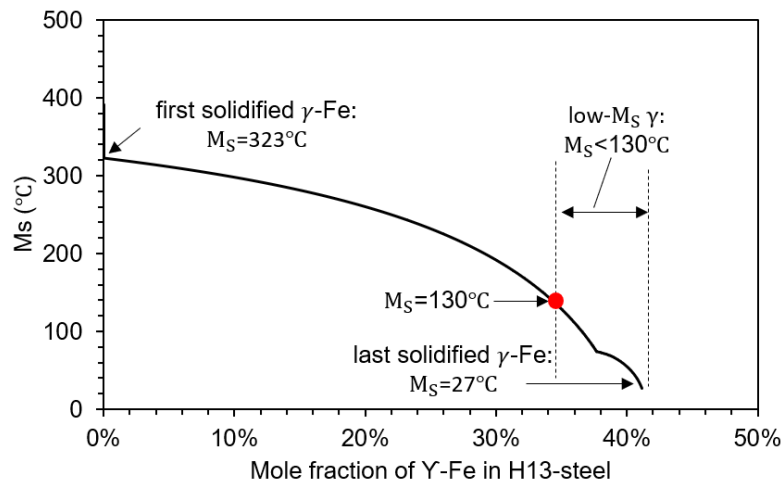


Fig 41 change of  $M_s$  temperature for  $\gamma$ -Fe formed from beginning to end of H13-steel solidification; calculation: based on comp% profile calculated by Scheil-Gulliver model (see Fig 40); low- $M_s$   $\gamma$ -Fe: referred to  $\gamma$ -Fe with  $M_s < 130^\circ\text{C}$ , as 50 °C above preheat temperature

The proposed mechanism also helps to explain no presence of cellular-network austenite in type (B) microstructure. Microsegregation was closely related to the solidification cooling rate[152][58][149]. Several arc and laser welding studies[153–155] showed experimentally and theoretically that local cooling rate variation existed between the regions near and away from melt pool edge during weldment solidification and that this variation was enlarged by a higher heat source travel speed and a smaller melt pool volume. Compared to the welding condition in previous studies[153–155], the laser scan condition investigated in this study adopted higher-level scan speed and the resulting LPBF

melt pools presented a smaller dimension than the welding melt pools. Thus, the H13-steel melt pools fabricated in this study was likely to present noticeable local cooling rate variation. By relating this likelihood of local cooling rate variation with the proposed assumption, we proposed a possible microstructure evolution route for H13 steel melt pool solidification to explain its microstructure inhomogeneity, as schematically shown in Fig 42:

During H13 steel melt pool solidification, the near-top region presents higher local cooling rate than near-bottom region in the melt pool, which result in different microsegregation behavior for these two regions: The near-top region presents a noticeably higher degree of solute pile-up in the last solidified austenite at cellular boundary compared to that in the near-bottom region. As mentioned earlier, the proposed assumption states that solute pile-up allows the existence of the  $\gamma$ -Fe with low  $M_s$  temperature, which is the  $\gamma$ -Fe that could be preserved in the solidified melt pool. On this basis, the near-top region in H13 steel melt pool should show presence of cellular-arranged  $\gamma$ -Fe, while the near-bottom region should not. As a result, the near top region exhibits type (A) microstructure and the near bottom region exhibits type (B) microstructure as exemplified by Fig 30. Calculation coupling DICTRA simulation and melt pool cooling rate profile calculation was conducted to examine the validity of this microstructure evolution mechanism, as shown further in chapter 6.2.3.

Another difference in type (A) and (B) microstructure lies in the presence of the large needle martensitic phase in type (B) but not type (A) microstructure. We intend to explain this phenomenon by the following concept: As mentioned earlier, the melt pool cooling rate profile at the end of solidification (Fig 43, chapter 6.2.3) suggests that the local region with type (A) microstructure presents noticeably higher cooling rate than the local region with type (B) microstructure. To distinguish, the cooling rate at end of solidification, that is, at the beginning of solid-state transformation, is referred to as “extremely high cooling” for type (A) microstructure and “lower-level cooling” for type (B) microstructure. This evident difference in cooling rate might result in two different solid-state phase transformation routes for type (A) and (B) microstructure as demonstrated below and schematically shown in Fig 42:

The solid-state phase transformation for type (A) microstructure is shown on the left side of Fig 42. For type (A) microstructure, the extremely high cooling rate suggests the possibility of suppressing  $\delta$ -Fe  $\rightarrow$   $\gamma$ -Fe phase transformation due to fast cooling from solidus temperature to  $A_{r3}$  temperature, in turn preserving  $\delta$ -Fe inside the  $\gamma$ -Fe cellular network. The preserve of  $\delta$ -Fe at room temperature has been observed by a series of welding-related studies using liquid-tin to quench welds of stainless

steel during solidification [63][90][155][156]. This renders the cellular microstructure with  $\delta$ -Fe at cell core, high-Ms  $\gamma$ -Fe at the inner side of cell boundary and low-Ms  $\gamma$ -Fe at the outer side of the cell boundary, as shown in Fig 42. With this microstructure, martensitic transformation could only occur for the high-Ms  $\gamma$ -Fe, which is restricted in the limited volume between  $\delta$ -Fe matrix and the low-Ms  $\gamma$ -Fe, indicating that the formed martensitic phase might only present fine sub-micron length scale, while the large-needle martensite in type (B) microstructure, which presents a dimension scale around 5 $\mu$ m, should show minimal chance to form in type (A) microstructure.

In contrast, for type (B) microstructure, the lower-level cooling rate suggests the cooling from solidus temperature to Ar3 temperature might not be sufficiently fast enough to completely suppress  $\delta$ -Fe  $\rightarrow$   $\gamma$ -Fe phase transformation, and thus part of  $\delta$ -Fe transform into  $\gamma$ -Fe. To distinguish from the  $\gamma$ -Fe formed during solidification (high-Ms and low-Ms  $\gamma$ -Fe in Fig 42),  $\gamma$ -Fe formed during solid-state  $\delta$ -Fe  $\rightarrow$   $\gamma$ -Fe transformation were denoted as  $\gamma'$ -Fe in Fig 42. This  $\gamma'$ -Fe should have a similar composition as  $\delta$ -Fe. Thus, Ms temperature of  $\gamma'$ -Fe was estimated by Ms relation developed by Barbier [150] using the  $\delta$ -Fe composition estimated by Scheil calculation from [35], which is the same method presented above. The result shows that Ms temperature of  $\gamma'$ -Fe was within the range of [316°C, 429°C], high enough to allow martensitic transformation to occur, and thus it was also denoted as high-Ms  $\gamma'$ -Fe in Fig 42. Therefore, martensitic transformation could occur for the high-Ms  $\gamma'$ -Fe evolved from solid-state phase transformation and the high-Ms  $\gamma$ -Fe from solidification, providing enough volume to allow the formation of large-length-scale martensitic phase in type (B) microstructure.

Above mechanism proposed for the microstructure evolution route for the non-homogeneous H13 steel melt pool are schematically presented in Fig 42, with the left side for type (A) microstructure and the right side for type (B) microstructure. This mechanism show consistency with the experimental observation of microstructure morphology, phase constituent, microsegregation and microstructure distribution for H13-steel single-track as summarized at the beginning of this chapter. However, it should be noted that the mechanism was proposed by analyzing the Scheil-model calculated result. Chapter 2.2.1 in the introduction shows the potential problem for Scheil-Gulliver model calculation when it is adopted for solidification of steel system. In this regard, further validation for the proposed mechanism was conducted to use DICTRA simulation for H13-steel solidification calculation, as shown below in chapter 6.2.3.

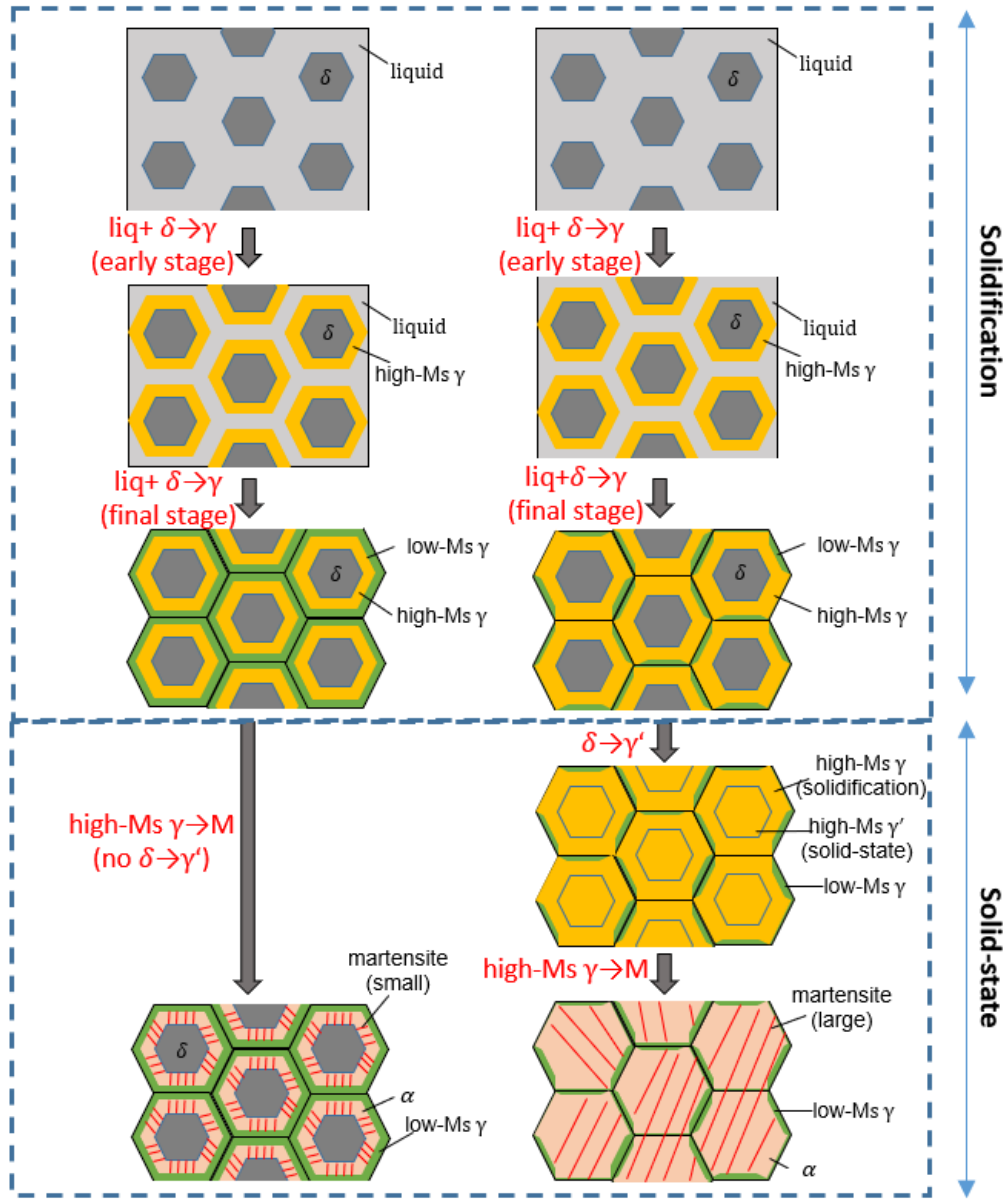


Fig 42 schematic of microstructure evolution mechanism for type (A) & (B) microstructure located at the near-top and near-bottom region of H13 steel melt pool(see Fig 30) ); high-Ms  $\gamma$ , low- Ms  $\gamma$ -Fe: austenite with  $M_s > 130^\circ\text{C}$  and  $M_s < 130^\circ\text{C}$ , defined in Fig 41;  $\gamma$  and  $\gamma'$ : austenite formed from solidification and solid-state phase transformation; M: martensite

- **Validate mechanism:**

**microstructure prediction vs. experimental observation**

In this work, a mechanism was proposed to explain the microstructure inhomogeneity for H13 steel

melt pool, as shown earlier in this chapter. It assumes the cellular-network microstructure and isolated-needle microstructure (type (A) and (B) microstructure) evolving at the near-top and near-bottom region of the melt pool as a result of different microsegregation behavior for local solidification at these two regions. The experimental results in Chapter 6.2.1 showed that vol% of type (A) microstructure in melt pool showed noticeable variation with P-V sets, as exemplified by Fig 36. Based on this observation, the validity of the proposed mechanism will be evaluated by predicting vol.% of type (A) microstructure for different P-V sets and then comparing them to the experimentally observed one for the corresponding P-V sets. The evaluation procedure was as follows:

For the P-V sets tested for H13 steel single-track, 6 of them were selected for microstructure prediction, as shown in Table 14. For these 6 P-V sets, their corresponding melt pool cooling rate profiles at the end of melt pool solidification were estimated by numerical calculation using a 3D transient heat transfer model. Two examples were presented for P-V#5 and #8, as shown in Fig 43(a-3) and (b-3). Fig 43(a-3) and (b-3) showed that for both cases, there is a region at the top corner of melt pool showing noticeably higher cooling rate than the nearby region, as indicated by the yellow color in Fig 43(a) and (b). A loop shape boundary could be found between this higher-cooling region and the nearby lower-cooling region, which appears to show correspondence to the experimental observation showing a loop-shape boundary separating local region with type (A) and (B) microstructure in the melt pool, which was presented earlier in Fig 30 and Fig 36. However, the melt pool cooling rate profile of P-V#8 was different because the higher-cooling region in the melt pool was not only limited to the melt pool top corner. The comparison between Fig 43(a-3) and (b-3) shows that for the melt pool of P-V#8, the region near the centerline of the melt pool (indicated by yellow color) also presents a higher cooling rate than the surrounding region. While this higher-cooling region was not found for the melt of P-V#5. For the other 4 P-V sets of selection, the melt pool cooling rate profile of P-V#3, #4 presents a similar trend as the one in Fig 43(a-3), while the melt pool cooling rate profile of P-V#6 and #14 shows a similar trend as the one in Fig 43(a-3). These higher-cooling regions were expected to show a high level of carbon and alloy solute pile-up at the cellular boundary based on the DICTRA simulation result, as shown below.

Table 14 Comparison of experimental and calculated vol% of type (A) microstructure in melt pools for different P-V sets

<b>type (A) microstructure: vol.% in melt pool</b>	<b>P-V#3</b>	<b>P-V#4</b>	<b>P-V#5</b>	<b>P-V#6</b>	<b>P-V#8</b>	<b>P-V#14</b>
calculated	17%	18%	22%	45%	54%	53%

experimental	19%	24%	28%	47%	62%	65%
standard deviation (experimental)	0.05	0.02	0.03	0.06	0.03	0.05

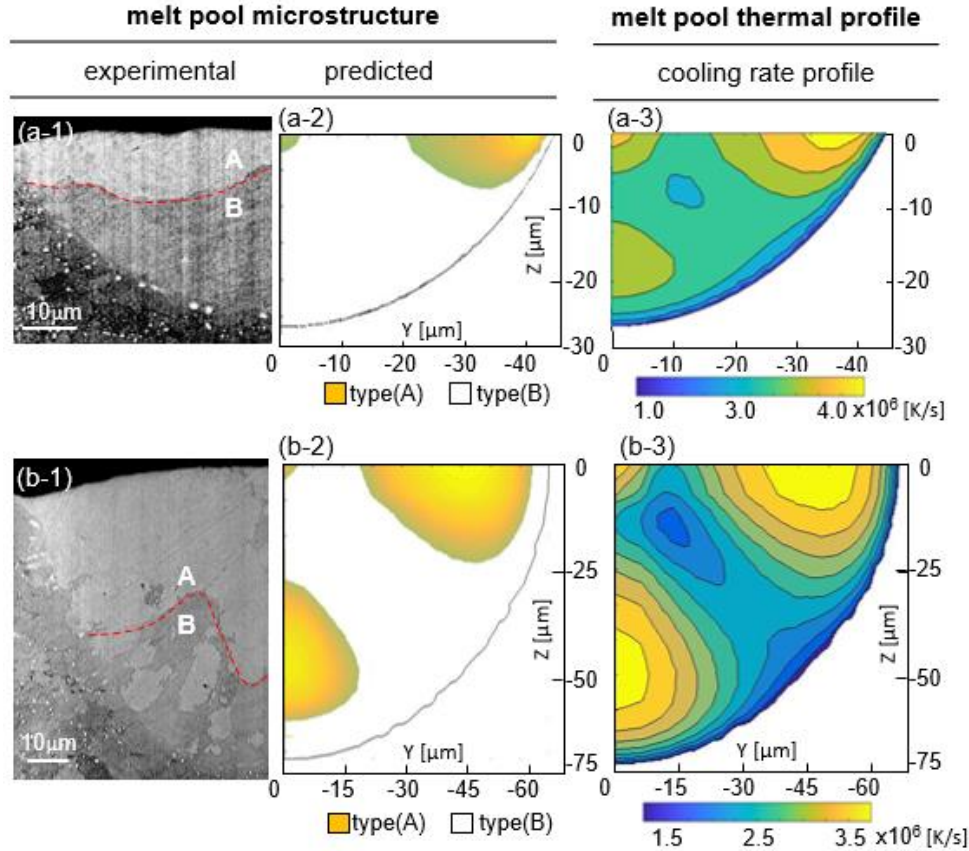


Fig 43 Comparison of predicted results(a,b-2) and experimental results(a,b-1) for H13-steel melt pool microstructure showing coexistence of type (A) and type (B) microstructure on cross section with process setting specified as P-V#5, #8, presented in (a-1,2,3) and (b-1,2,3) respectively; in (a,b-1): red dashed line indicates the boundary separating region with type (A) and (B) microstructure in melt pool, location of the two microstructure: indicated by letter “A” and “B”; microstructure prediction: based on calculation result for melt pool cooling rate profile (a,b-3) at end of solidification for corresponding P-V set.

Microsegregation during melt pool solidification was estimated by DICTRA simulation. Selective results are presented in Fig 44, showing the carbon concentration from cellular core to cellular boundary calculated for different cooling rates and compares them to the result from Scheil simulation. Results from other elements were qualitatively similar, so only plots for carbon are shown.

For DICTRA simulation, its thermal profile setup was based on the melt pool cooling rate profile calculated for each P-V sets of selection (exemplified in Fig 43(a-2),(b-2)), 10 cooling rates were selected for each melt pool, which led to melt pool 10-20 vol% increasing from one cooling rates to the other. The diffusion field length setup was based on the experimental measurement of cellular spacing for type (A) microstructure in multiple melt pool, with Fig 44(a) and (b) presenting two cases for DICTRA simulation: First case adopts same diffusion field length (i.e.,  $0.5\lambda=0.5\mu\text{m}$ ) to different cooling rates, as shown in Fig 44(a). This simulation setup was adopted since the cellular network spacing measurement for type (A) microstructure showed that the network spacing lies in the range of 0.4 to 1  $\mu\text{m}$ , with an average value of 0.63  $\mu\text{m}$ . However, we found potential convergence problem for DICTRA simulation with high cooling rate in the order or higher than  $10^6\text{C/s}$  and a small diffusion field less than 0.3 $\mu\text{m}$ , which could be seen from the fluctuated curves in Fig 44(b). Therefore, for cooling rates corresponding to type (A) microstructure (e.g.,  $5\times 10^6$  and  $10^7\text{C/s}$ , see Fig 43), we selected diffusion field (i.e.,  $0.5\lambda$ ) as 0.5  $\mu\text{m}$  for DICTRA setup, as indicated in Fig 44(a), which could ensure DICTRA calculation accuracy and also ensure that the resulting cellular spacing ( $\lambda=1\mu\text{m}$ ) is within the range of experimental measurement.

In the second case, different cellular network spacing was adopted to each cooling rate, which was shown in Fig 44(b). A correlation as  $\lambda \propto \dot{T}^{-n}$  was often found between cellular network spacing ( $\lambda$ ) and local cooling rate ( $\dot{T}$ ), with  $n$  as material constant [21]. Grant[157] showed that the material constant  $n$  was around 1/3 for various alloy systems, and thus it was used to approximate the cellular network spacing for different cooling rate in this study: for the highest cooling rate presented ( $10^7\text{C/s}$ ) in Fig 44(b), its corresponding cellular spacing was approximated as 0.5 $\mu\text{m}$ , a value approaching the lower limit of the cellular spacing range from experimental measurement. Then, based on the relation of  $\lambda \propto \dot{T}^{-1/3}$ , the cellular spacing for the other cooling rates were estimated and used for their corresponding the DICTRA calculation as shown in Fig 44(b). Besides, cellular network morphology was not found in type (B) microstructure. This simulation with cellular spacing varying with cooling rate in Fig 44(a) was expected to be more realistic compared to the first case with constant cellular spacing in Fig 44(a). However, as mentioned earlier, for the simulation in the second case, its setup that couples sufficiently high cooling rate and small diffusion field arouse the problem of instable DICTRA simulation, which could be seen from the fluctuated curves of  $10^6\text{C/s}$  and  $10^7\text{C/s}$  in Fig 44(b).

Fig 44(a) and (b) showed that no matter for constant or varied cellular spacing with the cooling rate, the simulation result always shows that solidification under all the presented cooling rates results in segregation with carbon pile up at 20-30nm near the cellular boundary. However, solidification with a cooling rate higher than  $3 \times 10^6 \text{C/s}$  results in a much higher C% pile up at the cellular boundary compared to the cooling rate lower than  $3 \times 10^6 \text{C/s}$ . The DICTRA simulation result in Fig 44 indicates that when cooling rate reaches  $3 \times 10^6 \text{C/s}$ , H13-steel solidification was expected to result in high-level solute pile-up in the last-solidified material comparable to Scheil-calculated result, suggesting that Scheil-based calculation as shown in Fig 40 and Fig 41 could provide reasonable estimation for this solidification condition. While for solidification with a cooling rate lower than  $3 \times 10^6 \text{C/s}$ , solute pile-up exists but was overestimated by Scheil-model calculation. In this solidification condition, Scheil model provided impractical estimation for H13-steel solidification.

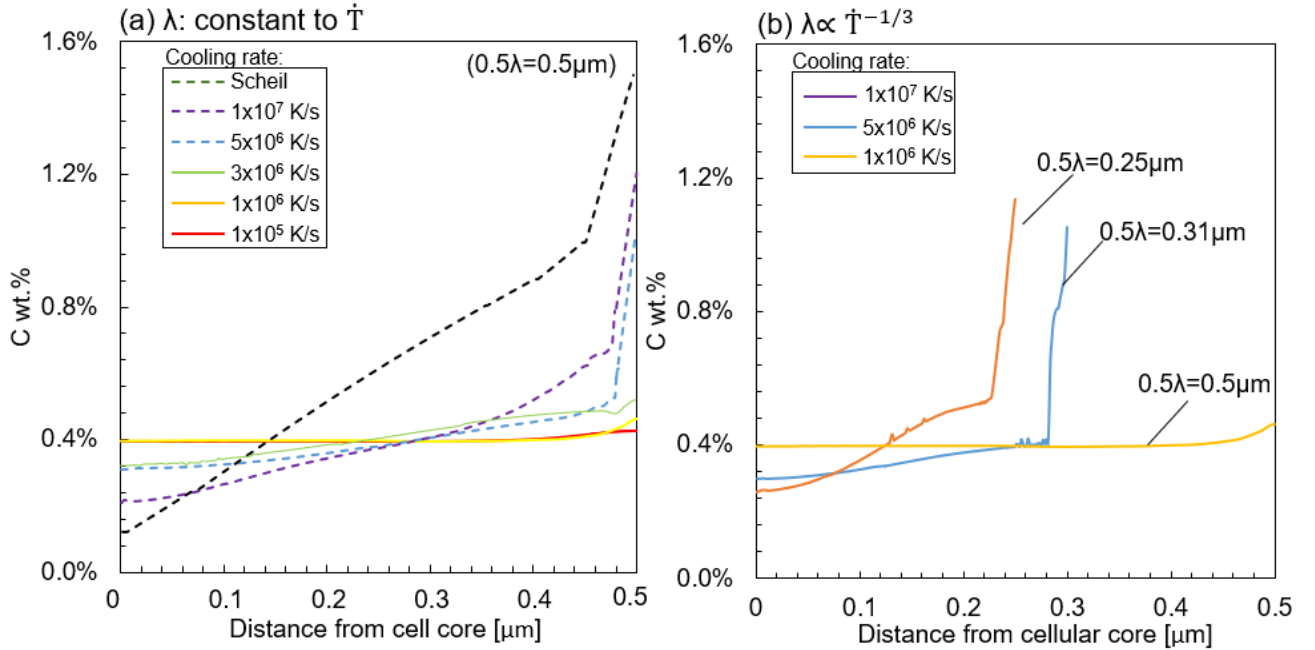


Fig 44 carbon concentration (wt.%) vs. distance from cell core to cell boundary (i.e., half of cellular network spacing ( $\lambda$ )) in type (A) microstructure of H13 steel (see Fig 30) for different solidification cooling rate ( $\dot{T}$ ) calculated by DICTRA simulation and compared with Scheil-Gulliver simulation; selected solidification cooling rates: within the range of LPBF melt pool solidification cooling rate estimated by melt pool thermal numerical calculation (see Fig 43); in (a): DICTRA setup adopted constant  $\lambda$  for different cooling rates; in (b): DICTRA setup adopted different  $\lambda$  for each cooling

rates based on the relation of  $\lambda \propto \dot{T}^{-1/3}$ ; Noted: (b) shows some curve fluctuation for setup of  $\lambda < 0.3 \mu\text{m}$  potentially due to convergence issue

According to the proposed mechanism, in H13 steel melt pool, the region with higher- and lower-level of solute pile-up at cellular boundary was expected to show type (A) and (B) microstructure respectively (microstructure morphology: see Fig 30(ii) and (iii)). Based on the DICTRA segregation calculation for each melt pool as exemplified in Fig 44, we predicted that type (A) the region showing cooling rate higher than  $3 \times 10^6 \text{C/s}$  in melt pool showed the presence of type (A) microstructure, and the rest region showed type (B) microstructure. The microstructure prediction was exemplified for the melt pools of the two aforementioned P-V sets, as shown in Fig 43(a,b-2). They were compared to the corresponding experimental melt pool microstructure fabricated by the same P-V sets, as presented in Fig 43(a,b,c-1). The comparison between Fig 43(a,b,c-1) and Fig 43 (a,b-2) suggests good agreement between the predicted and experimental results for both local distribution and vol.% of type (A) and (B) microstructure in the melt pool. Table 14 presented the predicted and experimental measured vol.% of type (A) microstructure in the melt pool for the 6 P-V sets of selection, which all show consistency to the experimental results.

The good consistency between the predicted and experimental melt pool microstructure across multiple P-V sets supports the validity of the mechanism proposed in this work, which considers the microsegregation during solidification to be responsible for the microstructure inhomogeneity observed in H13 steel LPBF-melt pool. It also shows the method by coupling DICTRA simulation with melt pool cooling rate numerical calculation as an effective approach for microstructure prediction in the non-equilibrium LPBF solidification condition. Scheil calculation, on the other hand, might not present appropriate estimation for the local solidification across the whole melt pool, as suggested by the result in Fig 44.

#### **6.2.4 Criteria for M2-steel columnar-to-equiaxed transition (CET)**

The experimental result in chapter 6.2.1 shows that columnar-to-equiaxed transition occurred during melt pool solidification of M2 steel at some P-V sets. And a microstructure P-V process map is developed for M2 steel based on experimental observation to present P-V windows for fully columnar, columnar+equiaxed mixed or mainly equiaxed microstructure, as shown in Fig 38(a). Temperature gradient (G) and solidification rate (R) are two dominant factors that govern the criteria for whether or not CET transition occurs during solidification [158]. To investigate the mechanism

for M2 steel microstructure inhomogeneity, we developed an analytical G-R model to determine CET occurrence under LPBF solidification condition based on the CET model of Gäumann et al [12]. Then this G-R criterion was coupled with numerical calculation of melt pool solidification thermal profile to calculate a P-V process map for M2 steel microstructure. We observed good agreement between the calculated and experimental P-V maps, while some discrepancies still exist, which were found to be related to the inaccurate estimation for melt pool with balling behavior. Based on this, the accuracy and application range for adopting the developed G-R criteria for predicting equiaxed microstructure under LPBF solidification was discussed.

- **Developing G-R criteria for the CET**

In this study, G-R solidification map was developed for M2-steel, as shown in Fig 45 (c), which was separated into regions of columnar and equiaxed microstructure by the dashed line. The dashed line represents the G-R criteria for the CET transition, which corresponds to Equation 13. It was determined based on the analytical model developed by Gäumann et al. [12]. This model has been applied to rapid solidification processes such as laser cladding and laser welding. The outline for obtaining Equation 13 is given below:

$$\text{Promoting equiaxed dendrite growth if: } \frac{G^{3.8}}{R} < 7.8 \times 10^{13} \quad \text{Equation 13}$$

The model from Gäumann et al. determined a functional relation among temperature gradient (G), solidification velocity (R) and volume fraction of equiaxed grain ( $\phi$ ), as shown in Equation 14. They confirmed that this model was only valid for solidification with a high temperature gradient, which is the case for LPBF solidification. This function was derived based on Hunt's model[75], with the details shown in [12] and thus not repeated here.

$$\frac{G^n}{R} = a \left\{ \sqrt[3]{\frac{-4\pi N_0}{3 \ln(1 - \phi)}} \cdot \frac{1}{n + 1} \right\}^n \quad \text{Equation 14}$$

Where G is temperature gradient at the interface, R is solidification rate;  $\phi$  is volume fraction of equiaxed grain,  $N_0$  is nuclei density of the alloy, n and a are material-related constants.

The criteria initially proposed by Hunt[75] assume fully equiaxed growth to occur for  $\phi > 0.49$  whereas fully columnar growth for  $\phi < 0.0066$ . On this basis, Gäumann et al. proposed that the G-R threshold condition for allowing equiaxed dendrite growth, which is obtained by substituting

$\phi=0.0066$  in Equation 14. The G-R criteria as shown in Equation 14 is then only dependent on nuclei density ( $N_0$ ) and the two material-related constants  $a$  and  $n$ .

The outline for determining the two material-related constants ( $a$  and  $n$ ) were as follow:

In this study, dendrite tip undercooling was estimated by Equation 15. The dendrite tip undercooling as defined in Equation 15 is composed of three constituent: constitutional, curvature and thermal undercooling, corresponding to the first, second and third term on the right side of Equation 15. The constitutional undercooling (the first term on the right side of Equation 15) is originated from the diffusion field ahead of dendrite arrays, which is taken as the summation of the individual diffusion field of each solute element for a multi-component system as M2 steel. For each solute element ( $i$ ), its corresponding liquid slope ( $m_i$ ) and partition coefficient ( $k_i$ , used for calculation of  $C_{l,i}$ ) in Table 15 is adopted for calculation of its individual contribution for M2 steel constitutional undercooling, which were obtained from Thermo-Calc calculation[35]. The original work from Gäumann et al.[12] approximated this constitutional undercooling (the first term on the right side of Equation 15) equal to dendrite tip undercooling ( $\Delta T_d$ ) by assuming that the tip curvature and the thermal contributions for dendrite tip undercooling were negligible. However, for LPBF process with sufficiently high- $G$  and high- $V$  value, this assumption might be questionable. In this regard, this study adopted the modified Kurz–Giovanola–Trivedi model (KGT model) as shown in Equation 15 to express the dendrite tip undercooling ( $\Delta T_d$ ). Previous studies showed that the modified KGT model was applicable for laser surface remelting of stainless steel[85]. According to this model, the relation among  $\Delta T_d$ ,  $G$  and  $R$  could be solved by Equation 16–Equation 18:

$$\Delta T_d = \sum m_i (C_{0,i} - C_{l,i}) + \frac{2\Gamma}{r_{tip}} + \frac{GD}{R} \quad \text{Equation 15}$$

Where  $\Delta T_d$  is the dendrite tip undercooling;  $C_{l,i}$ ,  $C_{0,i}$  and  $m_i$  are liquid concentration at the dendrite tip, nominal composition, and liquidus slope for component  $i$ ;  $\Gamma$  is Gibbs–Thomson parameter,  $r_{tip}$  is the dendrite tip radius, and  $D$  is the liquid interdiffusion coefficient.

In Equation 15, the liquid concentration at the dendrite tip ( $C_{l,i}$ ) and dendrite tip radius( $r_{tip}$ ) are given by:

$$r_{tip} = 2\pi \left[ \frac{C_{0,i}}{mg_c \xi_C - G} \right]^{1/2} \quad \text{Equation 16}$$

$$C_{l,i} = \frac{C_{0,i}}{1 - (1 - k_i)Iv(P_i)} \quad \text{Equation 17}$$

Where  $k_i$  is the partition coefficient of solute element  $i$ ,  $P_i$  is Peclet number, given by Equation 18:

$$\frac{\pi^2 \Gamma}{P_i^2 D_i^2} + \frac{m_i C_{0,i} (1 - k_i) \xi_{C,i}}{D_i [1 - (1 - k_i)Iv(P_i)]} R + G = 0 \quad \text{Equation 18}$$

In Equation 16 and Equation 17,  $Iv(P_i)$  is Ivantsov's solution:  $Iv(P_i) = P_i \exp(P_i) E_1(P_i)$ , with  $E_1$  as exponential integral;  $\xi_{C,i}$  is the absolute stability coefficient:

$$\begin{aligned} \text{for } P_i > \frac{\pi^2}{k_i^{1/2}}, \xi_{C,i} &= \frac{\pi^2}{k_i^{1/2} P_i^{1/2}} \\ \text{for } P_i \leq \frac{\pi^2}{k_i^{1/2}}, \xi_{C,i} &= 1 - \frac{2k_i}{[(1 + (\frac{2\pi}{P_i})^2)^{1/2} - 1 + 2k_i]} \end{aligned}$$

By solving Equation 15-Equation 18,  $\Delta T_d$  could be determined as a function of  $G$  and  $R$ . Then, following the method proposed by Gäumann et al[12], the two material-related constants in Equation 19,  $a$  and  $n$ , were obtained by finding the fitting parameter to approximate  $\Delta T_d$  as a simple function model in Equation 19:

$$\Delta T_d = (a \cdot R)^{1/n} \quad \text{Equation 19}$$

In this study, Equation 15-Equation 18 were solved numerically to obtain  $\Delta T_d$  for varied solidification velocity and temperature gradient. The material properties used for the calculation are listed in Table 15, which were collected from previous studies[159][160] and calculated using Thermo-Calc software [35]. On this basis, the value of  $a$  was determined as  $7 \times 10^3 \text{ K}^{3.4} \text{ m/s}$  and the value of  $n$  was found to be 3.8 for M2 steel. With these values good fitness was obtained between Equation 19 and  $\Delta T_d$  for  $G$ ,  $R$  in the limited range of  $10^4$ - $10^7 \text{ K/m}$  and  $0.1$ - $1 \text{ m/s}$ . As shown later in this chapter,  $G$  and  $R$  in such range is consistent with the magnitude of  $G$  and  $R$  for typical LPBF melt pool solidification condition (see Fig 47).

Table 15 material properties for CET criteria calculation

material properties	value
---------------------	-------

$T_f$ liquidus temperature (K)	1697
$\Gamma$ Gibbs Thomson coefficient (mK)	$2.8 \times 10^{-7}$
$k_i$ partition coefficient of i	C:0.1, W:0.75, Cr:0.9, Mo:0.7; V:0.6
$m_i$ liquidus slope for i (K/wt.%)	C:4, W:0.5, Cr:0.4, Mo:0.8, V:0.9

With  $a$  and  $n$  determined, the only unknown parameter for G-R criteria is the nuclei density  $N_0$ . In this study,  $N_0$  is obtained by fitting Equation 19 to the experimentally observed CET result for P-V #14 in this study, with the method as follow:

Experimental observation revealed that for melt pool of P-V#9, along melt pool centerline, about 25% of the total depth near melt pool top presents equiaxed dendrite morphology, while the rest 75% presents columnar dendrite microstructure. For this melt pool, the calculated  $G$  and  $R$  along melt pool centerline is shown in Fig 45, with  $G$  and  $R$  estimated by a 3D transient heat transfer model developed by Nick Jones. The arrow indicates the direction from melt pool top to bottom. For the location that separates equiaxed and columnar dendrite microstructure, its  $G$ - $R$  condition corresponds to point B in Fig 45. Then, theoretically, point B would also belong to the  $G$ - $R$  criteria for CET, as represented by the dashed line in Fig 45. In this regard, nuclei density  $N_0$  is estimated by substituting the  $[G, R]$  condition represented by point A into Equation 19 with the given  $a$  and  $n$ .

The obtained  $N_0$  is  $1.5 \times 10^7/\text{mm}^3$ . Experiment measurement of distance between adjacent equiaxed dendrites was used to evaluate the validity of this result. The measurement was conducted by image analyzing M2 steel single track top surface microstructure as exemplified in Fig 46. Compared to melt pool cross section (Fig 35), track top surface provides sufficient region for equiaxed dendrite distance measurement. The result shows that the distance between adjacent equiaxed dendrites presents an average value of  $3.5 \mu\text{m}$  and range of  $1.7\text{-}6 \mu\text{m}$ . This could be qualitatively shown in Fig 46(b). The derived  $N_0$  as  $1.5 \times 10^7/\text{mm}^3$  indicates an average distance around  $4 \mu\text{m}$  between equiaxed dendrite, which is in line with the experimentally-measured one. This suggests that the  $N_0$  derived from the above method provides reasonable approximation for the nuclei density. Besides, a recent study by Yang et al [161] investigated CET of Al-Mg-Zr melt pool produced by LPBF. They showed that the equiaxed grain size is around  $1.5 \mu\text{m}$ , which could result in a comparable nuclei density as derived in this study.

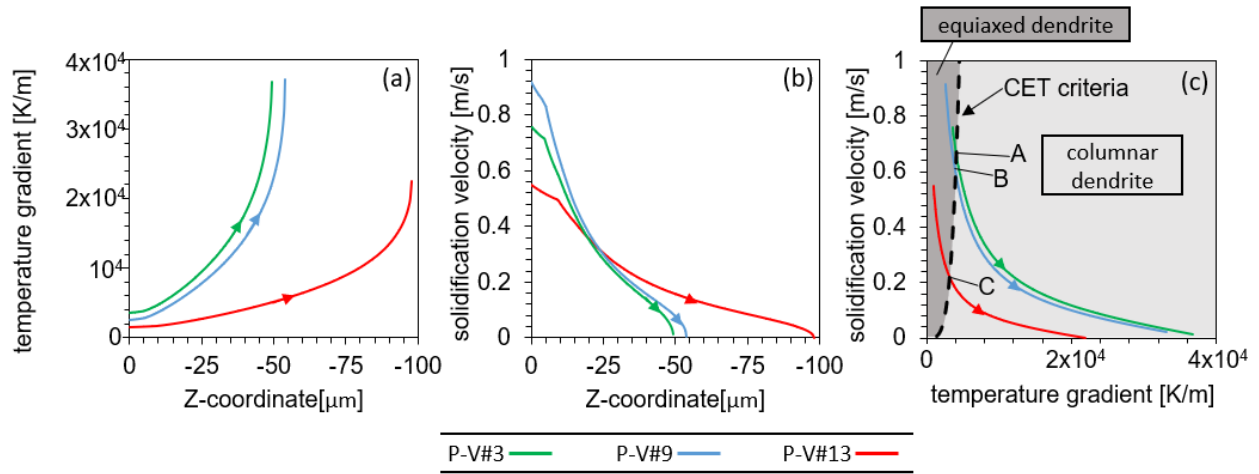


Fig 45 G-R microstructure map (c) for M2 steel showing the G-R condition for promoting equiaxed and columnar dendrite growth, as indicated by the dark and light shade in (c); criteria for CET occurrence: indicated by dashed line in (c); the three color-lines inserted in (c): represent the correlation between G and R for each location across whole melt pool depth at melt pool centerline, calculated for process condition of P-V#3, #9, #13; arrow on color line: indicate direction from melt pool surface to bottom; point “A”, “B”, “C”: represent the location at melt pool centerline separating equiaxed and columnar microstructure in melt pool of P-V#3, #9, #13; (a) and (b) show the evolution of G and R as function of Z at melt pool centerline (Z: melt pool depth; melt pool surface: Z=0); Note: whole melt pool thermal profile and microstructure prediction for the three P-V sets shown in Fig 47

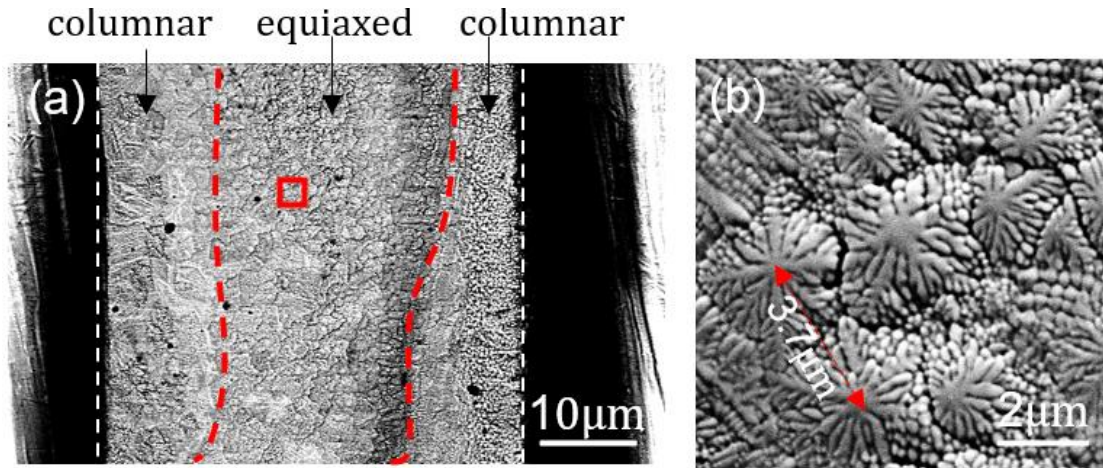


Fig 46 M2-steel single track top surface microstructure (a) used for measuring distance between adjacent equiaxed dendrite measurement (b); in (a): the white dashed lines: single-track boundary; in the single-track: local regions with equiaxed and columnar dendrite are separated by red dashed

lines and indicated by label above (a); (b) is the high magnification image of the red box in (a); in (b): double-arrow red line indicates the distance between adjacent equiaxed dendrite

- **Verifying G-R criteria:**

In chapter 6.2.1, a microstructure process map (Fig 38(a)) was developed based on experimental observation, which presents the different CET tendency observed in the M2 single-track melt pool for the 28 P-V sets selected in this study. This experimental process map was adopted to evaluate the validity of the G-R criteria developed in this chapter, as shown by Equation 13. The evaluation procedure was as follows:

The 28 P-V sets presented in the experimental microstructure process map were selected for calculation. For these 28 P-V sets, their corresponding melt pool thermal profiles at the end of melt pool solidification were simulated by an in-house heat transfer model. As shown earlier in chapter 6.2.2, the P-V sets in the experimental microstructure process map were categorized into three groups based on the equiaxed dendrite% in the resulting melt pool microstructure, which are CET promoting, transition and suppressing group. Fig 47 shows the typical simulation result for temperature gradient and solidification velocity profile for melt pools deposited by P-V sets from each of the three microstructure groups, exemplified by P-V#13 (promoting), #9 (transition) and #3 (suppressing). It could be found from Fig 47 (a-4)-(c-4) that for all three cases, there is a local region at the top center of the melt pool always presenting a sudden increase in solidification velocity, while for temperature gradient (Fig 47 (a-3)-(c-3)), it presents a gradually decreasing trend from melt pool top to bottom. This local variation in G- and R-value for each melt pool suggests the possibility of varied CET tendencies at different regions within the same melt pool. The calculated G- and R-distribution for each melt pool were then substituted into the CET criteria in Equation 13 to predict where equiaxed- and columnar-microstructure was present in the melt pool. For the three aforementioned P-V sets, their melt pool microstructure prediction was shown in Fig 47(a,b,c-2), with the region with equiaxed- and columnar-microstructure labeled by red and white color respectively. They were compared to the corresponding experimental melt pool microstructure fabricated by the same P-V set, as presented in Fig 47(a,b,c-1).

Remarkable consistency could be observed between the predicted and experimental results for equiaxed and columnar dendrite distribution in the melt pool. Table 13 presented the predicted and experimental measured equiaxed microstructure vol% in the melt pool for the three P-V sets of selection, which also show good agreement between predicted and experimental results. If adopting

the same categorization criteria used for the experimental process map (Fig 38(a)), P-V#13, #9 and #3 would be classified into CET-promoting, transition and suppressing group based on their melt pool microstructure prediction. Following this procedure, melt pool microstructure was predicted for the other 26 P-V sets of selection. A microstructure process map was then generated by summarizing the microstructure categorization predicted for all P-V sets, as shown in Fig 38(b).

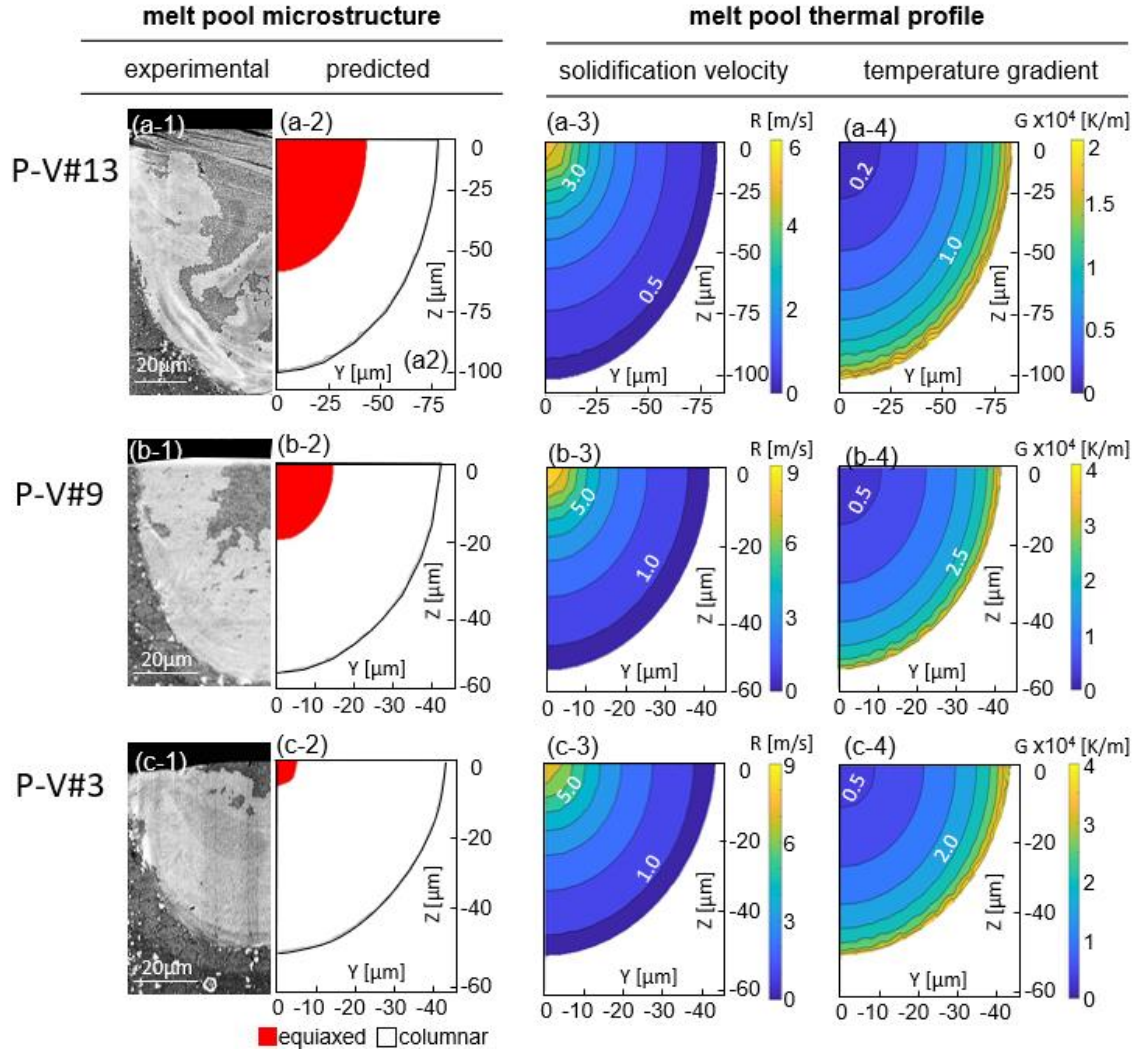


Fig 47 Comparison of calculated results(a,b,c-2) and experimental results(a,b,c-1) for equiaxed and columnar dendrite in M2-steel melt pool microstructure with process setting of P-V#13, #9, #3; experimental results in (a,b,c-1): equiaxed and columnar dendrite distribution: distinguished by dark-contrast and bright-contrast; microstructure prediction in (a,b,c-2): based on calculation of melt pool thermal profile at end of solidification for corresponding P-V sets (solidification velocity: a,b,c-3; temperature gradient:a,b,c-4);.Note: P-V #13, #9, #3 belong to different microstructure group in experimental microstructure process map of M2-steel (Fig 38(a));

Above comparison between the predicted and experimental microstructure process map suggests that: First, within the non-balling P-V space, the G-R criteria developed in this study (Equation 13) could be used as a safe criterion to predict the presence of equiaxed microstructure for LPBF solidification of M2 steel, as supported by the consistency between prediction and experiment result within this P-V space. While the validity of this G-R criteria might not be safely extended to the balling P-V space since some inaccurate predictions exist in this P-V region. This inaccuracy might result from the influence of unstable melt pool fluid flow and Marangoni convection on both equiaxed grain nucleation and melt pool thermal profile, which is further discussed in chapter 6.3.2.

Second, within the non-balling P-V space, the predicted and experimental microstructure process map in Fig 38 show a general trend that P-V parameter combining high P/V ratio and high scan speed lead to high fraction of equiaxed microstructure in melt pool. This trend is a combined result of a lower magnitude of temperature gradient as P/V ratio increases and a higher solidification velocity as V increases, which could be exemplified by the three P-V sets in Fig 47, namely P-V #3, #9 and #13. For P-V#3 and #9, their P/V ratio is comparable while scan velocity increases from 600 to 1000mm/s. For P-V#3 and #13, they have the same P-V value, while P/V ratio increases from 0.25 to 0.4 W·s/mm. Correspondingly, the resulting melt pool for P-V #3, #9 and #13 present vol.% of equiaxed microstructure around 5%, 25%, 50% respectively as shown earlier in Table 13, which could also be qualitatively seen in Fig 47. For these three P-V sets, their G- and R-evolution across melt pool depth at melt pool centerline are compared in Fig 45, which was calculated for the median plan of the melt pool, with  $x=0$ . Fig 45(a) shows that at similar melt pool depth, highest, moderate and lowest temperature gradient is achieved for P-V #3 and #13, with the one for P-V#9 in between. While the magnitude of solidification velocity shows a different trend: as shown in Fig 45(b), at same melt pool depth, the highest, moderate and lowest R-value is achieved by P-V#13, P-V#9 and P-V#3 respectively for most location along melt pool centerline, showing a reverse order than that for temperature gradient, except at region near melt pool surface, where the three P-V sets shows comparable R magnitude. As suggested by the CET criteria in Equation 13, lowering G and increasing R would promote the presence of equiaxed microstructure, since this creates a thermal condition during solidification that has sufficient undercooling to permit the nucleation of equiaxed dendrites. This suggests that P-V parameter selection could alter M2-steel melt pool microstructure through their influence on the melt pool G-, R-thermal condition, which further indicated the presented P-V process map in Fig 38 as an effective tool to control and even design microstructure of LPBF-built

M2 steel, as further discussed in chapter 6.3.2.

### **6.2.5 Microstructure inhomogeneity and hardness**

Melt pool hardness of H13 steel and M2 steel were measured by nano-indentation tests. The result is presented below, which indicates the existence of hardness inhomogeneity and its correlation with microstructure inhomogeneity in the melt pool:

- **H13 steel**

For H13 steel, nano indentation tests were conducted for a series of tracks, pads and cubes generated at the same P-V sets, with some representative examples shown in Fig 48. The pad and cube microstructure are further presented in chapter 6.3.1. In chapter 6.2.2, a microstructure P-V process map was presented for H13-steel single track(Fig 37), which classified the P-V sets into 4 categories based on their resulting melt pool microstructure. For melt pool hardness measurement, each selected P-V set in Fig 48 produced melt pool microstructure in a different microstructure category as shown in the microstructure P-V map. The example microstructure images for each microstructure category could be found in Fig 36. In Fig 48, it clearly showed that track, pad and cube all presented microhardness inhomogeneities in the melt pool, as suggested by the hardness variation between the two different microstructures (type(A) and (B) microstructure: see Fig 30 for track, see Fig 50 for pad, type(A') and (B') microstructure for cube: see Fig 52) in one melt pool. For track and pad, type (A) microstructure always showed 20% to 30% higher hardness than type (B) microstructure in the same melt pool, which is the case for all four different microstructure categories. Similarly, cubes always showed higher hardness for type (A') than type (B') microstructure in the same melt pool. One exception is for the pad of P-V#20, with its microhardness value for type (B) microstructure not presented in Fig 48. This was due to the minimal area% of type (B) microstructure found in each melt pool for this pad, as shown in Fig 50(a). Thus, it was hard to confirm a representative hardness value for type (B) microstructure for the pad.

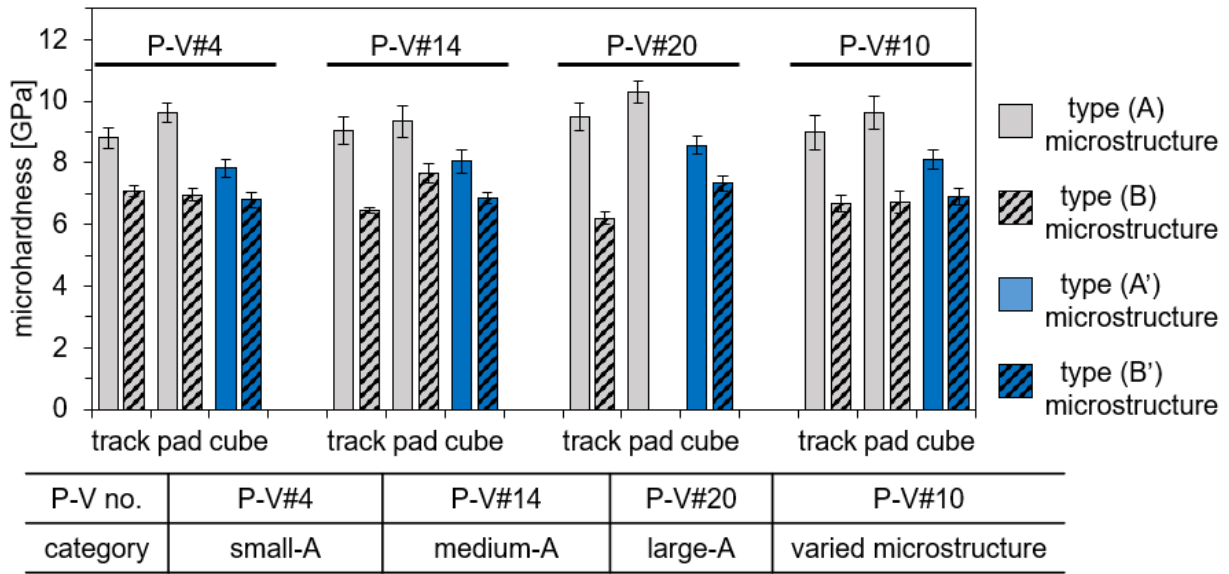


Fig 48 microhardness for track, pad, cube fabricated by P-V set #4, #14, #20, #10, each in different microstructure categories in P-V map (Fig 37), as presented in table below the chart; microhardness: measured for different microstructure found in track/pad/cube, as indicated by the label (microstructure: type (A), (B) see Fig.10(ii), (iii) for track, Fig 50(b-1),(b-2) for pad; type (A') and (B') see Fig 52(b), (c) for cube)

### • M2 steel

Chapter 6.2.2 shows that M2 steel melt pool produced by different P-V sets presented different vol.% of equiaxed and columnar dendrite microstructure, based on which a microstructure P-V process map was presented for M2 steel (Fig 38) to classify the P-V sets into CET promoting, transition and suppressing group based on their resulting melt pool microstructure. Nano indentation test was conducted to measure melt pool hardness for tracks generated by P-V sets in CET promoting group and CET suppressing group as shown in the microstructure process map (Fig 38), with the typical results presented in Fig 49. P-V sets in CET transition group were not selected considering that the resulting melt pools (Fig 35 (b)) do not provide sufficient area with solely equiaxed or columnar dendrite for hardness measurement.

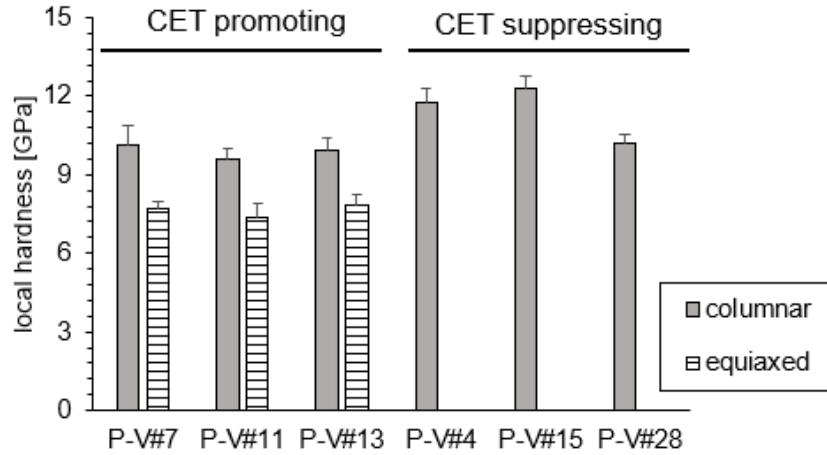


Fig 49 typical melt pool hardness measurement for P-V sets in CET promoting and suppressing group (microstructure groups: indicated by the labels at the top); for P-V sets of promoting group: local microhardness compared for the regions with equiaxed and columnar dendrite within same melt pool

As mentioned in chapter 6.2.2, for the CET promoting P-V sets in the microstructure P-V process map, the resulting melt pools presented co-existence of columnar and equiaxed dendrite microstructure, while melt pools generated by CET suppressing P-V sets present almost fully columnar dendrite microstructure. From Fig 49, it could be found that for CET suppressing P-V sets, the resulting melt pool presents consistent hardness across the whole melt pool depth, as indicated by the small error bar in Fig 49. On the contrary, for melt pools of CET promoting P-V sets, the local region with equiaxed dendrite microstructure presents about 70-80% hardness of the nearby region with columnar dendrite microstructure, indicating a sudden change in hardness across the boundary separating equiaxed and columnar microstructure in the melt pool. It should be noted that such hardness inhomogeneity between equiaxed and columnar microstructure in the same melt pool was observed for all the measured melt pool fabricated by CET promoting P-V sets.

## 6.3 P-V process optimization for LPBF of tool steel

### 6.3.1 H13 steel: P-V process optimization for cracking

- **Multi-track observation**

Chapter 6.2.2 shows microstructure inhomogeneity in H13 steel single-track melt pool for a fraction of P-V sets investigated in this study. On this basis, a sequential study was performed to fabricate

single-track, multi-track and 3D cube with H13 steel. The results are presented below, focusing on the trend among P-V parameter, microstructure inhomogeneity and cracking tendency observed from pad and cube characterization:

A microstructure P-V process map (Fig 37) was presented earlier in chapter 6.2.2, which shows the P-V windows leading to high-level and low-level microstructure inhomogeneity for H13-steel single-track. Under the guidance of the single-track microstructure P-V process map, eighteen P-V process combinations (marked by “P” in Table 7) were selected for multi-track pad fabrication, with 4 or 5 P-V sets belonging to each microstructure category. Multi-track melt pools showed microstructure inhomogeneities similar to that of single-track melt pools described in chapter 6.2.1. Two typical examples were shown in Fig 50 for P-V set #20 and P-V set #4. Their corresponding single-track melt pool microstructures were shown in Fig 36(a) and (c). Similar to single-tracks, multi-track pads exhibited both cellular-network microstructure and isolated-needle microstructure (i.e., type (A) and (B) microstructure) in the same melt pool, as distinguished by bright-contrast and dark-contrast in the multi-track melt pool cross section. Fig 50 shows that the vol% of type (A) and (B) microstructure in the multi-track melt pool cross section varies with P-V sets. Further characterization shows that for the 18 P-V sets of selection, the multi-track melt pools for all could be classified into the same microstructure category as the single-track melt pools generated by the same P-V set, indicating good consistency between the single-track and multi-track melt pool microstructure.

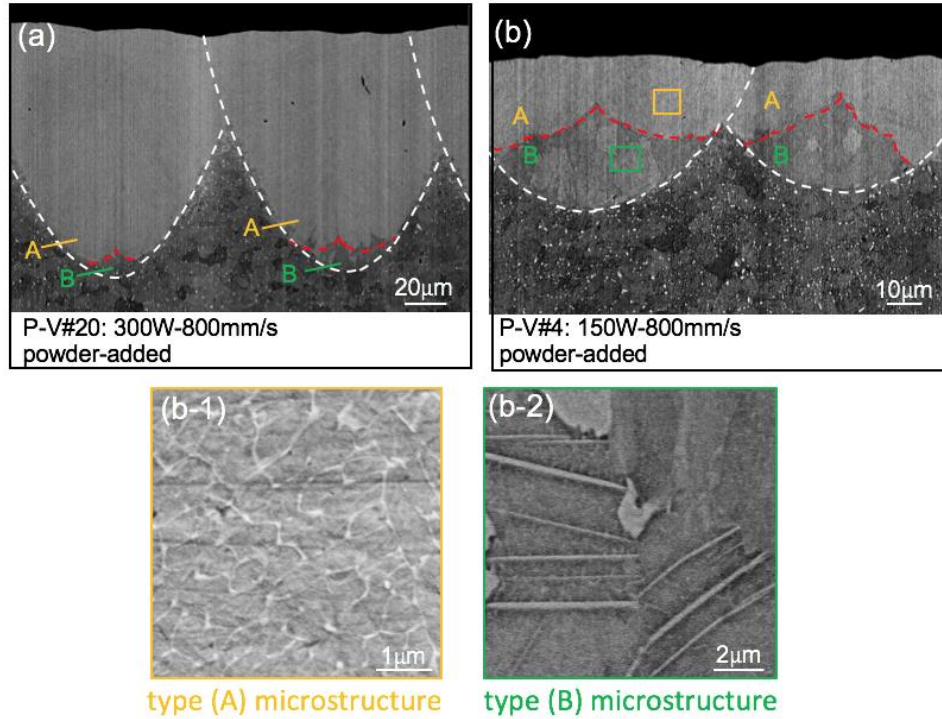


Fig 50 typical multi-track melt pool microstructure for P-V set of “large-A” type (a) and “small- A” type (b) in microstructure P-V map (Fig 37); exemplified by P-V #20 [300W-800mm/s] and P-V #4 [150W-800mm/s] (Fig 36(a), (c): corresponding single-track melt pool microstructure at same P-V set); microstructure inhomogeneity similar to single-track (Fig 30) was observed: each multi-track melt pool (melt pool boundary: marked by white dashed line) presented two types of microstructures, referred to type (A) and (B) microstructure, shown in (b-1) and (b-2) (zoom-in images of yellow and green box in (b)); in (a),(b): red dashed lines indicate the loop-shape boundary separating region with type (A) and (B) microstructure in each melt pool, distinguished by bright and dark contrast and denoted by letter “A” and “B”.

Cracks were found for the pads with melt pool microstructure belonging to “small-A microstructure” and “varied microstructure” categories, while no cracks were observed in the other. A typical cracking observation for the “small-A” microstructure is shown in Fig 51. Rather than propagating across adjacent melt pools, each crack appeared to be restricted to one melt pool, propagating in the region with type (B) microstructure, while the top of the melt pool with type (A) microstructure was crack-free.

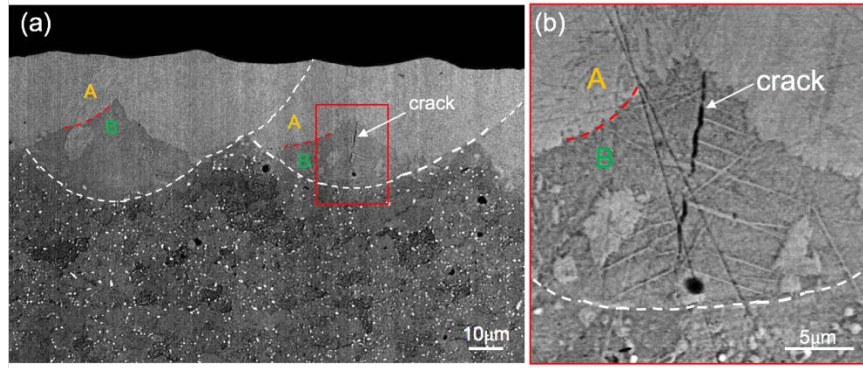


Fig 51 Typical cracking observation for H13 multi-track pad with “small-A” type microstructure; (b): zoom-in image of red box in (a); crack: indicated by white arrows; white dashed lines: melt pool boundary; a loop-shape boundary (partially marked by red-dashed line) separates local region with type (A) microstructure (bright contrast, indicated by “A”) and region with type (B) microstructure (dark contrast, indicated by “B”) in melt pool; (type (A) and (B) microstructure, see Fig 30(b-1) and (b-2));

### • 3D cube observation

The multi-track pad results indicated that more cracking would be observed if melt pool microstructures were of the type “small-A” and “varied microstructure”. Less cracking would be expected if melt pools were of the type “medium-A” and “large-A” microstructure. To test this, eight P-V sets (marked by “c” in Table 7) were selected and 3D cubes were built. A typical cube microstructure was presented in Fig 52(a) for P-V set #4, with the corresponding single-track and multi-track microstructure fabricated by the same P-V set shown in Fig 36(b) and Fig 50(c). The microstructure inhomogeneity was again evident with cellular-network and needle-like morphologies. They were denoted as type (A’) and (B’) microstructure.

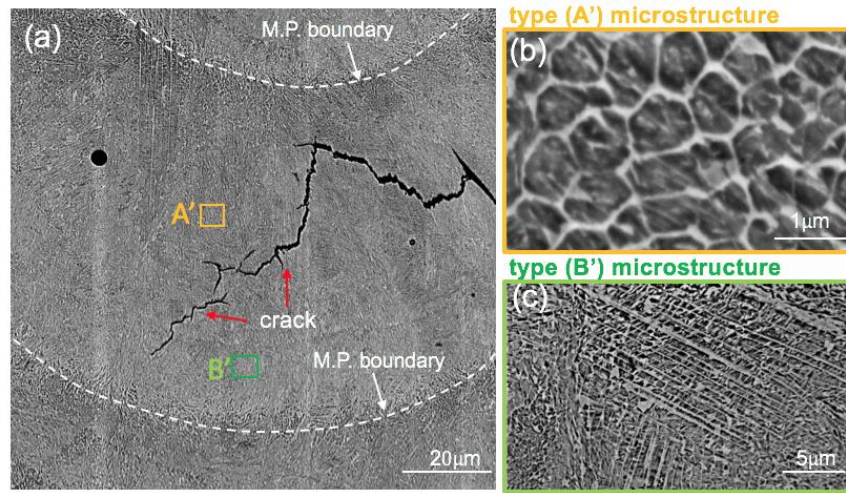


Fig 52 typical microstructure for H-13 cube with severe cracking (example provided by P-V#4); in (a): white dashed line: melt pool boundary (denoted as “M.P. boundary”) and red arrow: cracks; two microstructures observed in one melt pool: referred to as type (A’) and (B’), shown in (b) and (c) respectively; (b), (c): zone in image of yellow and green box in (a)

It should be noted that type (A’) and (B’) microstructure in the cube were not exactly the same as the type (A) and (B) microstructures found in single-tracks and pads. XRD analysis showed that for all eight P-V sets selected in this study, the H13 cubes showed much higher retained austenite levels compared to the pads generated at the same P-V set. A typical example is shown in

Fig 53 for P-V set #20[300W-800mm/s], which showed an increase in  $\gamma\%$  by 13% from pad to cube.

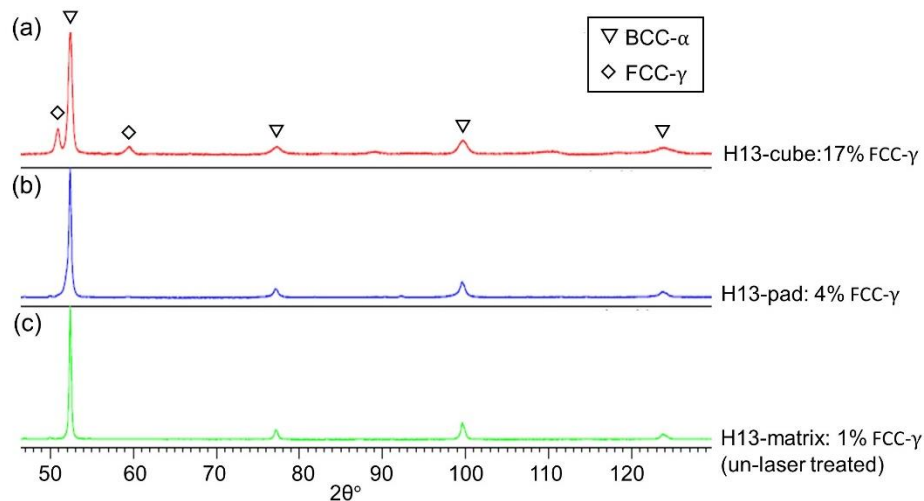


Fig 53 XRD pattern for H13 steel cube (a) and pad (b) processed by same P-V set (example provided by P-V set#20 [300W-800mm/s] compared to un-laser treated H13 steel matrix (c); microstructure: see Fig 51(a)); austenite vol.% for (a)-(c): listed on the right

The measured crack density observed on the cube cross-sections was presented in Fig 54. The P-V sets of “small-A” and “varied microstructure” categories resulted in higher crack densities than P-V sets of “medium-A” and “large-A” microstructure categories: the former not only showed much higher crack density than the latter (at least twice higher) but also presented higher variation in crack density, as indicated by their large error bar in Fig 54. The crack density measurement shows that the P-V sets predicted with higher crack tendency led to a noticeably higher value in crack density in the H13-cube than the P-V sets predicted with lower crack tendency, showing good agreement between the cracking prediction and the experimental measurement. Typical cracks for two different microstructure categories were compared in Fig 55(a) and (b): in Fig 55 (a) a single deep crack was found near the middle of the build and in Fig 55(b) shallow cracks were observed at several locations through the build direction.

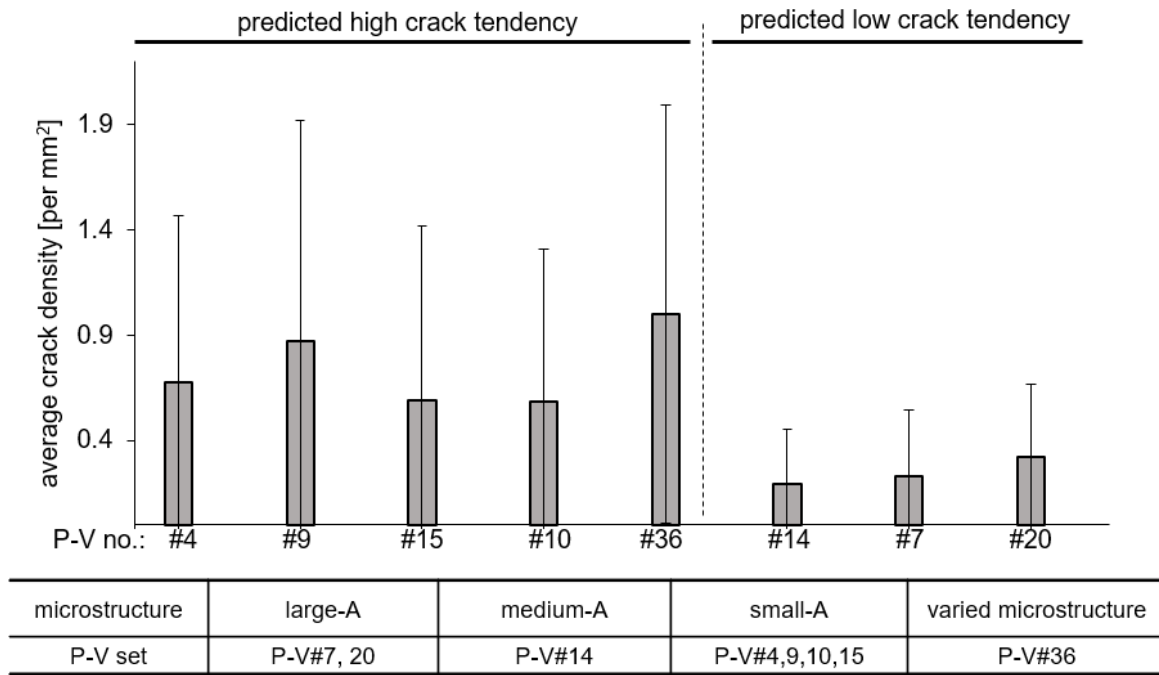


Fig 54 crack density measurement for H-13 steel cubes built by 8 P-V sets selected in this study (marked by “c” in Table 7), with their corresponding melt pool microstructure category summarized in the table below the figure; average crack density: measured from 120 sections (1mm<sup>2</sup>) per cube

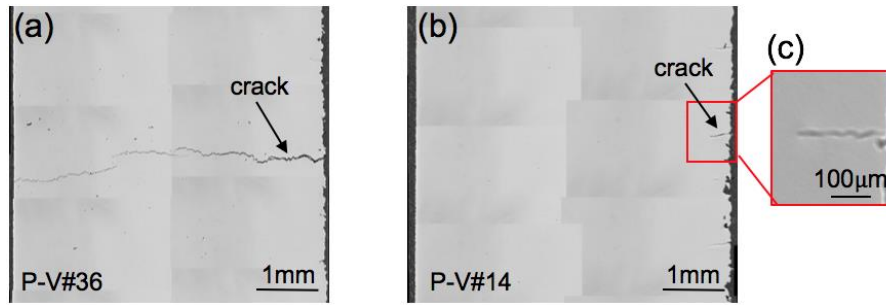


Fig 55 typical H-13 steel cube crack observation for P-V sets of “small-A” and “varied microstructure” categories (a) and P-V sets of “medium-A” and “large-A” microstructure categories (b), examples provided by cube of P-V # 36 and #14; (c): zoom-in image of the red box in (b); microstructure category: see chapter 6.2.2 and Fig 36

The pad and cube results both indicate that in the microstructure P-V process map in Fig 37, the P-V windows of “large-A” and “medium-A” microstructure categories led to low cracking density. For these P-V sets, only small cracks at the near-surface region of the cube were observed, which could potentially be removed by post HIP processing based on the research of Wang et al.[68,162]. However, the P-V window of “large-A” and “varied microstructure” categories led to much higher cracking density. Possible reasons for the differences in cracking tendency for H13 steel cubes built by P-V windows of different microstructure categories are discussed below.

According to Thermal Gradient Mechanism (TGM) from Mercelis and Kruth (2006), thermal contraction occurs during melt pool cooling, leading to shrinkage for the melt pool material that is restricted by the surrounding cold matrix material. Tensile stress accumulates along build direction for the melt pool material, which could cause fracture. Fig 48 showed much higher hardness for type (A) or (A') than that of type (B) or (B') microstructure in the same melt pool. As exemplified by the pad microstructure in Fig 50, in each melt pool, the near-top region was dominated by higher-hardness type (A) microstructure and the near-bottom region was dominated by lower-hardness type (B) microstructure. Thus, within one melt pool, the near-top and near-bottom region with two different microstructure exhibited different responses to the residual stress during H13 steel pad and cube fabrication, with cracks appearing to initiate at the boundary between the regions and propagating through the type (B) or (B') region (Fig 51 and Fig 52). This could also be observed from the longitudinal microstructure as shown earlier in Fig 31. For type(A) and (B) microstructure, their difference in phase constituent, phase continuity (network vs. needle) and phase distribution might

all play a role in their hardness difference; identifying the dominant factor requires further investigation.

Second, pad characterization provides reliable estimation for the as-deposited layer during LPBF part build. Therefore, for P-V sets of “large-A” and “small-A” microstructure categories, the as-deposited layer microstructure during H13 steel cube build might be estimated by the corresponding pad microstructure as shown in Fig 50(a) and (b) respectively. From the as-deposited layer (Fig 50) to the final-built cube microstructure (Fig 52), the major difference lies in the influence of successive layer deposition, which was commonly known to have a tempering effect on the previously-deposited layer. This tempering effect was supported by the increase in austenite% from pad to cube at the same P-V set as shown in

Fig 53. Thus, for P-V sets of “small-A” and “large-A” microstructure, their corresponding cube final microstructure might be comparable to the case of tempering with two significantly different starting microstructure in Fig 50(a) and (b), and thus lead to different cracking tendency. Studies by Krell et al [52] and Mercelis and Kruth (2006) suggested that the influence of successive layer deposition on H13 part cracking tendency mainly relies on the residual stress distribution during LPBF part build, rather than microstructure evolution. This study suggests that the part microstructure and the changes due to successive layer depositions are important considerations for cracking resistance.

### **6.3.2 M2 steel: P-V process optimization for promoting CET**

In chapter 6.2.4, we developed the G-R thermal criteria for CET occurrence to predict the microstructure morphology (equiaxed or columnar) for M2 steel under LPBF solidification condition. By combining the developed G-R criteria with the simulation work for melt pool solidification thermal profile, we calculated a P-V process map (Fig 38(b)) for LPBF solidification microstructure of M2 steel, which could guide P-V process optimization to promote CET of LPBF-processed M2 steel. The calculated microstructure process map was consistent with the experimental process map (Fig 38(a)) in most P-V space, except when balling occurred. Therefore, this chapter focus on the discussion regarding the application range of the calculation approach in chapter 6.2.4 for LPBF P-V process optimization. Promising P-V space and the limitation of P-V optimization for promoting equiaxed growth of LPBF-processing with M2 steel will also be discussed.

In the non-balling P-V space, the predicted and experimental microstructure process map in Fig 38 both show a general trend that P-V parameter combining high P/V ratio and high scan speed lead to

high fraction of equiaxed microstructure in melt pool, which suggests the potential for LPBF process to build M2-steel part with fully equiaxed microstructure at such P-V process condition. Such trend might be a combined result of a lower magnitude of temperature gradient as P/V ratio increases and a higher solidification velocity as V increases. This was exemplified by Fig 45, which shows the comparison of G-R evolution along melt pool centerline for three representative P-V sets (P-V #3, #9 and #13), as discussed earlier in chapter 6.2.4. This trend is also experimentally validated for EBM-AM fabricated IN718 alloy[27] and LENS-AM fabricated Ti6Al4V alloy [23]. In Fig 45, it should also be noted that for all three cases, solidification velocity is approaching zero as the depth reaches melt pool bottom, suggesting that solidification condition near melt pool bottom favors the existence of columnar microstructure for all three P-V sets. Thus, in this study, even for P-V space with both high P/V ratio and large V value, which is predicted as CET promoting group, the resulting melt pool still presents a mixed columnar+equiaxed microstructure rather than a fully equiaxed microstructure, since the near-bottom region shows the thermal condition that favors columnar dendrite growth. This could be exemplified by both prediction results and experiment observation for the melt pool of P-V#13, as shown in Fig 47(a-1) and (a-2). Therefore, this study indicates that P-V process optimization could effectively promote equiaxed microstructure in LPBF melt pool due to its capability to alter the G- and R-profile for melt pool solidification. The P-V space for promoting equiaxed growth was identified as P-V space with both high P/V and high V value, or more specifically, P-V parameters from CET promoting group as shown in the microstructure process map (Fig 38). They were shown theoretically and experimentally to result in melt pool microstructure with more than 50 vol.% equiaxed dendrite. On the other hand, the result also suggests that it is challenging to rely solely on P-V process optimization to reach high-vol.% equiaxed microstructure as the low solidification velocity at the bottom of the melt pool almost inevitably leads to columnar-microstructure growth. This limit of P-V process optimization might be amended by composition modification to introduce nucleant particles. The effectiveness of nucleant particle addition on promoting equiaxed growth in AM solidification is shown by the work of Bermingham et al[76], who effectively enhanced the vol.% of equiaxed microstructure in WAAM-fabricated part by adding a small amount of  $\text{La}_2\text{O}_3$  particles in Ti-3Al-8V-6Cr-4Mo-4Zr material. This suggests the promising potential to fabricate LPBF-part of fully equiaxed microstructure for M2 steel by adopting optimized P-V process parameters identified in this study combined with the approach of introducing trace amount of nucleant particles in steel substrate. This might be considered for future work.

Compared to the non-balling P-V space, the balling P-V space presents a more complicated

relationship between the CET tendency and P-V parameter. As mentioned earlier, discrepancies exist between the predicted and experimental microstructure process map for some P-V sets in the balling P-V space: the predicted process map in Fig 38(b) presents higher CET tendency for P-V region with higher P/V ratio and higher V value for the non-balling P-V space, consistent with the trend observed in the balling P-V space as described above; however, such trend is not observed in the balling P-V space of experimental process map (Fig 38(a)). In fact, the P-V parameters of similar CET tendency, i.e., the P-V parameters in the same microstructure group, were randomly scattered in the balling P-V space of experimental process map, and thus trend between CET tendency and P-V parameter could not be distinguished. The reason for such discrepancy between the prediction and experimental result in balling P-V space might be twofold:

First, the occurrence of balling phenomena indicates the existence of Marangoni convection in the melt pool, accompanied with which is intense fluid flow during melt pool solidification[164][45]. The strong fluid flow induced by Marangoni convection is beneficial for equiaxed grain nucleation since it promotes dendrite fragmentation and dendrite arm transportation, which could both act as nucleation sites for equiaxed grains. In this study, the G-R criterion for determining the CET tendency of each P-V parameter was developed on the basis of the CET model from Gäumann et al. (Equation 14) [12]. As shown in Equation 14, an important factor for CET tendency is the nuclei density ( $N_0$ ), which is determined by fitting with the experimental result of P-V#9 in this study as shown earlier in chapter 6.2.4. It should be noted that the melt pool of P-V#14 does not show evidence of balling occurrence. In this case, the estimated value for  $N_0$  might underestimate the actual nuclei density for the balling melt pool with the reason above. This inaccuracy in  $N_0$  estimation could in turn lead to inconsistency between the predicted and experimental microstructure map in the balling P-V space, as shown by the “error prediction” in Fig 38(b). The inaccurate estimation for  $N_0$  is also suggested by the observation as mentioned earlier in chapter 6.2.4, that for the predicted microstructure process map in Fig 38(b), the error predictions for the balling P-V space always underestimated the actual CET tendency as observed in the experimental process map. Due to this reason, the G-R criteria developed in this work is considered to be valid only within the non-balling P-V space for LPBF-M2 steel microstructure prediction.

Second, the heat transfer model adopted in this study makes a simple assumption of no convection in the liquid to decrease the computation complexity. However, such simplification might not be acceptable for melt pools with balling behavior. The presence of balling indicates intense and unstable melt pool fluid flow as a result of Rayleigh instability[46], which was likely to significantly influence

temperature gradient and solidification velocity by liquid convection. This contradicts the no-convection assumption adopted in the current model, and further suggests that the calculated G- and R- profiles for balling melt pool could deviate from the actual ones and in turn contributes to the inaccurate microstructure prediction in the balling P-V space.

Above discussion on the reliability of the G-R criterion and accuracy of melt pool thermal profile calculation shows that for the CET microstructure prediction approach presented in chapter 6.2.4, its application range is suggested to be within the non-balling P-V space for LPBF of M2 steel. This application range should be emphasized for future studies with the intention to adopt a similar approach to predict LPBF microstructure (equiaxed or columnar) for other alloy systems. While this limited application range might not cause practical problem for LPBF part build investigation, since the balling P-V space is usually not considered for LPBF part build due to the deleterious influence of balling on LPBF part quality as previously summarized in chapter 2.1.3 in Introduction.

Besides the vol.% of equiaxed microstructure in the melt pool, local distribution of equiaxed microstructure could also be obtained by the calculation approach in chapter 6.2.4. The accuracy of the prediction was supported by the consistency between the experimental-observed and calculated melt pool microstructure as shown in Fig 47. Chapter 6.2.5 shows that the region with equiaxed microstructure coincides with the region of low hardness in the melt pool. Thus, the calculated result for equiaxed microstructure distribution might be a useful indicator for LPBF part property homogeneity prediction. Although it is not the focus of current study, it might be interesting for future study to investigate the relation between the microstructure inhomogeneity and hardness inhomogeneity for LPBF of M2 steel as observed in this study, which might require a comprehensive characterization to capture more local microstructure information, including information regarding local phase constituent, carbide precipitate and dislocation.

## 6.4 Results Summary

This chapter investigated LPBF processing with two tool steel grades: H13 and M2 steel, focusing on finding the promising LPBF process window by studying the correlation among P-V parameter, melt pool microstructure inhomogeneity and property (hardness, cracking). The influence of powder layer presence on melt pool geometry and microstructure was also investigated. Conclusions obtained in this chapter were summarized below:

### **H13 steel**

1) P-V process maps of melt pool geometry were developed for both no-powder and powder-added laser scan with H13-steel. They showed great consistency to each other except a slight shift in balling P-V threshold, suggesting the influence of powder addition on balling formation.

2) Single-track and multi-track pads show microstructure inhomogeneity at some P-V combinations, exhibiting cellular-network microstructure and isolated-needle microstructure at top and bottom regions of one melt pool (referred to as type (A) and (B) microstructure in this document). C, Cr, V, Mo solute pile-up was found at the cellular boundary of type (A) microstructure, where retained austenite was present. Type (A) microstructure presented higher hardness than the nearby type (B) microstructure within the same melt pool.

3) Melt pool microstructure of the 40 tested P-V sets were classified into four categories, based on different inhomogeneity level. Based on this categorization, microstructure P-V process maps were developed for both no-powder and powder-added laser scan, showing great consistency to each other at most of the P-V space.

4) A microstructure evolution mechanism was proposed for the non-equilibrium solidification in LPBF melt pool of H13 steel. The mechanism explains the presence of retained austenite in type (A) microstructure of melt pool as a result of solidification microsegregation, which stabilizes the last-solidified austenite by lower its  $M_s$  temperature due to solute pile-up. This was supported by the experimental observation of solute segregation at the cellular boundary in type (A) microstructure,

where austenite is present. The mechanism explains the microstructure inhomogeneity in H13 steel melt pool as a result of varied microsegregation levels at local regions with different microstructure in the melt pool. This shows consistency with microsegregation estimation through coupling DICTRA simulation and melt pool thermal profile numerical calculation, showing the region with type (A) and (B) microstructure presenting noticeable and minimal segregation. Based on the calculated microsegregation result, prediction was made to estimate the vol% and distribution of type (A) and (B) microstructure in the melt pool. The prediction showed good agreement to the experimental observation of melt pool microstructure. This study shows the effectiveness of combining DICTRA and melt pool thermal calculation to predict LPBF solidification microstructure.

5) Pad characterization showed that melt pool with different microstructure inhomogeneity levels resulted in different cracking susceptibility, and their corresponding P-V space in the microstructure P-V process map was estimated as P-V window with higher and lower cracking tendency. Crack density was measured for cube built by P-V sets with different cracking tendency prediction. The result showed good agreement with the prediction.

## **M2 steel**

1) Single-track melt pools of M2 steel with fully columnar dendritic, columnar+equiaxed mixed and mainly equiaxed dendritic microstructure were observed for the 28 P-V sets selected in this study. A microstructure P-V process map was constructed to summarize single-track characterization. It shows a trend of higher vol.% of equiaxed dendrite in the melt pool by increasing laser power and scan velocity.

2) G-R criterion model was developed to determine CET occurrence for M2 steel LPBF solidification based on the analytical CET model from Gäumann et al. It predicts the thermal condition favoring equiaxed dendrite growth as  $\frac{G^{3.8}}{R} < 7.8 \times 10^{13}$ .

3) Vol.% and distribution of equiaxed dendritic microstructure in LPBF melt pool of M2 steel could be predicted by coupling the developed G-R criteria with numerical calculation for melt pool

solidification thermal profile. Based on this approach, a microstructure process map was calculated for LPBF of M2 steel to estimate the variation of CET tendency across P-V space. It indicates the P-V window favoring equiaxed dendrite growth as P-V space with both high P/V ratio and large V value.

4) The application range of adopting the developed G-R criteria to estimate CET in LPBF solidification is identified as P-V space with no balling phenomena, as confirmed by the good consistency between the experimental and predicted process map in this P-V space. Discrepancy between microstructure prediction and the experimental result was found in balling P-V space, which could arise from underestimating the nuclei density for melt pool with balling formation.

5) It is shown by both experimental results and numerical calculation that vol.% of equiaxed dendritic microstructure in LPBF melt pool of M2 steel could be remarkably enhanced from <5% (i.e., fully columnar) to about 50% by choosing different P-V parameters. Numerical calculation shows that the effectiveness of P-V process optimization on promoting equiaxed growth for LPBF microstructure lies in its capability to alter G-profile and R-profile for LPBF melt pool solidification. By coupling the developed G-R criteria and the calculated melt pool thermal profile, P-V window for promoting equiaxed grain growth was identified, which lies in the region with both high P/V ratio and high scan velocity. Same calculation approach could be adopted to estimate P-V map for LPBF solidification microstructure (columnar/equiaxed) with other alloys of interest. This could be helpful for understanding and designing LPBF part microstructure.

## 7 LPBF of Ti6Al4V-xB: composition evaluation

Chapter.5, chapter 6.1.2 and chapter 6.2.2 suggested the applicability of the powder-free method for LPBF investigation by confirming its assumption that melt pools deposited directly on bulk alloy could provide a reasonable dimensional, geometrical and microstructural approximation for melt pools generated on bulk alloy with a powder layer. In this chapter, the powder-free method was adopted for LPBF material candidate selection, with Ti6Al4V-xB as material system of interest. 4 candidate composition, Ti6Al4V-1%,2%,5%10%B (wt.%) was evaluated. The workflow of the powder-free method was introduced earlier for LPBF of H13 steel and is thus not repeatedly present here. This chapter focusses on presenting the final synthesized melt pool information and how to use them to identify the promising Ti6Al4V-xB composition suitable for LPBF processing route. The application range for adopting the powder-free method to LPBF alloy development will be introduced. Experimental results suggested that varying B% and P-V parameter led to solidification mode transition for the Ti6Al4V-xB melt pool. Based on this, an analytical equation model was presented in chapter 7.7, which integrated the influence of P-V parameter and material properties on Ti6Al4V-xB LPBF solidification microstructure. This model indicated the P-V window leading to coupled-eutectic solidification and non-equilibrium primary- $\beta$  solidification mode even for highly hyper-eutectic Ti6Al4V-5%B.

### 7.1 Assessment of test material (arc-melted Ti6Al4V-xB buttons)

This work used arc-melted Ti6Al4V-xB buttons as test material for LPBF laser scan experiment. Example microstructures from the arc melted Ti6Al4V-xB buttons are shown in Fig 56. The  $\text{TiB}_w$  precipitates ( $\text{TiB}_w$ : TiB,  $\text{TiB}_2$  or  $\text{Ti}_3\text{B}_4$ ) exhibited 2 morphologies: high-aspect-ratio whiskers and highly-faceted rods with hollow centers filled with Ti-matrix or a different  $\text{TiB}_w$  precipitate. XRD analysis confirmed that only TiB is present for the alloys with wt% B  $\leq 5\%$ . In the Ti6Al4V-10wt%B material, XRD detected TiB,  $\text{TiB}_2$  and  $\text{Ti}_3\text{B}_4$ . This result was in line with the prediction from the pseudo-binary Ti6Al4V-xB phase diagram (Fig 14).

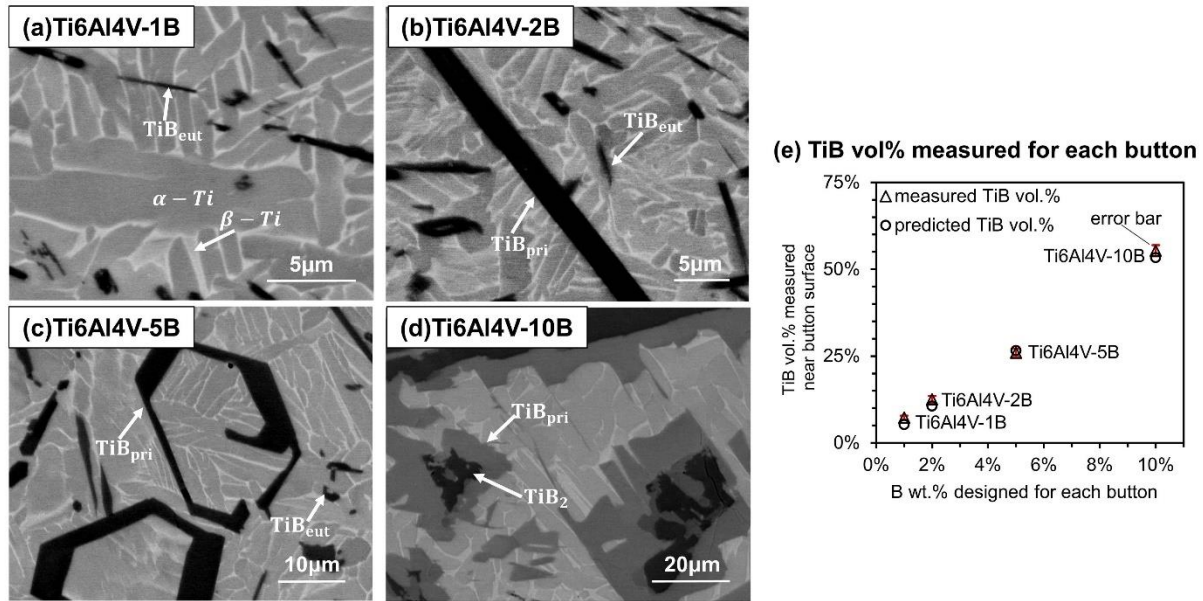


Fig 56 SEM images (BSE mode) of arc-melted microstructure for Ti6Al4V-xB alloy buttons of 4 trial compositions: Ti6Al4V-1B, 2B, 5B, 10B, shown in (a), (b), (c), (d) respectively; TiB<sub>eut</sub>—eutectic TiB; TiB<sub>pri</sub>—primary TiB; (e): measured TiB vol.% in laser-scanned region by SEM image process vs. predicted TiB vol.% for alloy buttons with different trial compositions; error bar (standard deviation) indicated by red label

To ensure consistency, the region that was going to be laser-scanned was examined. This region was defined from the button surface to 50 °C isotherm boundary during laser scan predicted by the Rosenthal model (approximately 1000  $\mu$ m from button surface). For each button, seven to ten images were taken at different locations from this region and then processed by ImageJ software [128] to quantify the local area fraction of TiB precipitate, which was assumed equal to the vol% of TiB precipitate. A similar method was adopted in the study of Galvan et al[165] and the study of Boehlert et al[106]. The result was shown in Fig 56(e). The small error bar (standard deviation) in Fig 56(e) indicated the small variation in vol.% of TiB at different locations of this region, showing that TiB precipitates were uniformly distributed across the whole button surface. Fig 56 (e) also shows that the average measured TiB vol.% in this to-be-scanned region in each button was in line with the corresponding vol.% TiB predicted by Thermo-Calc software [35] for all four B-containing trial compositions. Noted that the TiB<sub>w</sub> precipitate in the Ti6Al4V-10%B button, although uniformly distributed in the laser-scan related region, showed a typical length scale of 10~50  $\mu$ m for its primary TiB precipitate, as qualitatively shown in Fig 56 (d). This dimension was comparable to the dimension of laser focused diameter (~100  $\mu$ m for EOSM290), which was found to cause some potential

problems regarding the validity of the powder-free method. This will be further discussed in chapter 7.8.

## 7.2 Melt pool dimensions

Fig 57 shows the comparison of single-track melt pool width measurement for each trial Ti6Al4V-xB compositions. The melt pool widths were average values measured from the melt pool cross sections at three locations along each laser track. The laser absorptivity developed for bulk Ti6Al4V alloy (Equation 10) was adopted for the four Ti6Al4V-xB trial compositions to calculate Q in Fig 57. From suggestion by chapter 5, dimensions for melt pools with keyholing geometry features were not included in Fig 57.

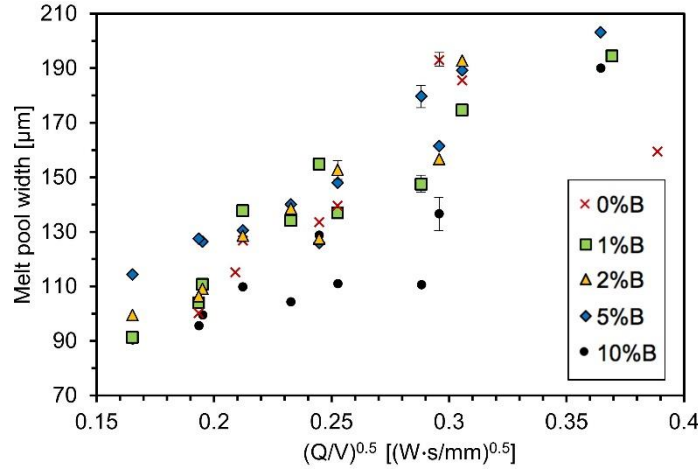


Fig 57 Comparison of single-bead melt pool width for different Ti6Al4V-xB trial compositions (Q: absorbed laser power; V: laser scan speed); melt pool width for each P-V sets; error bars were added to one of the data points for each trial Ti6Al4V-xB composition, representing the average standard deviation for 3 melt pool cross sections of each Ti6Al4V-xB trial compositions

Fig 57 showed an approximately linear relationship between  $(Q/V)^{0.5}$  and melt pool width for all five trial compositions. For the same Q-V combination, increasing B addition up to 5 wt.% did not lead to evident melt pool dimension variation compared to that of Ti6Al4V. However, a significant decrease in melt pool width was observed at 10 wt% B. Since the melt pool dimension is essentially determined by Q and V, the small melt pool dimension variation indicated that B addition up to 5 wt.% might not influence laser absorptivity and that the absorptivity model in Equation 10 obtained for Ti6Al4V might reasonably estimate Ti6Al4V-xB with  $B\% \leq 5\text{wt.}\%$ . Larger B additions at the level of 10 wt.%B

appeared to decrease absorptivity. The potential problem of this evident melt pool dimension deviation between Ti6Al4V and Ti6Al4V-10B is further discussed in chapter 7.6.

## 7.3 Melt pool geometry

### 7.3.1 P-V mapping for melt pool geometry

Following the same approach for developing melt pool geometry P-V mapping for H13 steel as shown in chapter 6.1, melt pool geometry P-V mappings were developed for each trial Ti6Al4V-xB composition as well as B-free Ti6Al4V base material, as listed in Fig 58. Noted that the under-melt criteria for Ti6Al4V-xB is  $D < 20\mu\text{m}$ . This is different from that of tool steel (see chapter 6.1.1) since the EOS machine default part build design for steel[7] and Titanium[5] adopt different layer thickness. Fig 58 specifically marked the P-V data points by “defect” label when the resulting melt pools were observed with evident porosity and cracks. An example of melt pool with defect was shown in Fig 59(c).

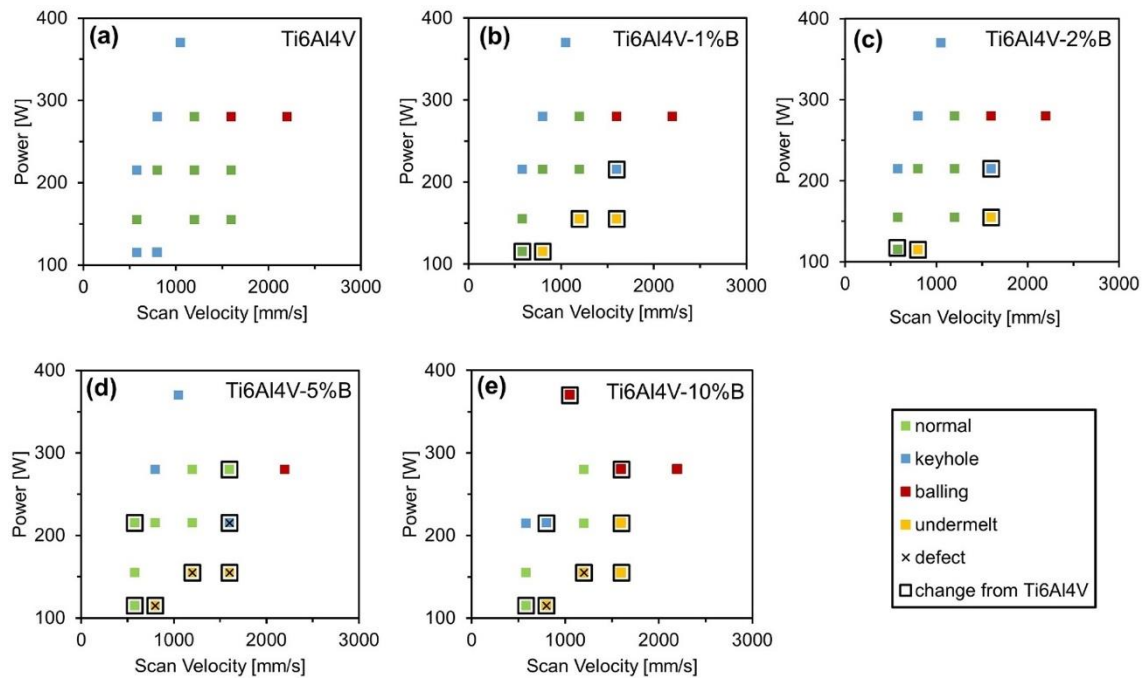


Fig 58 Melt pool geometry P-V mapping for B-free Ti6Al4V ((a)) and four Ti6Al4V-xB compositions (1%, 2%, 5%, 10%B: (b), (c), (d), (e))

Fig 58 also marks the P-V data points if their corresponding melt pool show geometrical change from the B-free Ti6Al4V melt pool generated by same P-V sets, an example of which is presented in Fig 59 for P-V set #9 (115W-800mm/s) tested with Ti6Al4V, Ti6Al4V-1%B and Ti6Al4V-10%B. From

Fig 59, it could be seen that at P-V set #9, as B% increases from 0wt.% to 1wt.% and 10 wt.%, melt pool changed from key-holing (Fig 59 (a)) to under-melt geometry (Fig 59 (b)) and under-melt pool geometry with evident defect (Fig 59 (c)).

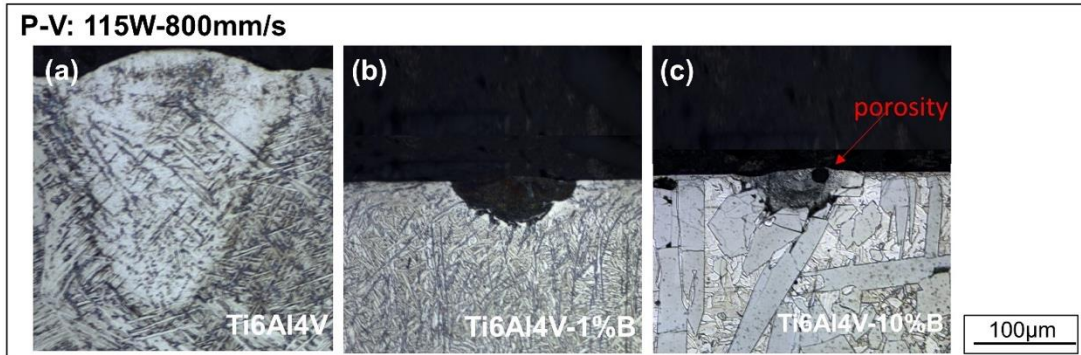


Fig 59 example showing change in melt pool geometry by different B addition with same P-V set (example shown for P-V set#9: 115W-800mm/s); (a): Ti6Al4V; (b): Ti6Al4V-1%B; (c): Ti6Al4V-10%B

From Fig 59, it could be seen clearly that B addition had significant and complicated influences on melt pool geometry. For 1 and 2 wt% B, only melt pool geometry in the low-power P-V space was altered from that of Ti6Al4V, while for 5 and 10 wt% B, the altered melt pool geometry extended to higher power regions. Keyholing was observed at high P, low V range, as expected [26]. However, evidence of keyholing was also observed in Ti6Al4V at a relatively low power range ( $P = 115$  W). This observation was in accordance to recent studies using dynamic x-ray radiography [39] showing deep and narrow vapor depressions can form at low power and result in keyholing. When B was present, the lower power observations of keyholing were shifted to 200 W. Chen et al [166] and Shigeta et al [167] showed that TiB-contained titanium alloy showed a different vaporization pressure than the TiB-free titanium alloy mainly because B has a much higher boiling point than that of Ti (boiling point:  $T_b^B = 4349$  K,  $T_b^{Ti} = 3591$  K). This indicates that the difference in keyholing P-V space for Ti6Al4V and Ti6Al4V-xB alloys observed in this study could be attributed to differences in vaporization behavior between the un-modified Ti6Al4V and the B-containing alloys.

### 7.3.2 P-V window for porosity control

In chapter 6.1, an approach was presented which estimated the P-V window for porosity control by the P-V space with normal melt pool geometry in the P-V mapping, which was identified by deriving Q-V thresholds for keyholing-, balling-, undermelt-geometries through model fitting with data points

in P-V mapping of melt pool geometry. The model was presented earlier in Table 12 and the workflow for data fitting was presented in chapter 6.1. Following the same approach, Q-V thresholds for keyholing-, balling-, undermelt-geometries were derived for each Ti6Al4V-xB as listed in Table 16.

Table 16 fitting model for the Q-V thresholds of different melt pool geometry for Ti6Al4V-1,2,5%B

Melt pool geometry	Q-V threshold: Fitting model	Model parameter: definition	Model parameter: fitted value
Key-holing Ref: [47]	$\frac{Q}{\sqrt{V}} \geq m_1$	$m_1 = \frac{kT_b d^3 \sqrt{\pi^3}}{\sqrt{D_1}}$	Ti6Al4V-1%, 2% B: $m_1=3.0$ Ti6Al4V-5%B: $m_1=3.2$ Ti6Al4V-10%B: $m_1=2.8$
Balling Ref: [141]	$QV > m_2$	$m_2 = \frac{3\pi^3 k \alpha (T_f - T_0)}{4e}$	Ti6Al4V-1%,2% B: $m_2=125600$ Ti6Al4V-5%B: $m_2=185154$ Ti6Al4V-10%B: $m_2=171602$
Under-melt Ref: [22]	$\frac{Q}{V} < m_3$	$m_3 = \frac{e\pi\rho C(T_f - T_0)d^2}{2}$	Ti6Al4V-1%B: $m_3=0.043$ Ti6Al4V-2%B: $m_3=0.031$ Ti6Al4V-5%B: $m_3=0.038$ Ti6Al4V-10%B: $m_3=0.053$

Where  $D_1$  is thermal diffusivity of molten material,  $d$  is layer thickness,  $T_b$  is boiling temperature,  $T_f$  is melting point of the alloy.

The calculated melt pool geometry Q-V thresholds (Table 16) was exemplified in Fig 60, with Ti6Al4V-1wt.%B as an example. Fig 60(a) shows experimental results for the 1 wt% B case. The P values could be converted to Q values using the absorptivity model in Equation 10. This enabled the experimental results to be compared to the boundaries calculated from Table 16, as shown in Fig 60(b). Good agreement was obtained for the region where a normal melt pool geometry would be expected, as indicated by the shadow area in Fig 60(b). It should be noted that this analysis was not applicable to Ti6Al4V-10 wt% B due to the likely differences of its absorptivity to that in Equation 10, as explained earlier in chapter 7.2.

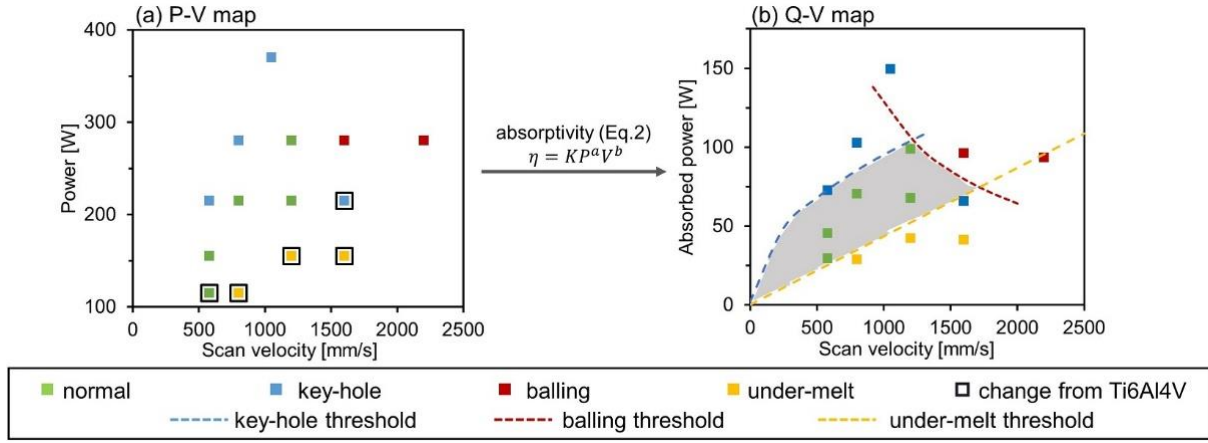


Fig 60 Workflow for generating preliminary process window for porosity control (shadow area in (b), i.e., area enclosed by dashed lines) for Ti6Al4V-xB using the melt pool geometry P-V map (example shown for Ti6Al4V-1%B)

## 7.4 Melt pool microstructure

### 7.4.1 Single-track: Microstructure P-V mapping

In this work, single-tracks were fabricated by 14 different P-V sets on 4 Ti6Al4V-x%B materials ( $x=1,2,5,10$ ), generating 56 B-modified melt pools with different [B%, P-V] combinations. Five distinct melt pool microstructures (referred to as type (i)-(v)) were distinguished for the 56 [B%, P-V] combinations. Their typical SEM images were presented in Fig 61. The TiB precipitates identified in type (i)-(v) microstructure was qualitatively confirmed to contain Ti and B by EDS measurements. These five different melt pool microstructures are likely to be the product of different solidification modes for each Ti6Al4V-xB material as summarized in Table 17, with the reasons shown further in chapter 7.7.2. Their major microstructure features were also compared below and summarized in Table 17. The presented microstructure features were summarized over melt pool cross-sections taken from three locations for each laser track.

- B-free Ti6Al4V: Baseline microstructure

Baseline microstructure in this study was referred to as the melt pool microstructure created on B-free Ti6Al4V arc-melted button. For all 14 P-V sets tested, coarse columnar prior  $\beta$  grain with lamellar  $\alpha'$  and acicular  $\alpha'$  martensite were observed, typical of LPBF-processed Ti6Al4V[168].

Prior  $\beta$  grains had high-aspect-ratio columnar morphology with widths 10-50  $\mu\text{m}$  and they appeared to extend from the bottom to top of the melt pool.

- Ti6Al4V-xB: type (i) microstructure

TiB precipitates: as indicated by the red arrow in Fig 61(a-2), TiB precipitates in type (i) microstructure were of a high-aspect-ratio, needle-shape whisker morphology, similar to that of arc-melted eutectic TiB (Fig 56). Their dimensions were 0.5~1  $\mu\text{m}$  for major-axis length and 0.1~0.17  $\mu\text{m}$  for minor axis length, greatly refined from arc-melted TiB. A uniform distribution across prior  $\beta$ -Ti grains was observed, with precipitate spacing 0.5~1.5  $\mu\text{m}$ , as qualitatively shown in Fig 56 (a-1).

Ti-matrix: little modification from baseline Ti6Al4V microstructure. Prior  $\beta$ -Ti grains still exhibited a high-aspect-ratio columnar morphology with grain size in the tens of microns. The Ti-matrix still exhibited both lamellar  $\alpha'$  & acicular- $\alpha'$  martensitic morphology.

- Ti6Al4V-xB: type (ii) microstructure

TiB precipitates: as indicated by the red arrow in Fig 61 (b-2), TiB precipitates in type (ii) were present as a continuous network that was substantially different from the TiB whisker morphology formed by arc-melting (Fig 56). The TiB network presents refined sub-micron cell spacing (0.1~0.5  $\mu\text{m}$ ) as shown in Fig 61 (b-2).

Ti-matrix: There was no evidence of columnar prior  $\beta$ -Ti grains as in unmodified baseline microstructure and type (i) microstructures.  $\beta$ -Ti grain, combined with the TiB network, was likely to be eutectic solidification product, as further discussed in chapter 7.7.2. The specific  $\alpha$  or  $\alpha'$  constituents in the Ti-matrix could not be determined.

- Ti6Al4V-xB: type (iii) microstructure

TiB precipitates: presented as a discontinuous network morphology, indicated by the dark-contrast boundaries pointed out by white arrow in Fig 61 (c-1). Similar to that of type (ii) microstructure, the TiB network in type (iii) microstructure also present sub-micron spacing was in the range of 0.1~0.5  $\mu\text{m}$ . At high magnification (Fig 61 (c-2)) the discontinuous TiB network appeared to be an agglomeration of isolated, nano-scale TiB whiskers. The dimension of each isolated TiB whisker was measured to be 70-120nm for major-axis length, much finer than that of type (i) melt pool microstructure.

Ti-matrix: similar to type (ii) microstructure, no columnar prior  $\beta$ -Ti grains were observed. As with type (ii) the  $\alpha$  or  $\alpha'$  constituents could not be determined.

- Ti6Al4V-xB: type (iv) microstructure

TiB precipitates: present two different size scales and two morphologies. The larger TiB precipitates, as indicated by the white arrow in Fig 61 (d-1), exhibited a faceted rod morphology. The rods had hollow centers filled with Ti-matrix, similar to the morphology of arc-melted primary TiB (Fig 56). The smaller TiB precipitates, as shown in Fig 61 (d-2), presented high-aspect-ratio needle-shape morphologies similar to arc-melted eutectic TiB (Fig 56). These two types of TiB precipitates in this microstructure were considered as primary and eutectic TiB, due to their morphological resemblance to the eutectic and primary TiB precipitates in arc-melted condition (Fig 56). The typical length scale for primary TiB precipitates was 1-3  $\mu\text{m}$  in major axis and around 0.5  $\mu\text{m}$  in minor axis. Eutectic TiB precipitates showed a much finer size of approximately 75-90 nm in major axis length.

It should be noted that compared to type (i) melt pool microstructure, this microstructure showed not only finer dimensions but also a much denser distribution for eutectic TiB whisker.

Ti-matrix:  $\beta$ -Ti grains showed an equiaxed hexagonal morphology with a typical grain size of 1~5  $\mu\text{m}$ . The white dashed line in Fig 61 (d-1) and (d-2) marked the  $\beta$  grain boundaries.

- Ti6Al4V-xB: type (v) microstructure

TiB precipitate: similar to type (iv), two types of TiB precipitates with different size scales were present. The smaller one presented a needle-shape morphology and larger one a rod morphology with a hollow center, which were also considered eutectic and primary TiB. Unlike type (iv) microstructure, the larger primary TiB in type (v) microstructure exhibited dendrite-like features, as shown by Fig 61(e-2). Besides, compared to type (iv), type (v) microstructures showed much denser distribution and a coarser length scale for primary TiB (major axes: 5-10 $\mu\text{m}$ ; minor axes: 1-2 $\mu\text{m}$ ), as shown by Fig 61(e-2). Eutectic TiB precipitates in type (v) microstructure were greatly similar to those in the type (iv) microstructure, presenting a high-aspect-ratio whisker morphology with nano-scale dimensions and a dense distribution. Due to the dense TiB precipitate distribution, it was not possible to determine the characteristics of the Ti-matrix microstructure.

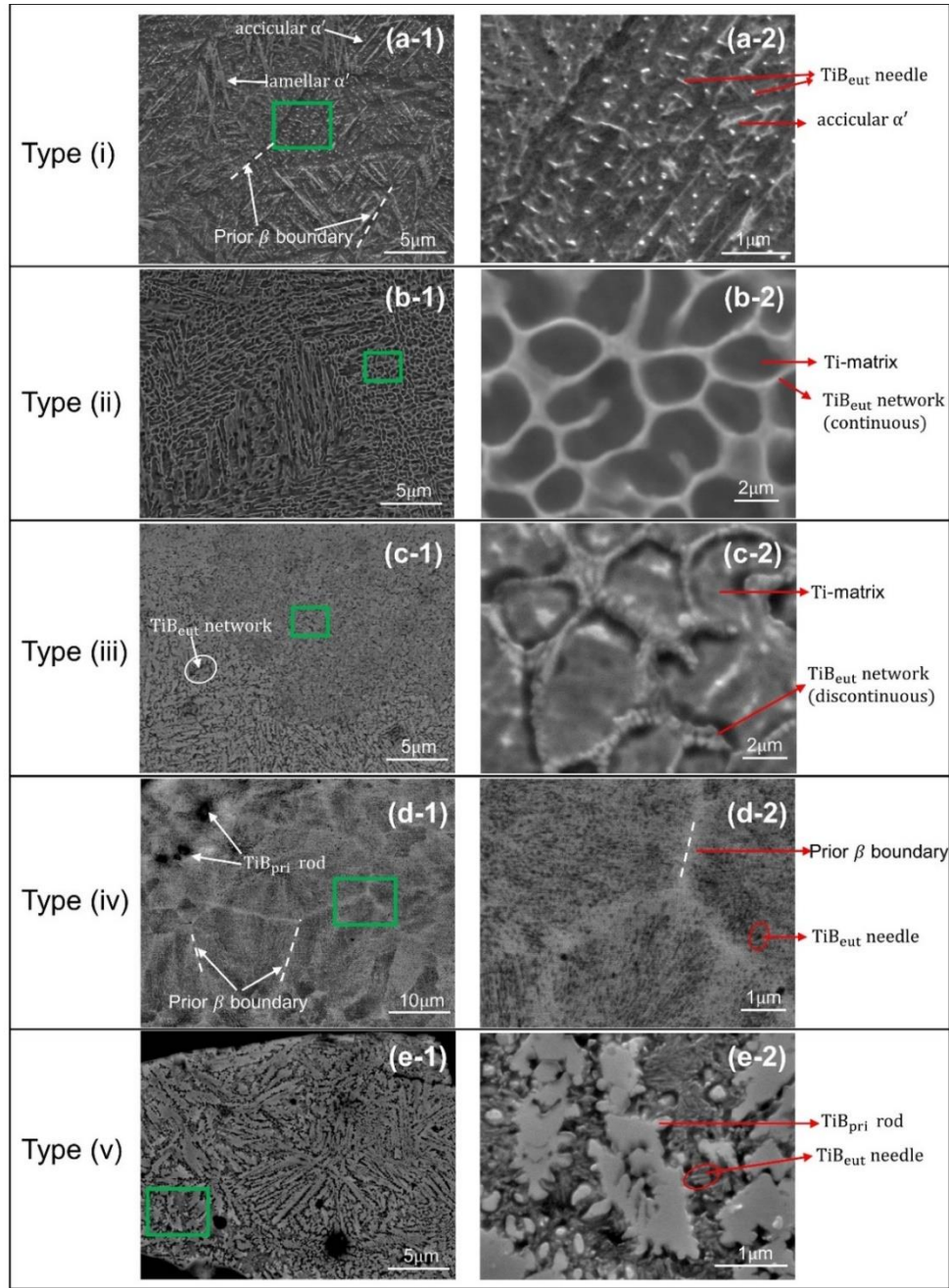


Fig 61 Typical SEM images of 5 different Ti6Al4V-xB melt pool microstructure observed for 56 tested [Ti6Al4V-xB, P-V ] combination, referred to as Type (i)~(v) microstructure, respectively showing uniformly-distributed  $\text{TiB}_{\text{eut}}$  whisker ((a-1), (a-2)), continuous TiB network ((b-1), (b-2)), discontinuous TiB network ((c-1), (c-2)), nano scale  $\text{TiB}_{\text{eut}}$  needle+  $\text{TiB}_{\text{pri}}$  rod ((d-1), (d-2)) and dendritic  $\text{TiB}_{\text{pri}}$  rod+ nano-scale  $\text{TiB}_{\text{eut}}$  needle ((e-1), (e-2)).  $\text{TiB}_{\text{eut}}$ : eutectic TiB;  $\text{TiB}_{\text{pri}}$ : primary TiB; (i-2) image on the right: high magnification image of green box in (i-1) image on the left, with

i as a, b, c, d, e

Table 17 five types of Ti6Al4V-xB melt pool microstructure: comparison of TiB precipitate feature, solidification mode and existence for laser deposition of Ti6Al4V-1,2,5% B

microstructure	TiB microstructure feature		solidification mode	existence
	morphology	Relevant dimension		
type (i)	needle-shape	main-axis length: 0.5~1.0 $\mu$ m	primary $\beta$ -Ti	1, 2% B
type (ii)	continuous cellular network	network spacing: 0.1~0.5 $\mu$ m	coupled eutectic	1, 2, 5%B
type (iii)	individual: needle-shape agglomerate: cellular network (discontinuous)	individual length: 70~120nm network spacing: 0.1~0.5 $\mu$ m	primary $\beta$ -Ti	5%B
type (iv)	primary: highly faceted rod eutectic: needle-shape	primary: 1~3 $\mu$ m eutectic: 75~90nm	primary TiB	5%B
type (v)	primary: highly faceted rod with dendrite arms eutectic: needle-shape	primary: 5~10 $\mu$ m eutectic: 75~90nm	primary TiB	5%B, 10%B

Based on above categorization, melt pool microstructure P-V mapping could be obtained for each Ti6Al4V-xB trial composition as shown in Fig 62. The numbers marked for each data point corresponds to the P-V set in Table 4. Sometimes different microstructures were observed in local regions of one melt pool, and these situations were indicated by overlapping colors, e.g. P-V set #11 in Fig 62(a). The position of each color in the semicircle was in accordance with the region in the melt pool cross section where their corresponding microstructure type is observed. Fig 62 shows that each Ti6Al4V-xB composition not only presented different types of melt pool microstructure but also different trends across P-V space. Some reasons for this are discussed below in chapter 7.7.

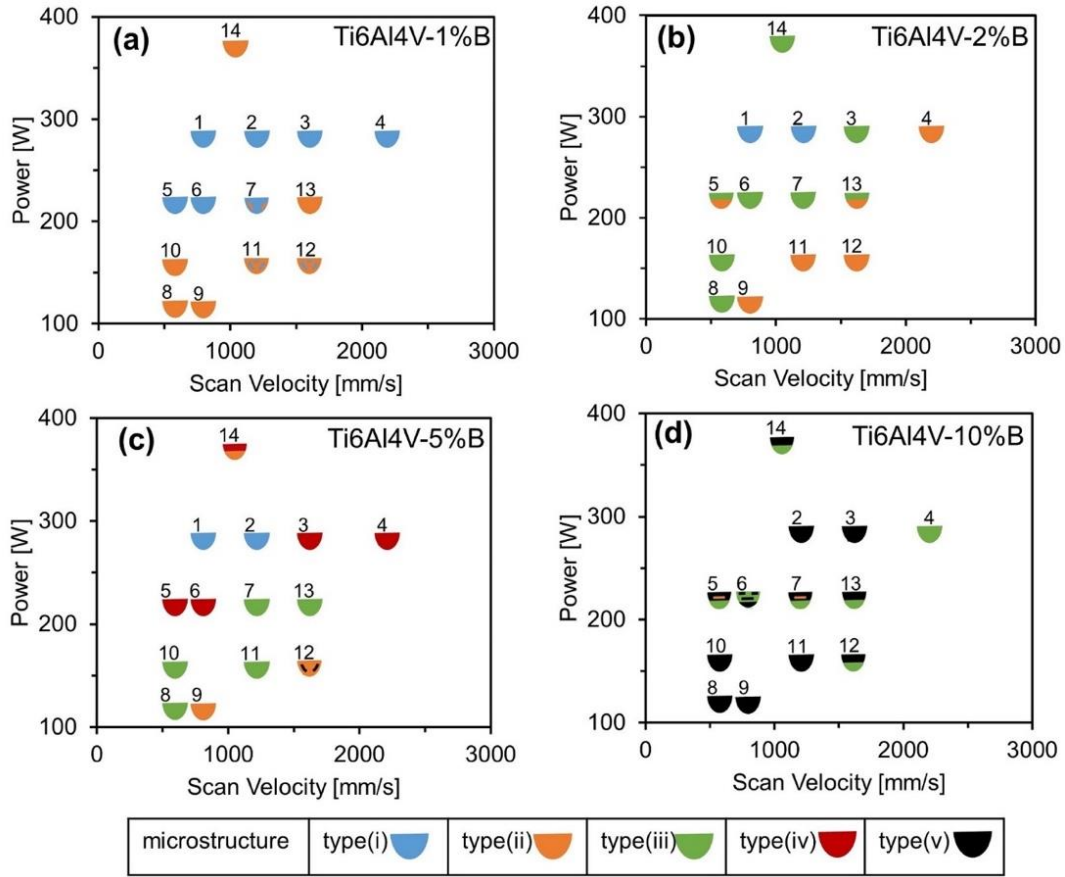


Fig 62 melt pool microstructure P-V mapping for each Ti6Al4V-xB candidate compositions, with Ti6Al4V-1%B, 2%B, 5%B, 10%B shown in (a), (b), (c), (d) respectively; Note: labels with multiple colors (e.g. #11 for Ti6Al4V-1%B in (a)) corresponds to different microstructures observed on a single melt pool cross section.

One observation worth noticing is that for a small portion of [B wt.%, P-V] combinations, the generated melt pool shows local inhomogeneous microstructure that was likely to be evidence of melt pool fluid flow. A typical example was shown in Fig 63. The melt pool cross section in Fig 63 (a) shows two vortex-shape traces, as distinguished by their brighter contrast compared to the nearby region in the melt pool. High magnification images in Fig 63(b) and (c) show that TiB precipitates at most of the region in the melt pool present isolated whisker morphology (Fig 63(b)), but at the bright-contrast vortex-shape region, TiB precipitates exhibit continuous network morphology (Fig 63(c)). They correspond to the TiB precipitates of type(i) and (ii) microstructure in Fig 61(a) and (c) respectively, with their morphological, distribution and dimension details described earlier. Fig 63(d) shows a possible melt pool fluid flow scenario leading to the formation of the vortex-shape traces with different TiB precipitate microstructure in the melt pool shown in Fig 63(a).

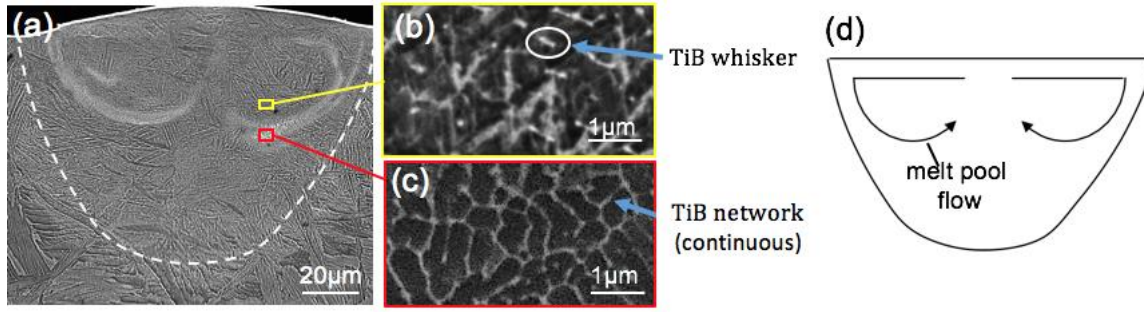


Fig 63 Ti6Al4V-xB melt pool showing local microstructure inhomogeneity: (a) melt pool cross section; white dashed line in (a): mark melt pool boundary; (b), (c): zoom-in image of yellow and red box in (a); blue arrow in (b)(c): mark TiB precipitate; (d): possible melt pool fluid flow scenario causing the melt pool microstructure inhomogeneity in (a)

Regarding Ti-matrix microstructure, two observations are worth mentioning: first, melt pools with different TiB microstructure show different prior  $\beta$ -Ti grain microstructure. If the melt pool shows sub-micron scale TiB whiskers (Fig 61(a-1)), the prior  $\beta$ -Ti grains in melt pool present coarse columnar morphology with tens of micron grain size. If the melt pool shows co-existence of both hollow-centered TiB rod and nano-scale TiB whiskers, as in Fig 61(d-1), prior- $\beta$  grain present equiaxed hexagonal morphology, with grain size greatly refined to 1~5  $\mu\text{m}$ , indicated by white dashed lines in Fig 61(d-1). Inside each prior- $\beta$  grain, a typical faceted/non-faceted eutectic  $\beta$ -Ti /TiB morphology was observed. For melt pools with either continuous or discontinuous TiB network, as shown in Fig 61(b-1) and Fig 61(c-1) respectively, prior  $\beta$ -Ti grain boundary was likely to be delineated by the continuous and discontinuous TiB network according to the EBSD analysis from the study of Hu et al [119], who also observed the similar TiB network microstructure in LENS-AM fabricated Ti-1.6wt.%B material. Therefore, for these melt pools, their prior  $\beta$ -Ti grains, as indicated by the TiB network spacing, present equiaxed-cellular grain morphology with greatly refined sub-micron grain size in the range of 0.1-0.5  $\mu\text{m}$ . This suggests that LPBF-built Ti6Al4V-xB material with different [B%, P-V] combination not only shows varied TiB precipitate microstructure but also has different Ti-matrix microstructure refinement effect.

#### 7.4.2 Single-track vs. Multi-track vs. Overlap-track

Multi-track and overlap-track tests were conducted for Ti6Al4V-1,2,5 wt.%B. Fig 64(a)-(c) shows the melt pool cross section for single-track, 1-layer pad and 2-layer pad, with melt pool boundaries indicated by white and red dashed lines. Microstructure characterization was conducted at multiple

regions in each melt pool, covering the location from melt pool center to melt pool boundary as indicated by the boxes in Fig 64.

Chapter 7.4.1 shows that for Ti6Al4V-1,2,5 wt.%B, their single track melt pool presented four different melt pool microstructures for the tested P-V sets, which are type (i)-(iv) microstructure as presented in Fig 61(a-d). For single-track with type (i)-(iv) microstructure, the corresponding multi-track and overlap-track melt pool microstructure generated by same [B%, P, V] combination were presented in Fig 65(a-d) respectively.

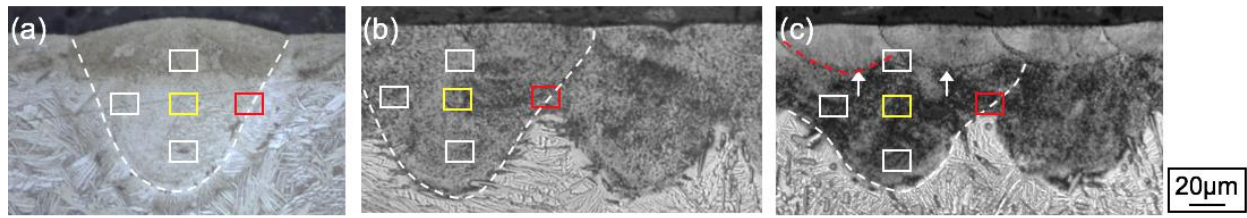


Fig 64 example OM image showing melt pool cross section for regular pad (a) & overlap pad (b): melt pool boundaries for regular-pad and first layer in overlap-pad: white; second-layer melt pool boundary in overlap pad: red; microstructure characterization location: indicated by inserted box in (a)-(c)

For the 1-layer and 2-layer pads, melt pool microstructure was characterized at multiple regions in each melt pool, as indicated by the boxes in Fig 64(b) and (c). The result shows that no matter for 1-layer pad or 2-layer pad, most of the melt pool region away from adjacent melt pool boundaries (white and yellow boxes in Fig 64(b),(c)) had consistent TiB precipitate morphology, dimension and distribution to the single-track melt pool generated at same [B%, P-V] combination. This microstructure similarity between track and pads holds for all the tested [B wt.%, P-V] combinations. This was exemplified by Fig 65 for the four [B%, P-V] combinations, which covers all four types of melt pool microstructure (type (i)-(iv)) observed in single-tracks of Ti6Al4V-1,2,5 %B with the tested P-V sets, as indicated by their microstructure process map in Fig 58 and Table 17.

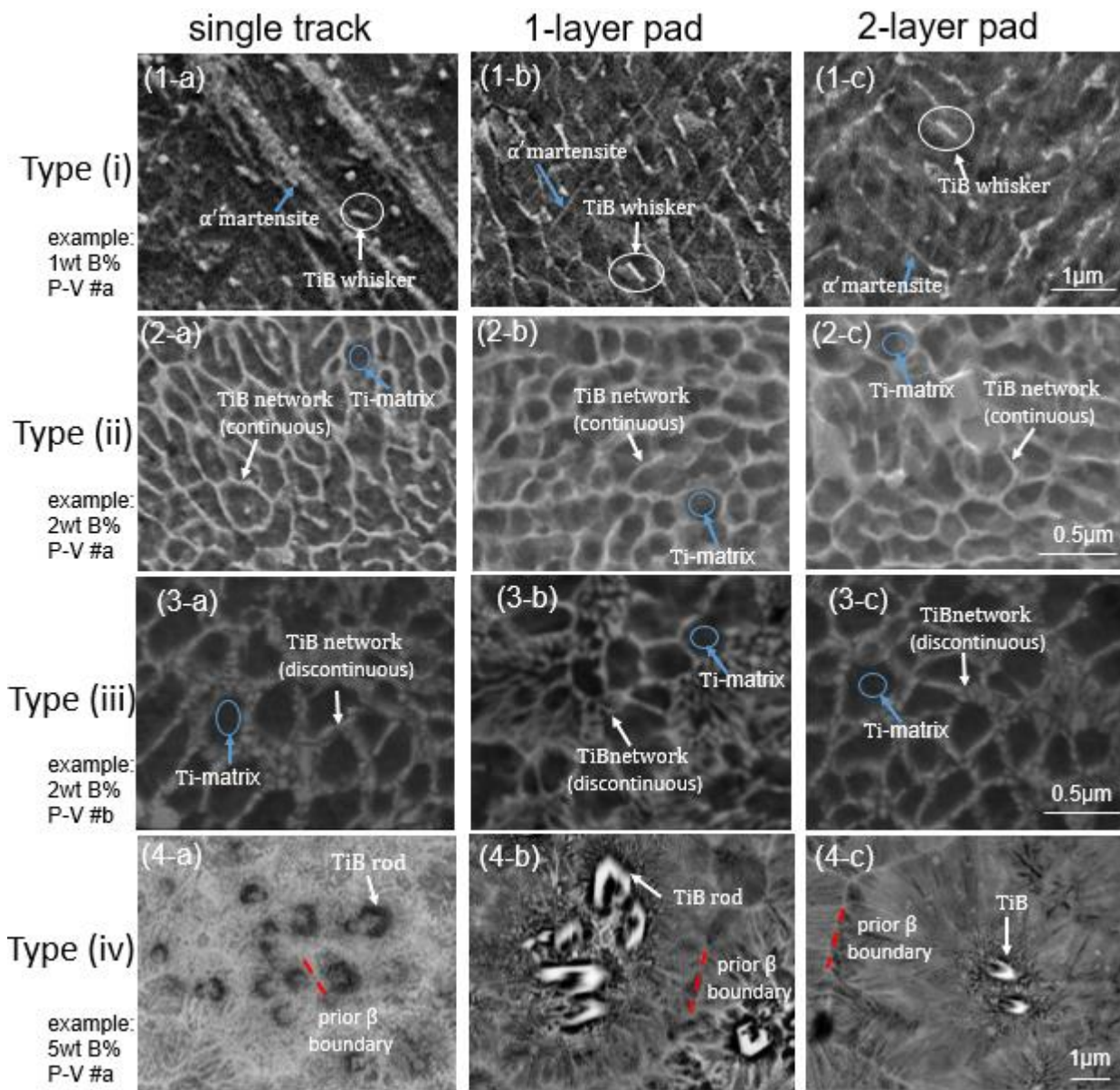


Fig 65 Typical melt pool microstructure observation of single-track, multi-track, overlap-track generated at same B wt.% level and P-V sets, with the corresponding single-track showing type (i)-(iv) melt pool microstructure (see chapter 7.4.1 and Fig 61 for details of type (i)-(iv) microstructure); [B wt%, P-V] of each examples: listed on the left side; microstructure characterization: at center of melt pool (yellow box in Fig 64(a)-(c)); TiB precipitate and Ti-matrix: marked by white and blue arrows respectively; red dashed lines in (4-a,b,c): mark prior  $\beta$ -Ti boundaries

However, for the 1-layer and 2-layer pads, the region near the boundary of two adjacent melt pools (red boxes in Fig 64 (b), (c)) show different TiB microstructure from that of single-track at same [B%, P-V] combination. Fig 66 provides two examples. As shown in Fig 66, there is a narrow region near

the boundary of two adjacent melt pools (marked by the dashed line in Fig 66(a)) with TiB microstructure inconsistent from the rest of the regions in the pad. For pad with TiB network microstructure (Fig 66(b)), this narrow region shows greatly coarsened TiB network spacing, measured to be around 1.5-2 times the TiB network spacing in the rest area of the pad. For pad in Fig 66(c), TiB precipitates present isolated whisker morphology in most regions but transform into continuous network morphology in this narrow region between two adjacent melt pools. In contrast, single-track melt pool does not show such localized TiB microstructure variation near the boundary of the melt pool and arc-melted matrix material.

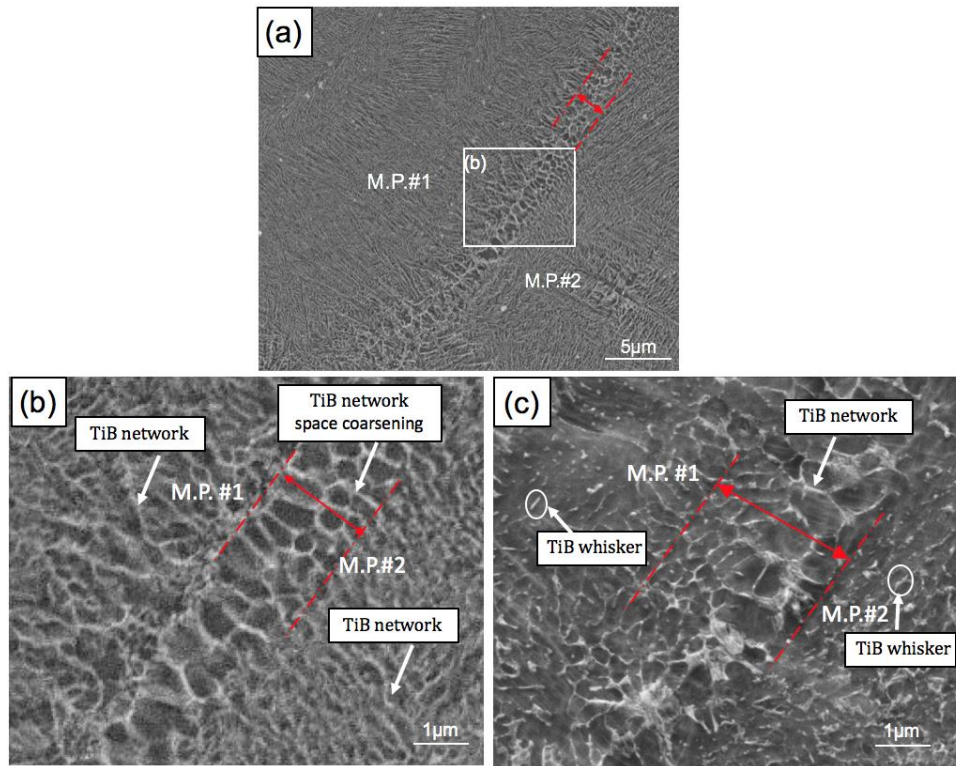


Fig 66 microstructure inconsistency in Ti6Al4V-xB pad (a): localized region near boundary between adjacent melt pools (marked by red dashed line in (a)-(c)) show different TiB distribution spacing (b) or different TiB morphology (c) compared to rest of the pad; M.P.: stands for “melt pool”; (b): zoom-in image of the white box in (a); examples provided by [2 wt.%B, P-V#a] and [1% wt.%B, P-V#a] for (b) and (c)

## 7.5 Melt pool hardness

Nano-indentation tests were conducted to measure the hardness for each single-track melt pools as well as arc-melted button, as presented in Fig 67. For each single-track, hardness for three melt pool

cross sections along the track was measured and their average value was presented as the melt pool hardness for the corresponding [B wt.%, P-V] combination. For each Ti6Al4V-xB trial compositions, their maximum and minimum laser-deposited melt pool hardness for the 14 selected P-V sets (Table 4) were compared with their arc-melted hardness in Fig 67, which shows that the four trial Ti6Al4V-xB (x=1,2,5) compositions, laser deposition with all the 14 tested P-V sets led to at least 35% hardness enhancement compared to the arc-melted Ti6Al4V-xB material, showing effective hardness improvement by LPBF laser deposition for Ti6Al4V-xB material. However, melt pools generated on the same Ti6Al4V-xB material showed hardness variability across the 14 P-V settings. With the tested P-V range, the hardness variation was approximately 20% for 1 wt.%, 2 wt.% and 5 wt.% B, but greatly increased to approximately 60% for 10 wt% B, which could be qualitatively shown by the difference between “max” and “min” label in Fig 67.

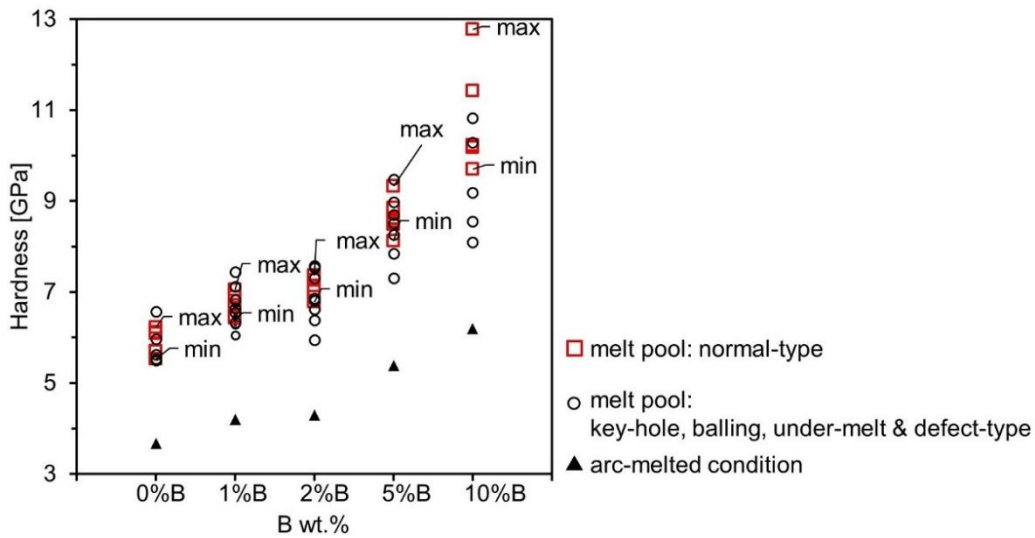


Fig 67 comparison of arc-melted Ti6Al4V-xB hardness & single bead Ti6Al4V-xB melt pool hardness. Max & min labels are indicated for the normal-geometry melt pool (see Fig 22, chapter 6.1.1)

For each Ti6Al4V-xB material, the general trend of melt pool hardness variation with P-V parameters was presented in Fig 68. Chapter 7.4.1 and chapter 7.4.2 shows that for Ti6Al4V-1,2,5%B, four different melt pool microstructure were observed for tracks and pads with different B% and P-V sets, referred to as type (i)-(iv) microstructure and presented in Fig 61. In Fig 68, each label indicates the solidification mode for type (i)-(iv) microstructure, which were summarized in Table 13. In Fig 68, hardness of B-free Ti6Al4V single-tracks fabricated is included to provide a reference for B-added Ti6Al4V-xB melt pool hardness by the same P-V parameters. Fig 68 shows that for boron-free

Ti6Al4V, melt pool hardness increase steadily as laser scan velocity increases but slightly decreases with higher laser power. For each Ti6Al4V-xB composition, if melt pools present the same type of solidification mode, their hardness shows a steady increasing trend with laser scan velocity similar to B-free Ti6Al4V. However, as laser scan velocity keep increasing, Ti6Al4V-1, 2, 5%B all show change in solidification mode, as indicated by the different label shapes in Fig 68. Accompanied with this is a sudden increase in melt pool hardness, which was observed no matter with laser power fixed at 215W or 280W, as shown in Fig 68(a) and (b) respectively. For Ti6Al4V-xB material, the melt pool hardness enhancement by higher laser scan velocity and change in solidification mode might be explained by higher-level microstructure refinement, which was further demonstrated in chapter 7.7.2.

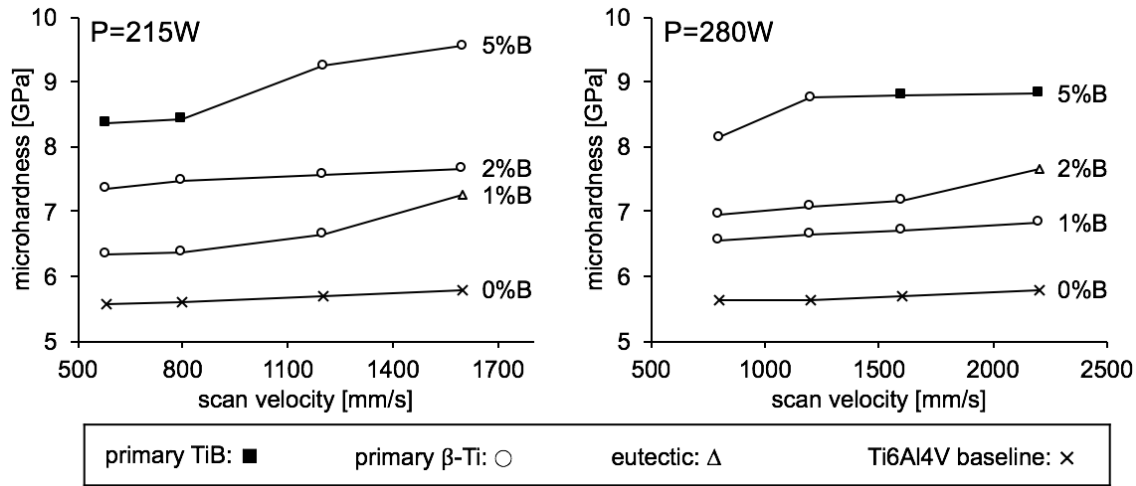


Fig 68 melt pool hardness for Ti6Al4V-0,1,2,5 wt.%B at different laser scan velocity when laser power fixed at 215W (a) and 280W(b); melt pool microstructure: indicated by different labels, with each microstructure category summarized in Table 17 and Fig 61

## 7.6 Promising LPBF composition identification

In this study, a powder-free method was used to investigate the Ti6Al4V-xB system. For each trial Ti6Al4V-xB composition, P-V process maps of melt pool geometry and microstructure were generated, melt pool dimension and hardness variation across P-V space were assessed. Based on these results, promising B contents for Ti6Al4V-xB alloys manufactured by LPBF were between 2-5 wt.% B for the reasons listed below.

- Melt pool dimension variation

Fig 57 showed that there were minimal deviations in melt pool dimension from B-free Ti6Al4V except at 10 wt% B. Therefore, part build strategies and part build model optimizations for Ti6Al4V, such as support structure design and heat transfer model optimization[51][164][169] might still be applicable to Ti6Al4V-xB with B levels less than 5 wt% due to their similar melt pool dimensions.

- Melt pool geometry

The melt pool geometry P-V mapping in Fig 58 showed that up to 5 wt% B, the P-V space leading to normal melt pool geometry was comparable to Ti6Al4V. While for Ti6Al4V-10B, a much narrower normal melt pool P-V space was observed, as shown both directly and indirectly in Fig 58 and Table 16. This means the likelihood of producing defect-free parts would be lower for Ti6Al4V-10B or at least there would be less flexibility in LPBF process parameter selection.

- Melt pool microstructure

Melt pool microstructure P-V mapping (Fig 62) showed the extent of the microstructural differences across P-V space was low when B levels were 2-5 wt.%: Ti6Al4V-2%B and 5%B presented type (ii), (iii) and type (ii), (iii), (iv), respectively, across P-V space. These microstructure types were similar in many ways, containing sub-micron-spacing TiB network for both type (ii) & (iii), and nano-scale TiB whisker for both type (iii) & (iv). While Ti6Al4V-1%B presented type (i) & (ii) melt pool microstructure at different P-V space. As shown in chapter 7.4.1, these two types of microstructure were drastically different in basically all microstructural features discussed for TiB precipitate and Ti-matrix. The same conclusion was reached for Ti6Al4V-10%B, which presented type (iii) & (v) in its microstructure P-V mapping. Substantial microstructure variation in P-V space could complicate the choice of optimal P-V parameters since LPBF-builds with slightly different P-V settings might lead to substantial property variations. Based on this, Ti6Al4V-xB with 2-5 wt.% B might be preferred.

More importantly, type (ii) and (iii) microstructure (Fig 61(b-1)-(b-2), Fig 61(c-1)-(c-2)) show the potential for promising property enhancement. As mentioned in chapter 7.4.1 (Table 17) and shown further in chapter 7.7, TiB network distribution in type (ii) microstructure suggested eutectic solidification, and type(iii) microstructure suggested non-equilibrium primary  $\beta$ -Ti solidification in hypereutectic Ti6Al4V-xB. From this point, the sub-micron TiB network spacing suggests significant microstructure refinement. Unlike type (iv) and (v), type (ii) and (iii) microstructure showed no

presence of primary TiB at 2 wt.% B and 5 wt.% B, which were typical hyper-eutectic compositions. One possible explanation for this was that rapid solidification altered the behavior from primary TiB growth to either coupled eutectic growth or even primary  $\beta$ -Ti growth, thus leading to type (ii) & (iii) microstructures with all eutectic TiB precipitates [170][84]. This was shown further in the discussion of solidification mode transition criteria for LPBF melt pool with Ti6Al4V-xB in chapter 7.7. For type (ii) microstructure, similar microstructure was also reported by the study of Hidenori et al [171], who observed the in-situ TiB network microstructure evolution in Ti-B alloy by laser scanning confocal microscopy. Apart from [171], This TiB network architecture has also been observed in wire-feed processed Ti6Al4V with 0.1 wt% B [125] and LENS-processed CP-Ti with 1.6 wt% B [119]. However, it should be noted that the TiB network spacing observed in type (ii) or (iii) microstructures (0.1-0.5  $\mu\text{m}$ ) was much finer than the ones in previous studies (25  $\mu\text{m}$  for [125]; 5-10  $\mu\text{m}$  for [119]). This could be attributed to the faster cooling rate of LPBF-solidification ( $10^6$ - $10^7$  K/S) compared to that of the other two AM process (around 150 K/S for [125]). The study in [119] also showed that the refinement in TiB network spacing would result in more effective mechanical property enhancement based on a Hall-Petch strengthening mechanism. This suggests the benefits of choosing LPBF method for Ti6Al4V-xB fabrication. TiB network architecture was also intentionally fabricated by Wang et al [116] using a multi-step powder metallurgy approach, who reported promising creep resistance and enhanced high-temperature tensile strength. This work showed that LPBF processing can produce similar microstructures.

- Melt pool hardness variation in Q-V space

From Fig 67, melt pools of all Ti6Al4V-xB trial compositions showed higher hardness value compared to the arc-melted Ti6Al4V-xB buttons with the same composition. In addition, all B-containing Ti6Al4V-xB alloys were harder than the B-free Ti6Al4V melt pool at the same P-V settings. The higher hardness might originate from the dimension refinement and morphology modification of both TiB precipitate and Ti-matrix. Although the hardness enhancements were highest for Ti6Al4V-10B, the largest hardness variability across the P-V settings tested was also observed at this composition. This might be attributed to dimension variations of the primary TiB rods, which were observed at different P-V settings. Therefore, this large hardness variation across tested P-V range suggests that Ti6Al4V-10wt.%B might not be suitable to be processed by LPBF route since there would be large variations in properties with slight changes to P-V parameters.

In summary, Ti6Al4V-xB with 2-5 wt% B was the most promising composition range. This range showed: (1) comparable melt pool dimensions to B-free Ti6Al4V melt pool across wide P-V space, (2) large P-V process window resulting in normal-geometry melt pool; (3) promising microstructures with sub-micron-dimension TiB network architecture and high-vol.% of refined-size TiB precipitates; (4) enhanced melt pool hardness with little variation across P-V space.

## **7.7 LPBF solidification mode transition criteria**

Chapter 7.4.2 shows microstructure consistency across Ti6Al4V-xB single-track, multi-track and overlap-track melt pool at the same [B%, P-V] combination. This suggests that the LPBF-built Ti6Al4V-xB microstructure is controlled by the solidification microstructure in the as-deposited melt pool. Therefore, it is essential to understand the phase transition of Ti6Al4V-xB material under LPBF solidification condition. Chapter 7.6 showed Ti6Al4V-10%B as inferior composition for LPBF processing and thus it was not investigated in this chapter. For the other three Ti6Al4V-x%B composition, namely Ti6Al4V-1,2,5%B, four types of single-track microstructure (type (i)-(iv) microstructure in Fig 61(a-d)) were observed for their melt pools fabricated by the 14 P-V sets tested in this study. For each tested [B%, P-V] combination, the resulting melt pool microstructure could be found in the microstructure process map in Fig 62. Fig 62 showed that melt pool microstructure varied with both B% content and P-V parameter, which was attributed to transition in solidification mode (primary  $\beta$ , primary TiB, eutectic). An analytical equation model was developed in chapter 7.7.1 as a function of P-V process parameters and material properties to determine the dominating Ti6Al4V-xB solidification mode for different [B wt.%, P-V] combinations.

### **7.7.1 Model for solidification mode transition**

Rapid solidification can result in far-from-equilibrium phase transitions compared to the phase diagram (Fig 14). The competitive growth principle is known to be applicable to such non-equilibrium rapid solidification [106][86], which determines the primary solidification mode by the solidification phase with highest solidification front temperature. It has been widely adopted to investigating the non-equilibrium solidification mode in welding condition, as presented earlier in chapter 2.2.3. By adopting the competitive growth principle, the equations below can be used to predict the Ti6Al4V-xB melt pool solidification mode for each [B%, P-V] combination following these three steps: First, it considers all phases (primary  $\beta$ , primary TiB, eutectic) possible to form; Then, the solid/liquid interface temperature for each solidification phase is estimated; Lastly, the dominating solidification

mode will be the phase with the highest interface temperature.

This study used the function in Equation 20-Equation 22 to relate Ti6Al4V-xB solidification phase interface temperature to absorbed laser power(Q) and scan velocity(V). It is derived as such:

For eutectic solidification, the equation model for typical irregular eutectic growth of f-nf material systems was adopted, as shown in Equation 20. As suggested by their entropy of fusion (Table 18), TiB is likely to solidify as a faceted phase while Ti-phase as non-faceted phase, rendering typical faceted and non-faceted (f-nf) solidification for Ti6Al4V-xB system. Kurz and Fisher [84] showed Equation 20 as a suitable mathematical model to estimate the undercooling of irregular eutectic growth for f-nf material systems. The linear relation  $\Delta T_{eut} \sim R^{0.5}$  and  $\Delta T_{eut} \sim G^{-0.5}$  in Equation 20 was experimentally supported by the eutectic growth for typical nf-f systems Al-Si alloy [172][173] and Fe-C system[174]. The model in Equation 20 corresponds to the relation of  $\lambda^2 R = AG^K$  ( $\lambda$ : interphase spacing, A, K: constant) rather than the assumption of  $\lambda^2 R = \text{constant}$  as in Jackson and Hunt's work [175], making it more appropriate to describe the local non-isothermal condition at solid/liquid interface in LPBF solidification.

For primary phase solidification (primary  $\beta$ -Ti and primary TiB in this case), the relation between undercooling, temperature gradient and solidification rate could be expressed by Equation 23. Assuming including zero nucleation undercooling assumption, steady-state assumption and smooth curvature assumption for primary phase morphology[84][176] and by applying undercooling minimization criteria and regression analysis, Equation 23 could be approximated as Equation 21 and Equation 22 for primary  $\beta$ -Ti and primary TiB respectively [84].

The equation model in Equation 21 and Equation 22 was originally proposed by Burden and Hunt [176] for non-faceted phase and then justified by Kurz and Fisher [84] for its applicability to both non-faceted and faceted phase, which was the case for Ti6Al4V-xB system as shown earlier. The viability to adopt the equation models in Equation 21 and Equation 22 for solidification in additive manufacturing is suggested by the work from Sahoo et al [177], which showed that for Ti6Al4V melt pool fabricated by electron beam additive manufacturing, remarkable agreement was achieved between the result estimated by the analytical model from Burden and Hunt [176] and the one predicted by phase-field simulation.

Galvin et al[170] also adopted the competitive growth criterion to understand microstructure variation for laser cladded Ti6Al4V-xB coating. In their work, a simple linear model  $\Delta T = KV$  was used to describe the undercooling of all three solidification phase based on the observation of microstructure

transition as scan velocity increases. But from the observation in this work, Ti6Al4V-xB microstructure transition was a combined result of B%, laser power and scan velocity, which could not be readily explained by the linear model in [170]. In this regard, the equation model in Equation 20-Equation 22 might be more appropriate to be used as a fitting model to approximate the undercooling for Ti6Al4V-xB rapid solidification. However, it should be noted that the assumptions involved in Equation 20-Equation 22 could lead to consequences such as neglecting columnar to equiaxed transition and neglecting microstructure instability caused by melt pool flow. Future work could be considered to involve adjustable parameters in Equation 20-Equation 22 that allow modification for these assumptions, which might help to present a more comprehensive description for undercooling in LPBF solidification process.

$$\Delta T_{\text{eut}} = A_{\text{eut}} R^{0.5} G^{-0.5} \quad \text{Equation 20}$$

$$\Delta T_{\beta-\text{Ti}} = \frac{GD_1}{R} + A_{\beta} R^{w_{\beta}} \quad \text{Equation 21}$$

$$\Delta T_{\text{TiB}} = \frac{GD_1}{R} + A_{\text{TiB}} R^{w_{\text{TiB}}} \quad \text{Equation 22}$$

$$\Delta T_{\text{primary}} = \frac{GD_1}{R} - mC_0 \{1 - 1/[1 + (k - 1)\Omega]\} - \frac{krGD_1}{R} + \frac{2\theta}{R} \quad \text{Equation 23}$$

Where  $\Delta T_{\text{eut}}$ ,  $\Delta T_{\text{TiB}}$ ,  $\Delta T_{\beta-\text{Ti}}$ ,  $\Delta T_{\text{primary}}$  are undercooling at the solid/liquid interface for eutectic phase, primary TiB phase, primary  $\beta - \text{Ti}$  phase and primary phase in general;  $m$  is liquidus slope;  $k$  is partition coefficient;  $\Omega$  is tip supersaturation for primary phase,  $\Omega = P \exp(P) E_1(P)$  for non-faceted phase and  $\Omega = (\pi P)^{0.5} \exp(P) \text{erfc}(P^{0.5})$  for faceted phase, where  $P$  is peclet number;  $\theta$  is Gibbs-Thompson coefficient;  $r$  is tip radius for primary phase;  $D_1$  is liquidus diffusivity of Boron;  $G$  is temperature gradient at the interface;  $R$  is solidification rate;  $A_{\beta}$ ,  $A_{\text{TiB}}$ ,  $A_{\text{eut}}$ ,  $w_{\beta}$ ,  $w_{\text{TiB}}$  are material-related parameters obtained by experimental data fitting.

Table 18 entropy of fusion for Ti-TiB system

	melting temp	enthalpy of fusion	entropy of fusion
	(kelvin)	(kJ/mol)	(J/mol·K)
TiB	3423	70.0	20.4: >2R
Ti	1943	18.7	9.6:< 2R

Where R is gas constant

LPBF-deposited melt pool shows locally varying solidification rate. The maximum local solidification rate in the melt pool usually occurs near the melt pool top, with its value approaching laser scan velocity [178]. In this study, solidification rate (R) in Equation 20-Equation 22 is taken to be equal to laser scan velocity, to address the upper threshold of local melt pool solidification rate that could be achieved by P-V parameters of investigation. Temperature gradient (G) in Equation 20-Equation 22 is given by Equation 24, which was derived from the Rosenthal solution [21].

$$G = \frac{2\pi k(T_i^* - T_0)^2}{Q} \quad (i = \text{eut}, \text{TiB}, \beta) \quad \text{Equation 24}$$

Where Q is absorbed laser power, V is laser scanning speed,  $T_{\text{liq}}(C_0)$  is liquidus temperature at composition  $C_0$ ,  $\alpha$  is thermal diffusivity, k is thermal conductivity,  $T_i^*$  is the temperature at the interface for solidification phase i as shown in Equation 20-Equation 22,  $T_0$  is temperature far from the heat source, taken as 35°C in this study

Therefore, by substituting Equation 24 into Equation 20-Equation 22, and reorganizing the equations, the interfacial temperature of primary  $\beta$ -Ti, primary TiB and eutectic solidification phase can be developed into the equation models listed in Table 19. The parameters in each equation ( $m_1$ ,  $m_2$ , etc.) are defined in Table 20, and all of them are only related to material properties and preheat temperature( $T_0$ ). Since this study used a constant powder bed temperature (35°C), i.e.,  $T_0$  in the parameter definitions in Table 20 was taken as 35°C.

Table 19 equation model for interfacial temperature of each solidification phase

eutectic	$T_{\text{eut}}^*(Q, V) = m_1 + \sqrt{m_2 - m_3 * \sqrt{QV}}$	Equation 25
primary $\beta$ -Ti	$T_{\beta}^* = -n_1\sqrt{QV} + n_1\sqrt{(QV)^2 - n_2 * QV * V^{w_{\beta}} + n_3 * QV} + T_0$	Equation 26
primary TiB	$T_{\text{TiB}}^* = -p_1\sqrt{QV} + p_1\sqrt{(QV)^2 - p_2 * QV * V^{w_{\text{TiB}}} + p_3 * QV} + T_0$	Equation 27

Table 20 Parameters for interfacial temperature equations in Table 19

Solidification mode	Material-related parameter in Equation 25-Equation 27
eutectic	$m_1 = \frac{(T_0 + T_{\text{eut}}^{\text{equ}})}{2}; m_2 = \frac{1}{4}(T_0 - T_{\text{eut}}^{\text{equ}})^2; m_3 = \frac{A_{\text{eut}}}{\sqrt{2\pi k}};$
primary $\beta$ -Ti	$n_1 = \frac{1}{4\pi k D_l}; n_2 = 8\pi k D_l A_{\beta}; n_3 = 8\pi k D_l (T_{\text{liq}-\beta}^{\text{equ}} - T_0);$
primary TiB	$p_1 = \frac{1}{4\pi k D_l}; p_2 = \pi k D_l A_{\text{TiB}}; p_3 = 48\pi k D_l (T_{\text{liq}-\text{TiB}}^{\text{equ}} - T_0);$

where  $T_{\beta}^*$ ,  $T_{TiB}^*$ ,  $T_{eut}^*$  are interface temperature of primary  $\beta$ -Ti, primary TiB & eutectic TiB/ $\beta$ -Ti phase for a fixed composition  $C_0$ ;  $T_{eut}^{equ}$ ,  $T_{\beta}^{equ}$ ,  $T_{TiB}^{equ}$  are the equilibrium eutectic temperature and equilibrium liquidus temperature or extrapolation of liquidus line for  $\beta$ -Ti phase & TiB phase at composition  $C_0$  in phase diagram(Fig 14);

Table 21 values for Ti6Al4V-xB material properties used in calculation of material-related parameters in Table 20

B%	$T_{eut}^{equ}$ (°C)	$T_{liq-\beta}^{equ}$ (°C)	$T_{liq-TiB}^{equ}$ (°C)	K (W/mk)	$D_l \times 10^{-5}$ (m <sup>2</sup> s <sup>-1</sup> )	$A_{eut}$	$A_{\beta}$	$A_{TiB}$	$W_{\beta}$	$W_{TiB}$	$\eta$
1%	1602	1633	1551	7.5	19.4	55	0.6		0.65		Equation 10
2%	1613	1588	1664	7.5	20.0	320	1.7		0.7		Equation 10
5%	1615	1422	1832	7.5	24.7	300	0.5	55	0.4	0.31	Equation 10

Fig 69 shows schematically how LPBF solidification process map for hypoeutectic and hyper-eutectic Ti6Al4v-xB is developed from the equations in Table 19. It should be noted that the product of absorbed laser power and laser scanning speed ( $Q \cdot V$ ) is fixed in Fig 69(a,b-2). As shown in Fig 69, for a fixed Ti6Al4v-xB composition,  $T_{eut}^*$  could be considered as a function solely dependent on the variable ( $Q \cdot V$ ), and  $T_{TiB}^*$  and  $T_{\beta}^*$  could be considered as functions with two variables, ( $Q \cdot V$ ) and  $V$ . Therefore, as laser scan velocity increases and laser absorbed power decreases to keep a fixed ( $Q \cdot V$ ) value,  $T_{TiB}^*$  and  $T_{\beta}^*$  decreases with different rates,  $T_{eut}^*$  does not change but it differs from the equilibrium eutectic temperature predicted in phase diagram (Fig 69(a,b-1)). Such different trends for  $T_{TiB}^*$ ,  $T_{\beta}^*$  and  $T_{eut}^*$  are schematically shown in Fig 69 (a-2) and (b-2), which results in that for all the [ $Q$ ,  $V$ ] combinations with a fixed ( $Q \cdot V$ ) value, there is a critical [ $Q$ ,  $V$ ] combinations for hypo-eutectic Ti6Al4v-xB, such as [ $Q, V$ ]=[ $R_2/V_A$ ,  $V_A$ ] for the curve with ( $Q \cdot V$ ) product fixed at  $R_2$  in Fig 69 (a-2). This [ $Q$ ,  $V$ ] combination makes  $T_{\beta}^*$  equal to  $T_{eut}^*$ , which corresponds to the solidification  $Q$ - $V$  process map in Fig 69 (a-3) that on the constant  $Q \cdot V$  curve with ( $Q \cdot V$ )= $R_2$ , solidification transition occurs at the dividing point [ $Q$ ,  $V$ ]=[ $R_2/V_A$ ,  $V_A$ ] resulting in primary- $\beta$  Ti solidification at low- $Q$  high- $V$  part of the curve (blue dashed line) and coupled eutectic solidification at high- $Q$  low- $V$  part of the curve (yellow dashed line). Following this procedure, the critical [ $Q$ ,  $V$ ] combinations for solidification mode transition could be found for each constant  $Q \cdot V$  curves, labeled as A-D in Fig 69 (a-3). By connecting these [ $Q$ ,  $V$ ] points for solidification transition on different constant  $Q \cdot V$  curves, the solidification transition  $Q$ - $V$  thresholds could be obtained for the hypoeutectic Ti6Al4V-xB, indicated

by the black bold line in Fig 69 (a-3). The Q-V process space above the threshold is expected to lead to primary- $\beta$  solidification, and the Q-V process space below the threshold is expected to result in coupled eutectic solidification, indicated by the regions with blue and yellow dashed lines respectively. Based on the same approach, solidification Q-V thresholds could be obtained for hyper-eutectic Ti6Al4V-xB, as shown in Fig 69 (b-1)-(b-3). Unlike hypo-eutectic Ti6Al4V-xB, hyper-eutectic Ti6Al4V-xB has two solidification transition Q-V thresholds, one for the transition from primary TiB solidification to primary- $\beta$  solidification, the other for the transition from primary- $\beta$  solidification to coupled eutectic solidification, shown as black and red bold lines in Fig 69 (b-3). These two thresholds divided the Q-V space into three regions, with each Q-V region corresponding to primary TiB, primary  $\beta$ -Ti and eutectic solidification mode respectively, as marked by the regions with red, blue and yellow dashed lines in Fig 69 (b-3).

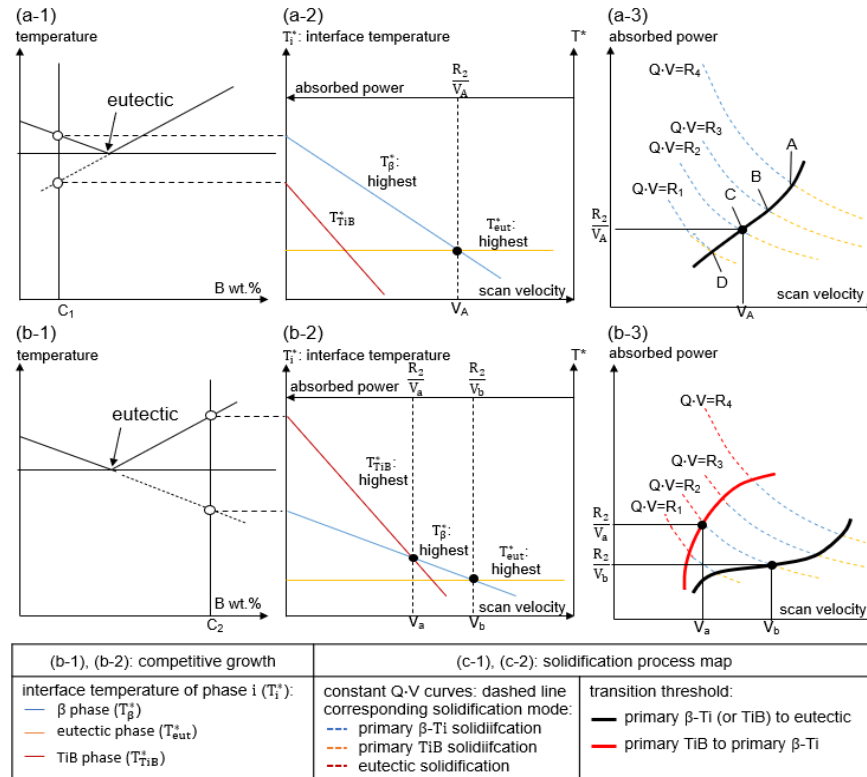


Fig 69 general workflow to develop LPBF process map for solidification microstructure selection for hypo-eutectic Ti6Al4V-xB alloy (a-1~3) and hyper-eutectic Ti6Al4V-xB alloy (b-1~3): (a-1), (b-1): schematic phase diagram; (a-2), (b-2): schematic showing the change of interfacial temperature of each solidification phase with absorbed power(Q) and laser scan velocity (V) for [Q, V] combinations with a fixed (Q·V) product; (a-3), (b-3): schematic to show how to develop Q-V threshold for solidification mode transition

### 7.7.2 Model evaluation

In chapter 7.7.1, an analytical criteria model to determine solidification mode transition for LPBF of Ti6Al4V-xB was developed. In this chapter, the validity of this model was evaluated by the experimental microstructure P-V process map for Ti6Al4V-1, 2, 5wt.%B, as shown in Fig 62(a-c). The microstructure process maps present four types of melt pool microstructure for the 3 B% level(1,2,5%B) and 14 P-V sets tested in this study. They were referred to as type (i)-(iv) microstructure in this work, with their typical microstructure image presented in Fig 61(a)-(d). Their corresponding solidification modes were summarized in Table 17. The solidification mode of type (i)-(iv) microstructure were identified by the following reasons: for these four microstructure, type(i) and (iii) (Fig 61(a), Fig 61(c)) show isolated TiB whisker microstructure, type(ii) (Fig 61(b)) show continuous TiB network and type(iv) (Fig 61(d)) shows coexistence of isolated TiB whisker and hollow-centered TiB rod. The isolated TiB whiskers and hollow-centered TiB rods are consistent with the eutectic-TiB and primary-TiB morphologies observed in the arc-melted Ti6Al4V-xB alloy button in this study (Fig 56) and also commonly observed from previous studies in traditionally-processed hypo-eutectic and hyper-eutectic Ti6Al4V-xB respectively [115][106][105]. Banerjee et al [115] fabricated Ti-B material by LENS-additive manufacturing and confirmed with orientation imaging microscopy (OIM) that the isolated TiB whiskers and hollow-centered TiB rods are the products of primary  $\beta$  solidification and primary TiB solidification respectively. On the other hand, the continuous TiB network in type(ii) microstructure (Fig 61 (b)) shows morphological similarity to coupled eutectic solidification microstructure of several laser-processed Titanium material systems, including Ti-B system[179], Ti-Al system[180] and Ti-Ni-Si system [181]. Based on this, type(i) and (iii) microstructure in Fig 61 (a) and (c) were distinguished as primary  $\beta$  solidification microstructure. Type (ii) microstructure in Fig 61 (b) was likely to be coupled eutectic solidification product. While type (iv) melt pool microstructure in Fig 61 (d)) were categorized as primary TiB solidification microstructure.

P-V maps for solidification mode were developed for Ti6Al4V-1, 2, 5 wt.%B, as listed in Fig 70. The experimental data point was obtained by relating the solidification mode to the microstructure type for each data point in the microstructure process maps (Fig 62). Besides the experiment results from this work, the experimental results from studies of Cai et al[182] and Attar et al[120] were also plotted in Fig 70. In Fig 70, the critical Q-V curves as the solidification mode transition thresholds were developed from the analytical model in chapter 7.7.1 (Table 19) through the procedure schematically

shown in Fig 69. For the equation models in Table 19, the value of the material-related parameters ( $m_1$ ,  $m_2$ , etc.) for Ti6Al4V-1, 2, 5 wt.%B were calculated using the material property values in Table 21. In Table 21,  $A_{TiB}$ ,  $A_\beta$ ,  $A_{eut}$ ,  $w_\beta$ ,  $w_{TiB}$  were estimated by fitting with experimental results, and the absorbed power ( $Q$ ) is calculated by a self-developed absorptivity in Equation 10. Details about developing the absorptivity model and its applicability to Ti6Al4V-1,2,5%B could be found in chapter 5 and chapter 7.2. Other material properties were obtained from previous studies as summarized in Table 5 or prediction using Thermo-Calc software[35].

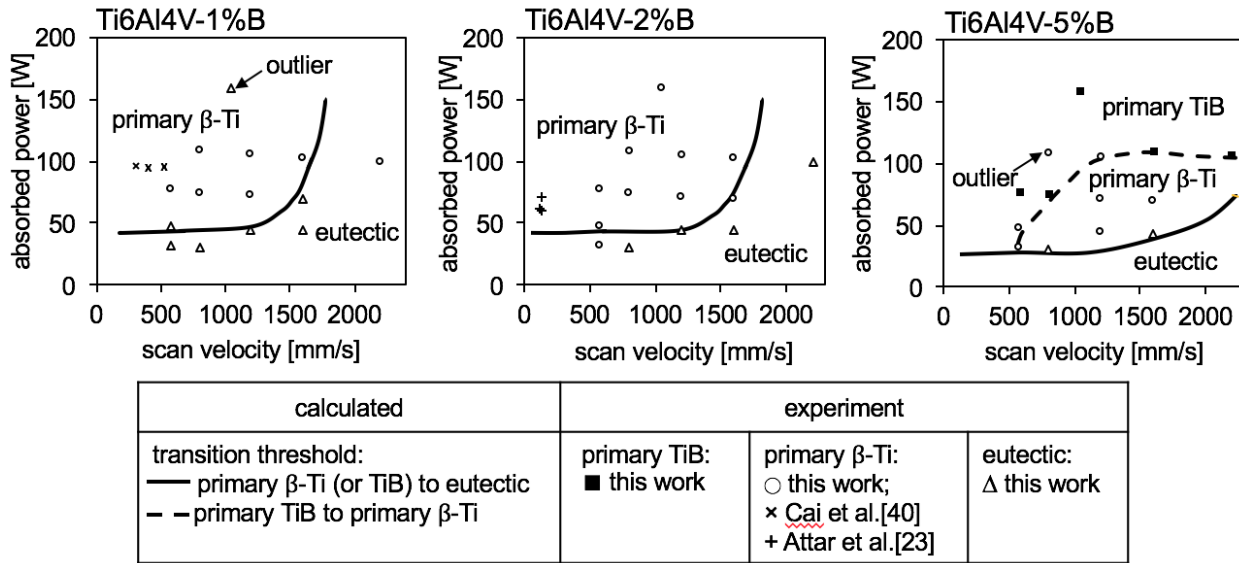


Fig 70 LPBF process map for solidification mode selection for Ti6Al4V-1, 2, 5 wt.%B: black bold and dashed lines: solidification mode transition thresholds, developed from equation models in Table 19; experimental data points: obtained from this work and studies from Cai et al[182] and Attar et al. [120], different labels represent different melt pool microstructure, with the typical image and solidification mode presented in Fig 61 and Table 17.

Fig 70 shows that for the three Ti6Al4V-xB material of investigation, their model-developed Q-V thresholds for solidification mode transition show good agreement to most of the experimental data points. However, there are two outliers, as marked by the arrows in Fig 70. For these two outliers, the corresponding melt pools were found to show typical keyholing geometry, as indicated by the P-V map of melt pool geometry for Ti6Al4V-xB in Fig 58. Therefore, the inconsistency between experimental result and model prediction at these two corresponding [B%, P-V] combinations might be explained by the unique laser-material interaction and complicated melt pool flow for keyholing mode.

The solidification P-V process map in Fig 70 suggests that for LPBF processing of Ti6Al4V-xB, no matter hypo- or hyper-eutectic, a considerable number of P-V combinations might lead to non-equilibrium solidification mode different from the prediction by phase diagram (Fig 14). A great advantage underlying is that LPBF processing of high-B% hyper-eutectic Ti6Al4V-xB might be able to alter its solidification mode from primary TiB solidification to coupled-eutectic or even primary  $\beta$ -Ti solidification mode, and thus allow all TiB precipitates to form as fine-size eutectic TiB and completely eliminates the existence of primary TiB in Ti-matrix. This advantage is exemplified by Ti6Al4V-5B in this study, which shows a considerably large Q-V space in its solidification process map (Fig 70) that lead to coupled-eutectic even primary  $\beta$ -Ti solidification. The resulting microstructures, as shown in Fig 61 (b) and (c) respectively, presents micron-scale TiB network architecture and nano-scale isolated TiB whisker for the former and latter. For LPBF processing, its ability to alter Ti6Al4V-xB solidification mode by choosing different P-V parameters not only brings the benefits of effective TiB precipitate refinement but also indicates the promising potential of LPBF processing as the microstructure engineering tool for TMC material, as a variety of TMC microstructures might be obtained by selecting P-V parameters within process window for different solidification mode.

Nevertheless, certain Ti6Al4V-xB melt pool microstructure transitions observed in this study were not readily addressed by this equation model. One is the transition between the melt pool microstructure of the type (i) and type(iii) microstructure (Fig 61(a), (c)). This could not be addressed by the model in chapter 7.7.1 as they belong to the same solidification mode (primary  $\beta$  solidification) as shown in Table 17. As shown in Table 17, they both show isolated-whisker TiB precipitates but with the first type showing uniform distribution while the second one showing distribution in a network arrangement. Table 17 also shows that the first microstructure type occurs in Ti6Al4V-1, 2%B while the second type only occurs in Ti6Al4V-5%B. Thus, a possible explanation for this difference in TiB distribution might be the much higher constitutional supercooling of Ti6Al4V-5%B compared to Ti6Al4V-1, 2%B. In this case, when they went through primary  $\beta$  solidification, primary  $\beta$ -Ti grain in Ti6Al4V-1,2%B and in Ti6Al4V-5%B might show planar/columnar morphology difference[183]. The other is the microstructure transition within one melt pool, such as the one shown in Fig 66, which was likely to be caused by melt pool flow in the melt pool. As shown earlier, the equation model for undercooling (Equation 25-Equation 27) was built on the steady-state assumption and thus could not address the influence of melt pool flow.

As shown earlier in chapter 7.6, TiB refinement to nano-scale and suppressing primary TiB growth is helpful to enhance mechanical properties of Ti6Al4V-xB material and the TiB-network architecture for TiB-TMC material was experimentally observed to increase creep resistance and corrosion resistance compared to their counterpart with uniformly-distributed TiB whisker microstructure. Above discussion indicates that these two microstructure effects were likely to be achieved by manipulating hyper-eutectic Ti6Al4V-5%B solidification into primary  $\beta$ -Ti solidification mode and by manipulating non-eutectic Ti6Al4V-1,2,5B into coupled-eutectic solidification mode under the guidance of the solidification P-V process map (Fig 70). This was supported by the melt pool hardness measurement presented in chapter 7.5: As shown in Fig 68, the hyper-eutectic Ti6Al4V-2%B and Ti6Al4V-5%B melt pool both exhibits a sudden hardness enhancement if the laser scan velocity increase alter the melt pool microstructure into coupled eutectic or primary-  $\beta$  solidification microstructure, which correspond to type(ii) with cellular-network TiB and (iii) microstructure with nano-scale TiB respectively (Fig 61(b),(c)). This hardness enhancement might be a combined result of nano-scale TiB precipitate refinement and the TiB network architecture as demonstrated in the previous studies [106,115,116,119,120]. In the solidification process map (Fig 70), the Q-V parameters leading to this sudden hardness increase corresponds to the transition thresholds for the process windows of coupled eutectic for Ti6Al4V-1,2,5%B or non-equilibrium primary-  $\beta$  solidification for Ti6Al4V-5%B. This suggests that the analytical equation model developed in this study might provide guideline for P-V process selection for LPBF fabrication of Ti6Al4V-xB to obtain superior mechanical property.

## 7.8 Powder-free method: range of application

In this study, we found three factors that must be considered when adopting the powder-free method for LPBF alloy development. The first factor was the dimensional inconsistency of powder/bulk melt pool when keyholing occurs (chapter 5) since the adopted laser absorptivity model (Equation 10) might under-estimate the absorptivity when keyholing occurs. However, the P-V threshold for keyholing was easily identified by melt pool geometry P-V mapping and can be excluded from analysis. The second factor was the reliability of the absorptivity model as composition changed. In this case, the absorptivity was likely to be different from Ti6Al4V-10wt.%B and Ti6Al4V. This deviation in absorptivity might be distinguished by the melt pool dimension deviation as presented in chapter 7.2. The third factor was the melt pool inconsistencies along the laser track length when starting material shows coarse precipitate. In this study, this observation again only occurred at 10

wt% B. As shown in Fig 71, the arc-melted Ti6Al4V-10B button contained boride precipitates were only partially melted at the bottom of melt pool (Fig 71 (b)), due to its length scale comparable to the laser beam diameter (100  $\mu\text{m}$  for EOS M290). This suggests microstructure and thermal property variation of arc-melted Ti6Al4V-10%B button at the scale of laser beam focused diameter. The inconsistent melt pool behavior for single-track on the arc-melted button would complicate its melt pool comparison to single-track on powder.

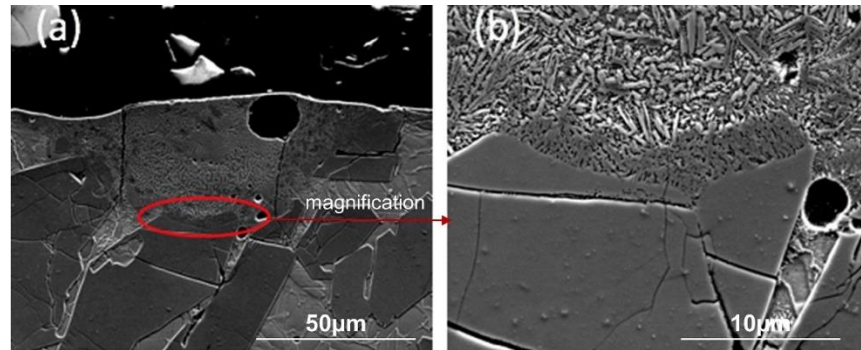


Fig 71 coarse boride pre-existing from arc-melting: (a) whole melt pool; (b) high magnification image of red circle area in (a)

In the context of this study, these limitations only influence the accuracy of Ti6Al4V-10wt.%B composition evaluation and the powder-free method still produced a significant amount of useful information for LPBF alloy and process design.

## 7.9 Results Summary

This chapter investigated LPBF processing with Ti6Al4V-xB, focusing on finding the promising LPBF composition range by studying the influence of B% content and P-V parameter on melt pool geometry and solidification microstructure evolution. Four trial Ti6Al4V-xB composition were investigated, with x= 1,2,5, 10 wt.%B. Conclusions obtained in this chapter were summarized below:

- 1) For each trial Ti6Al4V-xB composition, P-V process map for melt pool geometry and microstructure were developed and preliminary process windows were identified.
- 2) Five different melt pool microstructures were observed for the 56 tested [B%, P-V] combinations. The most promising were microstructures that exhibited continuous or discontinuous cellular TiB network architecture with a sub-micron network spacing, referred to as type (ii) and (iii) microstructure in this paper.
- 3) 2-5 wt% B was identified as a promising composition range for SLM processing route because its corresponding Ti6Al4V-xB alloy presented a large P-V process window, showed promising microstructures (type (ii) and (iii)) with little variation across P-V space, small melt pool dimension deviations from Ti6Al4V, and greatly enhanced and stable hardness across P-V space.
- 4) An analytical equation model based on the competitive growth mechanism was developed to determine the solidification mode transition criteria for LPBF melt pool solidification with Ti6Al4V-xB. The model was developed as an integral function of P-V process parameter and Ti6Al4V-xB material properties. The analytical model was used to produce P-V process maps for Ti6Al4V-1,2,5%B solidification mode selection (primary- $\beta$ , coupled eutectic and primary TiB solidification). The model-based process maps show good agreement to the experimental microstructure process map. This shows the presented approach for developing solidification mode transition criteria could be helpful to predict LPBF solidification microstructure.
- 5) The model prediction and experimental characterization both show that LPBF laser deposition allows process window for coupled-eutectic solidification to exist for Ti6Al4V-1, 2, 5%B, covering hypo- and hyper-eutectic range. The coupled-eutectic microstructure was likely to show continuous

TiB network morphology with micron-scale network spacing. The process map demonstrates the ability of LPBF processing to tailor TiB precipitate morphology and distribution architecture by manipulating solidification mode.

6) Ti6Al4V-1, 2, 5%B melt pool generated by the 14 P-V sets all show efficient extra hardening from the arc-melted counterpart with corresponding Ti6Al4V-xB composition. For the same Ti6Al4V-xB material, adopting different P-V sets led to evident variance in melt pool hardness, showing a general trend of hardness increasing with higher laser scan velocity and lower laser power. A sudden increase in hardness was observed when laser scan velocity increase across the P-V threshold for coupled eutectic solidification of Ti6Al4V-1, 2, 5%B presented in the calculated P-V process map.

## 8 Conclusion and Hypotheses Revisited

- **Hypotheses revisited:**

### **Hypothesis 1):**

For the same P-V parameters and alloy compositions, melt pool generated by laser re-melting bulk alloy surface (no-powder case) could provide sufficient approximation for dimension, geometry and microstructure of melt pool generated by laser melting of bulk alloy substrate with one powder layer addition (powder-added case).

### **Hypothesis 1) evaluation result:**

Chapter 5, chapter 6.1.2, chapter 6.2.2 provided evaluation for hypothesis 1).

Dimension, geometry and microstructure of powder-added melt pool could be sufficiently approximated by no-powder melt pool for most of the P-V space for LPBF operation. While some discrepancies exist in limited P-V region as following:

Dimensional: Chapter 5 compares the melt pool dimension for no-powder and powder-added H13 steel melt pools and Ti6Al4V melt pools across wide P-V process range, which shows small deviation within 7% was achieved between no-powder and powder-added melt pool width at same Q-V combinations except two cases: one is for melt pools with typical keyholing geometry; the other is for melt pools fabricated by high laser output approaching LPBF machine operation limit. Thus, the validity of hypothesis 1) was supported by the melt pool dimensional consistency with and without powder presence except for these two cases.

Geometrical: Chapter 6.1.2 compares the P-V mappings for no-powder and powder-added H13 steel melt pool geometry, which show consistency in P-V windows for keyholing and undermelt and most region in P-V window for balling. The only difference between the two maps is a slight shift in the P-V threshold for balling occurrence. Thus, the validity of hypothesis 1) was supported by the melt pool geometrical consistency with and without powder presence at most P-V space for LPBF operation, except at the small P-V space near the balling threshold.

Microstructural: H13 steel melt pool presented an inhomogeneous microstructure, as shown in chapter 6.2. The local vol% of inhomogeneous microstructure in melt pools fabricated by different P-V sets were measured and summarized into P-V mappings. The microstructure P-V maps for no-

powder and powder-added melt pools were consistent in most P-V space except the P-V region for under-melt geometry melt pool formation, indicating that the difference in the local vol% of inhomogeneous microstructure between no-powder and powder-added H13-steel melt pool fabricated by same P-V set is no more than 10% except when P-V setting is within the under-melt P-V region (see Table 23). Thus, the validity of hypothesis 1) was supported by the melt pool microstructure consistency with and without powder presence at most P-V space, except at the small P-V space leading to under-melt geometry, that is, melt pool with depth smaller than the powder layer thickness.

### **Hypothesis 2):**

LPBF melt pools of H13 steel and M2 steel were observed to show microstructure inhomogeneity. The source of the observed inhomogeneity was local thermal condition variation in different regions in the melt pool during solidification:

For H13 steel, the local cooling rate variation in melt pool result in different microsegregation behavior at different regions in the melt pool, in turn causing melt pool microstructure inhomogeneity.

For M2 steel, the local temperature gradient and solidification rate variation in melt pool causes columnar-to-equiaxed transition to occur in the melt pool.

### **Hypothesis 2) evaluation result:**

Chapter 6.2 provided evaluation for hypothesis 2).

Chapter 6.2.1 showed that: for H13 steel, microstructure inhomogeneity was present as cellular-network microstructure and isolated-needle microstructure co-existed in the same melt pool, which were referred to as type (A) and (B) microstructure. For M2 steel, microstructure inhomogeneity was induced by the occurrence of columnar-to-equiaxed transition (CET).

Based on hypothesis 2), a mechanism was proposed to explain the inhomogeneous microstructure evolution observed in the H13 steel melt pools. The proposed mechanism considers that during solidification, the local region with type (A) microstructure presented a higher-level cooling rate that induced sufficient solute pile-up at the cellular boundary due to microsegregation, which lowers the local  $M_s$  temperature at this location, and in turn preserves austenite in cellular-arrangement. While

the local region with type (B) microstructure presented different microsegregation behavior due to its lower-level cooling rate and thus presented large-needle martensite but no cellular-arranged austenite. Following the mechanism, we conducted theoretical analysis by coupling melt pool cooling rate profile numerical calculation with DICTRA simulation. The calculation was performed for various P-V sets across wide process range, which confirmed the existence of different microsegregation behavior for local region with higher and lower-level cooling rate in each resulting melt pool. They were predicted to show type (A) and (B) microstructure based on the proposed mechanism. The predicted vol% and local distribution of type (A) and (B) microstructure show agreement to the experimental microstructure observation in the corresponding melt pool. The consistency between theoretical calculation and experimental observation across wide P-, V-range supports the validity for hypothesis 2). Besides, austenite and microsegregation was also experimentally measured at the cellular network of type (A) microstructure, which provide further validation for hypothesis 2).

For M2 steel, P-V process map was developed based on experimental characterization of single-track microstructure for 28 P-V sets, which presents P-V windows leading to fully columnar dendritic, columnar+equiaxed mixed and mainly equiaxed dendritic melt pool microstructure. G-R thermal criteria (G: temperature gradient; R: solidification velocity) for CET of M2 steel under LPBF solidification condition was developed based on the CET model of Gäumann et al. Based on hypothesis 2), we combined the numerical calculation of melt pool G-, R- profile during solidification with the developed CET criteria to predict microstructure for the 28 selected P-V sets, which were summarized into a P-V process map for microstructure prediction (columnar/equiaxed). The predicted and experimental P-V process maps show good agreement to each other in the P-V process space with no balling occurrence, which supports the validity for hypothesis 2) in this P-V range. While some discrepancies between prediction and experimental microstructural observation exist in P-V space with balling occurrence, which could be caused by underestimating the effect of melt pool fluid flow on CET microstructural transition. Therefore, for hypothesis 2), its application range was considered to be within the non-balling P-V space, and it could be further revised by including both melt pool thermal and mass transfer effect on CET microstructural transition in M2 steel melt pool.

### **Hypothesis 3):**

For LPBF processing of Ti6Al4V-xB system, the rapid solidification during melt pool deposition leads to non-equilibrium coupled-eutectic solidification for hyper-eutectic Ti6Al4V-xB material

### **Hypothesis 3) evaluation result:**

A model for solidification mode transition was developed for Ti6Al4V-xB based on the competitive growth principle. Based on this model, P-V process map for Ti6Al4V-xB solidification mode transition was calculated, which showed the existence of P-V window leading to coupled-eutectic solidification for Ti6Al4V-5 wt.%B, a typical hyper-eutectic Ti6Al4V-xB. The developed P-V map shows good consistency with the experimental P-V map for solidification microstructure evolution. The consistency in theoretical analysis and experimental microstructure observation for coupled eutectic solidification existence supports the validity of hypothesis 3).

Other conclusions related to each alloy systems of investigation are summarized at the end of chapter 6 and chapter 7. They are also revisited here as given below:

### **H13 steel**

1) P-V process maps of melt pool geometry were developed for both no-powder and powder-added laser scan with H13-steel. They showed great consistency to each other except a slight shift in balling P-V threshold, suggesting the influence of powder addition on balling formation.

2) Single-track and multi-track pads show microstructure inhomogeneity at some P-V combinations, exhibiting cellular-network microstructure and isolated-needle microstructure at top and bottom regions of one melt pool (referred to as type (A) and (B) microstructure in this document). Retained austenite was found in the cellular boundary of type (A) microstructure, which presented segregation of C, Cr, V, Mo. Type (A) microstructure presented higher hardness than the nearby type (B) microstructure within the same melt pool.

3) Melt pool microstructure of the 40 tested P-V sets were classified into four categories, based on different inhomogeneity level. Based on this categorization, microstructure P-V process maps were developed for both no-powder and powder-added laser scan, showing great consistency to each other at most of the P-V space.

4) A microstructure evolution mechanism was proposed for the non-equilibrium solidification in LPBF melt pool of H13 steel. The mechanism explains the presence of retained austenite in type (A) microstructure of melt pool as a result of solidification microsegregation, which stabilizes the last-solidified austenite by solute pile up to lower its  $M_s$  temperature. This was supported by the experimental observation of microsegregation at the cellular boundary in type (A) microstructure, where austenite is present. The mechanism explains the microstructure inhomogeneity in H13 steel melt pool as a result of varied microsegregation behavior at local regions with different microstructure in the melt pool. This shows consistency with microsegregation estimation through coupling DICTRA simulation and melt pool thermal profile numerical calculation, showing the region with type (A) and (B) microstructure presenting noticeable and minimal segregation. Based on the calculated microsegregation result, prediction was made to estimate the vol% and distribution of type (A) and (B) microstructure in the melt pool. The prediction showed good agreement to the experimental observation of melt pool microstructure. This study shows the effectiveness of combining DICTRA and melt pool thermal calculation to predict LPBF solidification microstructure.

5) Pad characterization showed that melt pool with different microstructure inhomogeneity levels resulted in different cracking susceptibility, and their corresponding P-V space in the microstructure P-V process map was estimated as P-V window with higher and lower cracking tendency. Crack density was measured for cube built by P-V sets with different cracking tendency prediction. The result showed good agreement with the prediction.

## **M2 steel**

1) Single-track melt pools of M2 steel with fully columnar dendritic, columnar+equiaxed mixed and mainly equiaxed dendritic microstructure were observed for the 28 P-V sets selected in this study. A microstructure P-V process map was constructed to summarize single-track characterization. It shows a trend of higher vol.% of equiaxed dendrite in the melt pool by increasing laser power and scan velocity.

2) G-R criterion model was developed to determine CET occurrence for M2 steel LPBF solidification based on the analytical CET model from Gäumann et al. It predicts the thermal condition favoring equiaxed dendrite growth as  $\frac{G^{3.8}}{R} < 7.8 \times 10^{13}$ .

3) Vol.% and distribution of equiaxed dendritic microstructure in LPBF melt pool of M2 steel could be predicted by coupling the developed G-R criteria with numerical calculation for melt pool solidification thermal profile. Based on this approach, a microstructure process map was calculated for LPBF of M2 steel to estimate the variation of CET tendency across P-V space. It indicates the P-V window favoring equiaxed dendrite growth as P-V space with both high P/V ratio and large V value.

4) The application range of adopting the developed G-R criteria to estimate CET in LPBF solidification is identified as P-V space with no balling phenomena, as confirmed by the good consistency between the experimental and predicted process map in this P-V space. Discrepancy between microstructure prediction and the experimental result was found in balling P-V space, which could arise from underestimating the nuclei density for melt pool with balling formation.

5) It is shown by both experimental results and numerical calculation that vol.% of equiaxed dendritic microstructure in LPBF melt pool of M2 steel could be remarkably enhanced from <5% (i.e., fully columnar) to about 50% by choosing different P-V parameters. Numerical calculation shows that the effectiveness of P-V process optimization on promoting equiaxed growth for LPBF microstructure lies in its capability to alter G-profile and R-profile for LPBF melt pool solidification. By coupling the developed G-R criteria and the calculated melt pool thermal profile, P-V window for promoting equiaxed grain growth was identified, which lies in the region with both high P/V ratio and high scan velocity. Same calculation approach could be adopted to estimate P-V map for LPBF solidification microstructure (columnar/equiaxed) with other alloys of interest. This could be helpful for understanding and designing LPBF part microstructure.

### **Ti6Al4V-xB**

1) Four trial Ti6Al4V-xB composition were investigated, with x= 1,2,5, 10 wt.%B. For each trial Ti6Al4V-xB composition, P-V process map for melt pool geometry and microstructure were developed and preliminary process windows were identified.

2) Five different melt pool microstructures were observed for the 56 tested [B%, P-V] combinations. The most promising were microstructures that exhibited continuous or discontinuous cellular TiB

network architecture with a sub-micron network spacing, referred to as type (ii) and (iii) microstructure in this paper.

3) 2-5 wt% B was identified as a promising composition range for SLM processing route because its corresponding Ti6Al4V-xB alloy presented a large P-V process window, showed promising microstructures (type (ii) and (iii)) with little variation across P-V space, small melt pool dimension deviations from Ti6Al4V, and greatly enhanced and stable hardness across P-V space.

4) An analytical equation model based on the competitive growth mechanism was developed to determine the solidification mode transition criteria for LPBF melt pool solidification with Ti6Al4V-xB. The model was developed as an integral function of P-V process parameter and Ti6Al4V-xB material properties. The analytical model was used to produce P-V process maps for Ti6Al4V-1,2,5%B solidification mode selection (primary- $\beta$ , coupled eutectic and primary TiB solidification). The model-based process maps show good agreement to the experimental microstructure process map. This shows the presented approach for developing solidification mode transition criteria could be helpful to predict LPBF solidification microstructure.

5) The model prediction and experimental characterization both show that LPBF laser deposition allows process window for coupled-eutectic solidification to exist for Ti6Al4V-1, 2, 5%B, covering hypo- and hyper-eutectic range. The coupled-eutectic microstructure was likely to show continuous TiB network morphology with micron-scale network spacing. The process map demonstrates the ability of LPBF processing to tailor TiB precipitate morphology and distribution architecture by manipulating solidification mode.

6) Ti6Al4V-1, 2, 5%B melt pool generated by the 14 P-V sets all show efficient extra hardening from the arc-melted counterpart with corresponding Ti6Al4V-xB composition. For the same Ti6Al4V-xB material, adopting different P-V sets led to evident variance in melt pool hardness, showing a general trend of hardness increasing with higher laser scan velocity and lower laser power. A sudden increase in hardness was observed when laser scan velocity increase across the P-V threshold for coupled eutectic solidification of Ti6Al4V-1, 2, 5%B presented in the calculated P-V process map.

## 9 Project major contribution

### Methodologies

General	Developed and evaluated the efficiency of a powder-free experimental framework for LPBF investigation
H13 steel	Developed and validated a calculation method for LPBF melt pool microstructure inhomogeneity prediction
M2 steel	Developed and evaluated the application range of a G-R thermal criteria for predicting CET under LPBF melt pool solidification
Ti6Al4V-xB	Developed and validated an analytical model for P-V threshold leading to primary solidification mode transition

### Outcomes

H13 steel; M2 steel; Ti6Al4V-xB	Developed preliminary P-V process windows for porosity control
H13 steel	Developed P-V process map for microstructure inhomogeneity control
	Identified P-V process window for cracking control based on microstructure investigation
M2 steel	Developed P-V process map for promoting CET in melt pool solidification
	Identified composition range for developing promising LPBF material candidates
Ti6Al4V-xB	Developed analytical model for P-V threshold leading to LPBF solidification mode transition
	Identified P-V window for non-equilibrium coupled eutectic solidification for hyper-eutectic Ti6Al4V-xB composition

## Reference

- [1] Murr LE, Gaytan SM, Ramirez DA, Martinez E, Hernandez J, Amato KN, et al. Metal Fabrication by Additive Manufacturing Using Laser and Electron Beam Melting Technologies. *J Mater Sci Technol* 2012;28:1–14. [https://doi.org/10.1016/S1005-0302\(12\)60016-4](https://doi.org/10.1016/S1005-0302(12)60016-4).
- [2] Lewandowski JJ, Seifi M. Metal Additive Manufacturing: A Review of Mechanical Properties. *Annu Rev Mater Res* 2016;46:151–86. <https://doi.org/10.1146/annurev-matsci-070115-032024>.
- [3] Kruth JP, Badrossamay M, Yasa E, Deckers J, Thijs L, Van Humbeeck J. Part and material properties in selective laser melting of metals. 16th Int Symp Electromachining, ISEM 2010 2010:3–14.
- [4] Bourell DL (The U of T at A), Leu MC (Missouri U of S and T), Rosen DW (Georgia I of T). Identifying the Future of Freeform Processing. *Univ Texas Austin* 2009:92. <https://doi.org/10.1108/13552549910295514>.
- [5] EOS Titanium Ti64. n.d.
- [6] Material data sheet-FlexLine EOS Titanium TiCP grade 2. 2016.
- [7] EOS MaragingSteel MS1. n.d.
- [8] Francois MM, Sun A, King WE, Henson NJ, Tournet D, Bronkhorst CA, et al. Modeling of additive manufacturing processes for metals: Challenges and opportunities. *Curr Opin Solid State Mater Sci* 2017;21:198–206. <https://doi.org/10.1016/j.cossms.2016.12.001>.
- [9] Gusarov A V., Yadroitsev I, Bertrand P, Smurov I. Model of radiation and heat transfer in laser-powder interaction zone at selective laser melting. *J Heat Transfer* 2009;131:1–10. <https://doi.org/10.1115/1.3109245>.
- [10] Acharya R, Sharon JA, Staroselsky A. Prediction of microstructure in laser powder bed fusion process. *Acta Mater* 2017;124:360–71. <https://doi.org/10.1016/j.actamat.2016.11.018>.
- [11] Zinoviev A, Zinovieva O, Ploshikhin V, Romanova V, Balokhonov R. Evolution of grain structure during laser additive manufacturing. Simulation by a cellular automata method. *Mater Des* 2016;106:321–9. <https://doi.org/10.1016/j.matdes.2016.05.125>.
- [12] Gäumann M, Bezençon C, Canalis P, Kurz W. Single-crystal laser deposition of superalloys:

- processing–microstructure maps. *Acta Mater* 2001;49:1051–62. [https://doi.org/10.1016/S1359-6454\(00\)00367-0](https://doi.org/10.1016/S1359-6454(00)00367-0).
- [13] Yan Z, Liu W, Tang Z, Liu X, Zhang N, Li M, et al. Review on thermal analysis in laser-based additive manufacturing. *Opt Laser Technol* 2018;106:427–41. <https://doi.org/10.1016/j.optlastec.2018.04.034>.
- [14] Shi Q, Gu D, Xia M, Cao S, Rong T. Effects of laser processing parameters on thermal behavior and melting/solidification mechanism during selective laser melting of TiC/Inconel 718 composites. *Opt Laser Technol* 2016;84:9–22. <https://doi.org/10.1016/j.optlastec.2016.04.009>.
- [15] Sames WJ, List FA, Pannala S, Dehoff RR, Babu SS. The metallurgy and processing science of metal additive manufacturing. *Int Mater Rev* 2016;61:315–60. <https://doi.org/10.1080/09506608.2015.1116649>.
- [16] Montgomery CJ, Engineering BSM, Engineering MSM. The Effect of Alloys , Powder , and Overhanging Geometries in Laser Powder Bed Additive Manufacturing 2017.
- [17] Li Y, Zhou K, Tan P, Tor SB, Chua CK, Leong KF. Modeling temperature and residual stress fields in selective laser melting. *Int J Mech Sci* 2018;136:24–35. <https://doi.org/10.1016/j.ijmecsci.2017.12.001>.
- [18] AlMangour B, Grzesiak D, Cheng J, Ertas Y. Thermal behavior of the molten pool, microstructural evolution, and tribological performance during selective laser melting of TiC/316L stainless steel nanocomposites: Experimental and simulation methods. *J Mater Process Technol* 2018;257:288–301. <https://doi.org/10.1016/j.jmatprotec.2018.01.028>.
- [19] Lindgren LE, Lundbäck A, Fisk M, Pederson R, Andersson J. Simulation of additive manufacturing using coupled constitutive and microstructure models. *Addit Manuf* 2016;12:144–58. <https://doi.org/10.1016/j.addma.2016.05.005>.
- [20] Zeng K, Pal D, Stucker B. A review of thermal analysis methods in laser sintering and selective laser melting. 23rd Annu Int Solid Free Fabr Symp - An Addit Manuf Conf SFF 2012 2012:796–814.
- [21] Kou S. *Welding Metallurgy*. 2nd ed. Hoboken, N.J. : Wiley-Interscience; 2003.
- [22] Tang M, Pistorius PC. Inclusions, Porosity, and Fatigue of AlSi10Mg Parts Produced by Selective Laser Melting. 2017. <https://doi.org/10.1016/j.ijfatigue.2016.06.002>.

- [23] Bontha S, Klingbeil NW, Kobryn PA, Fraser HL. Effects of process variables and size-scale on solidification microstructure in beam-based fabrication of bulky 3D structures. *Mater Sci Eng A* 2009;513–514:311–8. <https://doi.org/10.1016/j.msea.2009.02.019>.
- [24] Dehoff RR, Kirka M, Sames WJ, Bilheux H, Tremsin AS, Lowe LE, et al. Site specific control of crystallographic grain orientation through electron beam additive manufacturing. *Mater Sci Technol* (United Kingdom) 2015;31:931–8. <https://doi.org/10.1179/1743284714Y.00000000734>.
- [25] Trapp J, Rubenchik AM, Guss G, Matthews MJ. In situ absorptivity measurements of metallic powders during laser powder-bed fusion additive manufacturing. *Appl Mater Today* 2017;9:341–9. <https://doi.org/10.1016/j.apmt.2017.08.006>.
- [26] King WE, Barth HD, Castillo VM, Gallegos GF, Gibbs JW, Hahn DE, et al. Observation of keyhole-mode laser melting in laser powder-bed fusion additive manufacturing. *J Mater Process Technol* 2014;214:2915–25. <https://doi.org/10.1016/j.jmatprotec.2014.06.005>.
- [27] Plotkowski A, Kirka MM, Babu SS. Verification and validation of a rapid heat transfer calculation methodology for transient melt pool solidification conditions in powder bed metal additive manufacturing. *Addit Manuf* 2017;18:256–68. <https://doi.org/10.1016/j.addma.2017.10.017>.
- [28] Childs THGC, Hauser G, Badrossamay M, Hauser C, Badrossamay M. Selective laser sintering (melting) of stainless and tool steel powders: Experiments and modelling. *Proc Inst Mech Eng Part B J Eng Manuf* 2005;219:339–57. <https://doi.org/10.1243/095440505X8109>.
- [29] Tang M, Pistorius PC, Beuth JL. Prediction of lack-of-fusion porosity for powder bed fusion. *Addit Manuf* 2017;14:39–48. <https://doi.org/10.1016/j.addma.2016.12.001>.
- [30] Soylemez E, Beuth JL, Taminger K. Controlling Melt Pool Dimensions over a Wide Range of Material Deposition Rates in Electron Beam Additive Manufacturing. *Proc 2010 Solid Free Fabr Symp* 2010:571–82.
- [31] Fabbro R. Melt pool and keyhole behaviour analysis for deep penetration laser welding. *J Phys D Appl Phys* 2010;43. <https://doi.org/10.1088/0022-3727/43/44/445501>.
- [32] Eagar TW, Tsai NS. Temperature Fields Produced By Traveling Distributed Heat Sources. *Weld J (Miami, Fla)* 1983;62:346–55.

- [33] Gu D, Yuan P. Thermal evolution behavior and fluid dynamics during laser additive manufacturing of Al-based nanocomposites: Underlying role of reinforcement weight fraction. *J Appl Phys* 2015;118. <https://doi.org/10.1063/1.4937905>.
- [34] Gan Z, Yu G, He X, Li S. Numerical simulation of thermal behavior and multicomponent mass transfer in direct laser deposition of Co-base alloy on steel. *Int J Heat Mass Transf* 2017;104:28–38. <https://doi.org/10.1016/j.ijheatmasstransfer.2016.08.049>.
- [35] Andersson JO, Helander T, Höglund L, Shi P, Sundman B. Thermo-Calc & DICTRA, computational tools for materials science. *Calphad Comput Coupling Phase Diagrams Thermochem* 2002;26:273–312. [https://doi.org/10.1016/S0364-5916\(02\)00037-8](https://doi.org/10.1016/S0364-5916(02)00037-8).
- [36] Rai R, Elmer JW, Palmer TA, Debroy T. Heat transfer and fluid flow during keyhole mode laser welding of tantalum, Ti-6Al-4V, 304L stainless steel and vanadium. *J Phys D Appl Phys* 2007;40:5753–66. <https://doi.org/10.1088/0022-3727/40/18/037>.
- [37] Wang H, Nakanishi M, Kawahito Y. Dynamic balance of heat and mass in high power density laser welding. *Opt Express* 2018;26:6392. <https://doi.org/10.1364/oe.26.006392>.
- [38] Gong H, Gu H, Zeng K, Dilip JJS, Pal D, Stucker B, et al. Melt pool characterization for selective laser melting of Ti-6Al-4V pre-alloyed powder. *Solid Free Fabr Proc* 2014:256–67.
- [39] Cunningham R, Zhao C, Parab N, Kantzos C, Pauza J, Fezzaa K, et al. Keyhole threshold and morphology in laser melting revealed by ultrahigh-speed x-ray imaging. *Science* (80- ) 2019;363:849–52. <https://doi.org/10.1126/science.aav4687>.
- [40] Francis Z. The Effects of Laser and Electron Beam Spot Size in Additive Manufacturing Processes. PhD Diss 2017.
- [41] He Y, Montgomery C, Beuth J, Webler B. Melt pool geometry and microstructure of Ti6Al4V with B additions processed by selective laser melting additive manufacturing. *Mater Des* 2019;183:108126. <https://doi.org/10.1016/j.matdes.2019.108126>.
- [42] Yasa E, Kempen K, Kruth J-P. Microstructure and mechanical properties of maraging steel 300 after selective laser melting. *Solid Free Fabr Symp Proc* 2010:383–96.
- [43] Li R, Shi Y, Wang Z, Wang L, Liu J, Jiang W. Densification behavior of gas and water atomized 316L stainless steel powder during selective laser melting. *Appl Surf Sci* 2010;256:4350–6. <https://doi.org/10.1016/j.apsusc.2010.02.030>.

- [44] Kruth JP, Froyen L, Van Vaerenbergh J, Mercelis P, Rombouts M, Lauwers B. Selective laser melting of iron-based powder. *J Mater Process Technol* 2004;149:616–22. <https://doi.org/10.1016/j.jmatprotec.2003.11.051>.
- [45] Gu D, Shen Y. Balling phenomena in direct laser sintering of stainless steel powder: Metallurgical mechanisms and control methods. *Mater Des* 2009;30:2903–10. <https://doi.org/10.1016/j.matdes.2009.01.013>.
- [46] Yadroitsev I, Smurov I. Selective laser melting technology: From the single laser melted track stability to 3D parts of complex shape. *Phys Procedia* 2010;5:551–60. <https://doi.org/10.1016/j.phpro.2010.08.083>.
- [47] Yang J, Han J, Yu H, Yin J, Gao M, Wang Z, et al. Role of molten pool mode on formability, microstructure and mechanical properties of selective laser melted Ti-6Al-4V alloy. *Mater Des* 2016;110:558–70. <https://doi.org/10.1016/j.matdes.2016.08.036>.
- [48] Scipioni Bertoli U, Guss G, Wu S, Matthews MJ, Schoenung JM. In-situ characterization of laser-powder interaction and cooling rates through high-speed imaging of powder bed fusion additive manufacturing. *Mater Des* 2017;135:385–96. <https://doi.org/10.1016/j.matdes.2017.09.044>.
- [49] Hooper PA. Melt pool temperature and cooling rates in laser powder bed fusion. *Addit Manuf* 2018;22:548–59. <https://doi.org/10.1016/j.addma.2018.05.032>.
- [50] Harrison NJ, Mumtaz K. Reduction of micro-cracking in nickel superalloys processed by Selective Laser Melting: A fundamental alloy design approach. *Acta Mater* 2015;94:59–68. <https://doi.org/10.1016/j.actamat.2015.04.035>.
- [51] Sames WJ, List FA, Pannala S, Dehoff RR, Babu SS. The metallurgy and processing science of metal additive manufacturing 2016:1–46. <https://doi.org/10.1080/09506608.2015.1116649>.
- [52] Krell J, Röttger A, Geenen K, Theisen W. General investigations on processing tool steel X40CrMoV5-1 with selective laser melting. *J Mater Process Technol* 2018;255:679–88. <https://doi.org/10.1016/j.jmatprotec.2018.01.012>.
- [53] Wang M, Li W, Wu Y, Li S, Cai C, Wen S, et al. High-Temperature Properties and Microstructural Stability of the AISI H13 Hot-Work Tool Steel Processed by Selective Laser Melting. *Metall Mater Trans B Process Metall Mater Process Sci* 2019;50:531–42. <https://doi.org/10.1007/s11663-018-1442-1>.

- [54] Holzweissig MJ, Taube A, Brenne F, Schaper M, Niendorf T. Microstructural Characterization and Mechanical Performance of Hot Work Tool Steel Processed by Selective Laser Melting. *Metall Mater Trans B Process Metall Mater Process Sci* 2015;46:545–9. <https://doi.org/10.1007/s11663-014-0267-9>.
- [55] Zhong M, Sun H, Liu W, Zhu X, He J. Boundary liquation and interface cracking characterization in laser deposition of Inconel 738 on directionally solidified Ni-based superalloy 2005;53:159–64. <https://doi.org/10.1016/j.scriptamat.2005.03.047>.
- [56] Li Q, Lin X, Wang X, Yang H, Song M, Huang W. Research on the Grain Boundary Liquation Mechanism in Heat Affected Zones of Laser Forming Repaired K465 Nickel-Based Superalloy. *Metals (Basel)* 2016;6:64. <https://doi.org/10.3390/met6030064>.
- [57] Saunders N, Miodownik AP. CALPHAD: Calculation of Phase Diagrams. A Comprehensive Guide. vol. 1. 1998. [https://doi.org/10.1016/S1470-1804\(98\)80034-5](https://doi.org/10.1016/S1470-1804(98)80034-5).
- [58] Won YM, Thomas BG. Simple model of microsegregation during solidification of steels. *Metall Mater Trans A Phys Metall Mater Sci* 2001;32:1755–67. <https://doi.org/10.1007/s11661-001-0152-4>.
- [59] Chen Q, Sundman B. Computation of Partial Equilibrium Solidification with Complete Interstitial and Negligible Substitutional Solute Back Diffusion. *Mater Trans* 2002;43:551–9. <https://doi.org/10.2320/matertrans.43.551>.
- [60] Tancret F. Thermo-Calc and Dictra simulation of constitutional liquation of gamma prime (  $\gamma'$  ) during welding of Ni base superalloys 2007;41:13–9. <https://doi.org/10.1016/j.commatsci.2007.02.008>.
- [61] Ojo OA, Tancret F. Clarification on “ Thermo-Calc and Dictra simulation of constitutional liquation of gamma prime (  $\gamma'$  ) during welding of Ni-base superalloys ”. *Comput Mater Sci* 2009;45:388–9. <https://doi.org/10.1016/j.commatsci.2008.10.014>.
- [62] Gregori A, Nilsson J. Decomposition of Ferrite in Commercial Superduplex Stainless Steel Weld Metals ; Microstructural Transformations above 700 H C 2002;33.
- [63] Garrison BYJABM. Weld Microstructure Development and Properties of Precipitation-Strengthened Martensitic Stainless Steels 1999:280–91.
- [64] Kou S, Le Y. EFFECT OF QUENCHING ON THE SOLIDIFICATION STRUCTURE AND

TRANSFORMATION BEHAVIOR OF STAINLESS STEEL WELDS. Metall Trans A, Phys Metall Mater Sci 1982;13 A:1141–52. <https://doi.org/10.1007/BF02645495>.

- [65] Kotecki DJ, Siewert TA. WRC-1992 Constitution Diagram for Stainless Steel Weld Metals: A Modification of the WRC-1988 Diagram Refined constitution diagram offers more accurate FN prediction for Cu-containing stainless steels and dissimilar metal joints. 1992.
- [66] Saluja R, Moeed K. Formation, Quantification and Significance of Delta Ferrite for 300 Series Stainless Steel Weldments. Int J Eng Technol Manag Appl Sci 2015;3:23–36.
- [67] Brooks JA, Baskes MI, Greulich FA. in High-Energy Density Stainless Steel Welds „," Ii Ic 1991;22.
- [68] Harrison NJ, Todd I, Mumtaz K. Reduction of micro-cracking in nickel superalloys processed by Selective Laser Melting: A fundamental alloy design approach. Acta Mater 2015;94:59–68. <https://doi.org/10.1016/j.actamat.2015.04.035>.
- [69] Kah DH, Dickinson DW. Weldability of Ferritic Stainless Steels. Weld J (Miami, Fla) 1981;60.
- [70] Kou S. Solidification and liquation cracking issues in welding. Jom 2003;55:37–42. <https://doi.org/10.1007/s11837-003-0137-4>.
- [71] Nishimoto K, Mori H. Hot cracking susceptibility in laser weld metal of high nitrogen stainless steels. Sci Technol Adv Mater 2004;5:231–40. <https://doi.org/10.1016/j.stam.2003.10.006>.
- [72] Noecker FF, DuPont JN. Microstructural development and solidification cracking susceptibility of Cu deposits on steel: Part I. J Mater Sci 2007;42:495–509. <https://doi.org/10.1007/s10853-006-1258-2>.
- [73] Dupont JN. Microsegregation and solidification cracking of an HR-160 weld overlay. J Mater Sci 1997;32:4101–7. <https://doi.org/10.1023/A:1018658025359>.
- [74] Fu CH, Guo YB. Three-Dimensional Temperature Gradient Mechanism in Selective Laser Melting of Ti-6Al-4V. J Manuf Sci Eng Trans ASME 2014;136. <https://doi.org/10.1115/1.4028539>.
- [75] Hunt JD. Steady state columnar and equiaxed growth of dendrites and eutectic. Mater Sci Eng 1984;65:75–83. [https://doi.org/10.1016/0025-5416\(84\)90201-5](https://doi.org/10.1016/0025-5416(84)90201-5).
- [76] Bermingham MJ, StJohn DH, Krynen J, Tedman-Jones S, Dargusch MS. Promoting the columnar to equiaxed transition and grain refinement of titanium alloys during additive

- manufacturing. *Acta Mater* 2019;168:261–74. <https://doi.org/10.1016/j.actamat.2019.02.020>.
- [77] Wei HL, Mukherjee T, DebRoy T. Grain Growth Modeling for Additive. *Proc 6th Int Conf Recryst Grain Growth, ReX GG* 2016 2016:265–9. [https://doi.org/10.1007/978-3-319-48770-0\\_39](https://doi.org/10.1007/978-3-319-48770-0_39).
- [78] Shinde MS, Ashtankar KM. Additive manufacturing–assisted conformal cooling channels in mold manufacturing processes. *Adv Mech Eng* 2017;9:168781401769976. <https://doi.org/10.1177/1687814017699764>.
- [79] Kou S. A criterion for cracking during solidification. *Acta Mater* 2015;88:366–74. <https://doi.org/10.1016/j.actamat.2015.01.034>.
- [80] Kou S, Le Y. Welding parameters and the grain structure of weld metal — A thermodynamic consideration. *Metall Trans A* 1988;19:1075–82. <https://doi.org/10.1007/BF02628392>.
- [81] Janaki Ram GD, Mitra TK, Shankar V, Sundaresan S. Microstructural refinement through inoculation of type 7020 Al-Zn-Mg alloy welds and its effect on hot cracking and tensile properties. *J Mater Process Technol* 2003;142:174–81. [https://doi.org/10.1016/S0924-0136\(03\)00574-0](https://doi.org/10.1016/S0924-0136(03)00574-0).
- [82] DebRoy T, Wei HL, Zuback JS, Mukherjee T, Elmer JW, Milewski JO, et al. Additive manufacturing of metallic components – Process, structure and properties. *Prog Mater Sci* 2018;92:112–224. <https://doi.org/10.1016/j.pmatsci.2017.10.001>.
- [83] Elmer JW, Allen SM, Eagar TW. Microstructural development during solidification of stainless steel alloys. *Metall Trans A* 1989;20:2117–31. <https://doi.org/10.1007/BF02650298>.
- [84] Kurz W, Fisher DJ. Dendrite growth in eutectic alloys: the coupled zone. *Int Mater Rev* 1979;24:177–204. <https://doi.org/10.1179/095066079790136408>.
- [85] Fukumoto S, Kurz W. Prediction of the .DELTA. to .GAMMA. Transition in Austenitic Stainless Steels during Laser Treatment. *ISIJ Int* 1998;38:71–7. <https://doi.org/10.2355/isijinternational.38.71>.
- [86] Pierantoni M, Gremaud M, Magnin P, Stoll D, Kurz W. The coupled zone of rapidly solidified AlSi alloys in laser treatment. *Acta Metall Mater* 1992;40:1637–44. [https://doi.org/10.1016/0956-7151\(92\)90106-O](https://doi.org/10.1016/0956-7151(92)90106-O).
- [87] Britain G, Press P. RAPID SOLIDIFICATION OF Al-Cu EUTECTIC ALLOY BY LASER

R E M E L T I N G 1989;37:3305–13.

- [88] Hashimoto T, Terasaki H, Komizo Y. Effect of solidification velocity on weld solidification process of alloy tool steel. *Sci Technol Weld Join* 2008;13:409–14. <https://doi.org/10.1179/174329308X300145>.
- [89] LIPPOLD J. Solidification behavior and cracking susceptibility of pulsed-laser welds in austenitic stainless steels. *Weld J* 1994;73:129.
- [90] Kou S, Le Y. Effect of Quenching on the Solidification Structure and Transformation Behavior of Stainless Steel Welds. *Metall Trans A, Phys Metall Mater Sci* 1982;13 A:1141–52. <https://doi.org/10.1007/BF02645495>.
- [91] Bahrami A, Anijdan SHM, Golozar MA, Shamanian M, Varahram N. Effects of conventional heat treatment on wear resistance of AISI H13 tool steel 2005;258:846–51. <https://doi.org/10.1016/j.wear.2004.09.008>.
- [92] Ning A, Mao W, Chen X, Guo H, Guo J. Precipitation behavior of carbides in H13 hot work die steel and its strengthening during tempering. *Metals (Basel)* 2017;7:1–15. <https://doi.org/10.3390/met7030070>.
- [93] Beck M, Berger P, Dausinger F, Huegel H. <title>Aspects of keyhole/melt interaction in high-speed laser welding</title> 1991:769–74. <https://doi.org/10.1117/12.25985>.
- [94] Jr MB, Corrêa AVO, Goldenstein H, Jr MB, Corre AVO. Rare earth metal induced modification of  $\gamma$ -M<sub>2</sub>C,  $\gamma$ -M<sub>6</sub>C, and  $\gamma$ -MC eutectics in as cast M2 high speed steel 2013;0836. <https://doi.org/10.1179/026708399101506355>.
- [95] Barkalow RH, Kraft RW, Goldstein JI. Solidification of M2 High Speed Steel 1972;3:919–26.
- [96] Narvan M, Al-Rubaie KS, Elbestawi M. Process-structure-property relationships of AISI H13 tool steel processed with selective laser melting. *Materials (Basel)* 2019;12:1–20. <https://doi.org/10.3390/ma12142284>.
- [97] Cottam R, Wang J, Luzin V. Characterization of microstructure and residual stress in a 3D H13 tool steel component produced by additive manufacturing. *J Mater Res* 2014;29:1978–86. <https://doi.org/10.1557/jmr.2014.190>.
- [98] Cottam R, Wang J, Luzin V. Characterization of microstructure and residual stress in a 3D H13 tool steel component produced by additive manufacturing. *J Mater Res* 2014;29:1978–86.

<https://doi.org/10.1557/jmr.2014.190>.

- [99] Mertens R, Vrancken B, Holmstock N, Kinds Y, Kruth JP, Van Humbeeck J. Influence of powder bed preheating on microstructure and mechanical properties of H13 tool steel SLM parts. *Phys Procedia* 2016;83:882–90. <https://doi.org/10.1016/j.phpro.2016.08.092>.
- [100] Liu ZH, Chua CK, Leong KF, Kempen K, Thijs L, Yasa E, et al. A Preliminary Investigation on Selective Laser Melting of M2 High Speed Steel 2011.
- [101] Asgharzadeh H, Simchi A. Effect of sintering atmosphere and carbon content on the densification and microstructure of laser-sintered M2 high-speed steel powder. *Mater Sci Eng A* 2005;403:290–8. <https://doi.org/10.1016/j.msea.2005.05.017>.
- [102] Ali H, Ma L, Ghadbeigi H, Mumtaz K. In-situ residual stress reduction, martensitic decomposition and mechanical properties enhancement through high temperature powder bed pre-heating of Selective Laser Melted Ti6Al4V. *Mater Sci Eng A* 2017;695:211–20. <https://doi.org/10.1016/j.msea.2017.04.033>.
- [103] Wang H, Zhang X, Wang GB, Shen J, Zhang GQ, Li YP, et al. Selective laser melting of the hard-to-weld IN738LC superalloy: Efforts to mitigate defects and the resultant microstructural and mechanical properties. *J Alloys Compd* 2019;807. <https://doi.org/10.1016/j.jallcom.2019.151662>.
- [104] Carter LN, Attallah MM, Reed RC. Laser powder bed fabrication of nickel-base superalloys: Influence of parameters; characterisation, quantification and mitigation of cracking. *Proc Int Symp Superalloys* 2012:577–86. [https://doi.org/10.7449/2012/superalloys\\_2012\\_577\\_586](https://doi.org/10.7449/2012/superalloys_2012_577_586).
- [105] Tjong SC, Mai YW. Processing-structure-property aspects of particulate- and whisker-reinforced titanium matrix composites. *Compos Sci Technol* 2008;68:583–601. <https://doi.org/10.1016/j.compscitech.2007.07.016>.
- [106] Boehlert CJ, Tamirisakandala S, Curtin WA, Miracle DB. Assessment of in situ TiB whisker tensile strength and optimization of TiB-reinforced titanium alloy design. *Scr Mater* 2009;61:245–8. <https://doi.org/10.1016/j.scriptamat.2009.03.054>.
- [107] Gofrey TMT, Goodwin PS, Ward-Close CM. Titanium Particulate Metal Matrix Composites – Reinforcement, Production Methods, and Mechanical Properties. *Adv Eng Mater* 2000;2:85–91. [https://doi.org/10.1002/\(sici\)1527-2648\(200003\)2:3<85::aid-adem85>3.3.co;2-l](https://doi.org/10.1002/(sici)1527-2648(200003)2:3<85::aid-adem85>3.3.co;2-l).

- [108] Cai C, Song B, Qiu C, Li L, Xue P, Wei Q, et al. Hot isostatic pressing of in-situ TiB/Ti-6Al-4V composites with novel reinforcement architecture, enhanced hardness and elevated tribological properties. *J Alloys Compd* 2017;710:364–74. <https://doi.org/10.1016/j.jallcom.2017.03.160>.
- [109] Morsi K, Patel V V. Processing and properties of titanium-titanium boride (TiBw) matrix composites - A review. *J Mater Sci* 2007;42:2037–47. <https://doi.org/10.1007/s10853-006-0776-2>.
- [110] Tamirisakandala S, Bhat RB, Miracle DB, Boddapati S, Bordia R, Vanover R, et al. Effect of boron on the beta transus of Ti-6Al-4V alloy. *Scr Mater* 2005;53:217–22. <https://doi.org/10.1016/j.scriptamat.2005.03.038>.
- [111] Tamirisakandala S, Miracle DB. Microstructure engineering of titanium alloys via small boron additions. *Int J Adv Eng Sci Appl Math* 2010;2:168–80. <https://doi.org/10.1007/s12572-011-0033-z>.
- [112] Hill D, Banerjee R, Huber D, Tiley J, Fraser HL. Formation of equiaxed alpha in TiB reinforced Ti alloy composites. *Scr Mater* 2005;52:387–92. <https://doi.org/10.1016/j.scriptamat.2004.10.019>.
- [113] Ferri OM, Ebel T, Bormann R. The influence of a small boron addition on the microstructure and mechanical properties of Ti-6Al-4V fabricated by metal injection moulding. *Adv Eng Mater* 2011;13:436–47. <https://doi.org/10.1002/adem.201000280>.
- [114] Tamirisakandala S, Bhat RB, Tiley JS, Miracle DB. Grain refinement of cast titanium alloys via trace boron addition. *Scr Mater* 2005;53:1421–6. <https://doi.org/10.1016/j.scriptamat.2005.08.020>.
- [115] Rajarshi Banerjee, A. Genç, P. C. Collins, H.L. Fraser. Comparison of microstructural evolution in laser-deposited and arc-melted In-Situ Ti-TiB composites. *Metall Mater Trans A* 2004;35:2143–52. <https://doi.org/10.1007/s11661-004-0162-0>.
- [116] Wang S, Huang LJ, Geng L, Scarpa F, Jiao Y, Peng HX. Significantly enhanced creep resistance of low volume fraction in-situ TiBw/Ti6Al4V composites by architected network reinforcements. *Sci Rep* 2017;7. <https://doi.org/10.1038/srep40823>.
- [117] Fan Z. *Microstructure and Mechanical Properties of Multiphase Materials* 1993.

- [118] Banerjee R, Collins PC, Fraser HL. Laser Deposition of In Situ Ti – TiB Composites. *Adv Eng Mater* 2002;4:847–51. [https://doi.org/10.1002/1527-2648\(20021105\)4:11<847::AID-ADEM847>3.0.CO;2-C](https://doi.org/10.1002/1527-2648(20021105)4:11<847::AID-ADEM847>3.0.CO;2-C).
- [119] Hu Y, Cong W, Wang X, Li Y, Ning F, Wang H. Laser deposition-additive manufacturing of TiB-Ti composites with novel three-dimensional quasi-continuous network microstructure: Effects on strengthening and toughening. *Compos Part B Eng* 2018;133:91–100. <https://doi.org/10.1016/j.compositesb.2017.09.019>.
- [120] Attar H, Bönisch M, Calin M, Zhang LC, Scudino S, Eckert J. Selective laser melting of in situ titanium-titanium boride composites: Processing, microstructure and mechanical properties. *Acta Mater* 2014;76:13–22. <https://doi.org/10.1016/j.actamat.2014.05.022>.
- [121] Kang N, Coddet P, Liu Q, Liao HL, Coddet C. In-situ TiB/near  $\alpha$  Ti matrix composites manufactured by selective laser melting. *Addit Manuf* 2016;11:1–6. <https://doi.org/10.1016/j.addma.2016.04.001>.
- [122] Shishkovsky I, Kakovkina N, Sherbakov V. Graded layered titanium composite structures with TiB<sub>2</sub> inclusions fabricated by selective laser melting. *Compos Struct* 2017;169:90–6. <https://doi.org/10.1016/j.compstruct.2016.11.013>.
- [123] Kühnle T, Partes K. In-Situ Formation of Titanium Boride and Titanium Carbide by Selective Laser Melting. *Phys Procedia* 2012;39:432–8. <https://doi.org/10.1016/j.phpro.2012.10.058>.
- [124] Chen Y, Zhang J, Dai N, Qin P, Attar H, Zhang LC. Corrosion Behaviour of Selective Laser Melted Ti-TiB Biocomposite in Simulated Body Fluid. *Electrochim Acta* 2017;232:89–97. <https://doi.org/10.1016/j.electacta.2017.02.112>.
- [125] Bermingham MJ, Kent D, Zhan H, Stjohn DH, Dargusch MS. Controlling the microstructure and properties of wire arc additive manufactured Ti-6Al-4V with trace boron additions. *Acta Mater* 2015;91:289–303. <https://doi.org/10.1016/j.actamat.2015.03.035>.
- [126] Xue A, Lin X, Wang L, Wang J, Huang W. Influence of trace boron addition on microstructure, tensile properties and their anisotropy of Ti6Al4V fabricated by laser directed energy deposition. *Mater Des* 2019;181:107943. <https://doi.org/10.1016/j.matdes.2019.107943>.
- [127] Ansara I, Dinsdale A, European MR-O for OP of the, 1998 undefined. Cost 507 definition of thermochemical and thermophysical properties to provide a database for the development of new light alloys: Thermochemical database n.d.

- [128] Schneider CA, Rasband WS, Eliceiri KW. NIH Image to ImageJ: 25 years of image analysis. *Nat Methods* 2012;9:671–5. <https://doi.org/10.1038/nmeth.2089>.
- [129] Joy Gockel JB. Understanding Ti-6Al-4V Microstructure Control in Additive Manufacturing via Process Maps. *Solid Free Fabr Symp* 2013:666. <https://doi.org/10.1007/s11837-005-0029-x>.
- [130] Klobčar D, Tušek J, Taljat B, Kosec L, Pleterški M. Aging of maraging steel welds during aluminium alloy die casting. *Comput Mater Sci* 2008;44:515–22. <https://doi.org/10.1016/j.commatsci.2008.04.011>.
- [131] Yan J, Zhou Y, Gu R, Zhang X, Quach WM, Yan M. A comprehensive study of steel powders (316L, H13, P20 and 18Ni300) for their selective laser melting additive manufacturing. *Metals (Basel)* 2019;9. <https://doi.org/10.3390/met9010086>.
- [132] Tolochko NK, Mozzharov SE, Yadroitsev IA, Laoui T, Froyen L, Titov VI, et al. Balling processes during selective laser treatment of powders. *Rapid Prototyp J* 2004;10:78–87. <https://doi.org/10.1108/13552540410526953>.
- [133] Sabuj SR, Hamamura M. Random cognitive radio network performance in Rayleigh-lognormal environment. *2017 14th IEEE Annu Consum Commun Netw Conf CCNC 2017* 2017;6:992–7. <https://doi.org/10.1109/CCNC.2017.7983268>.
- [134] Yang J, Sun S, Brandt M, Yan W. Experimental investigation and 3D finite element prediction of the heat affected zone during laser assisted machining of Ti6Al4V alloy. *J Mater Process Technol* 2010;210:2215–22. <https://doi.org/10.1016/j.jmatprotec.2010.08.007>.
- [135] Childs THG, Hauser G, Badrossamay M. Selective laser sintering (melting) of stainless and tool steel powders: Experiments and modelling. *Proc Inst Mech Eng Part B J Eng Manuf* 2005;219:339–57. <https://doi.org/10.1243/095440505X8109>.
- [136] Badrossamay M, Childs THG. Further studies in selective laser melting of stainless and tool steel powders. *Int J Mach Tools Manuf* 2007;47:779–84. <https://doi.org/10.1016/j.ijmachtools.2006.09.013>.
- [137] Dubčáková R. Eureka: software review. *Genet Program Evolvable Mach* 2011;12:173–8. <https://doi.org/10.1007/s10710-010-9124-z>.
- [138] Gong H, Rafi K, Gu H, Starr T, Stucker B. Analysis of defect generation in Ti-6Al-4V parts

- made using powder bed fusion additive manufacturing processes. *Addit Manuf* 2014;1:87–98. <https://doi.org/10.1016/j.addma.2014.08.002>.
- [139] Wycisk E, Solbach A, Siddique S, Herzog D, Walther F, Emmelmann C. Effects of defects in laser additive manufactured Ti-6Al-4V on fatigue properties. *Phys Procedia* 2014;56:371–8. <https://doi.org/10.1016/j.phpro.2014.08.120>.
- [140] Kasperovich G, Hausmann J. Improvement of fatigue resistance and ductility of TiAl6V4 processed by selective laser melting. *J Mater Process Technol* 2015;220:202–14. <https://doi.org/10.1016/j.jmatprotec.2015.01.025>.
- [141] Yadroitsev I, Gusarov A, Yadroitsava I, Smurov I. Single track formation in selective laser melting of metal powders. *J Mater Process Technol* 2010;210:1624–31. <https://doi.org/10.1016/j.jmatprotec.2010.05.010>.
- [142] Zhang Y, Evans JRG, Yang S. Corrected values for boiling points and enthalpies of vaporization of elements in handbooks. *J Chem Eng Data* 2011;56:328–37. <https://doi.org/10.1021/je1011086>.
- [143] Yan JJ, Zheng DL, Li HX, Jia X, Sun JF, Li YL, et al. Selective laser melting of H13 : microstructure and residual stress 2017:12476–85. <https://doi.org/10.1007/s10853-017-1380-3>.
- [144] Ghosh S, Ma L, Levine LE, Ricker RE, Stoudt MR, Heigel JC, et al. Single-Track Melt-Pool Measurements and Microstructures in Inconel 625. *Jom* 2018;70:1011–6. <https://doi.org/10.1007/s11837-018-2771-x>.
- [145] Roehling JD, Perron A, Fattebert JL, Haxhimali T, Guss G, Li TT, et al. Rapid Solidification in Bulk Ti-Nb Alloys by Single-Track Laser Melting. *Jom* 2018;70:1589–97. <https://doi.org/10.1007/s11837-018-2920-2>.
- [146] Narvan M, Al-Rubaie KS, Elbestawi M. Process-structure-property relationships of AISI H13 tool steel processed with selective laser melting. *Materials (Basel)* 2019;12. <https://doi.org/10.3390/ma12142284>.
- [147] Shakerin S, Hadadzadeh A, Amirkhiz BS, Shamsdini S, Li J, Mohammadi M. Additive manufacturing of maraging steel-H13 bimetal using laser powder bed fusion technique. *Addit Manuf* 2019;29. <https://doi.org/10.1016/j.addma.2019.100797>.

- [148] Speer J, Matlock DK, De Cooman BC, Schroth JG. Carbon partitioning into austenite after martensite transformation. *Acta Mater* 2003;51:2611–22. [https://doi.org/10.1016/S1359-6454\(03\)00059-4](https://doi.org/10.1016/S1359-6454(03)00059-4).
- [149] Liang Y, Cheng X, Wang H. A new microsegregation model for rapid solidification multicomponent alloys and its application to single-crystal nickel-base superalloys of laser rapid directional solidification. *Acta Mater* 2016;118:17–27. <https://doi.org/10.1016/j.actamat.2016.07.008>.
- [150] Barbier BD. Extension of the Martensite Transformation Temperature Relation to Larger Alloying Elements and Contents 2014:122–7. <https://doi.org/10.1002/adem.201300116>.
- [151] Roberts IA, Wang CJ, Esterlein R, Stanford M, Mynors DJ. A three-dimensional finite element analysis of the temperature field during laser melting of metal powders in additive layer manufacturing. *Int J Mach Tools Manuf* 2009;49:916–23. <https://doi.org/10.1016/j.ijmachtools.2009.07.004>.
- [152] Kenel C, Leinenbach C. Influence of cooling rate on microstructure formation during rapid solidification of binary TiAl alloys. *J Alloys Compd* 2015;637:242–7. <https://doi.org/10.1016/j.jallcom.2015.03.016>.
- [153] Bonifaz EA, Richards NL. Modeling cast IN-738 superalloy gas tungsten arc welds. *Acta Mater* 2009;57:1785–94. <https://doi.org/10.1016/j.actamat.2008.12.022>.
- [154] Grierson D, Slater A, Speirs J, Tucker GA. The appearance of polygalacturonase mRNA in tomatoes: one of a series of changes in gene expression during development and ripening. *Planta* 1985;163:263–71. <https://doi.org/10.1007/BF00393517>.
- [155] Liu W, Ma J, Atabaki MM, Pillai R, Kumar B, Vasudevan U, et al. Hybrid Laser-arc Welding of 17-4 PH Martensitic Stainless Steel. *Lasers Manuf Mater Process* 2015;2:74–90. <https://doi.org/10.1007/s40516-015-0007-2>.
- [156] Ma J, Atabaki MM, Liu W, Pillai R, Kumar B, Vasudevan U, et al. Laser-based welding of 17-4 PH martensitic stainless steel in a tubular butt joint configuration with a built-in backing bar. *Opt Laser Technol* 2016;82:38–52. <https://doi.org/10.1016/j.optlastec.2016.02.012>.
- [157] Grant NJ. Rapid Solidification of Metallic Particulates. *JOM J Miner Met Mater Soc* 1983;35:20–7. <https://doi.org/10.1007/BF03338180>.

- [158] Dantzig J, Rappaz M. Solidification: -Revised & Expanded 2016.
- [159] Miettinen J. Thermodynamic-kinetic simulation of constrained dendrite growth in steels. *Metall Mater Trans B Process Metall Mater Process Sci* 2000;31:365–79. <https://doi.org/10.1007/s11663-000-0055-6>.
- [160] Lima MSF, Vieira JD, Morato SP, Vencovsky P. Microstructural changes due to laser ablation of oxidized surfaces on an AISI M2 tool steel. *Mater Sci Eng A* 2003;344:1–9. [https://doi.org/10.1016/S0921-5093\(02\)00051-5](https://doi.org/10.1016/S0921-5093(02)00051-5).
- [161] Yang K V., Shi Y, Palm F, Wu X, Rometsch P. Columnar to equiaxed transition in Al-Mg(-Sc)-Zr alloys produced by selective laser melting. *Scr Mater* 2018;145:113–7. <https://doi.org/10.1016/j.scriptamat.2017.10.021>.
- [162] Wang F. Mechanical property study on rapid additive layer manufacture Hastelloy® X alloy by selective laser melting technology. *Int J Adv Manuf Technol* 2012;58:545–51. <https://doi.org/10.1007/s00170-011-3423-2>.
- [163] Mercelis P, Kruth JP. Residual stresses in selective laser sintering and selective laser melting. *Rapid Prototyp J* 2006;12:254–65. <https://doi.org/10.1108/13552540610707013>.
- [164] Gusarov A V., Yadroitsev I, Bertrand P, Smurov I. Model of Radiation and Heat Transfer in Laser-Powder Interaction Zone at Selective Laser Melting. *J Heat Transfer* 2009;131:072101. <https://doi.org/10.1115/1.3109245>.
- [165] Galvan D, Ocelík V, Pei Y, Kooi BJ, De Hosson JTM, Ramous E. Microstructure and properties of TiB/Ti-6Al-4V coatings produced with laser treatments. *J Mater Eng Perform* 2004;13:406–12. <https://doi.org/10.1361/10599490419919>.
- [166] Cheng Y, Shigeta M, Choi S, Watanabe T. Formation mechanism of titanium boride nanoparticles by RF induction thermal plasma. *Chem Eng J* 2012;183:483–91. <https://doi.org/10.1016/j.cej.2011.12.040>.
- [167] Shigeta M, Watanabe T. Multi-component co-condensation model of Ti-based boride/silicide nanoparticle growth in induction thermal plasmas. *Thin Solid Films* 2007;515:4217–27. <https://doi.org/10.1016/j.tsf.2006.02.042>.
- [168] Yang J, Yu H, Yin J, Gao M, Wang Z, Zeng X. Formation and control of martensite in Ti-6Al-4V alloy produced by selective laser melting. *Mater Des* 2016;108:308–18.

<https://doi.org/10.1016/j.matdes.2016.06.117>.

- [169] Hussein A, Hao L, Yan C, Everson R. Finite element simulation of the temperature and stress fields in single layers built without-support in selective laser melting. *Mater Des* 2013;52:638–47. <https://doi.org/10.1016/j.matdes.2013.05.070>.
- [170] Galvan D, Ocelík V, Pei Y, Kooi BJ, De Hosson JTM, Ramous E. Microstructure and properties of TiB/Ti-6Al-4V coatings produced with laser treatments. *J Mater Eng Perform* 2004;13:406–12. <https://doi.org/10.1361/10599490419919>.
- [171] Terasaki H, Saiki K, Yamamoto Y, Ikeda M, Komizo Y. Microstructure Control of Titanium Weld by Addition of Boron \* . *Q J Japan Weld Soc* 2009;27:130–3. <https://doi.org/10.2207/qjjws.27.130s>.
- [172] Hogan LM, Song H. Interparticle spacings and undercoolings in Al-Si eutectic microstructures. *Metall Trans A* 1987;18:707–13. <https://doi.org/10.1007/BF02649487>.
- [173] Tololi B, Hellawell A. Phase separation and undercooling in Al-Si eutectic alloy-the influence of freezing rate and temperature gradient. *Acta Metall* 1976;24:565–73. [https://doi.org/10.1016/0001-6160\(76\)90102-4](https://doi.org/10.1016/0001-6160(76)90102-4).
- [174] Magnin P, Kurz W. An analytical model of irregular eutectic growth and its application to Fe-C. *Acta Metall* 1987;35:1119–28. [https://doi.org/10.1016/0001-6160\(87\)90059-9](https://doi.org/10.1016/0001-6160(87)90059-9).
- [175] Jackson KA, Hunt JD. Lamellar and Rod Eutectic Growth. *Dyn Curved Front* 1988:363–76. <https://doi.org/10.1016/b978-0-08-092523-3.50040-x>.
- [176] Burden MH, Hunt JD. Cellular and dendritic growth. II. *J Cryst Growth* 1974;22:109–16. [https://doi.org/10.1016/0022-0248\(74\)90127-4](https://doi.org/10.1016/0022-0248(74)90127-4).
- [177] Sahoo S, Chou K. Phase-field simulation of microstructure evolution of Ti-6Al-4V in electron beam additive manufacturing process. *Addit Manuf* 2016;9:14–24. <https://doi.org/10.1016/j.addma.2015.12.005>.
- [178] Kurz W, Bezençon C, Gäumann M. Columnar to equiaxed transition in solidification processing 2001;6996. [https://doi.org/10.1016/S1468-6996\(01\)00047-X](https://doi.org/10.1016/S1468-6996(01)00047-X).
- [179] Ning F, Hu Y, Cong W. Microstructure and mechanical property of TiB reinforced Ti matrix composites fabricated by ultrasonic vibration-assisted laser engineered net shaping. *Rapid*

Prototyp J 2019;25:581–91. <https://doi.org/10.1108/RPJ-05-2018-0118>.

- [180] Liu YC, Yang GC, Guo XF, Huang J, Zhou YH. Coupled growth behavior in the rapidly solidified Ti-Al peritectic alloys. *J Cryst Growth* 2001;222:645–54. [https://doi.org/10.1016/S0022-0248\(00\)00946-5](https://doi.org/10.1016/S0022-0248(00)00946-5).
- [181] Guo H, Guo X. Microstructure evolution and room temperature fracture toughness of an integrally directionally solidified Nb-Ti-Si based ultrahigh temperature alloy. *Scr Mater* 2011;64:637–40. <https://doi.org/10.1016/j.scriptamat.2010.12.008>.
- [182] Cai C, Radoslaw C, Zhang J, Yan Q, Wen S, Song B, et al. In-situ preparation and formation of TiB/Ti-6Al-4V nanocomposite via laser additive manufacturing: Microstructure evolution and tribological behavior. *Powder Technol* 2019;342:73–84. <https://doi.org/10.1016/j.powtec.2018.09.088>.
- [183] Hunt JD, Lu SZ. Numerical modeling of cellular/dendritic array growth: Spacing and structure predictions. *Metall Mater Trans A Phys Metall Mater Sci* 1996;27:611–23. <https://doi.org/10.1007/BF02648950>.

## Appendix

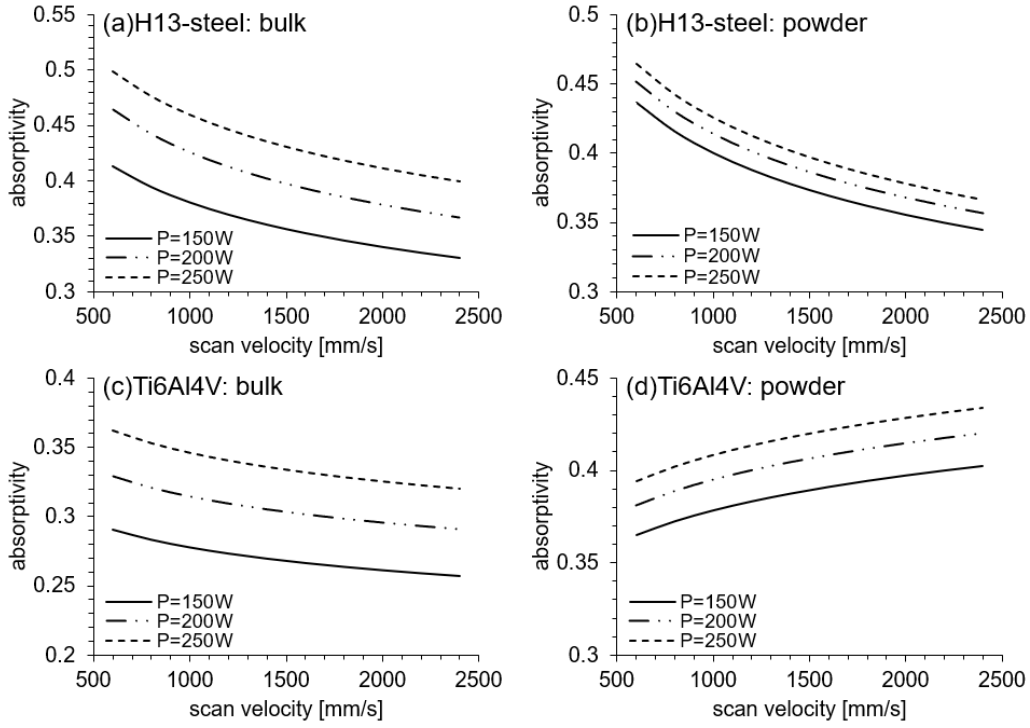


Fig 72 Change of absorptivity with laser scan velocity at laser power fixed at 150W, 200W, 250W for H13-steel in bulk-state(a) and powder-state(b) and Ti6Al4V in bulk-state(c) and powder-state(d);(a)-(d) adopts the P,V, material-related absorptivity model developed in this study (see Table 10).

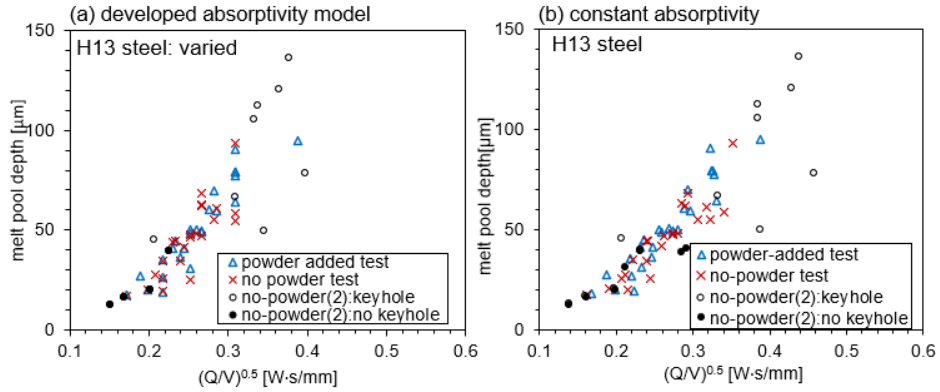


Fig 73 Comparison of melt pool depth between laser scan on bulk H13-steel and H13-steel powder layer for 3 datasets by adopting: (a) varying absorptivity model in Equation 10; (b) constant absorptivity; non-keyhole data point outlier: marked by red dashed circle; note: no-powder(2) dataset: validation data not used for data fitting

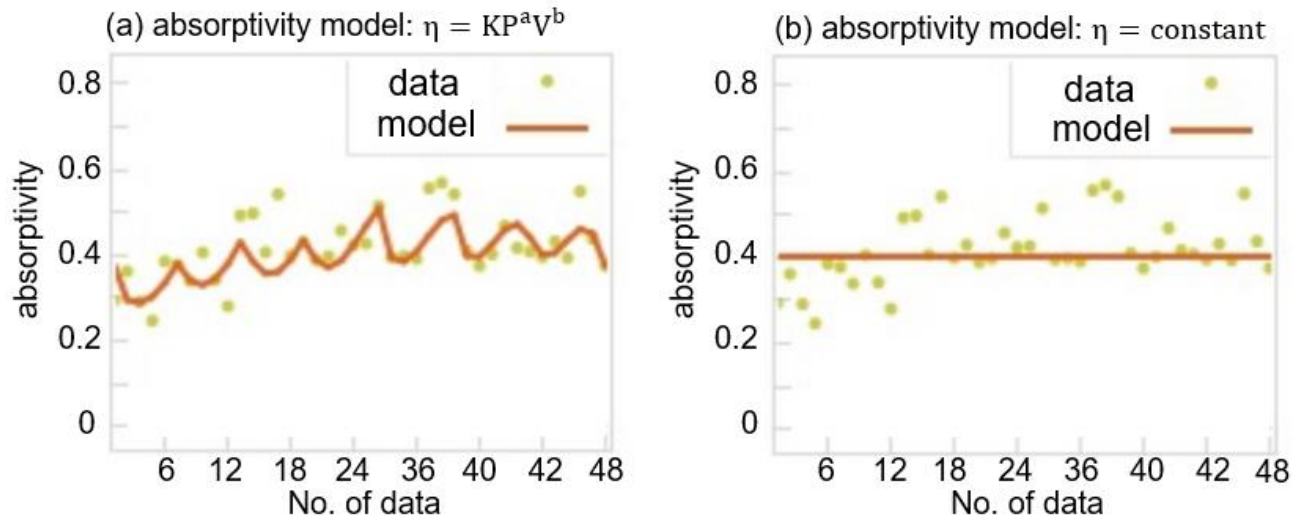


Fig 74 Fitness of the two absorptivity models for Ti6Al4V in powder state in Table 10 to the Ti6Al4V powder-added  $\eta_{pre}$  absorptivity datasets; (a) P-V varied absorptivity model and (b) constant absorptivity model; datasets: 48 data points included, corresponding to Powder-Ti64 dataset in Table 11;  $\eta_{pre}$ : defined in Equation 11, derived from experimental measurement of Ti6Al4V powder-added melt pool dimension

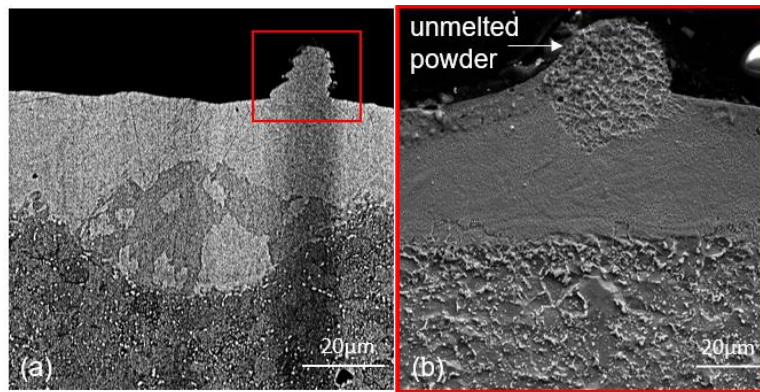


Fig 75 Observation of unmelted powder for H13 steel melt pool; (b): zoom-in image of the red box inserted in (a); (b) shows unmelted powder presents larger-scale cellular networking than the surrounding melt pool solidification microstructure

Table 22 no-powder and powder-added melt pool width deviation at same Q-V combination for Ti6Al4V and H13 steel

	Ti6Al4V: no-powder vs. powder added M.P. width deviation at same Q-V	H13 steel: no-powder vs. powder added M.P. width deviation at same Q-V
--	---	---

P-V datapoints	Exception #1:keyhole	Exception #2: P=370W	Other datapoints	Exception #1:keyhole	Exception #2: P=370W	Other datapoints
constant $\eta$	average: 20% max: 38%	32%	average: 6% max: 9%	average: 34% max: 72%	average: 20% max: 38%	average: 4.5% max: 8%
$\eta=KP^aV^b$ (Table 10)	average: 24% max: 41%		average: 3.5% max: 6%	average: 38% max: 72%		average: 5% max: 7%

( $\eta$ : absorptivity; M.P.: melt pool; P-V datapoints: see Table 11; details for exception datapoints: see Fig 20 and Fig 21)

Table 23 Experimental measurement for vol.% of type (A) microstructure in no-powder and powder-added melt pool fabricated by P-V no.#1-#40 (see Table 7)

P-V No.	Vol.% of type (A) microstructure		P-V No. (continue)	Vol.% of type (A) microstructure	
	No-powder	Powder-added		No-powder	Powder-added
#1	15%	21%	#21 <sup>P</sup>	49%	47%
#2	52	45%	#22 <sup>P</sup>	44%	54%
#3 <sup>P</sup>	12%	19%	#23		
#4 <sub>c</sub> <sup>P</sup>	15%	24%	#24	81%	85%
#5	22%	28%	#25 <sup>P</sup>	66%	60%
#6	53%	47%	#26 <sup>P</sup>	46%	49%
#7 <sub>c</sub> <sup>P</sup>	80%	75%	#27	62%	
#8	68%	62%	#28	82%	
#9 <sub>c</sub> <sup>P</sup>	28%	24%	#29	22%	47%
#10 <sub>c</sub> <sup>P</sup>	30%		#30	45%	50%
#11			#31 <sup>P</sup>	21%	29%
#12	62%	54%	#32	57%	47%
#13	80%	90%	#33		
#14 <sub>c</sub> <sup>P</sup>	58%	65%	#34	51%	45%
#15 <sub>c</sub> <sup>P</sup>	17%	26%	#35	61%	56%
#16 <sup>P</sup>			#36 <sub>c</sub> <sup>P</sup>		
#17 <sup>P</sup>	75%	78%	#37 <sup>P</sup>		
#18	81%	74%	#38 <sup>P</sup>	44%	53%
#19	84%	83%	#39	83%	77%
#20 <sub>c</sub> <sup>P</sup>	88%	75%	#40	45%	52%